Nd:YAG Based Laser Sources for Targeting Applications

James Beedell

A thesis submitted for the Engineering Doctorate in Photonics at Heriot-Watt University. The work was carried out at Selex ES in Edinburgh, from June 2008 to December 2012.

Submitted October 2013

Abstract

The aim of the research is to improve laser system products manufactured at Selex ES which are used primarily for airborne targeting applications. This is achieved by developments to the design that prevent failures during manufacture or improve beam parameters such as divergence.

A Q-switched diode-side-pumped Nd:YAG zig-zag geometry slab laser within a cross Porro prism resonator is investigated. This perturbation insensitive resonator design is used in laser systems operating over the full military environment of vibration and temperature.

A number of aspects of the design are computer modelled with experimental verification, such as the effects of thermal lensing in the Nd:YAG slab, and the polarisation states in the resonator. These were used to analyse a number of issues encountered during manufacture, such as the lack of control over the polarisation state for output coupling, pre-lase causing damage to optical elements, and thermal lensing producing variations in beam quality. A number of design changes were made and, after experiments to verify improved performance, they were successfully integrated into a number of laser production programmes.

The beam quality of laser systems was found to be affected by thermal lensing. A number of novel solutions were tested experimentally, which affected the thermal lens. Results of the alteration of the pump distribution in the Nd:YAG slab and the profile of conduction cooling are presented. 885 nm pumping instead of the traditional 808 nm pumping produced a reduction of the thermal lens by a factor of two from -0.1 D to -0.05 D, producing an improvement in the laser beam quality from M^2 6.5 to 3.5. An enhancement in brightness of 2.2 was demonstrated using a laser resonator incorporating a deformable bimorph mirror.

A new concept for a targeting laser source, which incorporated an eye-safe wavelength, was demonstrated using a common resonator intracavity OPO design. A conversion efficiency of 40% was achieved for 36 mJ output of 1573 nm eye-safe light from a 90 mJ laser at 1064 nm. The relative pointing directions of the two wavelength beams was measured to be within 250 µRad angular separation, which will be unaffected by ambient temperature variation. This level of performance is challenging to achieve in the current laser system design incorporating an extracavity OPO.

Acknowledgements

This work could not have been carried out without the help and support of my academic supervisor, Duncan Hand at Heriot Watt University and my industrial supervisors, Ian Elder and Sean Kudesia at Selex ES. I would also like to thank Dave Legge for his help particularly with computer modelling. There are many colleagues at Selex ES, who have helped me along the way. Thank you to Ian Thomson and others who have read through this thesis.

I would also like to thank the partners who have participated in the collaborative projects I have worked on during the programme of EngD research.

The EPSRC and Selex ES have both provided me with financial support to carry out the research programme, for which I am very grateful.

Last but not least, I would like to thank my family and friends, and in particular, my lovely wife Rhona, for their patience and support throughout my EngD programme.

Thank you!

ACADEMIC REGISTRY
Research Thesis Submission

Name*:*	James Beedell		
School/PGI:	Engineering and Physical Sciences		
Version: *(i.e. First, Resubmission, Final)*	Final	Degree Sought (Award **and** Subject area)	Engineering Doctorate in Photonics

Declaration

In accordance with the appropriate regulations I hereby submit my thesis and I declare that:

1) the thesis embodies the results of my own work and has been composed by myself
2) where appropriate, I have made acknowledgement of the work of others and have made reference to work carried out in collaboration with other persons
3) the thesis is the correct version of the thesis for submission and is the same version as any electronic versions submitted*.
4) my thesis for the award referred to, deposited in the Heriot-Watt University Library, should be made available for loan or photocopying and be available via the Institutional Repository, subject to such conditions as the Librarian may require
5) I understand that as a student of the University I am required to abide by the Regulations of the University and to conform to its discipline.

* *Please note that it is the responsibility of the candidate to ensure that the correct version of the thesis is submitted.*

Signature of Candidate*:*		Date:	

Submission

Submitted By *(name in capitals):*	
Signature of Individual Submitting:	
Date Submitted:	

For Completion in the Student Service Centre (SSC)

Received in the SSC by *(name in capitals):*			
Method of Submission *(Handed in to SSC; posted through internal/external mail):*			
E-thesis Submitted (mandatory for final theses)			
Signature:		Date:	

Table of Contents

List of Publications

J. Beedell, I. Elder, and D. Hand, *"Performance of a deformable mirror in a high-energy Nd:YAG laser"*, SPIE conference preceedings, p. 733805 (2009)

J. Beedell, I. Elder, K. K. Chen, S. Alam, D. J. Richardson, and D. Hand, *"Visible and mid-IR output using a fibre laser pump source"*, SPIE conference preceedings, p. 748307 (2009)

J. Beedell, I. Elder, D. Legge, and D. Hand, *"Intracavity, common resonator, Nd:YAG pumped KTP OPO"*, SPIE conference preceedings, pp. 85410Q-85410Q (2012)

J.D. Beedell, D. Legge, P.D. Thomson, E. Nisbet, J.R.M. Barr, S.S. Kudesia, *"Cost Savings and Improved Laser Performance for Targeting Laser Systems"*, Polaris Innovation Journal (Finmeccanica company journal), issue 14 (2013)

CHAPTER 1. INTRODUCTION

Selex ES manufactures laser systems primarily for one range of applications. These applications for the laser sources discussed in this thesis are outlined in section 1.1 and the performance specifications for a number of current products are summarised in section 1.2. Research and development of the laser products manufactured at Selex ES for these applications forms the original work contained within this thesis.

1.1 DESIGNATION, RANGE FINDING AND BURST ILLUMINATION LASER IMAGING APPLICATIONS

The principal line of products manufactured at Selex ES are used on military aircraft for the applications of target designation, range finding and Burst Illumination Laser (BIL) imaging at 1064 nm wavelength. The 1064 nm wavelength is termed the tactical mode. In addition, an "eye-safe" (retina safe) 1573 nm wavelength output is available for training purposes, and is thus called the training mode. For the duration of this thesis, the type of laser source which addresses all or most of these applications will be referred to as a targeting laser. The military environment demands the capability of operation over a wide range of temperature and vibration conditions, which vary from product to product. A key parameter for these applications is the boresight stability (pointing direction) over the environmental range and the co-boresight (relative pointing directions) of the tactical and training modes. Therefore, a laser source needs to employ a perturbation insensitive design. This means that the useful operation is not adversely affected by a small misalignment of any of the optical components. The footprint for the laser source is constrained so the laser designs incorporate folding optics within the laser resonator to reduce their maximum dimension.

1.2 TYPICAL SYSTEM PERFORMANCE SPECIFICATIONS

Typical specifications for targeting application laser systems are listed for both the tactical 1064 nm wavelength and the "eye-safe" training wavelength of 1573 nm in Table 1-1. From these current specifications, the requirements for a more advanced system can be inferred. The strategic aim is to offer subsequent laser system designs which have been developed to provide greater system performance offering enhanced capabilities, for use on an increasing number of military platforms.

	Energy (mJ) Tactical	**Energy (mJ) Training**	**Divergence (mRad) Tactical**	**Divergence (mRad) Training**	**Aperture (mm)**	**Repetition rate (Hz)**
Laser 1	> 220	> 80	< 0.2	0.75 to 3 (variable)	-	20
Laser 2	300	90	< 1	< 3	10	20
Laser 3	> 160	> 40	< 1.6	< 4.2	< 5	Single shot to 20

Table 1-1: Specifications for targeting laser systems produced at Selex ES [1].

Typically a pulsewidth of 10-20 ns is required for the ranging application, which means that pulse shortening of a standard Nd:YAG laser is needed, which is achieved by Q-switching.

1.3 AIRBORNE DEFENCE PRODUCT REQUIREMENTS

The typical operational temperature range for a laser system is -40°C to +55°C and the typical storage temperature is -54°C to +85°C. This large range of operating conditions means that the laser chassis can deform and makes the design of the laser resonator challenging. The vibration that the laser system must withstand means that a rugged mechanical design is required. The specification for the magnitude and frequency of vibration testing in each of the three axes depends entirely on the intended platform.

There are also challenging weight and size specifications, which also depend on the platform being considered. All these factors need to be taken into account at the start of the design phase when lab-based demonstrators are being assessed.

1.4 OUTLINE OF THESIS

An overview of the work presented in this thesis is summarised below. Chapter 2 will outline the important and relevant theoretical basis for the following research which aims to improve and develop the current design of laser systems for the targeting application. The background to this research is also reviewed, where other work, with similar aims, is discussed.

Chapter 3 investigates an issue with a targeting laser product at Selex ES, where output coupling control was limited. The resonator design was changed to provide a greater range of control.

Chapter 4 examines further development of the laser source, where another change to the resonator design was made to address pre-lase problems and reduce costs.

In Chapter 5, the root cause of slab thermal lensing in a laser resonator is investigated. In addition, thermally induced depolarisation and a number of techniques for slab thermal management are discussed.

Chapter 6 investigates the use of adaptive optics for laser brightness improvement of targeting lasers.

In Chapter 7, a novel laser system design is studied in which a laser and an intracavity optical parametric oscillator (OPO) share a common resonator. Finally, the conclusions drawn from this thesis are summarised in Chapter 8.

CHAPTER 2. THEORY AND BACKGROUND MATERIAL

This Chapter introduces the main topics of this thesis, the relevant theory and a review of the influential literature. A number of laser systems manufactured at Selex ES are based on laser diode-side-pumped Nd:YAG slab, cross Porro prism technology, which is considered state-of-art. The details of this resonator including the polarisation output coupling and Q-switching are explained using relevant literature. The reasons why this design is chosen and the use of an alternative ring resonator design is discussed. Technology, which is investigated in later Chapters and has the potential to extend laser system capability, including adaptive optics and intracavity OPOs, is also reviewed in this Chapter.

2.1 ND:YAG CRYSTAL LASING MEDIUM

The principal wavelength of operation for the targeting application is 1064±1 nm. Historically, the success of the ubiquitous Nd:YAG laser, which preferentially operates at 1064 nm wavelength, was the reason for this. The wavelength of operation is within the transmission wavelength region of the atmosphere but is invisible to the naked eye and is therefore covert. Laser sources which produce other wavelengths (other than in the eye-safe range) are unlikely to be considered due to the current detector equipment on missiles, range receivers and infrared cameras which operate at1064±1 nm.

Neodymium-doped yttrium aluminium garnet (Nd:YAG) is the most commonly used medium for solid-state lasers due to its favourable properties for laser operation. YAG is a hard crystalline material, with good optical quality and good thermal conductivity [2]. The radii of the Nd^{3+} ions which substitute the Y^{3+} ions in the $Y_3Al_5O_{12}$ crystal lattice differ by approximately 3%. Therefore, highly doped Nd:YAG results in strained crystals due to the distorted lattice of the YAG. In addition, as the doping level increases, concentration quenching increases, which reduces pumping efficiency. These factors limit the typical doping concentration to a maximum value of approximately 1%. The Nd:YAG laser is a four energy level system, which can have superior efficiency

when compared with a three-level laser system. This is because the lasing action is not impeded by a populated lower laser energy level for four level systems [2]. In addition, Nd:YAG has a large effective emission cross-section (2.8×10^{-19} cm^2 at 295 K) and a relatively long upper state lifetime (230 μs) allowing efficient generation of high energy pulses. An energy level diagram is shown in Figure 2-1, which illustrates the commonly used 808 nm pumping transition and the dominant 1064 nm laser transition. An alternative 885 nm pumping band is also shown. The non-radiative energy decay transitions associated with the 808 nm pumping transition and the 1064 nm laser transition, are indicated using dashed arrows.

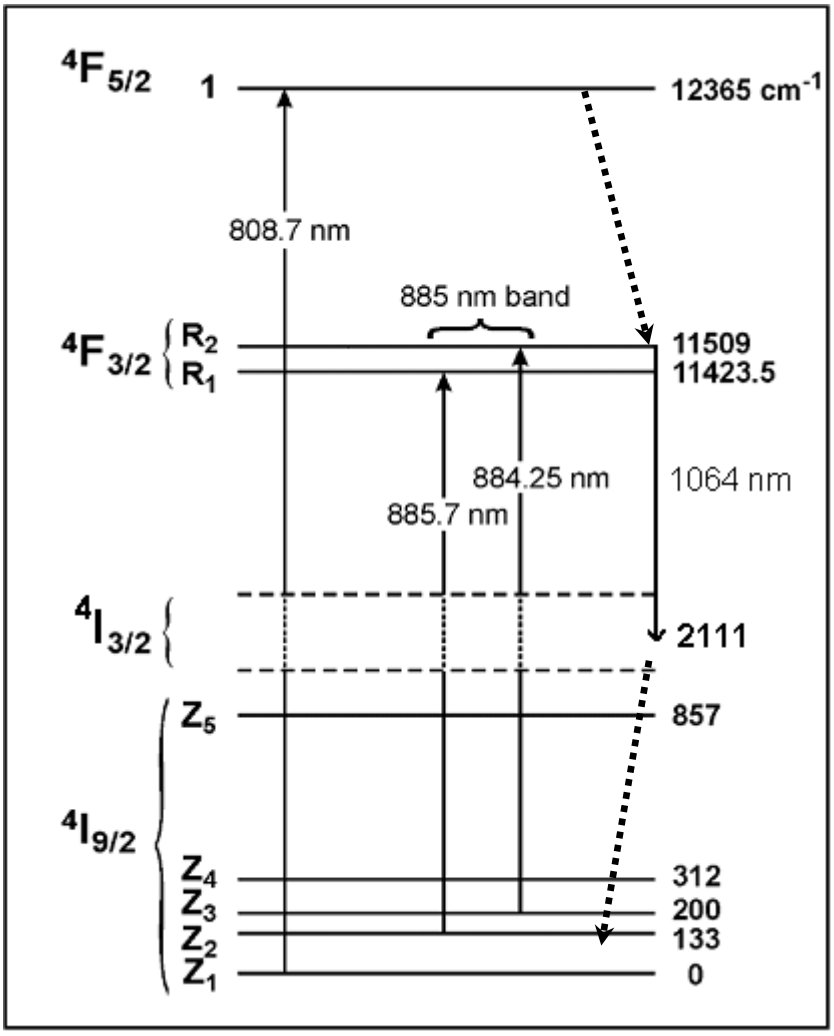

Figure 2-1: Energy level diagram which shows traditional 808 nm pumping and the alternative wavelength of 885 nm. The 1064 nm wavelength laser transition is also shown. [3]

In Figure 2-2, an absorption spectrum is shown for 1% at. doped Nd:YAG. Three arrows indicate the positions of absorption lines for pumping at wavelengths of ~808 nm, ~870 nm and ~885 nm. Nd:YAG has an upper state lifetime of 230 µs when operating at 1064 nm, so the diode laser pumping duration under QCW pumped Q-switched operation should be of that order to maximise efficiency.

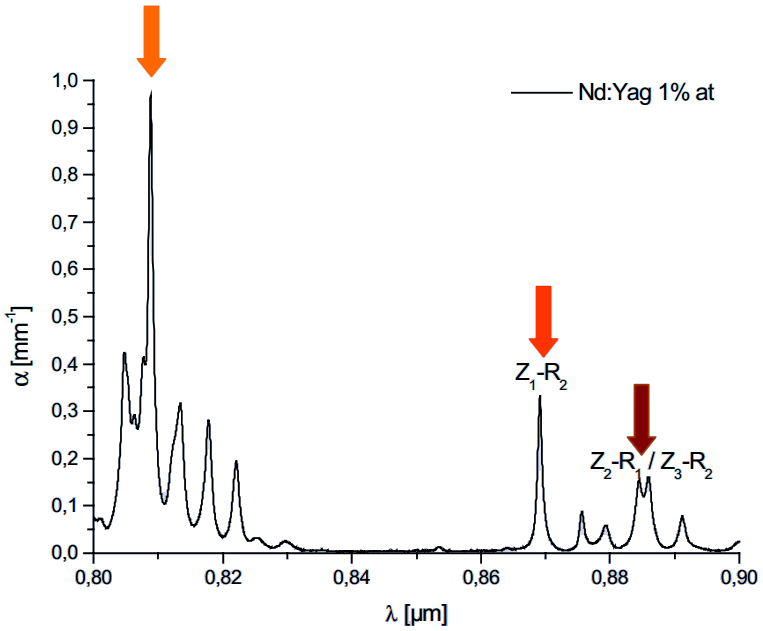

Figure 2-2: Absorption of 1% doped Nd:YAG [4] or [5]

The typical pumping wavelength used within the majority of this thesis is 808±2 nm, which is by far the most common pumping wavelength for Nd:YAG. [6] In Chapter 5, an alternative pumping wavelength of approximately 885 nm is investigated.

2.2 PUMPING SOURCE FOR ND:YAG

Legacy targeting laser systems produced at Selex ES utilise flashlamps (gas discharge lamps) to pump a Nd:YAG rod inside an elliptical pump chamber with reflective walls that focus the radiation from the flashlamp into the centre of the laser rod. It is stated in Koechner [2] that laser diode pumped laser systems are far more efficient than other

lasers pumped by other methods such as tungsten lamps or arc lamps. The main reasons for this are the low pump brightness and the broad emission wavelength range of the lamps compared with that achievable with laser diodes, where the design is tailored to generate a centre wavelength to match the absorption band of the laser gain medium. Compared to the lamp sources laser diodes produce narrow linewidth radiation, typically with linewidths of ≤ 3 nm. In addition flashlamps are less efficient than laser diodes. A greater heat load is produced when pumping with flashlamps, due to inefficient conversion from the electrical energy, and inefficient absorption of the pump energy. All current targeting lasers produced at Selex ES use 808 nm laser diode arrays. Typically, a Nd:YAG slab is side-pumped with five stacks of ten 80 W bars of laser diode emitters. These laser diodes are pulsed, with a typical firing duration of 150 µs at a typical pulse repetition frequency of 20 Hz.

Nd:YAG lasers are traditionally pumped into the strongly absorbing $^4F_{5/2}$ energy level, which introduces a parasitic quantum defect of approximately 900 cm^{-1} between the pump and emitting energy levels that transforms into heat. [7] The quantum defect can be reduced by pumping directly into the $^4F_{3/2}$ upper laser level. The strongest absorption line for pumping Nd:YAG into this level has a wavelength of 870 nm, with a narrow FWHM linewidth of less than 1 nm [7], when compared with a FWHM of approximately 3 nm for the 808 nm peak. A typical laser diode has a broader linewidth than the 870 nm absorption line and therefore provides a poor overlap and weak absorption. Ti:sapphire lasers have been used to pump at the 870 nm wavelength line with greater absorption efficiency due to their narrower linewidth [9]. This method of pumping is however unsuitable for the applications in this thesis, where cost, size and robustness are of importance. The typical targeting laser therefore uses laser diode pumping centred on the commonly used 808 nm line.

In Chapter 5, 885 nm laser diode pumping will be investigated as an alternative to the currently used 808 nm laser diodes. Although the absorption cross-section in this band is reduced when compared with 808 nm pumping, this wavelength provides direct pumping into the $^4F_{3/2}$ upper laser level, as for the 870 nm. However, the double peaked absorption line is wider than the 870 nm peak and is therefore more suitable for laser diode pumping (see Figure 2-2).

2.3 HEAT LOAD IN ND:YAG DUE TO PUMPING

The heat load produced in the Nd:YAG crystal due to laser diode pumping can be calculated using Equation 2.1. [7, 8]

$$\eta_{heat}(lasing) = 1 - \eta_p \left[(1 - \eta_l)\,\eta_{qe}\eta_{qdf} + \eta_l\eta_{qdl}\right] \quad (2.1)$$

where η_{heat}(lasing) is the heat fraction produced under lasing conditions when pumped at 808 nm, η_p is the pump level efficiency, η_l is the laser extraction efficiency, η_{qe} is the radiative quantum efficiency and η_{qdl} and η_{qdf} are the quantum defect for laser emission and spontaneous emission respectively.

If an alternative pumping wavelength is used, such as 885 nm, then the values for pump level efficiency and the quantum defects for laser emission and spontaneous emission will be different and alter the heat load. The values used for the parameters are summarised in Table 2-1 for the 808 nm and the 885 nm pumping wavelengths.

Parameter	**808 nm wavelength**	**885 nm wavelength**
Pump level efficiency	0.95[2]	1[9]
Radiative quantum efficiency	0.95[9]	0.95[9]
Fluorescence quantum defect	808/1038[8]	885/1038[8]
Laser transition quantum defect	808/1064	885/1064
Non-lasing heat fraction (calculated)	0.297	0.19
Lasing heat fraction (calculated)	0.287	0.178

Table 2-1: Summary of parameters for the 808 nm and 885 nm Nd:YAG pump bands.

2.4 PUMPING GEOMETRY

There are a number of solid-state laser gain medium geometries such as rods, slabs, discs, waveguides and fibres, which have all been used to create lasers. A slab geometry is the most suitable for this type of laser source, which is required to produce large pulse energies of >160 mJ. For a high-energy laser system a large pumped volume is needed to store the required amount of energy on the laser transition. Consideration of laser-induced damage means that relatively large optical apertures are also required. The high pump energy required favours the use of high peak-power diode stacks, with the simplest pumping scheme involving locating the stacks adjacent to the gain medium. All these factors favour the use of a side-pumped geometry rather than end-pumping.

When beam quality is not a first priority, a square cross-section slab can be used, which is ideal for side-pumping. A side-pumped slab will have a good overlap with a multi-mode laser beam, whereas an end-pumped rod would be better suited if a single-mode laser beam was required. If the laser medium is pumped from a single side, a slab has an advantage over a rod that the pump can be easily double-passed by simply coating the back surface of the slab with a high reflectivity coating for the pump wavelength. The double-pass-pumping increases the pump length and increases the absorption efficiency. A photograph of a typical Nd:YAG slab bonded onto a metal alloy mount is shown in Figure 2-3. The slab is pumped from one side and is cooled from the other via conduction. The trade-off for using a slab design with single-side-cooling rather than double-side-cooling is that a longer path exists to extract the heat and therefore there is a greater temperature gradient than double-side-cooling. Single-side-cooling is however a simpler design.

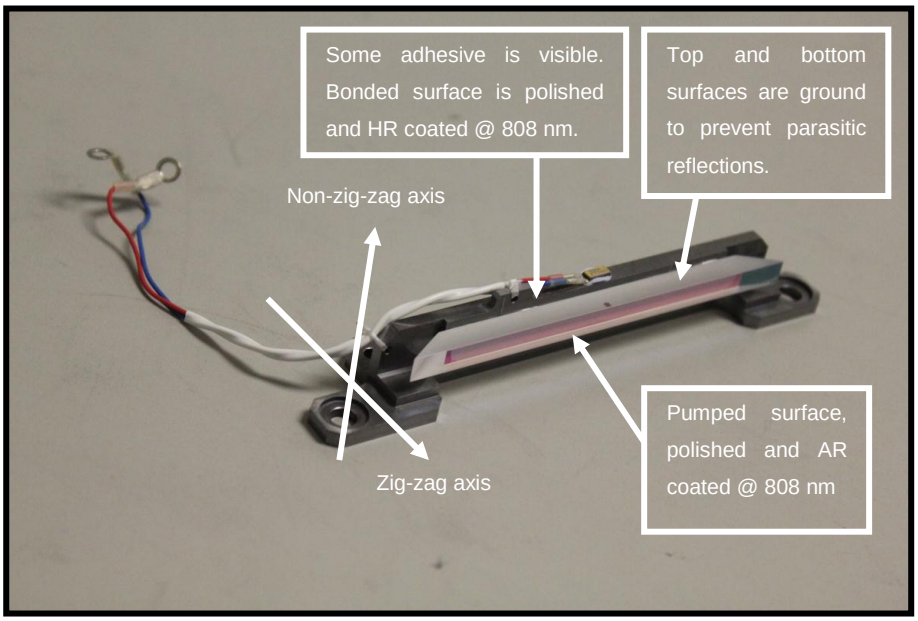

Figure 2-3: Typical Nd:YAG crystal slab bonded onto a metal alloy mount.

An isosceles trapezoidal shaped slab is used, which has a square cross-section and ends which are cut at 31° internal angle. A square cross-section is used rather than a rectangular cross-section to ensure that the laser mode is symmetrical about a diagonal line, and can be flipped about this line as will be described in Section 2.6.5 when the resonator is discussed. The refractive index of Nd:YAG is sufficiently high compared with the adhesive such that light is totally internally reflected by the slabs polished surfaces. The laser mode entering one face of the slab is refracted and then zig-zags inside the slab before refracting out of the other end. This pumping geometry is known as the zig-zag geometry and is shown schematically in Figure 2-4. The isosceles trapezoidal shape produces an odd number of internal bounces, whereas a parallelogram shaped slab would produce an even number of internal bounces.

Figure 2-4: Schematic diagram of trapezoidal laser slab showing zig-zag path of laser mode.

Typically a 5 mm square cross-section slab is used, which has nine internal bounces for a ray which enters the slab in the direction parallel with the slab as shown in Figure 2-4.

If the ends of the slab were uncoated, the s-polarisation state would be highly reflected and the p-polarisation (in the plane of the laser zig-zagging) highly transmitted, as the 31° angle is near Brewster's angle for Nd:YAG. The typical resonator design which will be discussed in Section 2.6.5 uses a polarisation state which has components both s-polarised and p-polarised states. To prevent the loss of the s-polarised light, the end surfaces have dielectric coatings to allow both polarisation states to pass with an equal loss of approximately 2%. The long faces have dielectric coatings to prevent significant loss of the pump light on entry to the slab and on reflection on the back surface, which double passes the pump light.

The advantages of zig-zag geometry slabs over conventional side-pumped slab geometries has been demonstrated [10]. This pump head geometry provides cancellation of thermal lensing in the zig-zag plane, which corresponds to the principal temperature gradient in the slab. This temperature gradient is the source of the dominant thermal lens. In the idealised case of perfectly uniform heat disposition in the slab, and no edge effects to consider (infinite length slab), the zig-zag geometry completely cancels out any dn/dT thermal lensing in the zig-zag plane [11, 12], producing a near-plane wavefront with no effect on the laser mode. Distortion of the slab due to the thermal gradient would not be cancelled out by the zig-zag path of the laser mode. In reality, where edge effects exist, complete cancellation of dn/dT in the zig-zag axis does not occur, and finite temperature gradients in the non-zig-zag plane leads to a thermal lens contribution in both of these axes. The optimised pump length for maximum cancellation of the thermal gradient is discussed in Chapter 5.

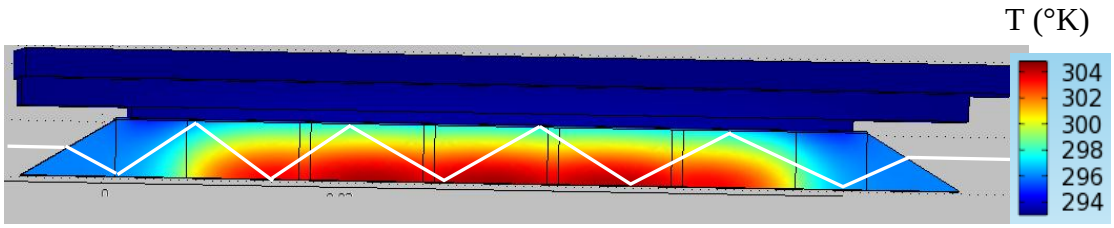

Figure 2-5: Diagram of a laser slab from above with a typical temperature distribution and the path of the central beam ray drawn on.

The temperature distribution in a typical slab assembly, when heated during side-pumping, is shown in Figure 2-5, by the colour. It can be seen that the edges of the hot region shown in red are not symmetrical across the slab width and do not abruptly stop at the end of a full zig-zag of the beam path (white line).

2.5 Q-SWITCHING

As stated in Chapter 1, a pulsewidth of 10-20 ns is required for the range-finding application, which means that pulse shortening of a standard Nd:YAG laser is needed, which is achieved via Q-switching. Active or passive Q-switching can be used. In this thesis, only active Q-switching is discussed as the current laser systems use active Q-switching techniques. An opportunity exists for the development of a low energy laser system utilising a passive Q-switching technique, which eliminates the requirement for a high-voltage Q-switch driver, and thus reduces the system complexity and cost. The wall-plug efficiency of the laser system may be increased or decreased depending on relative electrical power required for driving the active Q-switch and the efficiency reduction of the passively Q-switched laser system.

Passive Q-switching works by introducing a saturable absorber into the laser resonator, which holds the resonator in low Q up until the point in time when the absorber bleaches and rapidly switches the resonator to a high Q mode, releasing a short pulse of light. A typical material for use as a passive Q-switch for Nd:YAG is Cr:YAG. Passive Q-switching offers simplicity in laser design, compactness, low cost, and weight. However, relative to active Q-switching, passive Q-switching has several deficiencies:

1. A limited hold-off of ~6-8 dB for passive vs. >20dB for active Q-switches, which limits the build-up of gain and energy available for extraction,

2. A residual non-saturable absorption in the Cr:YAG that leads to a decrease in laser efficiency, and

3. A relatively large pulse-to-pulse timing jitter. For some applications it is this last deficiency, timing jitter, that mandates the use of the active Q-switching, despite the inherent increase in complexity and cost. [13]

2.5.1 Electro-Optic Q-switching

Electro-optic Q-switching is used in targeting lasers as opposed to acousto-optic Q-switching. This is because in the high pulse energy lasers the pump energy storage is many times the threshold and requires a large intracavity loss to prevent oscillation. A polarisation output coupled resonator with an electro-optic Q-switch can provide an extinction ratio of >23 dB, whereas an acousto-optic Q-switch would provide a lower extinction ratio with a single-pass loss of approximately 40% [2]. The higher extinction ratio provided with an electro-optic Q-switch is required to achieve hold-off in the laser resonator.

There are two types of crystals which are commonly used as Pockels cells in the Selex ES laser systems, which are lithium niobate ($LiNbO_3$ or LN) and Rubidium Titanyle Phosphate ($RbTiOPO_4$ or RTP). Either type of Q-switch can be successfully used in a laser resonator, but RTP is increasingly preferred due to the problem of static charge build-up on LN crystals when their temperature is altered, which decreases its effectiveness. Alpha particle radioactive sources can be utilised as one method to reduce the static charge build-up on LN crystals, but the required control of these sources increases the production costs. The practical design issue for switching from one type of Q-switch to the other, is the change in polarisation state requirements. The LN pockels cell requires a horizontal or vertical linear polarisation state, whereas the RTP pockels cell requires a diagonal polarisation state. (linear polarisation states rotated by 45º to the required state will be unaffected by the voltage applied to the pockels cell). A half waveplate can be used to rotate incident polarisation before a RTP Q-switch rather than rotating the crystals. An additional advantage of the RTP Q-switch is that the laser induced damage threshold is higher than for the LN Q-switch (Specified at 500 $MWcm^{-2}$ and 300 $MWcm^{-2}$ for RTP and LN crystals respectively).

2.5.2 The pre-lase problem

The electrooptic Q-switch uses polarisation as the switching mechanism. This means that a pure linear polarisation state is required in order for all of the light to be coupled out of the resonator during the low-Q resonator state. If instead of a linear polarisation state, a slightly elliptical polarisation state is present, a small amount of light could resonate in the time period before the Q-switch is opened.

The typical targeting laser system has an energy detector, which enables a measurement of energy that may be an indication of prelase, which would then trigger laser turn-off in order to prevent optical damage. Although prelase can be triggered by poor extinction ratio within the Q-switch section of the laser resonator, an alternative source of prelase could be parasitic oscillations. These are caused by a spurious reflection of the laser output beam back into the laser resonator. Parasitic oscillations are more likely when an amplifier stage is used in the laser system. The probability of parasitic oscillations is minimised by the use of antireflection coatings on optics, and the intentional introduction of a small off-set angle of the optics from normal (to the nominal laser mode).

2.6 RESONATOR DESIGN

2.6.1 Laser transverse modes

The optical field inside a laser resonator can be described as an incoherent superposition of independently oscillating Hermite-Gaussian transverse modes. These Hermite-Gaussian modes are termed $TEM_{m\,n}$ and are basically rectangular arrays of m+1 by n+1 peaks, with the higher order modes being larger in area as shown in Figure 2-6. When a beam is composed of a number of transverse modes, it is known as a multimode beam.

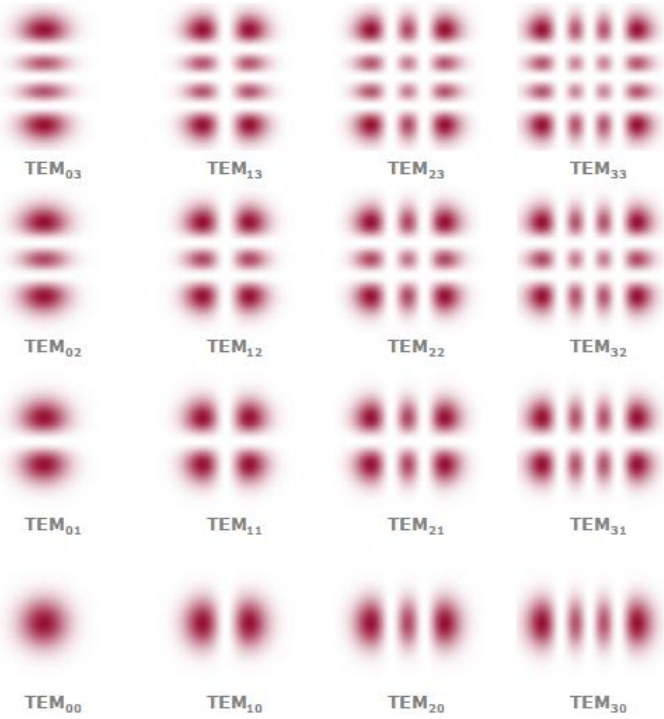

Figure 2-6: Intensity profiles of the lowest-order Hermite–Gaussian modes, starting with TEM_{00} and going up to TEM_{33}. [14]

If a resonator design allows a large number of these modes to oscillate simultaneously, they are able to independently overlap with the gain medium efficiently, which produces a uniform flat-top profile. However, the beam quality (M^2 value) of the higher order modes is worse than the lower order modes. Therefore, the divergence of the multimode beam will be greater than for a single-mode beam.

The design of the resonator will determine the size of the TEM_{00} mode at the position of the limiting laser aperture (the slab in this case). The resonator will then support modes up to the size of the aperture. Beam quality is determined by the ratio of the aperture to the TEM_{00} size.

To operate a laser efficiently, the pump profile must be similar to the mode profile, otherwise overlap is poor and pump energy is wasted (also producing heat in the laser medium). Targeting lasers produced at Selex ES produce multimode beams, and typically operate in a set of modes up to TEM_{33}. This is observed in the near field intensity pattern for some laser resonators. The set of modes used in a typical targeting laser represents an acceptable compromise between beam quality and efficient laser operation.

2.6.2 Resonator stability

It is often simpler to refer to resonators by their two-mirror equivalents with mirror radius of curvatures R_1 and R_2, separated by a length L [15, 16]. The stability of these resonators is shown on the stability diagram in Figure 2-7, where $g_1 = 1 - L/R_1$ and $g_2 = 1 - L/R_2$. L is the mirror spacing and R_1 and R_2 are the radii of curvature of the mirrors. The stability range is defined by $0 \leq g_1 g_2 \leq 1$, which is the shaded area of the diagram.

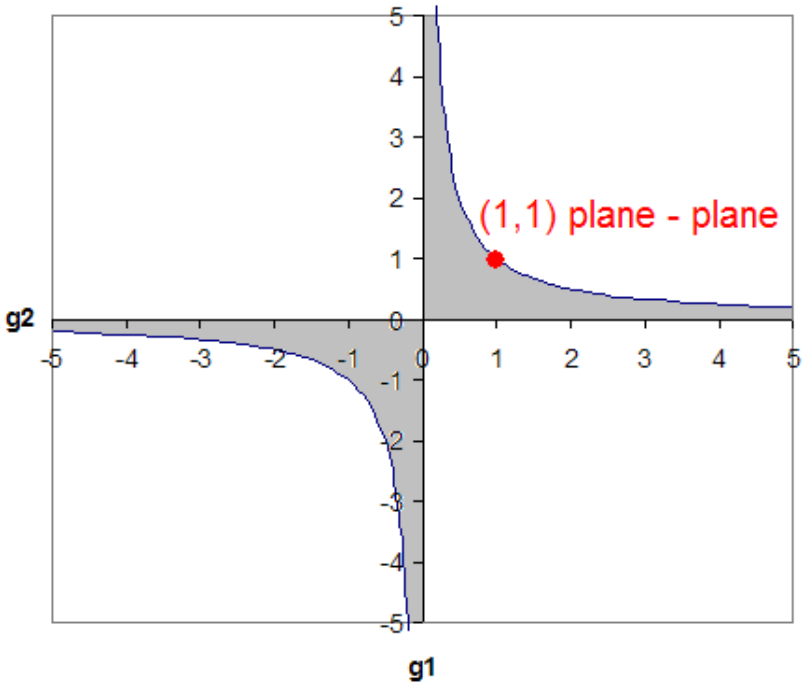

Figure 2-7: Stability diagram for a two-mirror optical resonator.

The most stable resonator (that is most resistant to perturbation) is the confocal case (0,0). The two resonator types on the limits of stability are concentric (-1,-1) and plane-plane (1,1). The crossed Porro resonator typically used in targeting lasers is a plane-plane type and is indicated on the diagram in Figure 2-7 by a dot.

It may seem odd to choose a resonator type which is on the absolute limits of stability but there are four good reasons for doing so.

1. The plane-plane resonator has the largest TEM_{00} waist size of all the resonator types. This means that for a given aperture, it will produce the least multimode beam and therefore best beam quality whilst maintaining a large mode volume to ensure efficient energy extraction.

2. A large beam size can produce high energy pulses with a reduced likelihood of laser induced damage to optical elements.

3. As the waist is so large, it can be considered to be essentially constant in size throughout the resonator (collimated), making it easier to accommodate optical elements such as polarisers and q-switches.

4. In reality, the plane-plane resonator is actually more stable than the purely geometrical stability diagram would suggest (if the gain in the resonator is high).

2.6.3 Plane-plane resonator

Diffraction will act to support modes slightly beyond the geometrical limit, at the introduction of some loss [17]. If the resonator has sufficient gain to offset this loss then the mode will be supported. Diffraction loss is higher for the higher order modes (because they are larger and hence experience greater clipping at the edges of the aperture). This is illustrated in Figure 2-8.

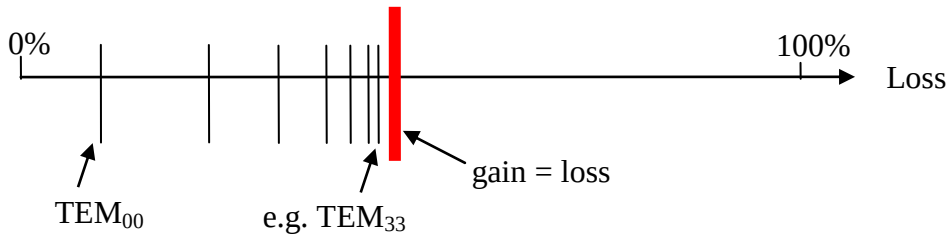

Figure 2-8: A schematic diagram of the losses for increasing transverse mode orders.

The vertical lines indicate the round trip loss experienced by each of the transverse modes: lowest order TEM_{00} on the left up to higher orders (e.g. TEM_{33}) on the right. The position of these lines is determined by the Fresnel number of the resonator. The thick red line indicates the round trip gain level. Modes that exhibit more round trip loss than gain will not be supported. In reality the round trip gain is slightly different for each mode (depending on the mode overlap) but this illustrates the general principle. Note that the difference in loss between the modes grows smaller as the mode number increases. The initial gain is much higher for Q-switched lasers (and changes over time) than for fixed-Q lasers and hence the beam quality will be slightly different in each case.

2.6.4 Effect of a lens in a plane-plane resonator

A weak negative lens in the resonator will act to increase the losses of all the modes, pushing the set of lines to the right in Figure 2-8. This will lead to the highest order modes no longer being supported, and hence an improvement in beam quality. This leaves more gain available for the lower order modes. Provided that the overlap is still sufficiently high, there will be very little drop in extracted energy. As the lens grows even stronger and the number of modes reduces, so the overlap drops and energy is left unextracted. For a typical targeting laser, the highest mode structure should be at least TEM_{22} to ensure good overlap with the gain. This is because a TEM_{00} mode is circular (as shown in Figure 2-6) and the slab cross-section is square. Conversely, a positive lens will reduce losses, allowing ever higher modes to be supported, reducing beam quality.

2.6.5 Cross Porro prism resonators

It was pointed out in Chapter 1 that the military environment demands a robust laser resonator design that is able to operate over a range of temperature and vibration conditions. A design which is insensitive to small misalignments of resonator optics, will perform better under these conditions. One such resonator design is the crossed

Porro prism resonator, which uses Porro prisms in the place of resonator mirrors. A near plane wave front oscillates in this resonator (in the absence of focal power inside the resonator). An optical path is always possible, due to the insensitivity of the Porro prisms to misalignment, in one axis each, which are set orthogonal to one another, and the resonator is therefore said to be "self-aligning". The optimisation of the resonating beam path position through the gain medium is achieved by rotating alignment wedges positioned adjacent to the Porro prisms.

As this type of resonator does not use mirrors, an alternative output coupling scheme is required. The favoured solution is to provide output coupling via polarisation control. A Nd:YAG laser within a crossed Porro prism resonator was built for the application of range-finding and was reported to successfully withstand 150 g's on a shock machine. [18] This design was a Nd:YAG rod pumped by a lamp and was actively Q-switched using a $LiNbO_3$ Pockels cell. The output coupling was via a calcite polariser and the level of output coupling was controlled via the combination of Porro prism-induced phase shift and prism azimuth angle. In the paper the equation for the Porro prism phase shift associated with total internal reflection is stated. This will be used in Chapter 4, when the Porro prism depolarisation is studied.

In the typical laser design at Selex ES, rather than using the Porro prism phase shift as part of the output coupling, a dielectric coating is applied to the total internal reflecting surfaces in order to compensate for the phase shift. This means that the Porro prism azimuth angle can be fixed, for a more robust design. A waveplate is used to adjust the output coupling instead.

Slab lasers are less affected by depolarization loss than rod lasers, as the majority of the stress that causes depolarization is along a single axis, which is cancelled by the zig-zag beam path. In the crossed Porro configuration, an advantage of the variable reflectivity resonator is that the depolarized component of the beam contributes to the output rather than acting as a loss, as in a conventional plane-plane resonator that utilises a partially reflecting mirror. This means that depolarisation loss does not degrade the efficiency of a crossed Porro resonator, so was an advantage for early designs which used rods within crossed Porro resonators. However, depolarisation can be detrimental to beam quality, so is minimised in current designs by the use of slab lasers with zig-zag beam paths.

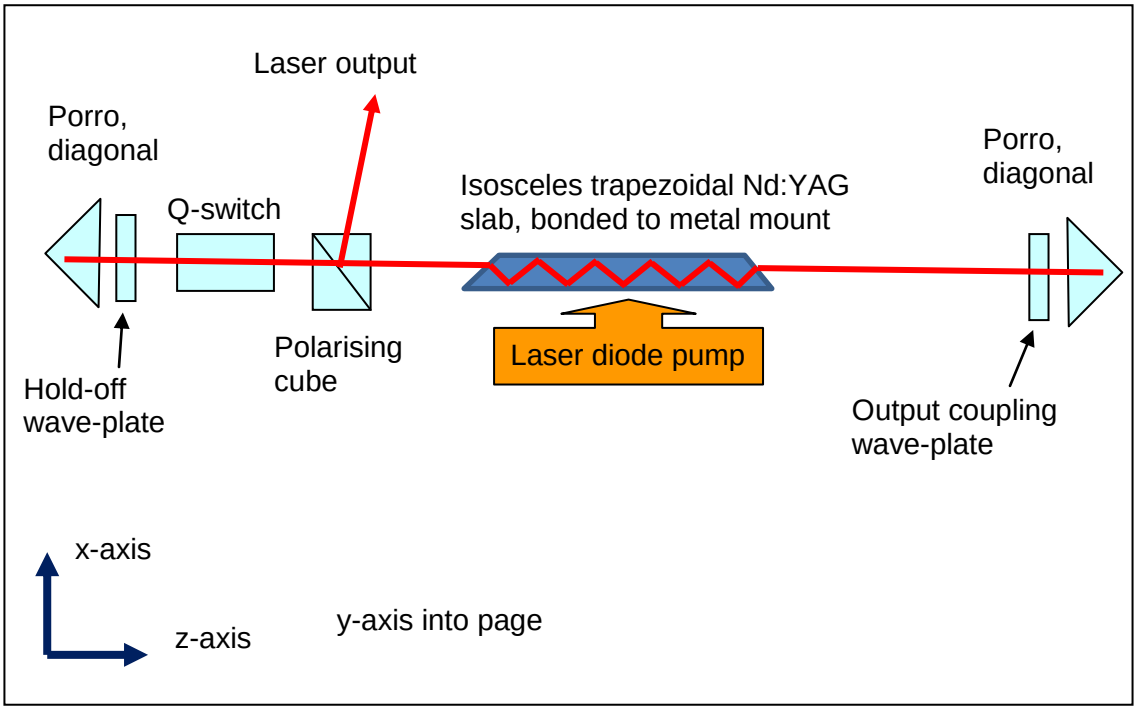

Figure 2-9: Schematic diagram of a cross Porro laser resonator incorporating all the important resonator optics that are found within a typical laser system produced at Selex ES.

The diagram in Figure 2-9 shows a typical cross Porro prism resonator design used for targeting applications. The isosceles trapezoidal shaped Nd:YAG slab is oriented such that the laser mode zig-zags in the x axis. The non-zig-zag axis is the y axis. The Porro prisms have their apex in a diagonal direction relative to the laser slab in the x-y plane. Isosceles trapezoidal shaped slabs produce an odd number of internal bounces of the laser mode, and thus act like a dove prism, flipping the laser mode. The rotation of the laser slab therefore affects the alignment of the laser resonator (in two out of three axes). In contrast, a parallelogram shaped slab would not affect the alignment of the laser resonator (apart from aperturing and amplifying the mode differently).

The output coupling is adjusted by rotating the output coupling half wave plate, which is on the slab side of the polarising output coupler, which is in the middle of the resonator. The Q-switch is located on the other side of the polarising output coupler, due to the lower power density, which is present on the left hand side of the polarising beam splitter. Typically, a dielectric coating is present on the Porro prisms to compensate for depolarisation that is introduced by the total internal reflections. This

depolarisation needs to be compensated for in order to achieve hold-off during Q-switching.

In the literature, a Nd:YAG laser used an electrooptic Q-switch within a crossed Porro prism resonator. [18] The Q-switch voltage associated with the minimum resonator reflectivity was non-zero. The Selex ES design, which has approximately zero phase shift from the Porro prisms, can use a zero voltage for the hold-off, which is the zero resonator reflectivity state of the laser. This is ideal, as for non-zero voltages, any fluctuations in the voltage could cause pre-lasing, which is a failure of the hold-off condition which prevents laser oscillation.

2.6.6 180° and 90° image rotation designs

The cross Porro prism resonator traditionally has the Porro prisms oriented orthogonal to each other. This design minimizes the resonators sensitivity to small perturbations of the resonator optics. An alternative design is also used a Selex ES, whereby the Porro prisms are orientated such that the image reflecting axis for each is crossed by 45° rather than the traditional 90°. This design is more sensitive to perturbations than the traditional cross Porro prism design, but still less sensitive than a plane-plane resonator. The reason for choosing the 45° cross Porro prism resonator design for some laser systems is the laser mode rotation per round-trip, which is 90° rather than 180° as for the traditional cross Porro prism design. The 90° beam rotation improves the circularity of the far field beam profile, which is a performance criterion for some systems.

2.6.7 Detuning of laser output energy

Polarisation output coupling is required for crossed Porro prism resonators. This is advantageous, as the optimum output coupling can be selected. In addition, if required, adjustment of output coupling to reduce the intracavity power density is possible in order to reduce the probably of laser induced damage of sensitive intracavity optical elements. As the reflectivity of the resonator is reduced from its optimum value, the

fixed-Q output pulse energy of the laser is reduced. However, for a reduction in energy of just 10%, the power density is reduced by 62% as will be shown in Chapter 3.

A model has been constructed at Selex ES, which predicts the Q-switched pulse energy using the equations in [19]. This model shows that for a typical targeting laser, the value for output coupling, which leads to a 10% reduction in fixed-Q pulse energy, in fact has near to optimum output coupling for the Q-switched case.

2.6.8 Ring resonator

The crossed Porro prism resonator may have been bought about by the replacement of the plane mirrors with Porro prisms, but in fact the crossed Porro prism resonator is a special case of the ring resonator. The crossed Porro prism resonator is a bi-directional non-planar ring resonator, whereby the two counter propagating beams are folded back on top of one another. This means that both the beams pass the laser gain medium, which improves the efficiency over a uni-directional ring resonator, which only passes the laser gain medium once per round trip of the resonator.

Unidirectional non-planar ring resonators can be used instead of crossed Porro resonators, with the same tolerance to misalignment of the resonator optics. Note that in Figure 2-10, the folding prism and corner cube at each end of the resonator are positioned at an angle 45° relative to the other components. This out-of-plane folding of the laser mode is the reason for the 90° rotation of the laser intensity pattern and for the insensitivity of the resonator to small perturbations of the resonator optics, meaning that an optical path is always possible, just like with the cross Porro prism resonator lasers described in section 2.6.5. A half-wave voltage is used by the Q-switch to rotate the linear polarisation by 90° to produce an effective gate for the laser mode. This design is used during the pump length investigation in Chapter 5.

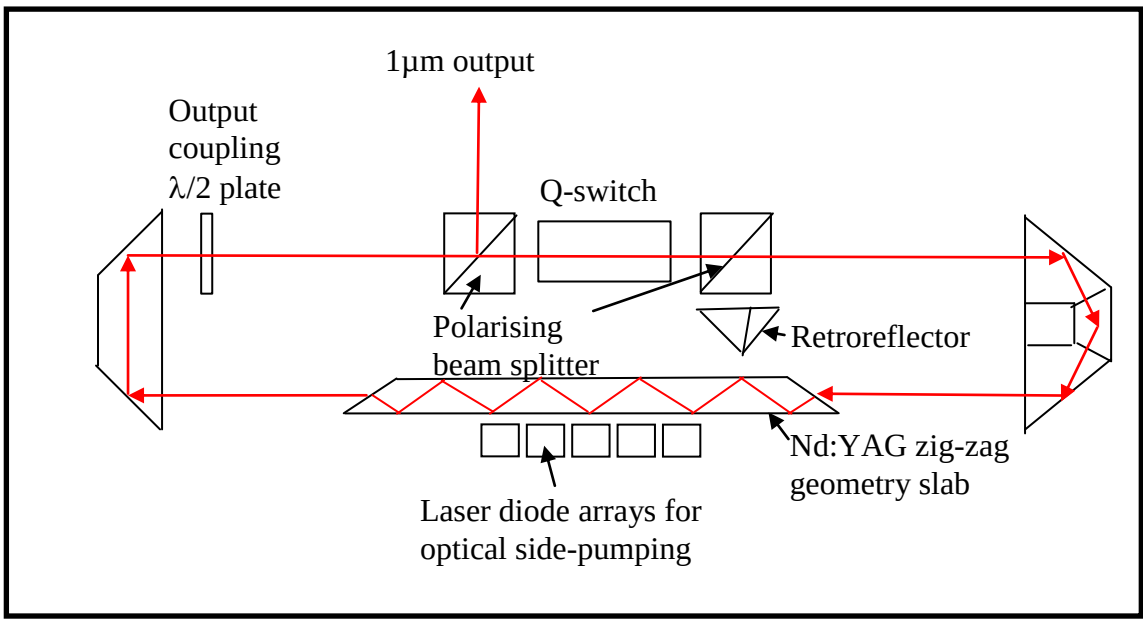

Figure 2-10 : Unidirectional non-planar ring resonator laser design.

2.6.9 Comparison of ring and plane-plane resonator lengths

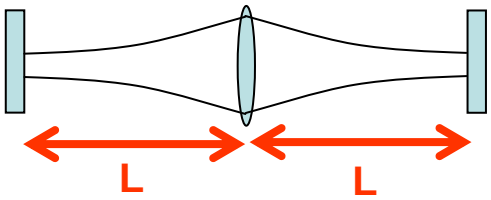

Plane-plane

- Diffractive length = 2L
- Round trip length = 4L

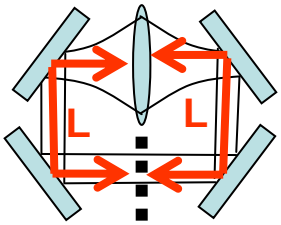

Unidirectional ring

- Diffractive length = 2L
- Round trip length = 2L

Figure 2-11: Diagrams of plane-plane and ring resonator designs.

When comparing plane-plane with unidirectional ring resonators, the ratio of the optical round trip length to diffractive length is different, as shown in Figure 2-11. Under the assumption that all optical elements are thin, a ring resonator with the same optical round trip length as a plane-plane resonator will have twice the diffractive length. The diffractive length of the resonator is an important parameter in determining the divergence of the laser, so it would be expected that the ring resonator would have a lower divergence (in effect the ring resonator has a lower Fresnel number).

A plane-plane resonator can be used if the diffractive length is matched to compare the divergence with a ring resonator. This will however have an optical round trip time which is twice as long. The efficiency will be less than for the ring resonator that has the same diffractive length. The resonator life time also affects the laser divergence, but this is affected by both the output coupling and the optical round trip length. If the output coupling is the same for both resonators, then the resonator lifetime will be the same as the optical round trip length is equal. The optical round trip time affects the resonator lifetime, which affects the build-up time of a laser or OPO pulse. The build-up time affects the efficiency of conversion, as if the build-up time is long, the threshold is increased.

2.6.10 Unstable resonators

It has been shown that unstable resonators can produce superior beam quality over a stable resonator design is some cases [20]. A unidirectional ring resonator is an ideal resonator for the use of unstable output coupling. This is achieved via beam expansion in one axis, and 50% beam clip output coupling, once per round trip of the ring resonator. 50% clipping is used, as this is approximately the optimum output coupling value for this type of resonator when Q-switched. A sharp edge or graded index beam scraper can be used to output couple 50% of the light. It has been demonstrated at Selex ES, that a reduction in divergence of a factor of approximately 2 can be achieved using an unstable resonator design, when compared with an equivalent stable ring resonator. Further development of this design to improve the near-field beam intensity pattern is required before it is utilised.

2.6.11 Folded resonator designs

All practical laser resonator designs, typically 1 m long, produced at Selex ES include turning optics to fold the laser mode around to allow a smaller footprint to be occupied e.g. a cross Porro resonator will, as a minimum, use a corner cube to fold the resonator path in two. The platform intended for the laser system dictates the footprint (typically 300-400 mm length) and the turning optics required. These additional optics can clearly introduce wavefront error, reflected loss and stress induced birefringence into the beam path. These effects are assumed small throughout this thesis, and all resonator set-ups used in investigations do not include any fold optics. In most cases, this is a fair assumption, although some optics can cause problems if they do not perform as specified in the technical drawings.

2.6.12 Amplifier

A number of laser systems produced at Selex ES have an amplifier stage which follows the laser resonator, to increase the output pulse energy. Typically the amplifier uses an identical laser slab to the laser resonator and an identical pumping regime. There are reasons for using an amplifier in a Master Oscillator Power Amplifier (MOPA) system, rather than increasing the power produced in the resonator. These include the reduction of thermal lensing in the resonator and the avoidance of laser pulse shortening to levels below the specified minimum pulsewidth. This thesis does not include research into developments of an amplifier.

2.7 OPTICAL PARAMETRIC OSCILLATORS (OPOS)

2.7.1 Extracavity OPO

Typical targeting laser systems produced at Selex ES use Q-switched Nd:YAG laser technology to generate output at 1.064 µm. End user training requirements dictate that output in the eye-safe 1.573 µm region must also be provided i.e. the laser output has to be switchable between either wavelength. One of the most common routes for generation of large pulse energies at 1.5 µm is to use nonlinear wavelength conversion in an optical parametric oscillator (OPO) to shift the output of a Q-switched Nd:YAG laser at 1064 nm to the eye-safe waveband. The ideal nonlinear crystal for this OPO is potassium titanyl phosphate (KTP). It has a high damage threshold suitable for generation of large pulse energies, and shifts 1064 nm from Nd:YAG to 1573 nm in a noncritically-phasematched (NCPM) geometry, which is insensitive to both the angle and temperature of the KTP, hence ideal for use in fieldable laser systems.

Current Selex ES targeting laser systems in full production incorporate an extracavity 90° image rotating ring resonator KTP OPO to convert the 1064 nm light to 1573 nm light. These typically use three KTP crystals with dimensions 9 mm square cross-section and 20 mm long. The KTP crystals are non-critically-phase-matched and therefore no walk-off of the 1064 nm and 1573 nm is introduced. As the KTP crystals are non-critically-phase-matched, the output wavelength and energy are insensitive to the angle of the crystals in the phase-matching (x-z) plane. This is confirmed using Select Non-Linear Optics (SNLO) public domain software developed by Dr. Arlee Smith [21]. In Figure 2-13, it is shown that neither the signal wavelength or the nonlinear coefficient d_{eff} are significantly affected by the angle of the crystals in the x-z plane. In the x-y plane, the angle of the crystal is even less important. Therefore, the crystals can be usefully angled away from normal to the beam in the x-y plane by a few degrees to prevent spurious reflections without affecting the signal wavelength or d_{eff} significantly as shown in Figure 2-12. The translation of the beam can be easily compensated for when a number of crystals are used within an OPO. The Type II interaction is used, in which the 1573 nm radiation produced by the KTP crystals is of the same linear polarization state as the 1064 nm pump incident at the crystals.

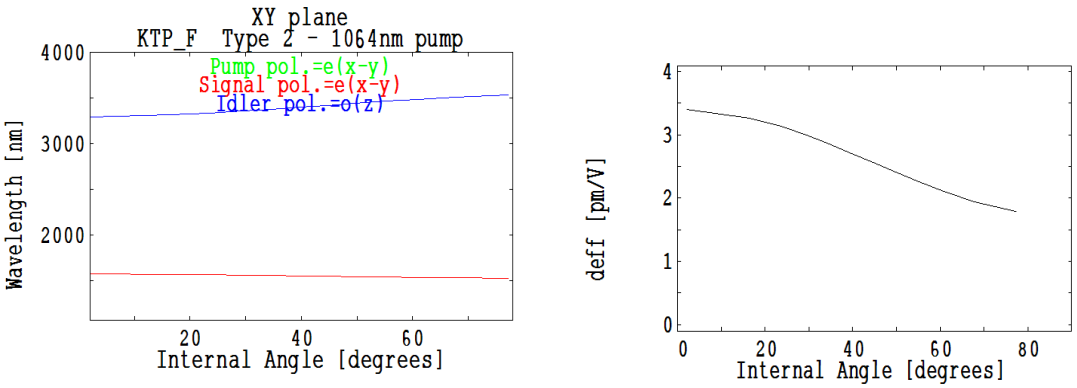

Figure 2-12 : Plots from SNLO showing the signal and idler wavelengths for varying internal angle in the xy plane for a KTP crystal (left) (Temperature = 293K) and d effective for varying internal angle (right).

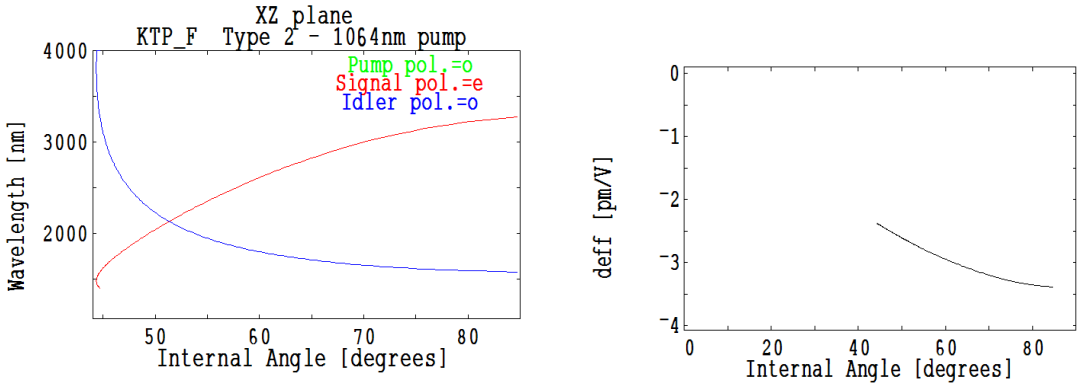

Figure 2-13 : Plots from SNLO showing the signal and idler wavelengths for varying internal angle in the xz plane for a KTP crystal (left) (Temperature = 293K) and d effective for varying internal angle (right).

The extracavity OPO has a physical round-trip length of approximately 200 mm and typically has an optical to optical efficiency of 35%.

If a relatively low energy laser design is used without an amplifier stage, the efficiency can be improved by using a telescope to reduce the pump beam size and increase the pump power density. Additional folding optics are required to overlap the OPO output with the laser output beam paths to ensure that the two beams are pointing in the same direction to a high degree of accuracy (boresighted). The output wavelength is selected using a mechanically driven periscope.

2.7.2 Output optics

The boresighted beams are directed through an output telescope, which increases the beam diameter in order to reduce the divergence to the required value. In some laser systems, a circular scraper aperture is used, to ensure that all the laser energy is within the required aperture size on exiting the laser system. If the square near field intensity pattern produced by the square cross-section laser slab inside the resonator is not well within this aperture as designed, then some energy will be lost due to clipping of the corners of the beam profile, affecting the system efficiency.

2.7.3 Ring and standing wave OPO designs

The ring geometry OPO is useful as feedback of the pump back into the pump laser is not likely so an optical isolator or deliberate misalignment is not required. This may not be the case for a plane-plane resonator with optics at normal incidence, particularly if the pump was double passed in an attempt to increase the efficiency. In addition, a ring resonator will have a shorter round-trip time for a given diffractive length than an equivalent plane-plane resonator, as discussed in section 2.6.9. As phase matching and therefore gain is only provided in one direction through the KTP, the shorter build-up time of the ring resonator compared with the plane-plane resonator will increase its efficiency.

The typical ring OPO produced at Selex ES uses a non-planar ring geometry, so careful alignment is not required. An optical path is always possible, just like the non-planar unidirectional ring resonator lasers as described in section 2.6.8.

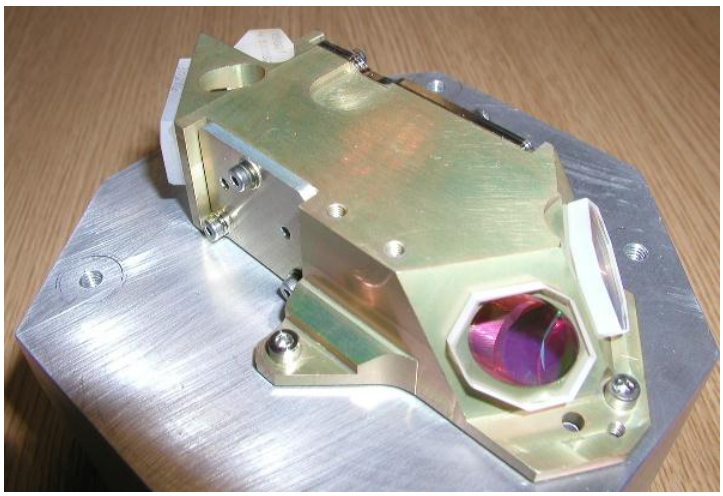

Figure 2-14: Photograph of the non-planar ring extracavity OPO.

This non-planar ring OPO, as shown in Figure 2-14, is used within the typical targeting laser system and has improved divergence and boresight stability over an equivalent planar ring resonator OPO. Selex ES has applied for a patent for the non-planar ring resonator OPO design (WO/2008/074762).

2.7.4 Intracavity OPOs

The typical laser systems produced at Selex ES use an extracavity Nd:YAG pumped KTP OPO with an optical-to-optical conversion efficiency of 35% for generating 1573 nm. The efficiency of the OPO is dependent on the intensity of the pump (fundamental) beam. By using an alternative intracavity geometry for the OPO the maximum pump intensity is available, thereby lowering the OPO threshold and enhancing conversion efficiency. The intracavity OPO acts as the output coupler for the pump laser. In a low loss (or high gain) design the intracavity OPO will couple out a large fraction of the equivalent fundamental 1064 nm laser mode pulse energy. Intracavity OPOs are particularly useful in reducing the threshold when pumped using continuous-wave lasers [22]. A reduced threshold can also be achieved by using a doubly-resonant OPO, but this is considered a less desirable method due to high mechanical stability requirements and limitations on the output wavelength.

There have been a number of published works on intracavity OPOs based on Q-switched Nd:YAG and KTP. 40 mJ from a flashlamp-pumped Nd:YAG intracavity KTP OPO, at a conversion efficiency of 0.6% from the input electrical energy to the flashlamp, has been reported [23]. A compact flashlamp-pumped intracavity OPO source which generated 10 mJ pulses of duration 1.1 ns has also been demonstrated [24] Higher efficiencies have been achieved using diode-pumped Nd:YAG; 97 mJ pulse energies at pulse repetition rates up to 30 Hz, with pulsewidths of 3.6 ns, have been reported from a diode side-pumped Nd:YAG rod laser with a KTP intracavity OPO at 4.2% wall plug efficiency [25]. Also, a conversion efficiency of 10.4% with respect to diode-laser input energy has been reported for a diode side-pumped Nd:YAG rod laser with an intracavity KTP OPO producing an output of 31.5 mJ, 1572 nm signal at 10 Hz [26].

Very few publications could be found where the OPO shared a common resonator with the pump laser. In one report [27] a comparison is made between shared and coupled OPO cavities in a diode-pumped Nd:GdVO4 laser. The efficiency of the 60 mm long end-pumped shared resonator is reported as 75% of the coupled resonator efficiency. However in this case the laser is passively Q-switched, so is different to an actively Q-switched laser, where externally modulation of the Q-switch can be applied and is independent of the intracavity power density. Residual losses in the Q-switch are significant in a passively Q-switched laser and may affect the efficiency comparison. In addition, this paper compared a 25 mm long coupled resonator with a 60 mm long shared resonator. It is well known that lengthening of an OPO resonator will extend the build-up time and reduce its efficiency.

These quoted results all use a short OPO resonator inside the pump laser resonator. One of the primary reasons for this is to reduce the build-up time and duration of the OPO pulse relative to the pump pulse. These results are also for designs where only the OPO signal wavelength is output.

In Chapter 7, results are presented for a common (or shared) resonator intracavity OPO design based on laser diode pumped Nd:YAG and KTP. With this design the output can be rapidly switched between 1064 nm and 1573 nm via electrical control of the intracavity polarisation states. These outputs will have a common boresight due to the intracavity mode at each wavelength sharing a common beam path. The common boresight of the two wavelengths during harsh environmental conditions is a key parameter for a real world laser source switching between the two wavelengths. To the

knowledge of the author, this was the first reported demonstration of a common resonator, intracavity KTP OPO inside an image rotating Nd:YAG ring laser, when it was presented at the 2012 SPIE Security & Defence conference in Edinburgh [28].

2.8 ADAPTIVE OPTICS

The field of adaptive optics has been developed largely for applications in astronomy, where images from telescopes can be improved by the adaptive control of the received wavefront to compensate for distortions caused by atmospheric aberrations. In Chapter 6, the use adaptive optics to compensate for wavefront aberrations which occur inside a laser resonator, such as thermal lensing in an Nd:YAG slab, is investigated. This is carried out in order to assess the potential improvement to the brightness performance of the laser resonator.

2.8.1 Intracavity adaptive optics for improvement of laser performance

Thermally-induced distortions in the laser gain medium are one of the major impediments to be overcome in developing high power or high energy solid-state lasers [11]. Performance is degraded in general by a combination of thermally induced birefringence and thermal lensing due to quantum defect heating upon absorption of pump light [2]. Careful selection of birefringent host media or depolarisation compensating laser resonator designs can reduce the thermal birefringence problem [29], but do not address the thermal lensing issue. Simple resonator design can alleviate the effects of the unaberrated spherical component of the thermal lensing [30]; however the non-spherical aberrations remain uncorrected, and scale significantly with increasing power. Detailed knowledge of the thermally induced distortions can allow an appropriate phaseplate to be manufactured and incorporated as an intracavity component. However the correction provided is for a fixed operating power only and does not consider transient effect of thermally induced distortions, which can be significant for some laser designs. Furthermore long-term drifts in performance can occur due to the reduction in pump power as laser diodes degrade with time, or

degradation of the thermal interface of the laser gain medium, which will alter both the magnitude and the distribution of the thermally-induced distortions. Lasers required to operate over a wide range of temperatures or during harsh platform vibration can suffer from changes in beam pointing direction (boresight) and/or resonator misalignment. The use of adaptive optic technology as part of the laser resonator design offers the prospect of addressing all of these issues.

Although an adaptive optic positioned outside the resonator could produce some useful beam shaping as reported in [31], where the beam profile is elongated in one axis for laser machining, the wavefront correction that is possible with an intracavity placement of an adaptive optic has the ability to improve resonator alignment as well as resonator efficiency and beam quality. Clearly for high power or high energy lasers a high damage threshold ruggedised adaptive optic technology is essential. In Chapter 6, results of an experimental programme are presented, which was carried out to determine the suitability of two sample deformable bimorph mirrors as intracavity adaptive optics for a diode-pumped Nd:YAG slab laser resonator, which is typical of those manufactured at Selex ES and used for the targeting application.

2.8.2 Feedback mechanism (system performance metric)

To optimise the performance of a laser using an adaptive optic, a mechanism that measures the performance of the laser in a feedback loop is required, so that the adaptive optic can be adjusted in the appropriate way.

The use of a wavefront sensor (Shack-Hartmann sensor) is the most direct measurement of the resonating beam and therefore produces a quick route to optimisation of the adaptive optic. A single measurement provides enough information for wavefront correction using an adaptive optic to provide significant improvement to the beam quality [32]. This method requires that the adaptive optic is programmable to produce a given shape.

Other methods of feedback can be used which do not require any knowledge of the adaptive optic response, or of the wavefront inside the laser resonator. A photodiode can be placed behind an aperture, which is at focal plane of an optic, providing a direct measurement of the laser brightness. This is known as a power-in-a-bucket

measurement, which is performed in the far-field of the laser beam in this case. Using this method, the laser pulse energy and divergence, which are equally important parameters for the intended application of laser targeting, both contribute to the system performance metric.

A technique which is used to produce a specified beam intensity pattern uses a CCD camera to measure the laser far-field spatial beam profile and compares it to a custom defined target profile by calculating the root mean square error [31]. This is particularly suited to laser machining applications where different beam intensity patterns are required in different situations. For applications such as laser targeting, where the laser brightness is the important parameter, the use of a CCD camera and the computation involved in obtaining a measurement of performance was considered over-complicated.

A novel laser brightness sensor based on second-harmonic-generation has been demonstrated [33], which was used to assess the progress of the laser towards optimisation. Although this is shown to produce a good optimisation of the adaptive optic, this was considered more costly than the brightness measurement provided by the spatially filtered far-field measurement described previously.

2.8.3 Adaptive optic devices

There are many different types of adaptive optics which can control the wavefront of an incident laser beam in a more complex manner than an adjustable lens, or a tip-tilt stage. One reference [34] lists 14 different types of wavefront modulating devices used as adaptive optics. Spatial light modulators can be used to produce a variation in the refractive index of a transmitted or reflected laser beam. They can also be used to produce binary gratings of phase or amplitude to diffract an incident beam. In contrast, the class of adaptive optics that have been investigated in this thesis use the distortion of continuous reflective surfaces (mirrors) to adjust the wavefront profile of an incident laser beam. A common type, which has been used within laser resonators, has position piezoelectric actuators acting perpendicular to the deformable surface and is called a piezoelectric deformable mirror (PDM). In contrast a bimorph mirror (BM) produces a bending moment due to piezoelectric actuators acting parallel to the deformable surface.

2.8.4 Bimorph mirrors

Multiplate bimorph designs have two or more piezoelectric actuator plates bonded together, and the plates are controlled to generate opposing deformations (in-plane expansion and contraction) and thus to induce a bending moment [34]. Parallel-bimorph and series-bimorph wiring designs both exist, which are both shown schematically in Figure 2-15.

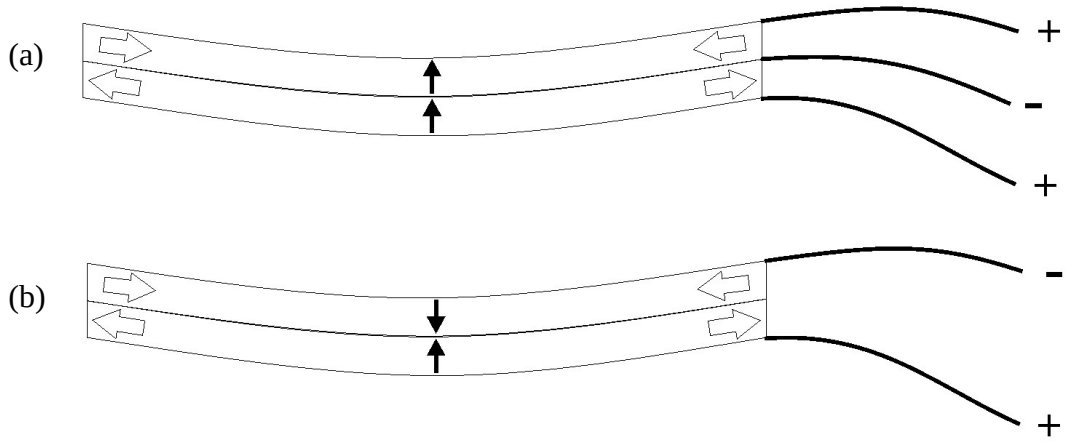

Figure 2-15: Bimorph mirror designs. (a) parallel-bimorph and (b) series-bimorph [33].

The difference is that the parallel-bimorph design develops twice the deflection of a series-bimorph for the same applied voltage. In multiplate-bimorph designs a thin mirror can be deposited directly onto the surface of the piezoelectric actuator plate. The piezoelectric actuator plate can be divided up into a pattern of actuators, which can then be addressed separately to produce a mirror shape that is more complicated than a spherical lens. The development of bimorph mirrors, similar to the type used in Chapter 6, are reported in [35].

Bimorph mirrors have been used to improve laser brightness. In one paper, closed adaptive systems are demonstrated with controllable bimorph mirrors [32]. These mirrors are used extracavity to correct for wavefront errors of high power femtosecond lasers. In one of the laser systems described, two bimorph mirrors are used and the far

field beam profile is optimised to increase the power density at the laser focus by a factor of 67 times. A Shack–Hartmann sensor was used to measure the wave front in order to provide information to optimise the bimorph mirror shape.

The transient effects within a solid-state laser can limit the time to full brightness due to the time required to establish a thermal lens in the lasing medium upon which the resonator is optimised [36]. In this paper, the fundamental mode-size is kept constant during the warm-up phase of an Nd:YLF rod laser using a 31-element, deformable bimorph mirror. This reduced the time to full brightness by a factor of 3.

2.8.5 Optimisation algorithms

An algorithm is required to optimise the shape of an adaptive optic in order to produce the maximised laser performance, by altering the voltages supplied to the piezoelectric actuators. The algorithm fitness value is the laser beam performance parameter chosen that is optimised in the feedback loop. For the targeting application, the brightness of the laser beam on the target is the crucial performance criteria. Therefore, the fitness value could be obtained from a measurement of the laser pulse energy within an aperture placed at the focal plane of a focusing lens or spherical mirror.

A number of groups of optimisation algorithms exist including, genetic algorithms, hill-climbing algorithm, simple random search, simulated annealing and simplex algorithms. The Nelder-Mead algorithm used within this thesis belongs to the simplex type of algorithm. An advantage of this type of algorithm over some of the others is that the starting values are random and therefore the optimisation will not be biased by chosen starting values. It was shown in one paper that a simplex algorithm had the advantages over a hill-climbing method, of being more stable and rapid [37].

2.9 LASER MODELLING

2.9.1 Fresnel propagation laser model

A computer model is used to simulate a targeting laser resonator, and was written by David Legge at Selex ES, using the MathCAD programming language. This model is termed the "Fresnel Propagation model" and is useful in predicting the beam intensity pattern for the laser beam after leaving the resonator and as it is propagated into the far-field. This model also predicts the output pulse energy and incorporates a polarisation matrix used to calculate the resonator output coupling. A number of laser products are modelled including cross Porro prism resonators and non-planar ring resonators.

The direction of the resonating beam is found by using beam geometry and Snell's law to calculate the reflection and refraction when encountering each resonator optical element in turn. The laser is self-aligning as described in Section 2.6.5, as a beam path always exists which completes a round trip. This beam path is defined as the ray which has the same initial position and direction vectors as that after one round trip. One method for finding this ray is by using an iterative algorithm which minimises the position and direction vector differences. For the best overlap of the laser mode with the gain in the Nd:YAG slab, a real laser uses alignment wedges to position the centre of the beam profile (the central ray) in the centre of the slab. When the best overlap is achieved the laser pulse energy is optimised. This optimum beam path is found in the model by using an iterative algorithm to find the angles of the wedges that achieve optimum overlap. If the alignment of the optical elements is altered from the nominal positions in the computer model (or in a real laser), the wedges can be rotated to optimise the alignment through the slab for maximum pulse energy once again. The laser optical beam is represented by a complex amplitude distribution using a rectangular computer array, centred on the resonating ray path. This is a similar method to that used by the GLAD physical optics and laser analysis software developed by Applied Optics Research, which is described on their website [38]. The aperture of each optical element is summed and applied to the complex amplitude distribution.

Random noise initiates an intensity pattern across the aperture of the laser slab, which is amplified during each round trip of the laser resonator by a gain sheet, which is

calculated from the distribution of stored energy in the Nd:YAG slab. Once per round trip of the resonator, the gain applied to the complex amplitude distribution is calculated by the overlap and gain depletion results. A phase-sheet is included in the resonator model so that the effect due to the phase distortion introduced by thermal lensing in the Nd:YAG slab can be investigated.

The diffraction per round trip is also calculated and the out-coupled light on each round trip is summed to produce the near-field intensity pattern. The effect of diffraction for a given propagation length is calculated using the Fast Fourier Transform (FFT) function, which is built into the MathCAD software. The method used to Fourier-analyse the complex amplitude distribution is called the angular spectrum decomposition method [39]. The distance travelled is used to calculate the transfer function of the diffraction propagation. The inverse FFT function is then used to find the resultant complex amplitude distribution.

Finally, the diffraction procedure is repeated on the out-coupled complex amplitude distribution to propagate into the far-field regime. This is carried out in multiple steps, as a resizing of the rectangular array is required along the way as the beam intensity pattern grows (diverges).

2.10 CONCLUSION

In this Chapter, the background information presented describes a typical targeting laser system and some of its variations, which are in full production at Selex ES. Commonly, this is a diode-side-pumped Nd:YAG slab laser which uses a zig-zag beam path within a cross Porro resonator. It is insensitive to perturbations of the resonator optics, as required for the targeting application when used over the full military environmental conditions. Polarisation control is used to achieve output coupling and active electro-optic Q-switching is used to provide short pulses. The 1064 nm light is converted to an eye-safe wavelength of 1573 nm using an extracavity non-planar ring OPO, based on NCPM KTP. The two wavelengths are combined into a common beam path (co-boresighted).

In the following Chapters, research into areas of development to this typical laser system to improve the efficiency of production by reducing the occurrence of problems and to extend the product offering at Selex ES, are described. In the later chapters of this thesis, intracavity adaptive optics and intracavity OPOs are explored. Both of these topics have been introduced in this Chapter.

2.11 REFERENCES

[1] *Selex ES website*. "www.selex-es.com"

[2] W. Koechner, "*Solid-State Laser Engineering",* Springer New York (2006)

[3] V. Lupei, G. Aka, and D. Vivien, *"Quasi-three-level 946 nm CW laser emission of Nd:YAG under direct pumping at 885 nm into the emitting level"* Optics Communications, vol. 204, pp. 399-405 (2002)

[4] M. Frede, "*Effective Pumping Scheme for Nd:YAG Lasers",* "http://www.ligo.caltech.edu/docs/G/G010360-00.pdf" (2001)

[5] Z. N. a. Z. X.-F. a. M. Q.-L. a. W. B.-S. a. C. D.-F. a. P. Q.-J. a. X. Z.-Y. a. P. Y.-B. a. Feng, Xi-Qi, *"Comparison of Nd:YAG Ceramic Laser Pumped at 885 nm and 808 nm"* Chinese Physics Letters, vol. 26, p. 054211 (2009)

[6] F. Q. Li, X. F. Zhang, N. Zong, J. Yang, Q. J. Peng, D. F. Cui, *"High-Efficiency High-Power Nd:YAG Laser under 885 nm Laser Diode Pumping"* Chinese Physics Letters, vol. 26 (2009)

[7] N. Pavel, V. Lupei, J. Saikawa, T. Taira, and H. Kan, *"Neodymium concentration dependence of 0.94-, 1.06- and 1.34-μm laser emission and of heating effects under 809- and 885-nm diode laser pumping of Nd:YAG"* Applied Physics B: Lasers and Optics, vol. 82, pp. 599-605 (2006)

[8] T. Y. Fan, *"Heat generation in Nd:YAG and Yb:YAG"* IEEE J. of Quantum Electronics, vol. 29, pp. 1457-1459 (1993)

[9] R. Lavi and S. Jackel, *"Thermally Boosted Pumping of Neodymium Lasers",* Applied Optics, vol. 39, pp. 3093-3098 (2000)

[10] T. Kane, R. Eckardt, and R. Byer, *"Reduced thermal focusing and birefringence in zig-zag slab geometry crystalline lasers"* IEEE J. of Quantum Electronics, vol. 19, pp. 1351-1354 (1983)

[11] J. Eggleston, T. Kane, K. Kuhn, J. Unternahrer, and R. Byer, *"The slab geometry laser-Part I: Theory"* IEEE J. of Quantum Electronics, vol. 20, pp. 289-301 (1984)

[12] T. Kane, J. Eggleston, and R. Byer, *"The slab geometry laser-II: Thermal effects in a finite slab"* IEEE J. of Quantum Electronics, vol. 21, pp. 1195-1210 (1985)

[13] B. Cole, L. Goldberg, C. W. Trussell, A. Hays, B. W. Schilling, and C. McIntosh, *"Reduction of timing jitter in a Q-Switched Nd:YAG laser by direct bleaching of a Cr4+:YAG saturable absorber"* Optics Express, vol. 17, pp. 1766-1771 (2009)

[14] *RP Photonics website*, accessed on 16/06/13, "http://www.rp-photonics.com/"

[15] H. Kogelnik and T. Li, *"Laser beams and resonators"* Proceedings of the IEEE, vol. 54, pp. 1312-1329 (1966)

[16] A. E. Siegman, "*Lasers"*, University Science Books (1986)

[17] A. G. Fox and T. Li, *"Resonant modes in a maser interferometer"* Bell Syst. Tech. Journal, pp. 453–88 (1961)

[18] M. K. Chun and E. A. Teppo, *"Laser resonator: an electrooptically Q-switched Porro prism device"* Applied Optics, vol. 15, pp. 1942-1946 (1976)

[19] J. J. Degnan, *"Theory of the optimally coupled Q-switched laser"* IEEE J. of Quantum Electronics, vol. 25, pp. 214-220 (1989)

[20] K. Kuba, T. Yamamoto, and S. Yagi, *"Improvement of slab-laser beam divergence by using an off-axis unstable-stable resonator"*, Optics Letters, vol. 15, pp. 121-123 (1990)

[21] *SNLO software*, "http://www.as-photonics.com/?q=SNLO"

[22] D. J. Stothard, J. M. Hopkins, D. Burns, and M. H. Dunn, *"Stable, continuous-wave, intracavity, optical parametric oscillator pumped by a semiconductor disk laser (VECSEL)"*, Optics Express, vol. 17, pp. 10648-10658 (2009)

[23] E. V. Raevsky, V. L. Pavlovitch, and V. A. Konovalov, *"Efficient eye-safe intracavity KTP optical parametric oscillator*", Proceedings of SPIE, vol. 4630, pp. 75-81 (2002)

[24] P. D. Mason and B. J. Perrett, "*High-Energy, Sub-Nanosecond Pulse Duration Intracavity Pumped KTP OPO at 1572 nm"*, Advanced Solid-State Photonics p. MB9 (2007)

[25] X. Liu, C. Lu, X. Wang, B. Sun, Y. Cheng, and J. Chen, *"Efficient intracavity optical parametric oscillator with diode side-pumped electro-optic Q-switched laser"* Chinese Optics Letters, vol. 4, pp. 664-666 (2006)

[26] Y. Y. Wang, K. Zhong, D. G. Xu, P. Wang, and J. Q. Yao, "*High-energy pulsed eye-safe intracavity optical parametric oscillator at 1.57 μm",* Proceedings of SPIE, vol. 7276, p. 727603 (2009)

[27] Y. F. Chen and L. Y. Tsai, *"Comparison between shared and coupled resonators for passively Q-switched Nd:GdVO4 intracavity optical parametric oscillators"* Applied Physics B: Lasers & Optics, vol. 82, pp. 403-406 (2006)

[28] J. Beedell, I. Elder, D. Legge, and D. Hand, *"Intracavity, common resonator, Nd:YAG pumped KTP OPO*" Proceedings of SPIE, vol. 8541, pp. 85410Q-85410Q (2012)

[29] W. A. Clarkson, N. S. Felgate, and D. C. Hanna, *"Simple method for reducing the depolarization loss resulting from thermally induced birefringence in solid-state lasers"* Optics Letters, vol. 24, pp. 820-822 (1999)

[30] D. Burns, G. J. Valentine, W. Lubeigt, E. A. Bente, and A. I. Ferguson, *"Development of high-average power picosecond laser systems*" (Invited Paper) [4629-29], pp. 129-143 (2002)

[31] R. J. Beck, J. P. Parry, J. D. Shephard, and D. P. Hand, *"Adaptive extracavity beam shaping for application in nanosecond laser micromachining"* Proceedings of SPIE, vol. 7913, p. 79130D (2011)

[32] A. G. Aleksandrov, V. E. Zavalova, A. V. Kudryashov, A. L. Rukosuev, P. N. Romanov, and V. V. Samarkin, *"Closed adaptive systems with controllable bimorph mirrors"* J. Opt. Technol., vol. 71, pp. 737-741 (2004)

[33] W. Lubeigt, G. J. Valentine, and D. Burns, *"Brightness enhancement of a solid-state laser using an intra-cavity deformable mirror"*, Proceedings of SPIE, vol. 6018, p. 60180I, (2005)

[34] A. H. Greenaway and J. G. Burnett, "*Industrial and Medical Applications of Adaptive Optics",* Technology Tracking (2004)

[35] C. Boulet, M. Griffith, L. C. Laycock, and A. McCarthy, *"Development of a small aperture bimorph deformable mirror for a free-space optical communications system"*, Proceedings of SPIE, vol. 7833, pp. 78330D-78330D (2010)

[36] W. Lubeigt, M. Griffith, L. Laycock, and D. Burns, *"Reduction of the time-to-full-brightness in solid-state lasers using intra-cavity adaptive optics"*, Optics Express, vol. 17, pp. 12057-12069 (2009)

[37] S. S. Chesnokov and I. V. Davletshina, *"Simplex method in problems of light-beam phase control"*, Applied Optics, vol. 34, pp. 8375-8381, (1995)

[38] *Applied Optics Research website*, accessed on 16/06/13, "http://www.aor.com/"

[39] J. W. Goodman, "*Introduction to Fourier optics"*, McGraw-Hill (1968)

CHAPTER 3. IMPROVED CONTROL OF CROSS PORRO PRISM RESONATOR OUTPUT COUPLING

As discussed in Chapter 2, Selex ES manufactures Nd:YAG slab laser systems for targeting applications, which use a cross Porro prism resonator design. The output coupling is achieved via control of the polarisation state in the resonator. In this Chapter, a computer model is used to analyse the polarisation state inside the laser resonator. An investigation into the degree of control of the output coupling via rotation of a half wave plate resulted in a design change which provides a greater degree of control. Experimental work was carried out to confirm the predicted output coupling achievable in a laser resonator using both half and quarter waveplates.

3.1 INTRODUCTION

The schematic diagram of the typical laser resonator in Figure 2-9 in Chapter 2 (Section 2.6.5), shows the type of resonator investigated in this Chapter. The cross Porro prism resonator shown has a polarising beam splitter (PBS) through which the output is reflected out of the resonator. The level of output coupling is adjusted by changing the polarisation state preceding the PBS by rotating a half waveplate. In Figure 2-9 the polarisation state is linear at the position of the half wave plate, which is used to rotate the polarisation angle. The complication to this scenario is that the resonator investigated in this Chapter is folded by a periscope, a folding prism and a corner cube prism, using total internal reflections (TIRs). All of these TIRs produce a relative phase shift between the s-pol and p-pol states.

3.1.1 Folded resonator design

Laser systems installed on board aircraft for the targeting application have a requirement for a compact footprint (approximately 300 mm long), which necessitates the folding of the laser resonator. Figure 3-1 shows a diagram of the folded laser resonator that is investigated in this Chapter.

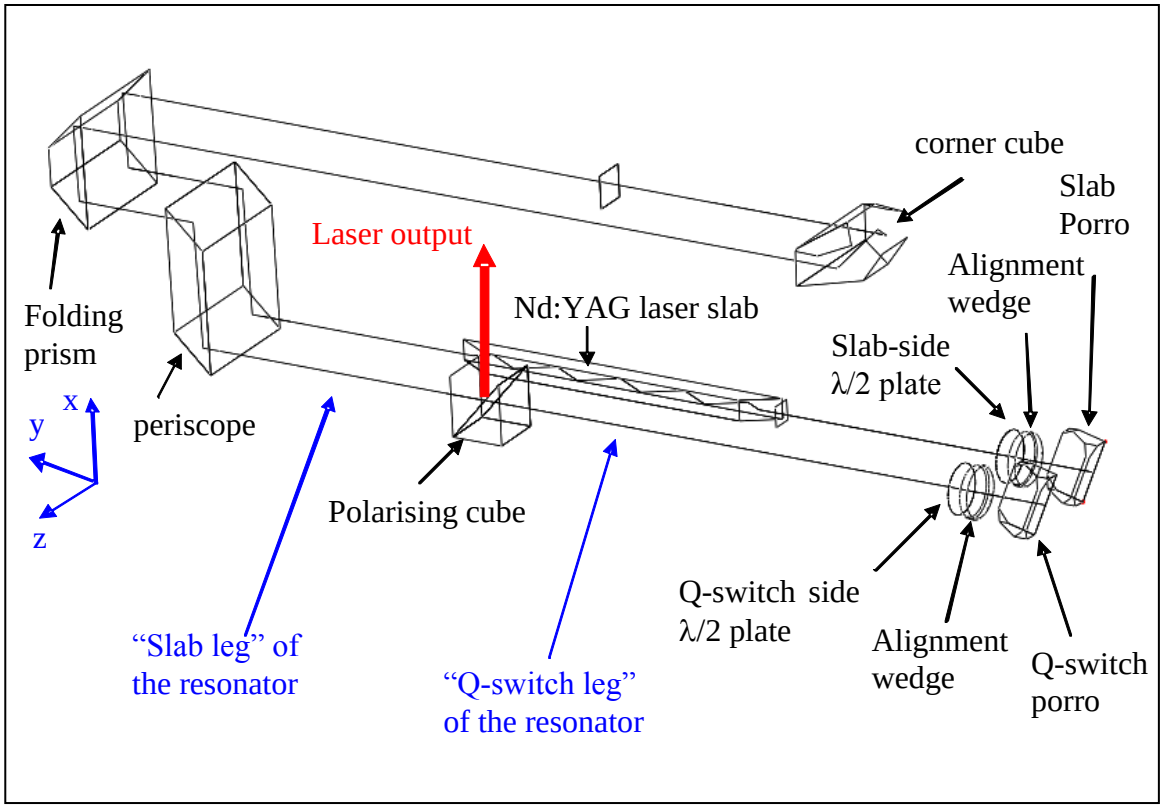

Figure 3-1: Folded resonator design.

The folded cross Porro prism resonator rotates the beam image by 180° each round-trip. A variation of this resonator has one of the Porro prisms rotated by 45° (apex set vertical along the x axis). This changes the round-trip beam image rotating to 90°, which improves beam uniformity. The apex angle of this Porro prism does not affect the output coupling, which is only affected by the polarisation state on the slab-side of the PBS in the resonator. The polarisation state in the Q-switch-side of the PBS is important for the hold-off of the laser resonator when it is Q-switched. The apex angle of the Porro prism will however have a minor effect on the alignment of the laser resonator.

The “slab leg” and the “Q-switch leg”, labelled in Figure 3-1, refer to the parts of the resonator on either side of the PBS, in which the laser slab and Q-switch are located. A Q-switch is however not present during this investigation, or in the diagram.

The Q-switch leg is not folded as a linear polarisation with a high extinction ratio is required for laser hold-off, and total internal reflections would introduce depolarisation. The slab-leg is much longer and is folded by a periscope, a folding prism and a corner cube prism. The laser beam passes through the periscope and the folding prism fours time per resonator round-trip and the corner cube prism twice. The isosceles trapezoidal shaped Nd:YAG slab, which is passed twice per resonator round trip, also produces a relative phase shift.

No appreciable depolarisation occurs until the laser beam reaches the corner cube prism, in which the plane of total internal reflection differs to the axis of linear polarisation. After the corner cube prism, all the optical elements encountered produce a significant depolarisation.

3.1.2 Laser pulse energy detuning

During laser manufacture at Selex ES, the laser resonator pulse energy is routinely reduced to 90% of its maximum value, which is referred to as detuning the laser. The resonator is energy detuned to reduce the intracavity optical intensity to reduce the risk of laser induced damage to resonator optical elements. Typically the Q-switch is the most sensitive optical element, with a specified damage threshold of 300 MW/cm^2.

It is important that adequate margin exists to prevent laser induced damage of optical elements, and to allow for variations in output coupling and laser efficiency which can occur when the full environmental range is considered (vibration testing and temperatures ranging -40°C to +55°C). At lower temperatures (down to -40°C) the Nd:YAG lasing medium becomes more efficient than at room temperature due to the increase in the stimulated emission cross-section [1], increasing the gain and hence the intracavity optical intensity. This increases the likelihood of laser induced damage and loss of hold-off. In addition, changes in the birefringence of optical elements, variations in the retardance of waveplates and movement of optical elements all have the potential to change the output coupling and increase the intracavity optical intensity. Laser pulse

energy detuning is achieved by adjusting the output coupling of the resonator away from its optimum value by rotating the slab-side half waveplate.

3.1.3 Reduction in optical intensity when a laser is energy detuned

An illustration of the output power and the intracavity optical intensity against output coupling, is shown in Figure 3-2.

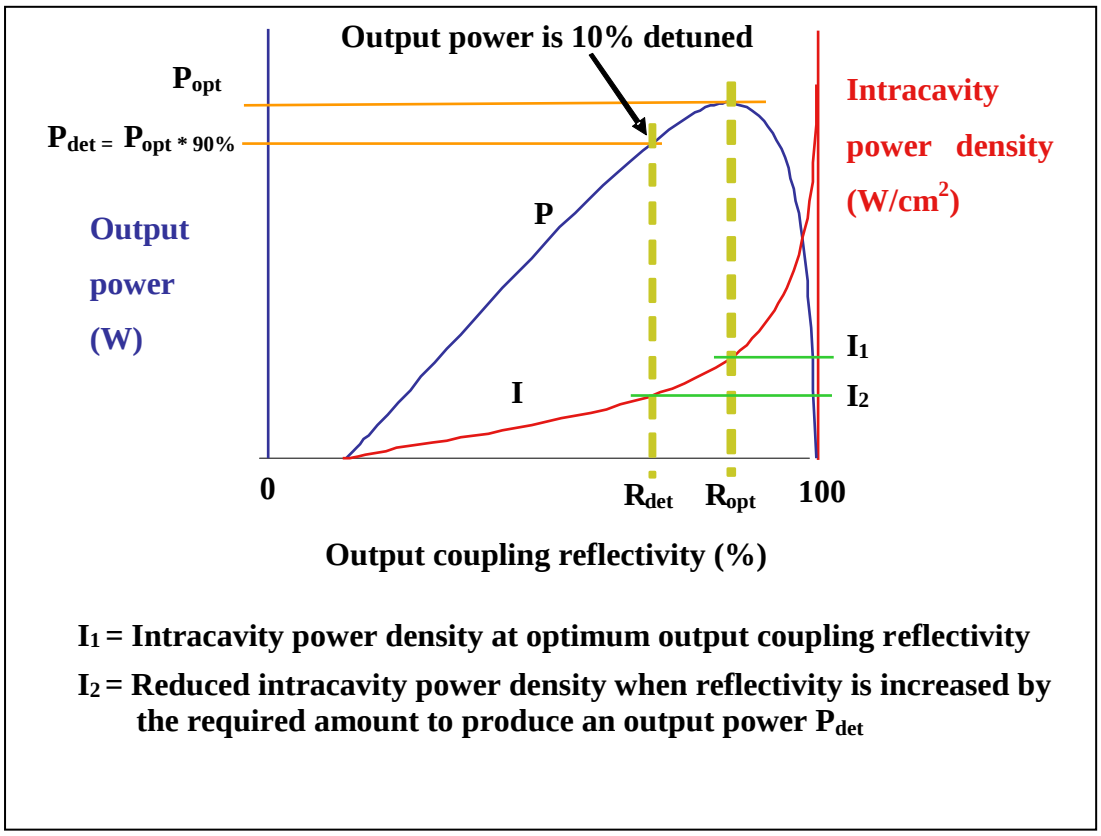

Figure 3-2: An illustration of the dependence of both the output power and the intracavity optical intensity on the output coupling.

If the output coupling transmission is increased such that a decrease in output energy of 10% is experienced, an associated reduction in intracavity optical intensity is observed, which is greater than 10%. This provides a greater reduction in the likelihood of laser induced damage over the environmental range, for the same reduction in laser efficiency. The magnitude of this reduction in optical intensity is calculated using a measurement of the output coupling for a sample laser resonator which was carried out in Section 3.3.

The intracavity optical intensity in a 10% energy detuned laser is calculated using equations (3.1) for the highest optical intensity at the position after second pass of the laser slab in the slab-leg and (3.2) for the Q-switch leg.

$$I_{intracavity} = I_{output}\left(\frac{1+R}{1-R}\right) \quad (3.1)$$

$$I_{intracavity} = I_{output}\left(\frac{2R}{1-R}\right) \quad (3.2)$$

Using the measured values for output coupling reflectivity of 54% and 33% for optimum and 10% energy detuned output energy values respectively, the reduction in optical intensity was calculated to be 62% in the Q-switch leg of the resonator.

The amount of energy detuning required is not investigated here, as it is accepted that the reduction of intracavity intensity that 10% energy detuning provides, is the correct value to provide adequate margin. Therefore, it is imperative that the energy can be detuned by the full 10% requirement.

3.1.4 Motivation behind investigation

During manufacture of laser systems at Selex ES, some of the laser resonators have been declared failures due to insufficient control of the polarisation state, which prevents energy detuning of 10%. The aim is to investigate the parameters that affect the output coupling control within the folded resonator and identify a design change which will ensure that the lasers can be consistently energy detuned by 10%.

3.1.5 What factors affect the ability to detune a laser?

The depolarisation effects of optical elements and the detuning that can be achieved is affected by many factors. These are expressed in the fish-bone diagram in Figure 3-3.

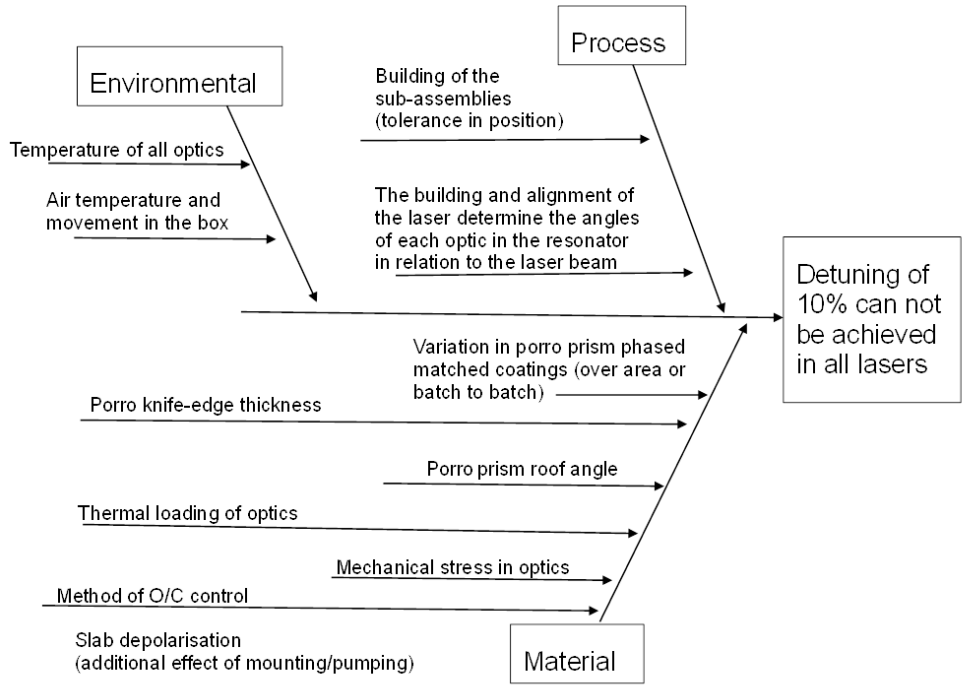

Figure 3-3: Fishbone diagram to show the contributing factors that prevent required level of detuning in a laser resonator.

It was decided that the effect of the angular positions of all the optical elements on the polarisation state was the first area that should be investigated.

3.2 COMPUTER MODEL SIMULATION OF POLARISATION STATES

A computer model was used to predict the effects of optical element misalignments in the laser resonator. This model finds the optimum laser beam path for a given set of optical element positions, as explained in more detail in Chapter 2 (Section 2.9.1).

The Fresnel equations [2] are used to calculate the E-field complex amplitude of light through an optical path with total internal reflections. For example, a 45º internal reflection in Fused Silica produces a relative phase shift of 24.8º (at a wavelength of 1064 nm, n = 1.44963). For an incident linear polarisation, a depolarisation will be introduced if there is a component of the E field in both the s-pol and the p-pol axes. This depolarisation changes the polarisation state from linear to an elliptical state. In a laser resonator round trip path, there will be 22 total internal reflections in the three folding optics that produce a similar phase shift, which can be calculated using the computer model.

Table 3-1 describes the input, process and output of the folded resonator model that is used to investigate misalignments of the optical elements in the resonator. The assumptions that are made in the model are also listed.

Input	Process	Output
The positions of all optical elements are imported from the CAD computer program which stores the mechanical data. Misalignments of optical elements are then added.	An algorithm is used to find the cross Porro prism resonator closed laser beam path. Fresnel equations are then used to predict the polarisation state throughout the resonator.	A graph of output coupling reflectivity as a function of slab-side half waveplate angle.
Assumptions		
1. The wedge positions are set at their nominal 45° angle. 2. The Porro prisms are assumed to provide no depolarisation due to the application of a phase-matched coating. The angular dependence of the coating performance is ignored. 3. The slab behaves as the Fresnel equations predict, with no effect due to the coatings on the reflecting surfaces and the end surfaces of the Nd:YAG slab.		

Table 3-1: Model input, process, output and assumptions.

The computer model includes a function which optimises the orientation of the alignment wedges. It finds the wedge angles which produce a resonating mode as close to the centre of the laser slab as possible. This alignment would correspond to maximum energy output with the largest near field beam size. This wedge angle optimisation function takes approximately 10 minutes to complete, which makes its use impractical when a large number of interrogations are required. The change in polarisation state due to the change in alignment of the resonator when using the wedge angle optimisation function was found to be negligible in a few examples, so the function was not used.

The Porro prisms are specified to provide a linear polarisation state on reflection, with a tolerance of less than 3º relative phase shift between the horizontal and vertical components of light, when the Porro prism apex is at 45º to these components. This departure from the linear polarisation state will have a small effect on the polarisation extinction ratio. Information about the Porro prism phase matched coating layer materials and thicknesses is proprietary to the supplier and therefore unavailable for inclusion in the computer model. The same is true for the coatings on the pump incidence and pump reflecting surfaces of the slab. Experimentally, the depolarisation due to the Porro prisms is known to be small, as hold-off is readily achieved in the Q-switched resonators.

The Nd:YAG slab is the type described in Chapter 2, with end surface coatings designed to produce an equal loss of approximately 2% for the p-pol and the s-pol states, allowing any polarisation state to be transmitted by the slab with equal loss. In addition, the pumped surface is antireflection coated and the opposite surface is coated for high reflectivity at the pump wavelength of 808 nm. All these coatings could affect the relative phase shift of the horizontal and vertical components of light. However, the computer model using the Fresnel equations to calculate the relative phase shifts, assumes that a perfect TIR exists, ignoring any effect of the coatings.

3.2.1 Partial experimental validation of the model

Of the three assumptions made in the computer model, the depolarisation of the laser slab was the greatest unknown factor (assumption 3 in Table 3-1), so the effect of depolarisation during each pass of the laser slab needed to be tested to compare with the effect of perfect TIR interactions, which are used in the model.

3.2.2 Depolarisation produced during transmission through the slab

The depolarisation due to a single pass of a laser slab was measured using the experimental set-up shown in Figure 3-4.

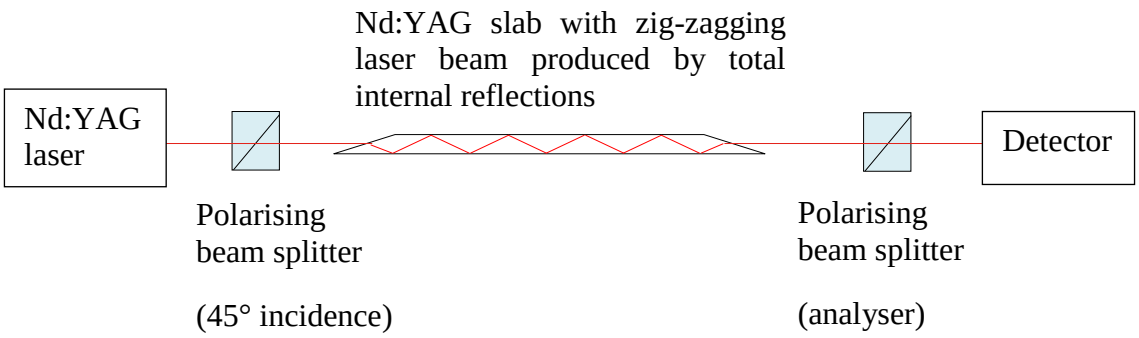

Figure 3-4: Set up for laser slab depolarisation testing viewed from above.

The laser slab was bonded on its metal assembly and was unpumped during the test. Linearly polarised light at 45º relative to the vertical axis was incident on a laser slab. The slab was aligned to be parallel to the incident 1064 nm wavelength laser beam. A graph that shows the transmission as a function of analyser angle for the two cases (with and without a laser slab in the path) is shown in Figure 3-5. The theoretical plots from the computer model are also shown on the graph.

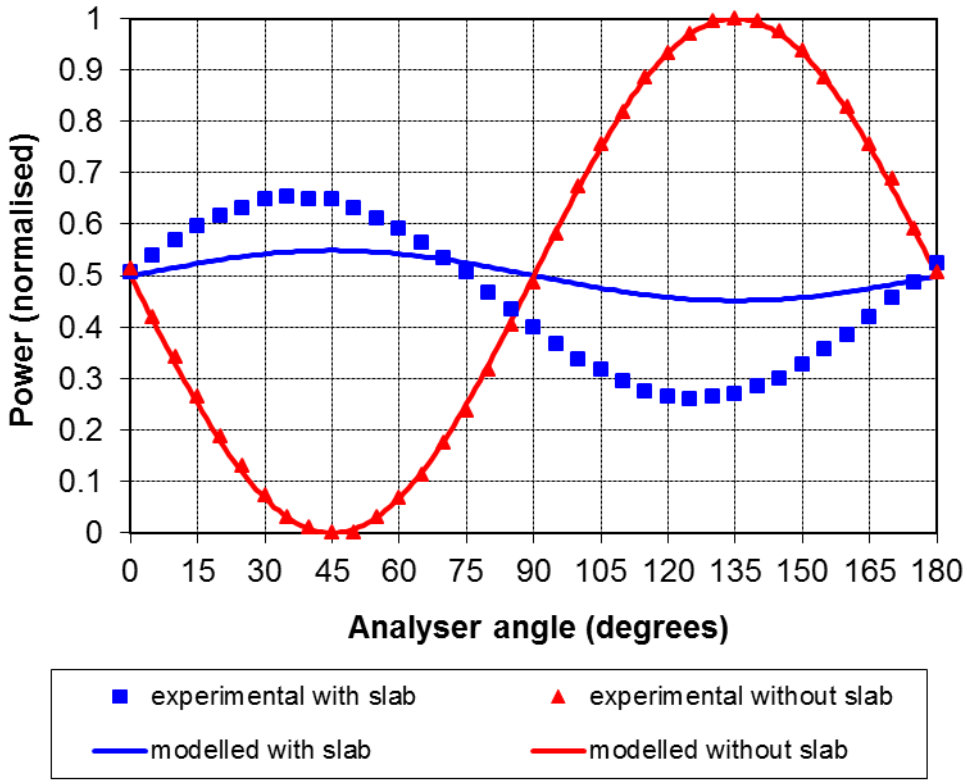

Figure 3-5: Graph of polarisation state with and without a laser slab.

As shown in Figure 3-5, there is some disagreement between the output polarisation state predicted and experimental data, which can be attributed to the effect of the slab end surfaces coatings or the reflecting surfaces coatings. It is not clear how to change the computer model to reflect this discrepancy in polarisation states, but a similar result can be achieved by the addition of an 11° waveplate. Although this discrepancy will affect the absolute value of the calculated output coupling reflectivity for nominal alignment of the resonator components, it is expected that the change to this output coupling value due to optical element rotations will be of a similar magnitude.

3.2.3 Predicted effects of optical element misalignments on output coupling control.

To investigate the effect of angular misalignments of resonator optical elements from the nominal positions and to ascertain which ones affect the polarisation state the most, the computer model was used. First nominal alignment was assessed and then in turn, each optical element was misaligned about each of the three axes by an angle of ±1º. A league table can be seen in Table 3-2 that lists the most influential angular misalignments at the top.

Increase in minimum reflectivity	Optic	Rotation axis	Rotation angle (degrees)	minimum Reflectivity (%)
0	Nominal optic positions----------			26.3
3	Slab	y	-1	29.3
2.1	Fold prism	y	1	28.4
1.3	Cornercube	z	-1	27.6
1	Cornercube	x	1	27.3
1	Cornercube	y	-1	27.3
0.8	Periscope	y	-1	27.1
0.8	Fold prism	x	1	27.1
0.7	Periscope	z	1	27
0.6	qsw porro	x	0.9	26.9
0.6	qsw porro	z	0.6	26.9
0.5	Periscope	x	-1	26.8
0.3	Fold prism	z	-1	26.6
0.3	Slab	z	-1	26.6

Table 3-2: League table of optical element angular misalignments in the folded crossed Porro prism resonator design, ordered according to their effect on the minimum output coupling.

The minimum reflectivity is the important parameter, which can prevent adequate energy detuning if its value is too high. These tabulated values suggest that no single optical element angular misalignment of 1° increases the minimum reflectivity to more than the required 30% for 10% energy detuning. However, in a real laser, a number of optical elements could be misaligned at once.

The computer model predicts that the four most influential optical elements are the slab, the fold prism, the corner cube and the periscope. An angular misalignment of the slab about the y-axis due to mechanical position tolerances is more likely than in the other axes due to the small dimension of the slab width compared with its length. The corner cube prism has an angular uncertainty due to mechanical tolerances in all three axes.

However, the x-axis rotation shows the greatest uncertainly due to the movement which is possible because the bolts which hold the assembly in place are smaller than the holes in the assembly. The fold prism y-axis rotation also has some uncertainty, which is again due to large holes compared with the bolt diameter, although to a lesser degree than the corner cube prism. The comparatively large effects due to the misalignments of the fold prism and the periscope are unsurprising due to the large number of passes of these optics during a round trip of the resonator.

3.2.4 Are the modelled optical element angular misalignments representative?

The analysis using the model assumes that all angular misalignments are 1° from the nominal position for all optical elements in order to assess which misalignments the resonator detune ability is most sensitive to. However, some optical elements will be more susceptible to angular errors due to their length, mechanical mounting, and their adjustment during resonator alignment.

For the fold prism and the periscope assemblies, mechanical tolerance analysis predicts that the greatest angular error in the x and z axes will be <0.1°.

Rotation of the fold prism has the greatest effect on detuning ability about the y-axis. The total error in this axis rotation has been estimated to be ±0.8°. A jig is used to ensure accurate alignment during the process of bonding the optics onto the assembly.

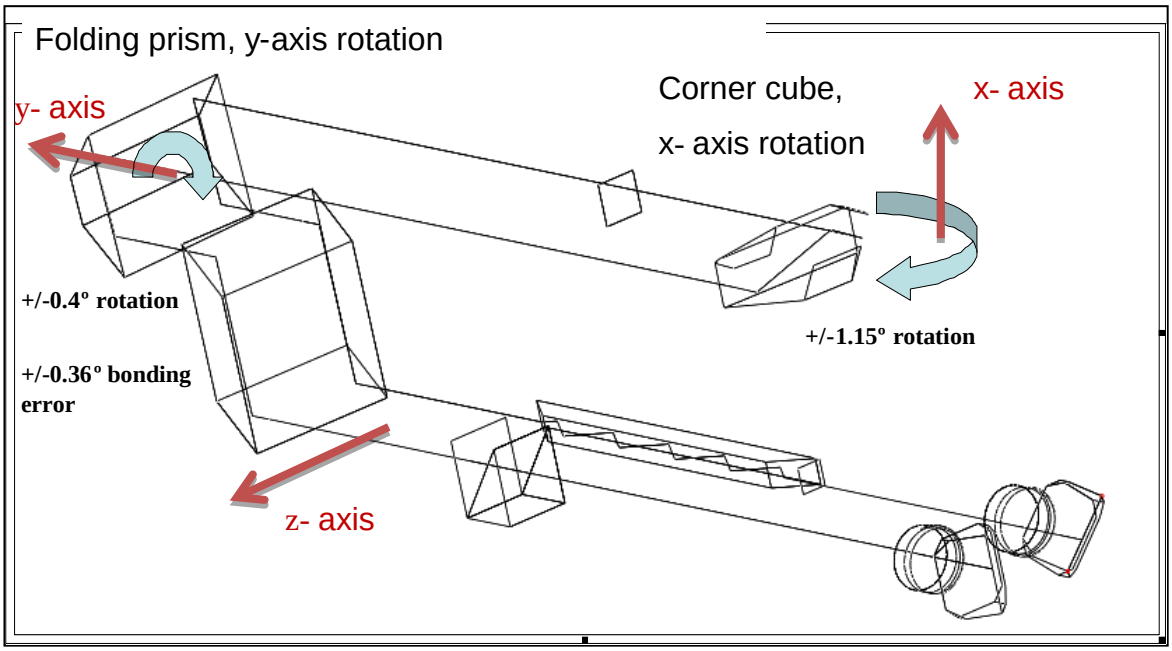

Figure 3-6: Three dimensional diagram of the folded resonator design with the degrees of freedom and limits shown for two optical elements that can be adjusted.

Angular error about the y axis is difficult to measure experimentally using a laser refection due to the frosted finish on the sides of the optics. Two optical element angular adjustments which have been measured for the folded resonator are shown in Figure 3-6. These two angular adjustments can be set in the laser resonator during alignment and could be in any position within the tolerance.

These two optical elements can be positioned to produce good detuning, with a minimum resonator reflectivity of 23% or, for comparatively poor detuning, a minimum resonator reflectivity of 29%. These numbers assume that all other optical elements are in the nominal positions. This presents an opportunity to improve the energy detuning ability of the resonator, by adjusting the alignment procedure to ensure that these two optical element positions are beneficial to energy detuning.

3.2.5 Method of output coupling control

The reason that a half waveplate has less control over the polarisation state than required is due to the polarisation state at the position of the waveplate. For example, circularly polarised light, which occurs when the horizontal and vertical components have 90° relative phase shift, would be completely unaffected by the angle of a half waveplate. It is possible that a quarter waveplate could be used to replace the half waveplate, which is used as standard. This change in waveplate was investigated using the computer model and a minimum resonator reflectivity of 11% is possible even when the two known detrimental optical element rotations are applied. This replacement is therefore recommended, as the output coupling can be controlled over a larger range, with greater margin for energy detuning.

3.3 EXPERIMENTAL MEASUREMENT OF LASER PULSE ENERGY AND OUTPUT COUPLING

An experimental investigation into the output coupling level in a sample folded laser resonator was carried out to verify the output coupling control predicted by the computer model. The set-up is shown schematically in Figure 3-7.

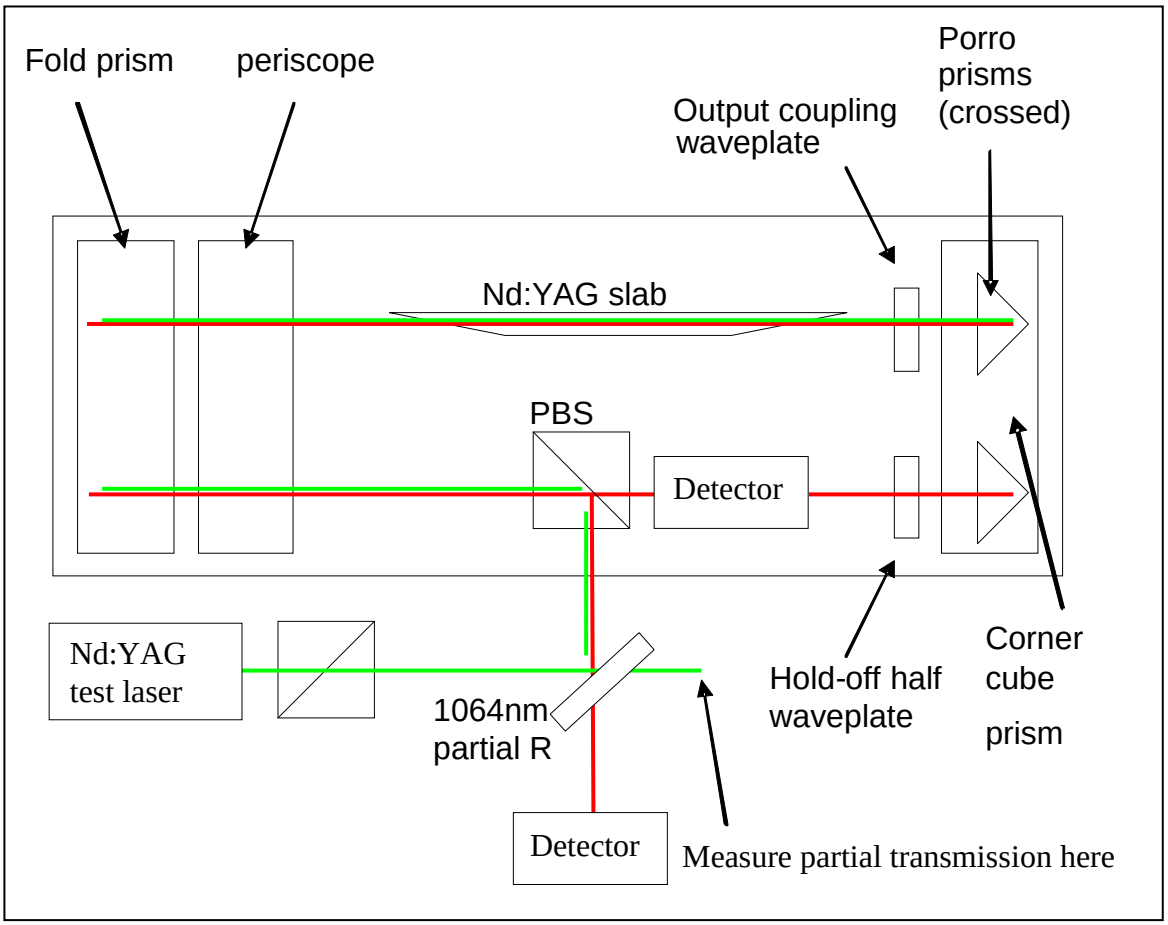

Figure 3-7: Set up to investigate level of output coupling.

A Nd:YAG test laser was co-aligned with the folded resonator output to measure the output coupling via the polarising beam splitter (PBS). In the diagram, the green line shows the laser ray entering the sample laser resonator and traveling around to the slab-side Porro prism. The red line then shows return path from the slab-side Porro prism and back out of the resonator. The whole range of output coupling was measured using both a half wave plate and a quarter wave plate. For each value of resonator output

coupling reflectivity the laser output energy was measured. The relationship can be observed in Figure 3-8.

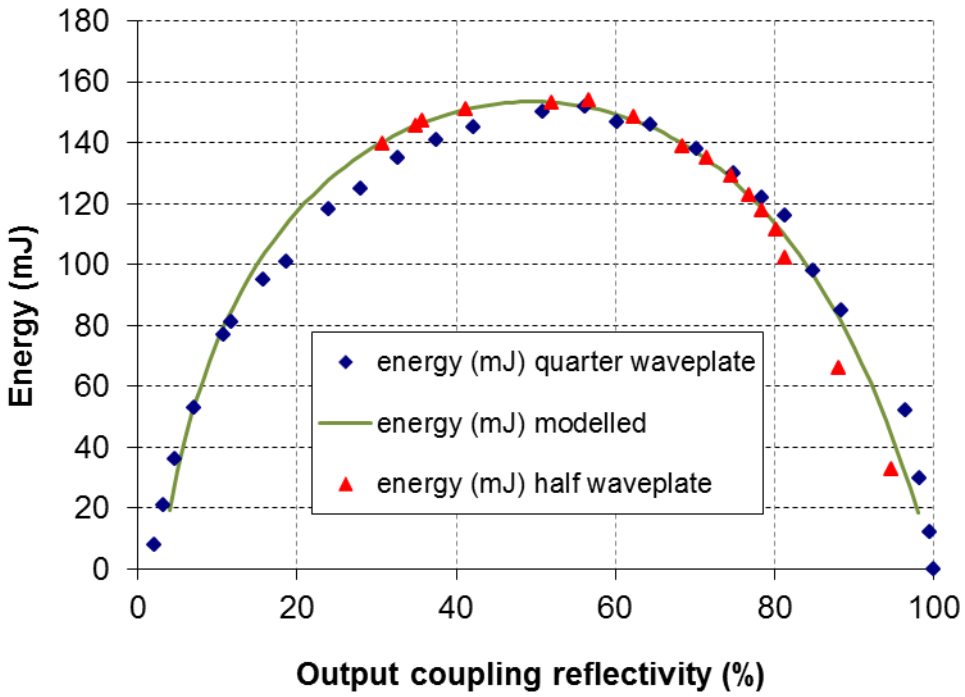

Figure 3-8: The dependence of pulse energy on resonator reflectivity, measured using both a quarter waveplate and a half waveplate.

The threshold pump pulse width for laser output was also measured for each resonator reflectivity to allow the total resonator loss to be calculated using the Findlay-Clay method [3]. However, the loss value was found to be sensitive to the pump pulse width, which had an associated uncertainty due to the discrepancy between the requested and the delivered current pulsewidth from the diode driver.

The predicted pulse energy was calculated using Rigrod analysis [4] and is shown in Figure 3-8, with good agreement with the experimental data. The intracavity loss (coating reflections plus diffractive loss) was adjusted to achieve this fit, and the value used was 20%. It is estimated that the intracavity losses in this resonator due to reflections at optical surfaces are approximately 10%, which implies that the diffractive loss is approximately 10%. Other factors such as non-optimal resonator alignment and

the uncertainty in the pump power could affect the output energy measurement, and produce an error in the assumed loss value.

As shown in Figure 3-8, both the experimental values and the modelled pulse energy show that an output coupling reflectivity of 54% is required for optimum energy in fixed-Q operation, and a reflectivity of 33% is required for 90% of the optimum energy.

3.4 CONCLUSIONS AND RECOMMENDATIONS

The optical element rotations that most affect the detuning ability of the folded laser resonator have been identified. In addition, two optical elements have been identified, which have some angular freedom about dowel or screw positions. These optical element rotations are the fold prism about the y-axis and the corner cube about the x-axis and have been shown in the computer model to cause a significant effect to the ability to detune the laser energy when combined with other optical element misalignments (minimum reflectivity ranging between 23% and 29%).

A short-term solution to the detuning issue that was implemented was an adjustment to the alignment procedure to allow greater output coupling control. This stated that the corner cube should be twisted fully clockwise during the initial resonator alignment and the folding prism should be twisted fully away from the slab.

A long term, more robust solution, which was also implemented, was to replace the half wave plate with a quarter wave plate. This improves modelled detuning ability to acceptable levels with ample margin, even if the two misalignments described above are in the detrimental position. This improvement in polarisation control was investigated experimentally using a sample folded resonator laser. The result confirmed the modelled predictions for output pulse energy as a function of output coupling and the quarter waveplate was shown to provide energy detuning to nearly 100%. In this example, the energy detuning provided when using a half waveplate was less than 10%, which demonstrated the issue that was being experienced during laser manufacture.

In Chapter 4, the folded resonator design is updated where a change to the Porro prism design is introduced. As a consequence of this change, the relative phase shift that is produced by the Porro prism is altered. Therefore, the computer model was used to

repeat the analysis of the energy detuning ability, and it was found that a change of the slab-side waveplate was required again (back to a half waveplate). The model has successfully been used to predict the required waveplates for adequate energy detuning in other laser resonator designs, which have different resonator folding optical elements.

The laser resonator modelling capability at Selex ES is continuously being improved by updating the model. It is recommended that the assumptions are challenged and that the computer model is validated using experimental data whenever it is used for predictions in performance. Further testing is recommended with a larger sample of laser slabs to determine if the effect of the slab coatings is consistent. It is also recommended that a slab be tested for depolarisation while being pumped (this will be carried out in Chapter 5).

The computer model could be verified with experimental data using a breadboard laser with known optical element angular positions. This investigation would require measurement of the angles of all optical elements, possibly using an alignment HeNe laser. The significant effort in carrying out this investigation was not considered to be worthwhile given the success of the computer model in finding solutions to the issue.

Investigation into production processes which produce angular errors, in particular for the optical elements that have been confirmed large contributors to depolarisation, is recommended. This would include the analysis of rejected optical assemblies, such as a periscope/fold prism assembly, to determine whether stress induced birefringence in the optical elements is having a significant effect on the polarisation state.

The damage thresholds of sensitive optical elements including Q-switches could be investigated and the requirement for detuning could be reviewed. A theoretical investigation into the Q-switched output energy as a function of output coupling has revealed that for this laser resonator design, the output coupling level for 10% detuned energy in fixed-Q mode is actually close to the optimum output coupling value for Q-switched operation. Therefore, in this example, the value of 10% detuning is confirmed to be a good choice, and it is recommended that this procedure of energy detuning continues.

3.5 REFERENCES

[1] A. Rapaport, S. Zhao, G. Xiao, A. Howard, and M. Bass, *"Temperature Dependence of the 1.06-µm Stimulated Emission Cross Section of Neodymium in YAG and in GSGG",* Applied Optics, vol. 41, pp. 7052-7057, (2002)

[2] E. Hecht, "*Optics",* Addison-Wesley, 4th Edition (2002)

[3] W. Koechner, "*Solid-State Laser Engineering",* Springer New York (2006)

[4] A. E. Siegman, "*Lasers",* University Science Books (1986)

CHAPTER 4. DESIGN IMPROVEMENT FOR REDUCTION OF LASER RESONATOR PRELASE PROBLEMS AND COST SAVING

In this Chapter, a major issue occurring during the production of laser resonators resulting in prelase was addressed by changing the resonator design. This design change resulted in the removal of the phase-matched coating on the Porro prism and the generation of a new specification for the retardance value of the waveplate adjacent to the Porro prism. A computer model was used to find a number of solutions for the waveplate retardance and angle required. The best option was selected by consideration of both the waveplate alignment and the performance over the full temperature range of -40 to 55°C. The performance of the new design was verified experimentally for the available temperature range of 20 to >100°C and an experimental alignment tolerance analysis was carried out to ensure the new design was robust. The original design was also tested experimentally so that the performance improvement could be assessed. The performance of the new design was found to be superior, so it was implemented across a number of laser production programmes. This design change has resulted in the prelase failure rate falling to zero after implementation in over 1000 laser system units. As a result of the design change Selex ES has saved a significant sum of money, both in material and labour costs. This has attracted recognition through the awarding of a gold level Finmeccanica innovation award.

4.1 INTRODUCTION

In this Chapter, a potential design change in the Q-switch leg of the folded resonator design shown in Figure 3-1 in Chapter 3, Section 3.1.1, is investigated. The Q-switch leg is shown in Figure 4-1. The Porro prism used in this resonator is an optical element which requires precise physical attributes. The precision of the 90° angle and the thickness of the apex edge are critical for good beam quality from the laser resonator. The front surface of the Porro prism, which is at normal incidence to the laser beam, is coated with a dielectric coating for antireflection at the laser wavelength of 1064 nm. In addition, the original Porro prism design used in the resonator has a dielectric coating on the back surfaces. These coatings are applied to compensate for the relative phase shift of the s- and p-pol components of the laser light during total internal reflection (TIR) [1], and are termed phase-matched coatings.

During laser resonator manufacture, a variation in the hold-off performance of laser resonators has been attributed to a variation in performance of the phase-matched coating. The coating performance variation from batch to batch of Porro prism orders, or variation in coating performance over the width of the Porro prism, could be the cause of prelase. Prelase can produce beams with high spatial frequency variation across the intensity pattern, which in turn can cause laser induced damage of optical elements. In addition to the prelase problem, a variable supply of the phase-matched coated Porro prisms threatened continuous laser manufacture. These optical elements are expensive to manufacture as they are produced by separate optical component and coating suppliers, with low yield. An alternative design without phase-matched coatings was desired to reduce cost, and to allow the possibility of alternative suppliers to increase security of supply.

A new design is explored which uses Porro prisms without phase-matched coatings, instead using a suitable waveplate to compensate for the relative phase shift of the s- and p-pol components of the laser light during the two total internal reflections. To ensure that this approach is viable this investigation was undertaken to model the polarisation state in the Q-switch leg of the laser resonator and to verify the performance experimentally.

4.2 THE ORIGINAL DESIGN

The original design of the Q-switch leg of the folded resonator uses the set-up shown in Figure 4-1.

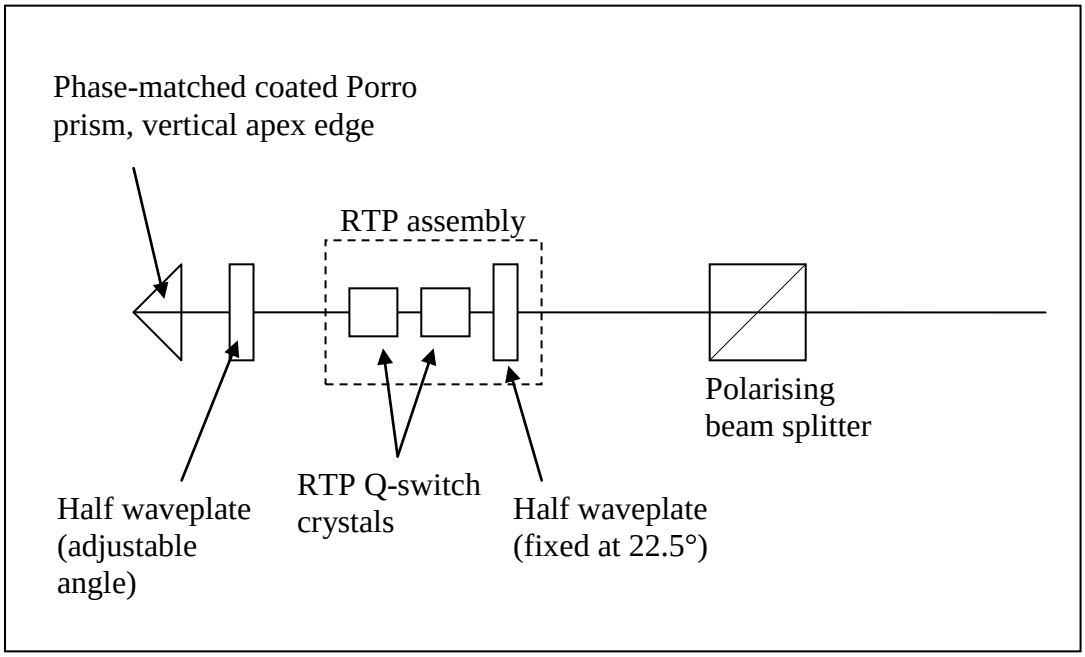

Figure 4-1: Current Q-switch leg design for the folded laser resonator.

Vertical linearly polarised light enters the Q-switch leg of the laser resonator through the polarising beam splitter. The light is rotated by 45° by the half waveplate. The RTP Q-switch crystals then change the light to circularly polarised, when the quarter-wave voltage is applied. The coated Porro prism is designed to produce a relative phase shift of $\pi/2$, which means that the reflected light is again vertically linearly polarised when it reaches the polarising beam splitter and it is all transmitted to the other side of the resonator (high-Q). When the Q-switch voltage is removed, the light returning to the polarising beam splitter is horizontally polarised so it is reflected out of the resonator (low-Q).

The phase-matched coating on the Porro prism is designed to compensate for the phase shift between the s-pol and p-pol components of the beam, which would otherwise occur during total internal reflection. If the Porro prism coating is perfect and the angles of all the optical elements in the laser resonator are nominal, the Q-switch leg is

in the hold-off state without the adjustable half waveplate being inserted. The reasons for it to be included in the design are:

1. To adjust for angular errors in other optical elements, such as the Porro prism or the polarising beam splitter.
2. To adjust the Q-switch leg to high Q factor so that the resonator can operate in the fixed-Q regime. This is required to set the resonator output coupling to detune the laser pulse energy, as discussed in Chapter 3.

4.2.1 Porro prism characteristics which affect hold-off

The ability of the laser resonator to achieve hold-off is determined by the extinction ratio of the polarisation state at the polarising beam splitter. If the extinction ratio is 20 dB, then 1% of the light will be transmitted by the polarising beam splitter to the slab-leg of the laser resonator. If this is sufficient feedback for gain to overcome loss in the resonator, then the hold-off condition will fail and prelase will occur.

The important characteristics of the original Porro prism design, which affect the performance of the laser resonator are:

1. Roof angle accuracy, which is specified as 90°0'0"±0°0'2". If the roof angle is not 90°, then the far-field beam profile splits into two, due to differing ray directions depending on the path through the Porro prism.
2. The accuracy of the apex edge. If the thickness of the apex is large, a direct reflection into the resonator could result and reduce performance. The beam profile will have a line through the centre if the apex edge is thick.
3. The consistency of the phase matched coating affects the hold-off performance of the laser.
4. Anti-reflection coatings are important to minimise intracavity loss in order to maximise the efficiency of the laser and also to reduce feedback which could cause prelase.

5. Transmitted wavefront aberrations need to be minimised to maintain a plane wavefront in the resonator. Aberrations almost always result in a reduction in beam quality.

During this investigation it is assumed that the omission of the phase-matched coating does not change the physical properties of the Porro prism. The hold-off performance measured using the extinction ratio is the important parameter for investigation.

The phase-matched coatings on the TIR surfaces of the Porro prism are designed for an incident beam with a linear polarisation at 45º to the Porro prism apex angle. The reflected laser beam has a 180º phase shift as required for hold-off. In the new resonator design, omitting the phase matched coating from the TIR surfaces introduces a phase shift which is not 180°. To compensate for the incorrect polarisation state, the half waveplate is replaced with a waveplate of an appropriate retardance to produce the correct phase shift resulting in a linear polarisation state as required to achieve hold-off in the laser.

4.2.2 Difficulties in alignment of the hold-off waveplate

During alignment of the original laser resonator, four waveplate angles for extinction ratio minima were observed. These four angles all produced differing levels of extinction ratio. In the folded resonator design, angular adjustment of the half waveplate angle is awkward resulting in limited angular precision. The extinction ratio is not directly measured, only the width of the hold-off region is estimated in terms of waveplate angle. Therefore, it is difficult to effectively assess the performance of each waveplate position that produces an extinction ratio minimum. These factors can result in a non-optimal position being used. Stress on the waveplate due to tightening the waveplate retaining screw also affected the extinction ratio. It is recommended that this mechanical design issue is investigated separately.

The effect of an ambient temperature variation on the Q-switch leg extinction ratio was unknown. The temperature dependence of the coating could not be modelled as the details of the coating design were proprietary to the supplier. Drying out of the coating was known to produce a degradation in performance of some coatings.

4.2.3 The tooling waveplate

In the original laser resonator design the RTP Q-switch required an incident linear polarisation at 45º to its horizontal mounting surface. As the incident beam from the polarising beam splitter was polarised along the vertical axis, a half waveplate is mounted on the Q-switch mount nominally at 22.5º to rotate the linear polarisation angle to the correct state. During laser resonator alignment the fixed-Q performance must be measured before the Q-switch is inserted. Therefore a tooling waveplate is inserted in the position of the half waveplate, which is part of the Q-switch assembly. The tooling waveplate is nominally set to the same angle as the Q-switch half waveplate. However, a discrepancy in the waveplate angles may exist due to a ±0.5º uncertainty in the waveplate axes, which are marked by the supplier, and a ±0.5º uncertainty in the accuracy when mounting the waveplate. A comparatively small angular error in the mounting accuracy of the Q-switch mount due to washer thickness variations and machining errors, also contributes to the uncertainty.

4.2.4 Use of the Q-switch for compensation

The angular errors may be different for the tooling waveplate and the Q-switch waveplate. This means that it is possible that hold-off is achieved in fixed-Q operation but not in Q-switched operation or vice-versa. If hold-off is not achieved while the Q-switch is inserted, the RTP crystals can be rotated in the horizontal plane in order to compensate for the phase shift due to the error in the waveplate angle. It is unclear to what degree the rotation of the Q-switch assembly was utilised in the original resonator design and what the consequences were as the thermally-induced stress in the RTP crystals changed over the full temperature range.

4.3 COMPUTER MODEL TO DETERMINE THE APPROPRIATE WAVEPLATE RETARDANCE AND ANGLE

A computer model written in the MathCAD programming language was used to determine the theoretical performance of both the original resonator design and the uncoated Porro design that is proposed, both without the Q-switch. The computer model simulated the polarisation state through the optical elements shown in Figure 4-2. The red line represents the incident laser beam path, which is reflected back along the same path by the Porro prism. The polarising beam splitter reflects the entire laser beam if hold-off is perfect. In reality, the polarising beam splitter transmits a small portion of the light, even if all the light is in the correct polarisation state for reflection. Typically, the extinction ratio of the polarising beam splitter is 30 dB, which is the value assumed in the model.

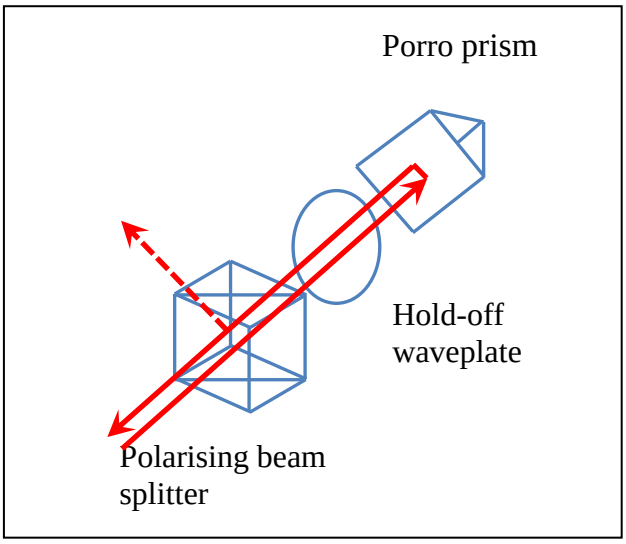

Figure 4-2: Arrangement of optical elements that were modelled.

This model uses Jones matrices to represent the optics, which are used to calculate the reflected s-pol and p-pol components of the incident light. The Jones matrix for the Porro prism was taken from the literature [2]. The MathCAD solve feature was used to calculate the appropriate values for the angle and retardance of a waveplate that gives

exactly 180º phase shift between the components for the resultant beam. After passing the polarising beam splitter, the incident linear polarisation state is at 45° to the Porro prism apex angle. Temperature dependence of the waveplate retardance was included in the model. The quartz waveplate retardance is dependent on temperature, because the birefringence and the waveplate thickness change with temperature [3]. This source quotes a measured value for the normalised temperature dependence of retardance (γ) for SiO_2 of -1.23×10^{-4} K^{-1}. The Porro prism material is N-BK7, which has a refractive index of 1.50669 at 25°C. The temperature dependence of the Porro prism phase shift is calculated using the temperature coefficient of N-BK7 optical glass refractive index, which is 2.4×10^{-6} K^{-1} [4].

The RTP Q-switch crystals were absent from the computer model. This is because it was not clear how to represent the biaxial crystals as a Jones matrix, or how their birefringence changes with temperature. The same Q-switch is used regardless of the Porro prism and waveplate used, so a comparison could be made without the Q-switch. It is recommended that the Q-switch be modelled in future work, to increase understanding of potential prelase issues.

An alternative solution was tested experimentally, which involved using a half and a quarter waveplate together to achieve the correct retardance for the hold-off condition. Although a high extinction ratio was achieved by iterating the two waveplate angles, this alignment was time consuming and the design was considered a more complicated change, and was therefore disregarded.

A simpler design uses a single waveplate with a calculated retardance, which can be angled to produce the desired relative phase shift. Two different retardance values for the waveplate were calculated, using the computer model, which produced the required result. These retardance values were 38º and 142º or higher order values such as 398° and 502°. The waveplates needed to be first order waveplates to enable practical use without breaking the waveplates on contact, so the waveplate retardance values procured for testing were 398° and 502°. Both waveplates were tested experimentally, and the plots are shown in Figure 4-3 with good agreement with the theoretical curves.

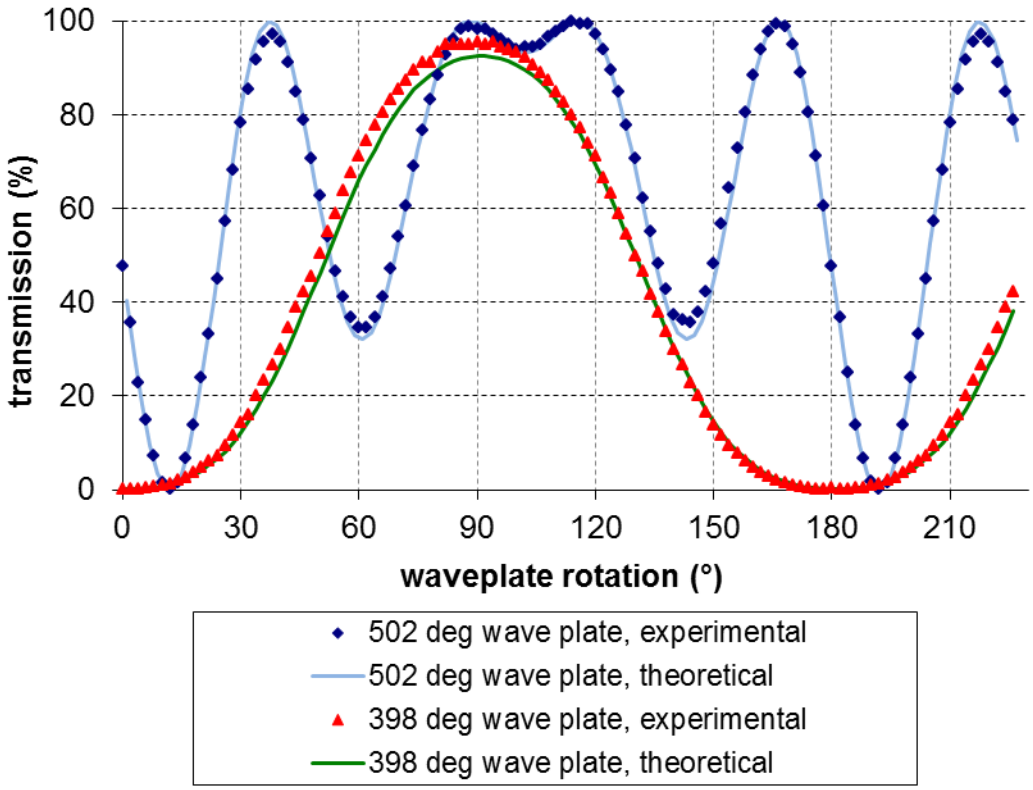

Figure 4-3: Proposed uncoated Porro design, single waveplate options.

The 398º waveplate produced a much wider curve about the hold-off position (minimum transmission) than the 502° waveplate, so the sensitivity to alignment of the waveplate was reduced. In addition, the theoretical sensitivity of the extinction ratio to waveplate temperature is less for the 398° waveplate than the 502° waveplate. For these reasons, the 398º waveplate was chosen for the hold-off waveplate in the folded laser resonator. The 398° quartz waveplate was approximately 140 µm thick, which was 74% of the first order half waveplate thickness used in the original design (540°).

In Figure 4-4, the transmission of the polarising beam splitter for varying waveplate angle is shown. The original design, and the proposed design using an uncoated Porro prism and the 398° waveplate, are plotted for comparison.

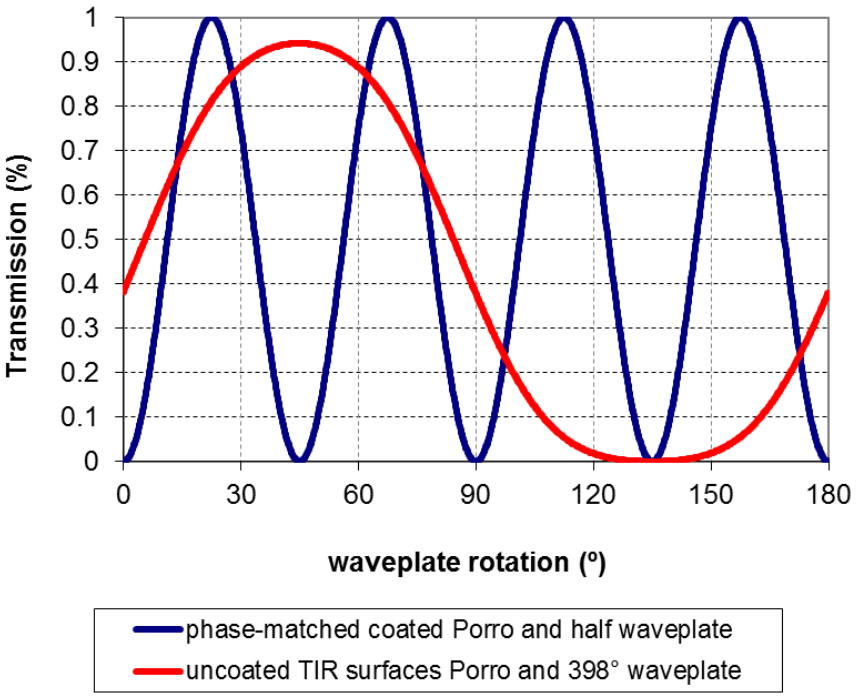

Figure 4-4: Proposed uncoated Porro design, compared with current design.

The hold-off performance is measured by the extinction ratio which is derived from the ratio of the maximum and the minimum transmission (the transmission is maximised when the Q-switch is turned on or a quarter waveplate is used to simulate it). The four minima of the original design can be seen as the blue line in Figure 4-4. The proposed uncoated Porro design is shown to have just one minima position, which is much wider in terms of waveplate angle.

The 398º waveplate was designed to produce a 180º relative phase shift when combined with the two TIRs of an uncoated Porro prism. The waveplate cannot be set to any angle to produce a 0º phase shift, which corresponds to maximum output energy in fixed-Q operation. Therefore, a 6% loss is introduced when the waveplate is rotated to maximise energy in fixed-Q operation, as shown in Figure 4-4. When the Q-switch has voltage applied to produce a quarter wave retardance, this loss is no longer observed, so does not impact the conversion efficiency of the laser in Q-switched mode.

To ensure that the correct energy detuning level is achieved, the full fixed-Q energy should be available from the laser resonator. This can be achieved by removing the tooling waveplate, which means that the polarisation of the incident light will then be

perpendicular to the Porro prism knife-edge and any relative phase shift will not affect the resonator Q-factor. An alternative solution using a quarter waveplate to substitute the Q-switch, allows accurate setting of the detuning level.

4.4 EXPERIMENTAL ANALYSIS OF Q-SWITCH LEG DESIGNS OVER TEMPERATURE

The experimental set-up is shown in Figure 4-5 which allowed the Porro prism and hold-off waveplate to be tested over a temperature range from ambient temperature (20°C) to 140°C using a hot plate. The performance of the original design and the uncoated Porro prism design were compared over the temperature range. The test was carried out twice for the original phase matched coating Porro prism and twice for the uncoated Porro prism. In each case, the experiment was carried out with the test waveplate inside and outside the heated box. This was to separate the effects of the Porro prism temperature and the waveplate temperature on the extinction ratio. The Porro prism temperature variation alone was found to have an insignificant effect on the extinction ratio in the uncoated Porro prism case. In the coated Porro prism case, the extinction ratio was worsened to less than 20 dB, which was attributed to the drying out of the optical coating.

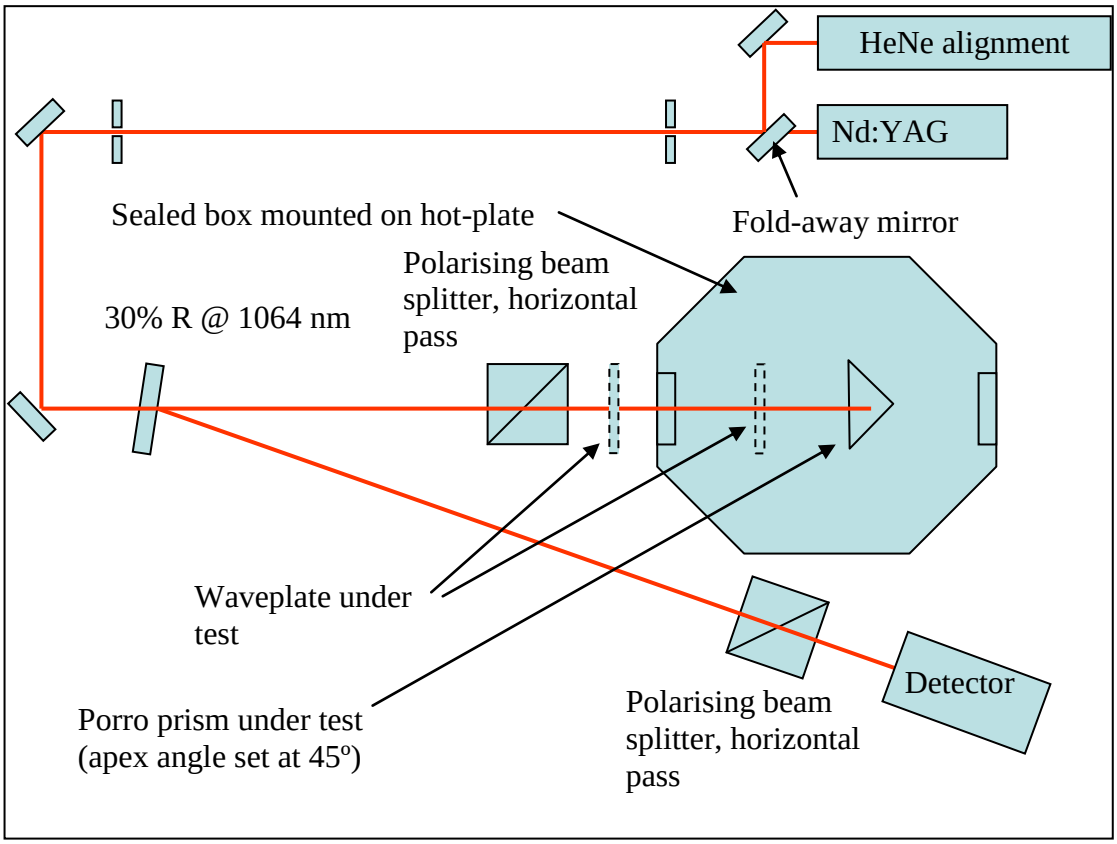

Figure 4-5: Set-up for testing of the uncoated Porro prism design, compared with the original design.

Experimental testing of the uncoated Porro Q-switch leg set-up, shown in Figure 4-5, has provided results that show good correlation with theoretical performance over a temperature range as can be seen in Figure 4-6. Theoretical data plots are shown for the cases where the 398º waveplate is of nominal value and also for 398º+1º and 398º-1º to reflect the uncertainty in the supplied waveplate retardance. The model predictions and the experimental results show that an extinction ratio of >20 dB is achieved over the full temperature range. Based on this analysis, the original waveplate retardance tolerance value, which was ±2° for the supplier specification, was tightened up to ±1°, to ensure sufficient performance margin.

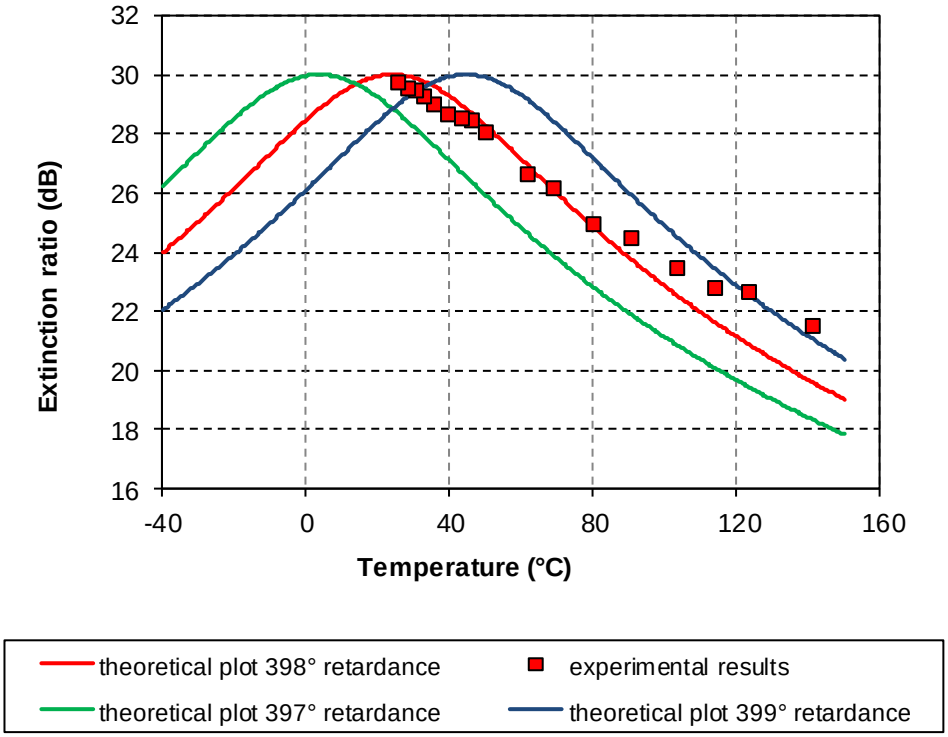

Figure 4-6: Experimental results of testing proposed uncoated Porro design over temperature, compared with theoretical data. Uncertainty in waveplate retardance is also plotted.

It is assumed in the model that the phase-matched coating on the Porro prism is ideal with zero temperature variation. Therefore, the temperature dependence of the Q-switch leg using a coated Porro prism predicted by the model is not useful. A coated Porro and half waveplate sample were also tested in the experimental set-up. It is shown in Figure 4-7 that the optimum extinction ratio was not at ambient temperature as would be expected, as was the case for the uncoated Porro prism set-up. Therefore it is concluded that the assumption of an ideal phase-matched coating with zero temperature variation that was used in the model was far from adequate for this Porro sample. It is also possible that the half waveplate retardance was not accurate.

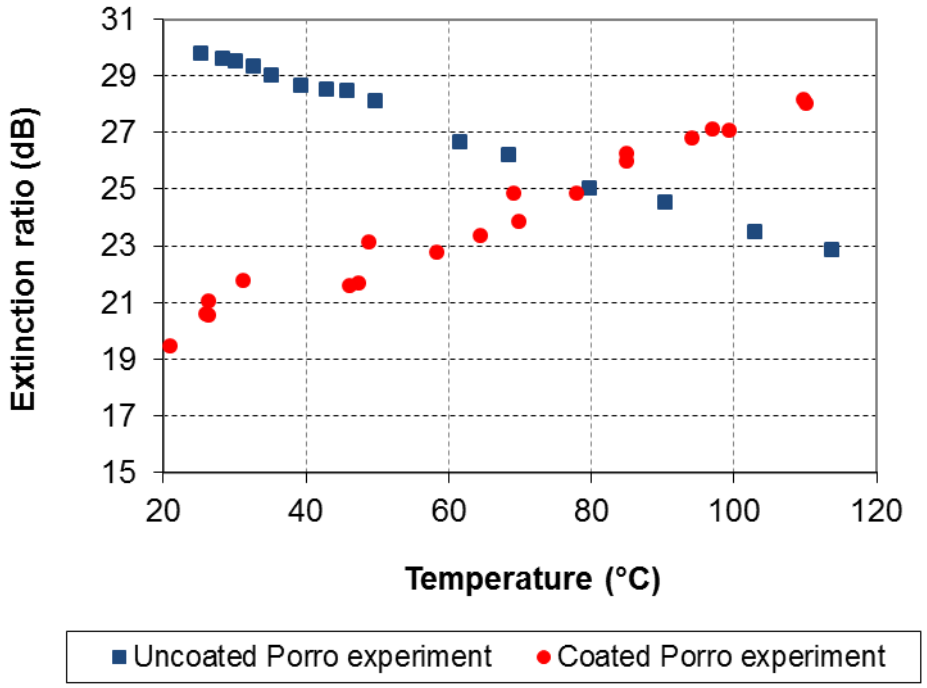

Figure 4-7: Experimental results of extinction ratio performance over temperature for both the uncoated Porro design and the original coated Porro design.

There were difficulties in achieving reliable results at temperatures <20°C inside the environmental chamber due to temperature varying birefringence effects of the chamber windows and misalignment due to thermal expansion. Therefore, the uncoated Porro prism design was integrated into three folded laser resonators for testing. The lasers were built using the standard laser production alignment and testing procedures. The laser resonator hold-off was tested for at various pump levels, at the temperature extremes of -20ºC and +55ºC. No pre-lase was detected at ambient temperature even when the oscillator diodes were driven at the maximum current and pulse duration possible. The only case of pre-lase was seen in one of the lasers at a temperature of -20ºC, when the oscillator diodes were driven at an increased current of 120 A (25% greater than normal). This gives an indication of the margin that is available before pre-lase is detected.

4.5 ANALYSIS OF OPTICAL ELEMENT ANGULAR TOLERANCES

An experimental and a theoretical investigation of the angular tolerances of the Q-switch resonator leg optical elements were carried out for the new design using uncoated Porro prisms. This was carried out to ensure that the new design was robust and to highlight any alignment issues, which may exist. The angular tolerance of the biaxial RTP Q-switch crystals was investigated experimentally only, due to the difficulties in modelling them.

4.5.1 Experimental analysis of tolerances

An experiment was set up to replicate the Q-switch leg of the laser as shown in Figure 4-8.

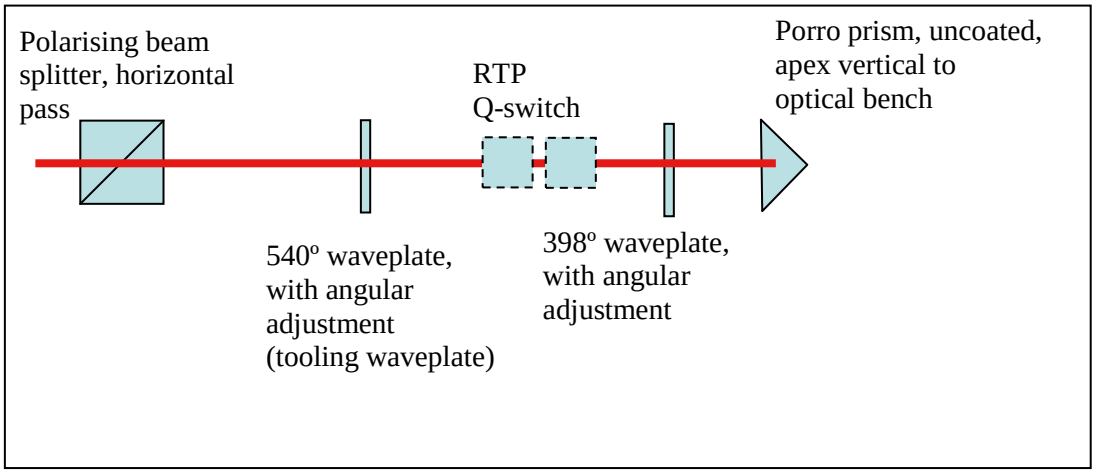

Figure 4-8: Experimental set up for testing the angular tolerance of the optics in the proposed uncoated Porro design.

An Nd:YAG laser was used to measure the extinction ratio of the optical set-up. A quarter waveplate was used in the position of the Q-switch to switch between low-Q (hold-off) and high-Q operation. The reflected portion from the polarising beam splitter was measured in each case and used to calculate the extinction ratio of the Q-switch leg

set-up. Using the uncoated Porros, before a Q-switch was inserted an extinction ratio of approximately 30 dB was routinely achieved by optimising the angle of each optical element iteratively. It is known from previous investigations that the requirement for extinction ratio is >23 dB to ensure that hold-off is maintained over the full range of environmental conditions. Each optical element in this set-up was then individually rotated in turn and the effect on the extinction ratio was observed.

4.5.2 Experimental results and comparison with theoretical values

The graph in Figure 4-9 shows how the extinction ratio is affected by the rotation of the tooling waveplate.

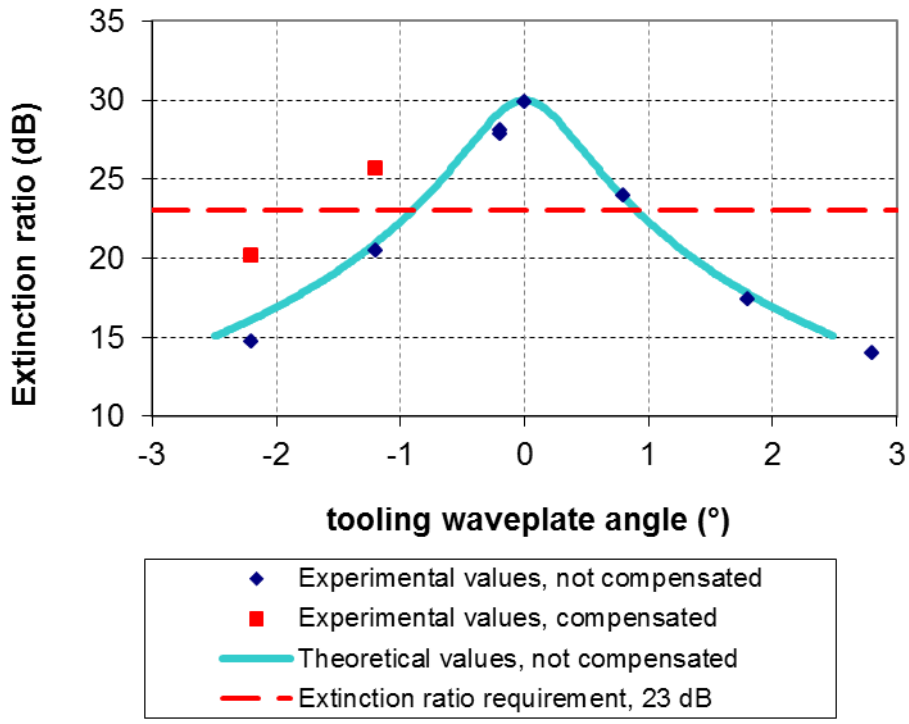

Figure 4-9: Graph of extinction ratio variation against tooling waveplate angle.

The blue plot shows the effect of rotating the tooling waveplate only and the red plot shows the effect while the 398º waveplate is used to compensate for the degradation in extinction ratio. This shows that for an angular misalignment of approximately 1º an extinction ratio of 26 dB is achieved, which is within acceptable levels. However, for

an angular misalignment of approximately 2º an extinction ratio of 20 dB is achieved, which is outside of acceptable levels.

The graph in Figure 4-10 shows the extinction ratio level plotted as a function of the 398º waveplate angle, for each of the three tooling waveplate angles. As can be seen, the variation of the 398º waveplate is adjusted by approximately 9º when used to compensate for the tooling waveplate misalignment of 1º.

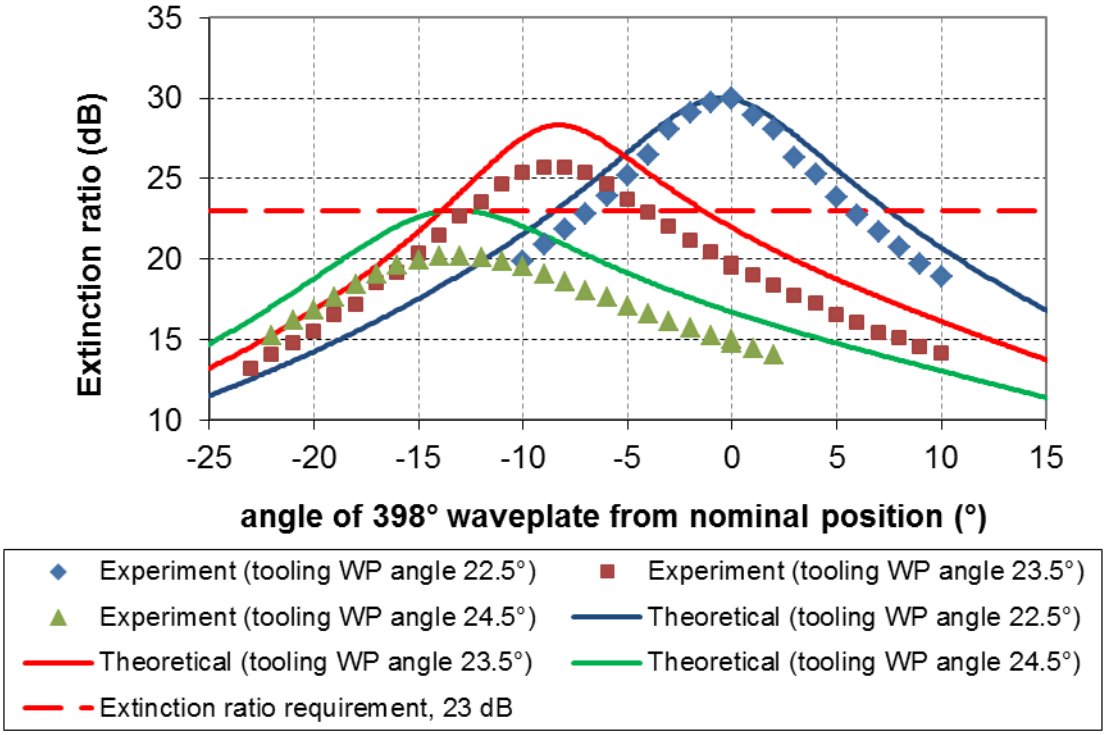

Figure 4-10: Graph of the extinction ratio dependence on the 398° waveplate angle. Three tooling waveplate angles were tested.

The ratios of the peaks and their positions fit well with theory for the three tooling waveplate angles. The model accurately predicts the trend of extinction ratio dependence on tooling waveplate angle. The extinction ratio is not as sensitive to adjustment of the 398º waveplate as to the tooling waveplate, as shown in Figure 4-10. A rotation of ±7º is possible while achieving an extinction ratio of >23 dB. In the case that the tooling waveplate is rotated off by approximately 1º, a rotation of ±3º is possible while achieving an extinction ratio of >23 dB.

The graphs in Figure 4-11 and Figure 4-12 show the effect on the extinction ratio due to rotation of the polarising beam splitter and the Porro prism respectively. The data points are joined, simply to visually separate the three plots. One of the plots shows the effect on extinction ratio due to rotation of the polarising beam splitter or Porro prism only. The other plots show the effect with the additional adjustment of the 398º waveplate and for the adjustment of the 398º waveplate and the RTP Q-switch in the horizontal plane together. When the additional adjustments are made, some compensation for the misalignment is possible to recover the extinction ratio.

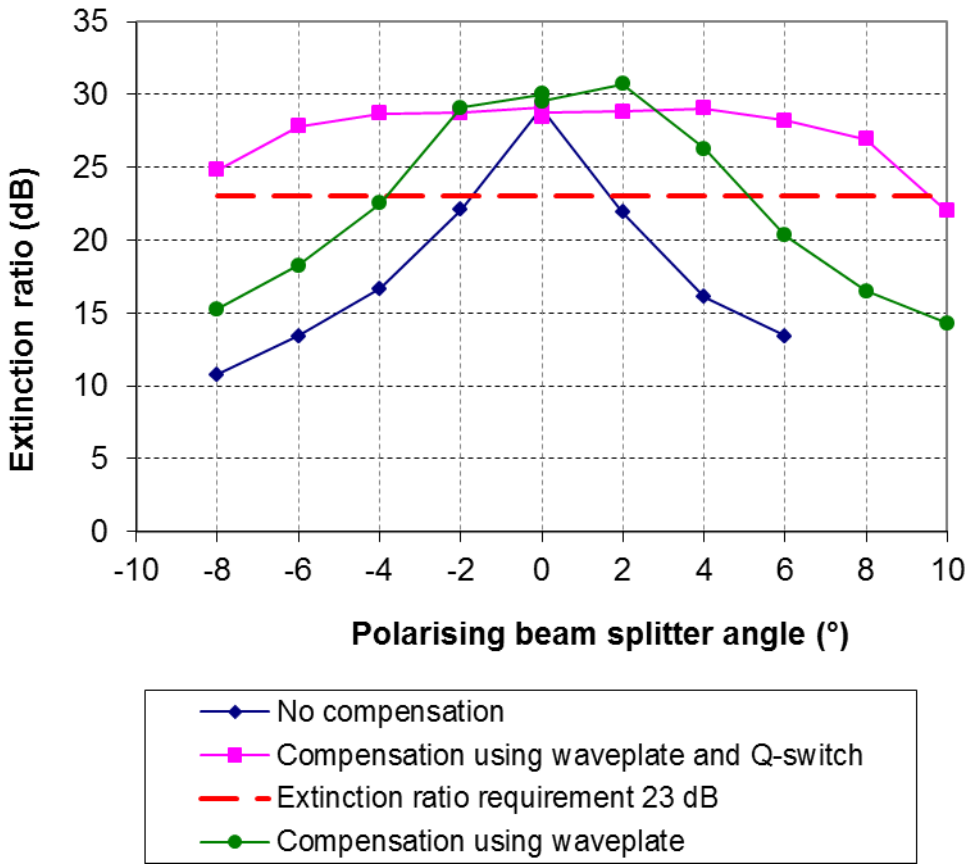

Figure 4-11: Extinction ratio variation as the polarising beam splitter is rotated about the incident beam.

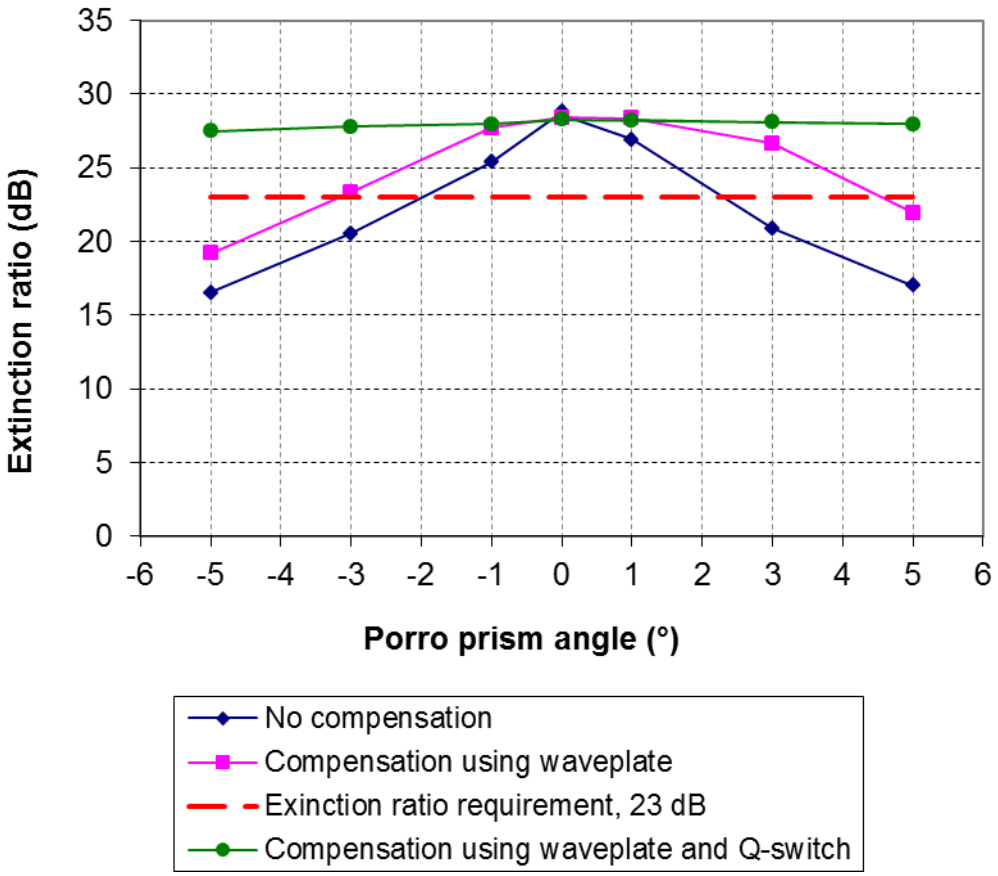

Figure 4-12: Extinction ratio variation as the Porro prism is rotated about the incident beam.

Both the polarising beam splitter and the Porro prism can be misaligned by ±5º while achieving an extinction ratio far in excess of >23 dB if the additional compensation adjustments are made. If the Q-switch is not to be used in this way and only the 398º waveplate is used for compensation, a misalignment of more than ±3º is still possible while achieving an extinction ratio of >23 dB. Figure 4-13 and Figure 4-14 show the dependence on the angle of the RTP Q-switch assembly which incorporates a half waveplate, in the horizontal and vertical axes respectively.

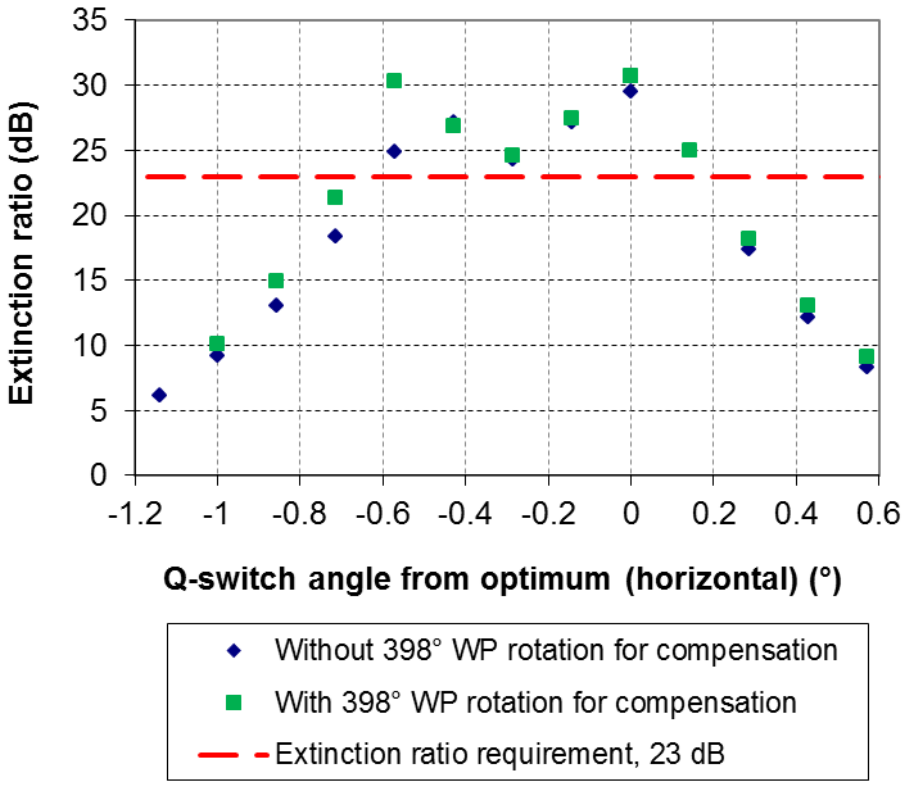

Figure 4-13: Extinction ratio variation with Q-switch assembly angle in the horizontal axis. Plots are shown for extinction ratio with and without compensation by rotation of the 398° waveplate.

Rotation of the half waveplate in the horizontal plane does not have a significant effect on the extinction ratio so it can be neglected. Rotation of the Q-switch assembly showed that the extinction ratio when optimised was on one of two peak values. The reason for this double peak is unclear and could be further investigated in other Q-switch assemblies. It could be that the two RTP crystals are mounted in such a way that only one crystal can be optimally aligned at a time due to mounting error of the two crystals. Adjustment of the 398º waveplate angle compensated for some phase shift introduced by the misaligned Q-switch and improved the extinction level by a small amount.

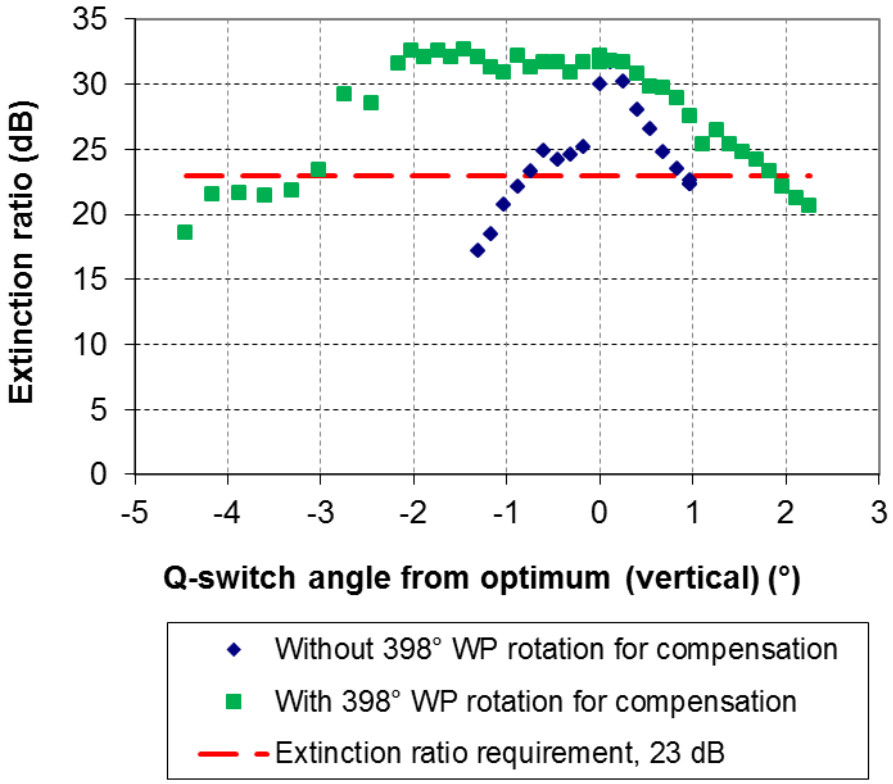

Figure 4-14: Extinction ratio variation with Q-switch assembly angle in the vertical axis. Plots are shown for extinction ratio with and without compensation by rotation of the 398° waveplate.

The Q-switch assembly tested could be misaligned in the horizontal plane by +0.2º or -0.6º while achieving an extinction ratio of >23 dB. Adjustment is available in this axis in order to optimise extinction ratio, so if the adjustment is precise the optimum position can be found where the extinction ratio is acceptable over the full range of environmental conditions.

As shown in Figure 4-14, the sensitivity to misalignment of the Q-switch in the vertical axis is highly dependent on the ability to compensate using the angle of the 398º waveplate, unlike misalignment of the Q-switch in the horizontal axis. With no compensation the Q-switch assembly can be misaligned in the vertical plane by ±0.7º while achieving an extinction ratio of >23 dB. With compensation, the Q-switch assembly can be misaligned in the vertical plane by +1.8º or -3º while achieving an extinction ratio of >23 dB. The data produced when rotating the Q-switch in the vertical axis also shows some evidence of a double peak, although not as clearly as in the horizontal case.

4.6 CONCLUSIONS

A change to the folded laser resonator design has been investigated, in which a coating on the TIR surfaces of a Porro prism was removed, and the retardance of an existing waveplate was altered so that the relative phase shift of the reflected light was corrected. A computer model was used to find two solutions for the waveplate retardance of 398° and 502° (first order waveplates). They were tested experimentally, and the polarisation states matched those predicted by the computer model. The 398° waveplate was chosen for use in the resonator, due to its reduced angular tolerance compared with the 502° waveplate and with the original design. The performance of the uncoated Porro prism and the 398° waveplate over the full operating temperature range was modelled and tested experimentally, for temperatures of ambient and greater. The modelled and experimental results were in good agreement. The performance of the original design was inferior over the temperature range that was tested experimentally. The theoretical performance of the original design could not be fully modelled because information about the phase matched coating was proprietary to the supplier.

Angular tolerance analysis was carried out for the new design, to show the precision with which each optical element must be mechanically positioned. Although the extinction ratio was sensitive to the angle of the optical elements in isolation, such as the polarising beam splitter and the Porro prism, the degrees of freedom during alignment allowed for the partial compensation of the relative phase shift to recover the extinction ratio performance to greater than the required level of 23 dB. These degrees of freedom were the adjustment of the Q-switch assembly angle in the horizontal axis and the angle of the 398° waveplate. It was useful to discover the double peak in extinction ratio which is possible when adjusting the Q-switch angle. Adjustment of the Q-switch assembly angle in the vertical axis is not possible, but it was shown that the tolerance which is better than ±0.5° would not cause an issue, as the 398° waveplate angle can be adjusted to ensure the extinction ratio is optimised. The tooling waveplate is required to be positioned with an angular tolerance of ±1°, which is ensured in the design.

Three fully engineered laser systems were built with the uncoated Porro prism and 398° waveplate incorporated and tested over the full temperature range, which showed that

there were no prelase issues. In addition, there were no issues during laser resonator alignment due to angular tolerances of the optical elements.

The new Porro prism design brings advantages in addition to the reduced risk of prelase over the operating temperature range. There is a cost reduction due to absence of the phase matched coating. The Porro prism yield is improved and the use of multiple suppliers, which is now possible, allows for an uninterrupted supply, and further cost reduction due to supplier competition.

Unlike the original design, the relative phase shift introduced by the uncoated Porro prism can be modelled over temperature to predict the design performance, which will aid problem solving in the future if it is necessary. The removal of the coating reduces the risk of laser induced damage to the TIR surfaces. The total wave front error measured for uncoated Porros was less than for coated Porros, therefore producing fewer aberrations in laser beams and potentially a better beam profile. In fact, testing of both Porro prism designs using a common laser resonator showed that the beam profiles exhibited no significant differences. The unpredictability in the design due to an unknown variation in the coating across the beam profile area was eliminated in the uncoated Porro design.

The new design was implemented across a number of laser production programmes, which shared a common resonator design. This has saved Selex ES a significant sum of money, both in material and labour costs. This investigation and solution was submitted to the Finmeccanica Innovation Awards 2012 and was successful in being chosen for a Gold Award. This was chosen in recognition of this successful improvement to a common laser resonator design, which has now been incorporated into a number of laser products. Over 1000 units share the new resonator design, with the defects per unit (DPU) falling from 13% to 0%, for pre-lase problems that were traced back to the Porro prism assembly (which includes the waveplate).

4.7 RECOMMENDATIONS

The half waveplate could be moved from the Q-switch assembly to the polarising beam splitter assembly. This would remove the need for the tooling waveplate, and therefore the unknown discrepancy in angle between the Q-switch assembly half waveplate and the tooling waveplate. It should be noted that if the waveplate was moved and made non-removable, a quarter waveplate jig would be required in place of the Q-switch to allow alignment in fixed-Q operation with full energy and accurate energy detuning. Changing of the half waveplate shape, from circular to square, has the potential to improve laser hold-off, by reducing the angular uncertainty of the waveplate.

It was not clear how to represent the biaxial RTP Q-switch crystals as Jones matrices, or how their birefringence changes with temperature. Further investigation into the possibility of modelling the Q-switch is recommended, to increase the understanding of potential prelase issues.

4.8 REFERENCES

[1] E. Hecht, "*Optics"*, pages 114-115, Addison-Wesley, 4th Edition (2002)

[2] M. K. Chun and E. A. Teppo, *"Laser resonator: an electrooptically Q-switched Porro prism device"*, Applied Optics, vol. 15, pp. 1942-1946 (1976)

[3] S. M. Etzel, A. H. Rose, and C. M. Wang, *"Dispersion of the temperature dependence of the retardance in SiO2 and MgF2"*, Applied Optics, vol. 39, pp. 5796-5800 (2000)

[4] Schott company website, *"www.us.schott.com/advanced_optics"*

CHAPTER 5. MITIGATION OF SLAB THERMAL LENSING

In this Chapter, the effects of a thermally induced lens in a zig-zag geometry laser slab are investigated. The thermal lens was measured in a number of nominally identical slab assemblies. One particularly poorly performing slab assembly produced a near-field beam intensity pattern that degraded over time. This slab was used to test a number of potential solutions, with the goal of reducing or compensating for the thermal lens and its effect on beam quality.

5.1 INTRODUCTION

The aim of the work was to improve the laser near-field beam intensity pattern of a laser system in the presence of thermal and static aberrations in order to reduce the chances of a failure during production. Typically a failure is due to a beam parameter such as the beam diameter falling outside of a specified range of beam sizes. In addition, an enhanced range of operating average power is sought after, allowing higher pulse repetition rates to be used, than the standard 20 Hz.

In this chapter, the development of laser diode side-pumped Nd:YAG slab lasers is discussed. These lasers use cross Porro prism or non-planar ring resonators, which were both introduced in Chapter 2. The important parameters of these lasers allowing them to perform their targeting application are pulse energy, pulsewidth and divergence. The near-field beam intensity pattern is also of importance, as optical elements which are introduced downstream from the laser system have a limited aperture size and damage threshold. In addition to this, the laser near-field beam intensity pattern must be small enough to fit through the exit aperture of the chassis without significant loss in energy due to beam clipping.

During the production of lasers at Selex ES over a two year period the resonator slab assembly has been rejected on a significant number of units due to concerns over the near-field beam intensity pattern homogeneity. This rejection at the early stages of alignment was often a judgement call based solely on the experience of the laser aligner,

with no quantitative metric to fail them on. It is understandable that the production team act on the side of caution to avoid repeating the timely alignment process, which is required if a failure is discovered during the final testing of the laser system. As a result, a significant number of laser slab assemblies have been rejected, and in the majority of cases, scrapped. The significant cost of scrapped slab assemblies and wasted alignment time has justified this investigation.

The aim of the work described in this Chapter is to establish the root cause for these laser failures, so that a change could be proposed in order to prevent future failures and to extend the lasers range of operation thereby improving the product. An effort was made in order to minimise the cost of any proposed design change. Although the laser slab assembly was the rejected component, it may not have been the cause of failure in every case. The aberrations of the laser slab are strong when the slab is pumped. However, there are other optical assemblies in the laser resonator, through which the beam passes multiple times per round trip, and therefore also have the potential to contribute significant wavefront errors to the beam path and affect laser performance. For example, a folding prism is passed four times per round-trip (through two areas of the prism).

After investigating the reasons for failed laser slabs during the early stages of laser production, it was discovered that for one line of laser systems, a regularly occurring failure mode was described as the near-field beam intensity distribution changing over time. As the laser slab is the only component which will have a significant thermal load during operation, it is clear that the laser slab is the cause of this failure. Therefore, this failure mode was the focus of this investigation. In other examples of slab failures where the slab assembly was rejected, it was not conclusive that the slab assembly was defective.

The slab assembly (Figure 5-1) is an isosceles trapezoidal shaped Nd:YAG slab bonded on one of its sides to a thermal-expansion-matched material (Aluminium-Silicon alloy). This material is used in order to minimise the stress imparted to the slab as the ambient temperature is varied over the defence operational temperature range of -55°C to 85°C. The isosceles trapezoidal shaped slab is utilised to give rise to zig-zagging of the laser mode inside the slab as described in chapter 2. The adhesive used to bond the slab to the mount was a layer of epoxy with a nominal thickness of 160 µm. When used in a real laser system, the mount would be attached to the laser chassis at the bottom. This contact provides the path for conduction cooling of the slab and the mount.

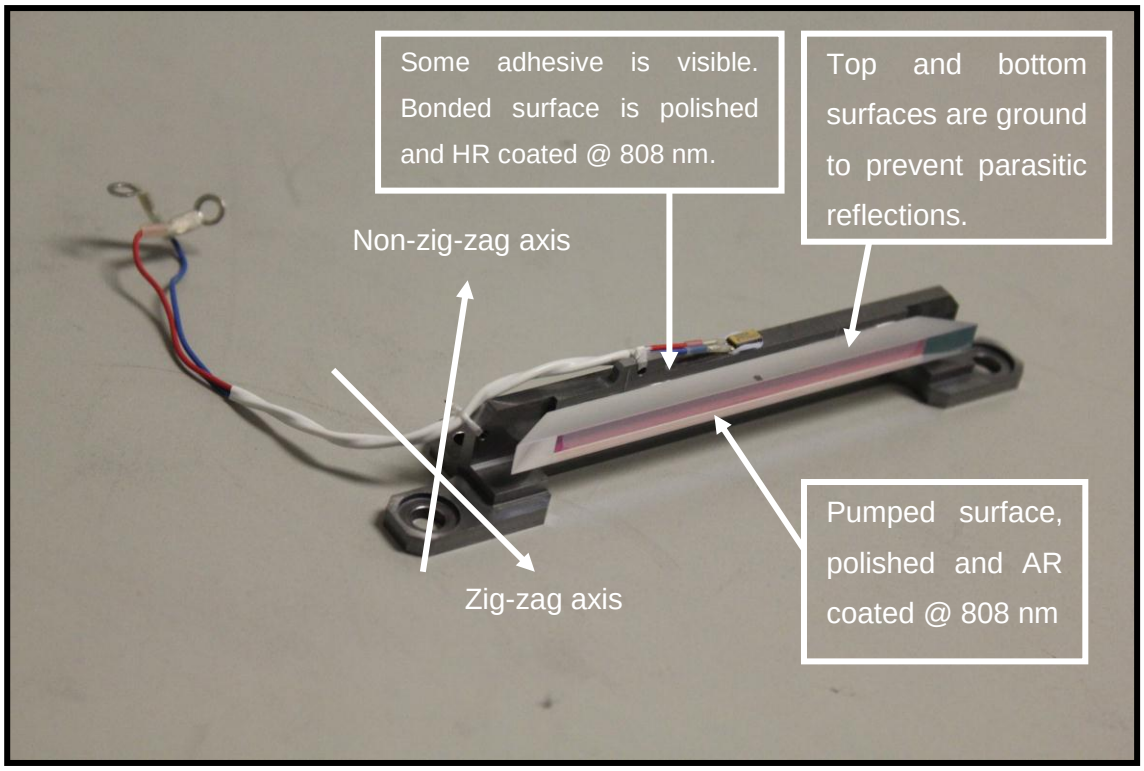

Figure 5-1: Photograph of a typical slab assembly. The zig-zag geometry slab is pumped from one side and bonded to a mount on the other side, through which it is conduction cooled.

The Nd:YAG slab has a passive wavefront error, which introduces aberrations to an incident plane wave in addition to any thermal aberrations. This aberration has been measured for a number of slab assemblies using an interferometer. Typically, a slab has a positive lensing effect in the non-zig-zag axis, which is considered to be introduced by polishing of the pumped and the bonded slab surfaces during fabrication of the slabs. The laser mode is totally internally reflected by the pumped and bonded slab surfaces, five and four times respectively and therefore an aberration caused by surface error will be additive with each of the bounces. Therefore, a small flatness error can have a significant effect on the laser mode. In the zig-zag axis, typically no significant aberration is present, but positive or negative lensing can be present in some cases. When the slab is bonded onto a mount, a change to the passive aberration is possible. However, on a sample of six slab assemblies, a repeatable pattern was not observed. This is shown in the first two bars of the graphs in Figure 5-2.

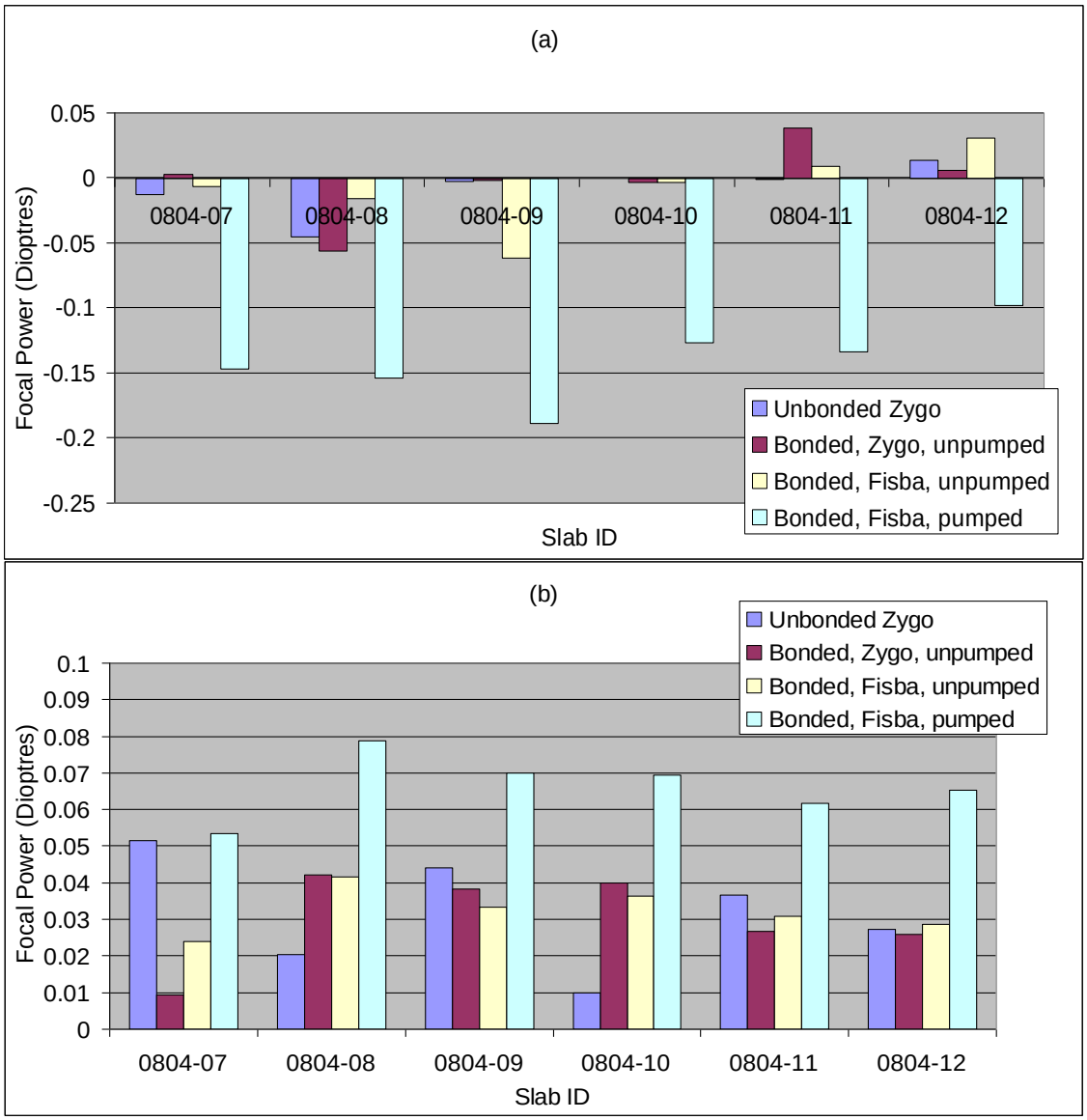

Figure 5-2: Graphs to show the focal power of the lens of the slab in the (a) zig-zag and (b) non-zig-zag axes. Three difference scenarios and two difference interferometers were used. The three scenarios were, unbonded slab unpumped, mounted slab unpumped and mounted slab pumped by an array of laser diodes.

In addition to this passive aberration, thermally induced aberrations are introduced when the slab is side-pumped by a laser diode source. As the laser slab is pumped during a firing period, the slab is heated mainly due to the quantum defect between the pump and laser wavelengths. Non-radiative phonon decay of excited states results in a heat load in the slab. This heat load causes a thermal expansion of the Nd:YAG laser slab and a change in its refractive index. A thermal mismatch between the laser slab and the adhesive that is used to bond the laser slab to the mount will cause some stress to be

applied to the laser slab. This stress will also cause a change in the refractive index of the laser slab (the photoelastic effect [2]). It was not known what the extent of this effect is in a typical slab assembly, or how it compares with the effect of refractive index change due to the temperature gradient or effects due to shape deformation of the laser slab. The combination of all the effects due to the thermal gradient on the aberration in the slab was measured using a Fisba interferometer. These results are shown in the fourth bars of the graphs in Figure 5-2.

This work package was broken down into three sections which form the basis of this chapter.

1) Investigate root cause of mode structure of slab resonators (section 5.2)

The Fisba interferometer was used to measure the wavefront error introduced by the pumped slab assembly. The performance of the slab assembly in a simplified resonator was measured. A clear correlation between the average (of zig-zag and non-zig-zag axis) thermal lens and the laser performance was not found. A trend that showed a reduction in transmission of near-field beam intensity pattern through an aperture with increasing lens power could be observed.

2) Investigate effects of depolarisation within slabs (section 5.3)

A set-up was used to experimentally assess the change in polarisation of light passed through the slab assembly when it was pumped. As a result of this work, birefringence in the slab assembly was discounted as a failure mode in the resonator and effort was placed to reduce the wavefront aberrations produced by the slab assembly.

3) Trial novel techniques for slab thermal management (section 5.4)

A number of techniques have been attempted to reduce the thermal lens in the laser slab and to improve the performance of the resonator. From this work, recommendations were made to improve the design of the laser or to be considered for future laser system designs.

5.2 INVESTIGATE ROOT CAUSE OF MODE STRUCTURE OF SLAB RESONATORS

For one particular laser design, which will be referred to as the Type A laser from now on, the dominant reason for failure is "poor near-field beam intensity pattern". During this investigative work, the problem has been broken down into two failure modes.

1. Poor beam homogeneity of the oscillator near-field beam intensity pattern leading to a failure of the near-field homogeneity specification at final testing.
2. Failure of output energy at final testing due to a drop in energy caused by clipping of the beam intensity pattern as it passes through a 10 mm circular aperture beam scraper.

The second failure mode is far more common and is the focus of efforts to find a short-term solution. In addition to these issues which form the short-term objectives for this work package, there are strategic objectives which aim to extend the capability of our product range. The aspirations are to increase the output energy and/or the repetition rate of the laser resonator while avoiding a detrimental effect on other laser parameters, such as divergence and near-field beam intensity pattern uniformity. The challenge to address is the increase in thermal lens that will result from an increase in average power output from the laser, if the pump average power is increased. This work should result in improved resonator designs which have a greater tolerance to the variation in slab assemblies, by reducing the aberrations produced due to thermal load.

5.2.1 Resonator set-up

A number of laser systems share a similar design with similar slab assemblies and laser diode pump heads. Therefore this work is relevant to a range of products.

In most cases a cross Porro prism resonator is used as described in Chapter 2, and investigated in Chapters 3 and 4. Laser performance was investigated using a cross Porro prism resonator set-up around a zig-zag geometry Nd:YAG slab, single-side pumped by a series of laser diode stacks. The other side of the slab was bonded to a mount providing conduction cooling of the slab. The main features of the resonator are shown in Figure 5-3.

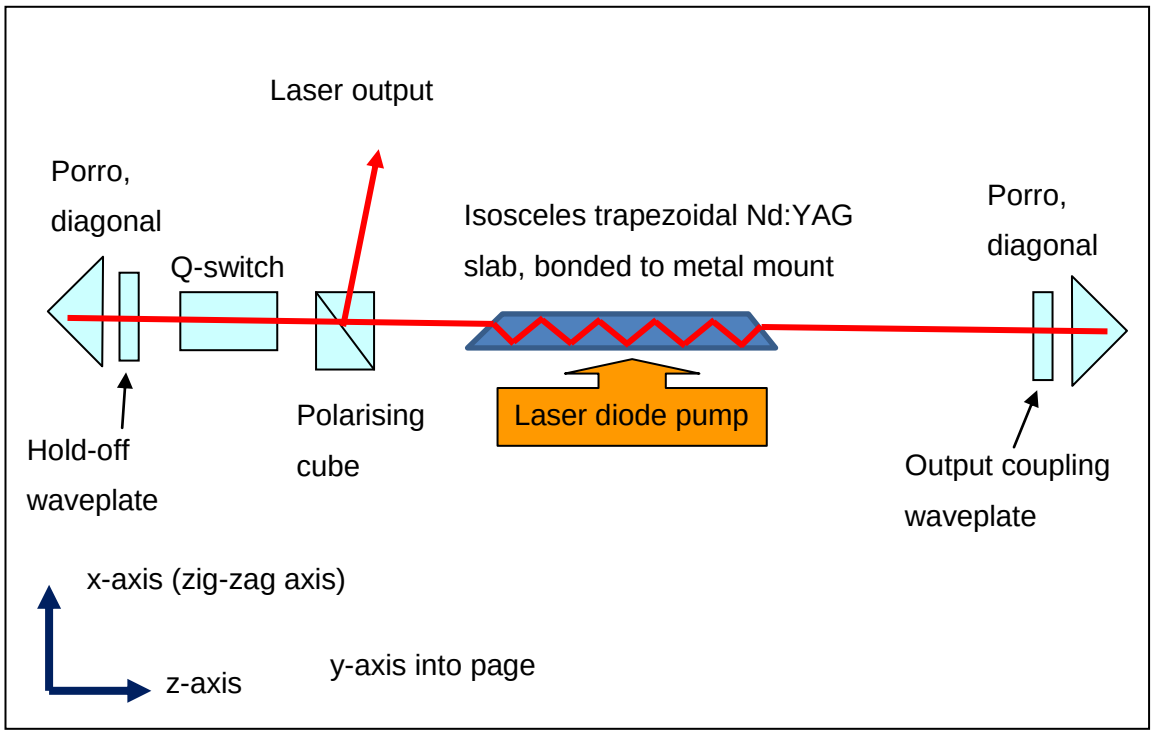

Figure 5-3: Schematic diagram of a cross Porro laser resonator incorporating all the important resonator optics that are found within a typical laser system produced at Selex ES.

This pump head geometry provides cancellation of thermal lensing in the zig-zag plane, which corresponds to the principle temperature gradient in the slab. This temperature gradient is the source of the dominant thermal lens. In the idealised case of perfectly uniform heat disposition in the slab, and no edge effects to consider (infinite length slab), the zig-zag geometry completely cancels out any dn/dT thermal lensing [3, 4], producing a near-plane wavefront with no effect on the laser mode. Distortion of the slab due to the thermal gradient would not be cancelled out by the zig-zag path of the laser mode. In reality, where edge effects exist, complete cancellation of dn/dT in the zig-zag axis does not occur, and there is a temperature gradient in the non-zig-zag plane. Therefore, there is a thermal lens contribution in both of the axes. In addition, imperfections in the unpumped slab and in the other resonator optics produce additional static wavefront aberrations on the output beam. The cross Porro resonator is chosen due to its tolerance to misalignment and has the benefit of rotating the laser mode by 90º between each pass of the slab. This has the desirable effect of averaging the dn/dT lens of the zig-zag and non-zig-zag planes. Note that it is only desirable in this case due to

the opposite polarities of the two lenses (positive in the non-zig-zag axis and negative in the zig-zag axis).

As the cross Porro resonator is used, polarisation output coupling is required. Therefore the resonator performance is sensitive to depolarisation effects, whether passive, stress induced, or thermally induced birefringence in the slab. Resonator lengths on the order of one metre are typically used to produce the correct pulse length and divergence for the application. In order to keep the laser footprint small, folding prisms are introduced into the resonator. These prisms add to the potential birefringence and wavefront aberrations. To simplify this investigation, folding prisms and corner cubes are not included in the resonator under test.

The polarising beam splitting cube in Figure 5-3 is used for output coupling of one linear polarisation state. The slab has end face coatings applied in order to enable equally low loss transmission of both s and p polarisation states. (loss of approximately 2% per surface for randomly polarised light). The output coupling percentage is selected by rotating the output coupling wave plate (half-wave plate).

This set-up was used to establish the laser performance for a range of slab assemblies. The physical length of this laser resonator was approximately 1000 mm, which was chosen to match the diffraction length of the Type A laser resonator. This was done in order to ensure that the test resonator would produce comparable output beam divergence. The simplified resonator however, has fewer optical elements. This means that there will be fewer sources of aberration than with a Type A laser resonator and also fewer sources of variation. This allows for a fairer test when comparing slab assemblies, as the path through the optics can be altered during alignment of the resonator with each slab assembly. The round trip time and therefore the pulsewidth of the simplified resonator will be slightly different to the Type A resonator, but this will be a small difference of the order 10% and was not considered relevant to the thermal lens investigation.

The correlation between the slab thermal lens and the laser performance was investigated using the simplified resonator. The slab thermal lens was measured for a range of slab assemblies. The figure of merit used for the slab thermal lens was the average focal power. The average of the zig-zag axis focal power and the non-zig-zag axis focal power was calculated. This is justified as the laser mode is effectively rotated by ninety degrees between each pass of the laser slab by the Porro prism, which has its

apex at 45° to the beam intensity pattern. The average focal power value is half of the focal power that acts on the beam during each round trip, since the laser mode passes the laser slab twice per round trip.

5.2.2 Laser resonator measurements

A number of slab assemblies were tested in a representative but simplified resonator set-up, shown in Figure 5-3. Testing was carried out in fixed-Q and Q-switched modes. The energy, near-field beam intensity pattern and far-field beam intensity pattern were recorded over a duration of 60 s. Peak to average intensity values of the near-field beam intensity pattern were analysed over this duration. In only one case did the peak to average value significantly increase over the firing duration to recreate the problem reported during laser production. This slab assembly (marked A4), has enabled the testing of possible solutions to reduce the effect of thermal aberrations. The alignment of the resonator has some impact on the performance, but the variability due to the slab assembly far outweighs the variability due to alignment. To minimise operator bias as a source of systematic error, the resonator was aligned in order to maximise output energy, without reference to the beam intensity pattern. During production at Selex ES, the beam intensity pattern, as well as the energy is used to optimise the perceived laser performance, to maximise chances of passing all tested parameters.

5.2.3 Diameter measurement

It has been observed that the Spiricon LBA software is not a reliable method of calculating the beam diameter of the near-field intensity profile when the profile has a hole in the centre. This intensity profile is typical for a number of Type A lasers once the slab thermal lens has been established.

The standard way of measuring a near-field intensity profile diameter at Selex ES for laser production, is the 90% encircled diameter, even though the intensity profiles are closer to a square shape than a circle. The two beam intensity pattern pictures in Figure 5-4 demonstrate two methods of measuring the beam intensity pattern diameter. The top beam intensity image shows a white circle, which is manually increased in size until

over 90% of the energy incident on the camera array is inside the circle, this is commonly referred to as a 'power in the bucket' measurement. The circle diameter is 4.7 mm.

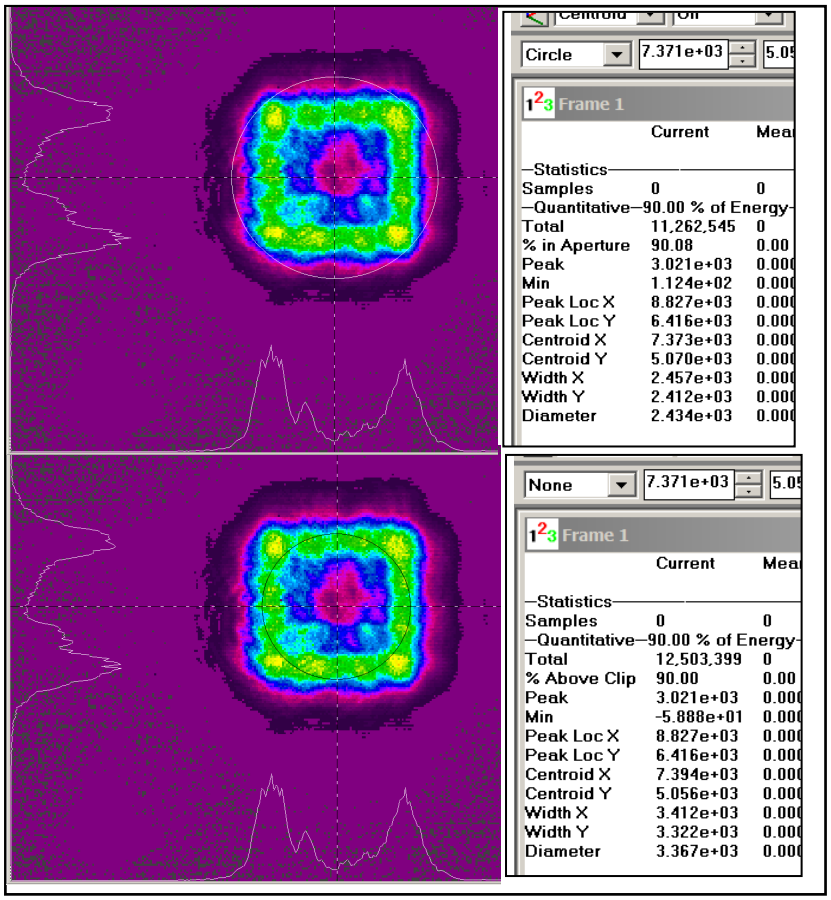

Figure 5-4: A Type A laser resonator near-field beam intensity pattern measured using Spiricon LBA software and analysed using two different methods. The statistics that the software produced in each case are adjacent to each beam intensity pattern.

The bottom beam intensity image shows a black circle which shows the diameter of the beam which contains 90% of Energy as calculated by the LBA software. The diameter reported is 3.4 mm, approximately 2/3 of the diameter calculated using the manual fit.

It is clear from visual inspection that in this second case, more than 10% of the energy falls outside of the calculated diameter (black circle). The reason for this is due to the way that the software calculates the diameter. All the pixel intensity values are listed from highest to lowest and all pixel intensities are summed until 90% of the intensity is

totalled. A circle which contains this number of pixels is then created. This method can only work for beam intensity patterns where all the most intense pixels are close to the centroid of the beam. As this is not always the case with the resonator beam intensity patterns being investigated, the beam diameter measurement as measured by the LBA software is unlikely to be an accurate measure of the beam size. Therefore, the method of measurement to use for these types of laser beam intensity patterns should be the circular aperture containing 90% of the energy, rather than the LBA software diameter measurement. The replacement for the "Spiricon LBA-PC" software is called "BeamGage" and has an additional diameter measurement type called "D_{epsa} –prog ISO". This is an Encircled Power Smallest Aperture Diameter measurement where the percentage enclosed is user programmable. For these measurements, the BeamGage software provides a direct measurement which is more appropriate.

5.2.4 Measurement of slab aberrations

It was not possible to measure the thermally-induced aberrations in the slab whilst it was lasing, however it was possible to make such measurements on a slab separate from a resonator, so it could be actively pumped but not lasing. In this set-up the slab under test was pumped using laser diodes, while carrying out a measurement of the aberrations produced using a 633 nm Fisba interferometer. As the laser slab was not inside a resonator, no significant stimulated emission was produced. However, spontaneous emission will still occur. This interferometer uses a 633 nm laser, so the 1064 nm wavelength spontaneous emission did not affect the measurements. The absence of a representative level of stimulated emission will mean that the aberrations produced by the laser slab are not exactly the same as would be the case inside a lasing cavity. This is because the average wavelength of spontaneous emission is different from the wavelength of stimulated emission (1064 nm). However, the heat fraction in a Nd:YAG slab laser when lasing, of typical Nd doping of 1-1.1%, has been calculated to be approximately 97% of the value of a slab when pumped but not lasing. The equation for the heat fraction given in the Chapter 2, Section 2.3 is discussed in the literature [5]. Therefore, the aberrations measured in the non-lasing case are approximately the same as the lasing case.

5.2.5 Modelled performance of the slab assembly

The laser slab is modelled using COMSOL Multiphysics software [6]. The 3D geometry is modelled to produce a temperature distribution in the slab. A fixed temperature of 20ºC is assumed for the bottom of the slab assembly, which is conduction-cooled by the laser chassis. To a first approximation, the temperature gradient across the slab is assumed to be dominated by conductive heat flux, ignoring convective heat flux and radiation. This assumption considerably reduces the model complexity and computation time. Figure 5-5 shows an image that was produced by a typical thermal model of a slab assembly, which shows the temperature at every position in the slab represented by a false colour map.

The temperature profile produced was the result of pumping with five laser diode stacks, which together produced a total optical power of 11.3 W. The laser diode stacks were 5 mm high and 10 mm wide. The slab was also 5 mm in the non-zig-zag axis, so the pump radiation matched the slab size, with the pump distribution modelled as an array of Gaussian beams. This is calculated assuming a repetition rate of 20 Hz and a laser diode pulse length of 150 µs, which is the typical pumping level required in order to produce an output pulse energy of approximately 150 mJ. This pumping leads to a total heat load of 3.2 W, which is largely due to the quantum defect between the pump wavelength and the laser wavelength. Other pumping inefficiencies also contribute to this heat load, as discussed in Chapter 2, Section 2.3.

If the laser resonator was not aligned, an additional heat load would exist due to increased non-radiative decay from the upper laser level. The heat load would then be increased to 3.4 W. Without a resonator, 7.9 W of spontaneous emission is generated, which is non-directional. Some of this light is likely to be absorbed by the adhesive and the mount. This additional heating is ignored in the model.

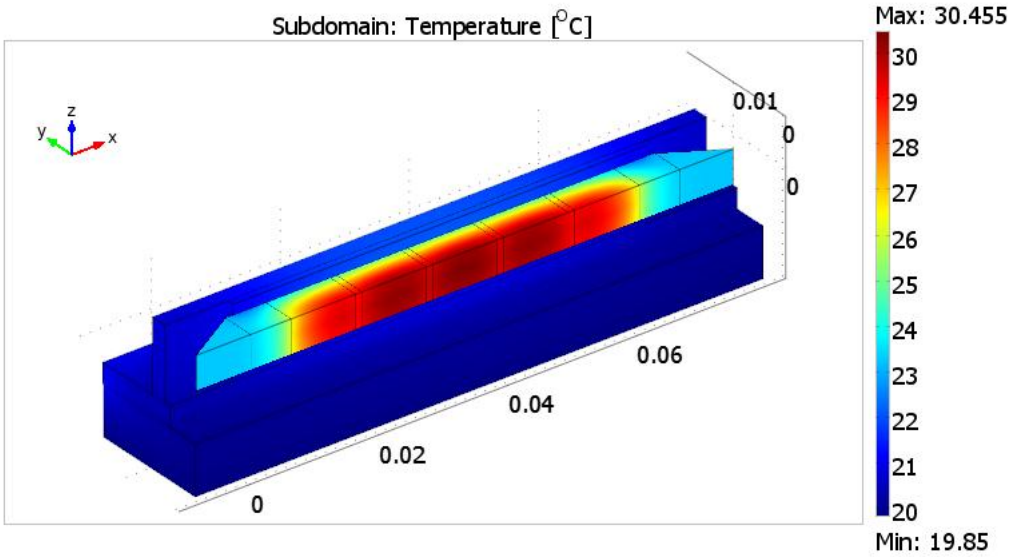

Figure 5-5: Image produced by a thermal model of the Type A laser slab assembly.

Once the temperature map is calculated by the model, it is exported to a ray tracing program written in the Matlab programming language by Stephen Moore, a fellow laser engineer at Selex ES. This model traces a uniform array of rays across the full beam width through the zig-zag laser slab. Each ray sees a different dn/dT profile as it propagates through the slab resulting in a differing optical path length for each ray. The path length of each ray can then be used to calculate the thermally induced wavefront aberration produced by one pass through the pumped slab. The major aberrations introduced are cylindrical lensing of opposite sign in each axis. Due to the temperature profile in the laser slab, produced by the 3.2 W heat load (when lasing), a positive lensing effect of approximately 0.049 Dioptres is generated in the non-zig-zag axis and a negative lensing effect of approximately -0.058 Dioptres is generated in the zig-zag axis. This modelling does not take into account any passive aberrations that are present in the unpumped laser slab. Effects due to thermal expansion of the laser slab, such as end bulging and stress induced index change, are not considered in this model.

A separate investigation was carried out by Ian Thomson, a fellow laser engineer at Selex ES, to calculate the contribution to thermal lensing in a laser diode-side-pumped laser slab produced by the mechanical distortion of the slab due to thermal expansion. This was carried out due to concerns that the curvature of the long face of the slab could create an accumulative lens due to the multiple bounces from this face during a single pass through the slab.

COMSOL Multiphysics software was used to model a 7-bounce isosceles trapezoidal shaped Nd:YAG zig-zag geometry slab side-pumped using a laser diode array which introduced a 10 W heat load. This is shorter than the typical 9-bounce slab, and will therefore be a worst case result. (The magnitude of end surface tilt is found to be an order of magnitude less for a 9-bounce slab over a 7-bounce slab) The heat load is also approximately three times the heat load used in this thesis, and is therefore also a worst case.

The distorted slab shape was exported from COMSOL and imported into Zemax ray-tracing software in order to analyse the resulting wavefront distortion of a propagating beam. Due to the non-continuous nature of the imported CAD based geometry data, the Zemax program interpolated the data to make the surfaces of the imported slab continuous. The effect of this and rounding errors produced by the ray-tracing introduced noise to the transmitted wavefront. Analysing the transmitted wavefront over a central 4.5mm mask showed no transmitted wavefront error due to the small magnitude of the mechanical deformation. Therefore, using this method, the thermal lens due to thermal distortion is found to be insignificant.

In conclusion, the dn/dT effect is considered to be the major contributor to thermal lensing in the slab, while distortion due to thermal expansion, can be assumed to be insignificant. The magnitude of aberrations introduced by index change due to thermally induced stress in the slab, when compared with the dn/dT effect is not known. At this time, the dn/dT effect is assumed to be dominant, but further work is recommended to verify this assumption.

The predicted radius of curvature of the thermal lens is relatively long compared to the resonator length (18 m compared with approximately 1 m, respectively). Even so, this relatively weak thermal lens can have a significant effect on the plane-plane resonator due to its position on the stability diagram. The resonator becomes unstable with any non-zero value of negative lens as discussed in Chapter 2, Section 2.6.2. Both diffraction and high levels of gain in the Q-switched laser, help the laser to continue to operate under these conditions.

An in-house model used at Selex ES, named “The Fresnel propagation model” (described fully in Chapter 2, Section 2.9), can be used to predict the near-field and far-field beam intensity patterns for given values of lens focal power in the laser slab. Alternatively, the measured wavefront profile of a particular slab assembly can be input

into the model. The model predicts the beam intensity pattern by predicting the effects of diffraction on the profile as it propagates around the resonator on each round trip and then into the far-field once it is out-coupled.

A slab with typical passive lensing and typical thermal lensing for the unpumped and pumped regimes, has been modelled. This predicts the first pulse performance and the steady state performance assuming that the thermal lens has no effect on the first pulse. It was shown that the far-field beam intensity patterns produced by the model, changed dramatically from first pulse, to steady-state, whereas in reality, the far-field beam intensity pattern produced by a typical cross Porro prism resonator showed negligible variation. In addition, the modelled near-field beam intensity pattern did not develop a hole in the centre as the thermal lensing was altered (regardless of lens strength). This model is therefore unhelpful in explaining the change to the near-field beam intensity pattern as thermal lensing is increased. A flow-diagram is shown in Figure 5-6, which summarises the use of the three models.

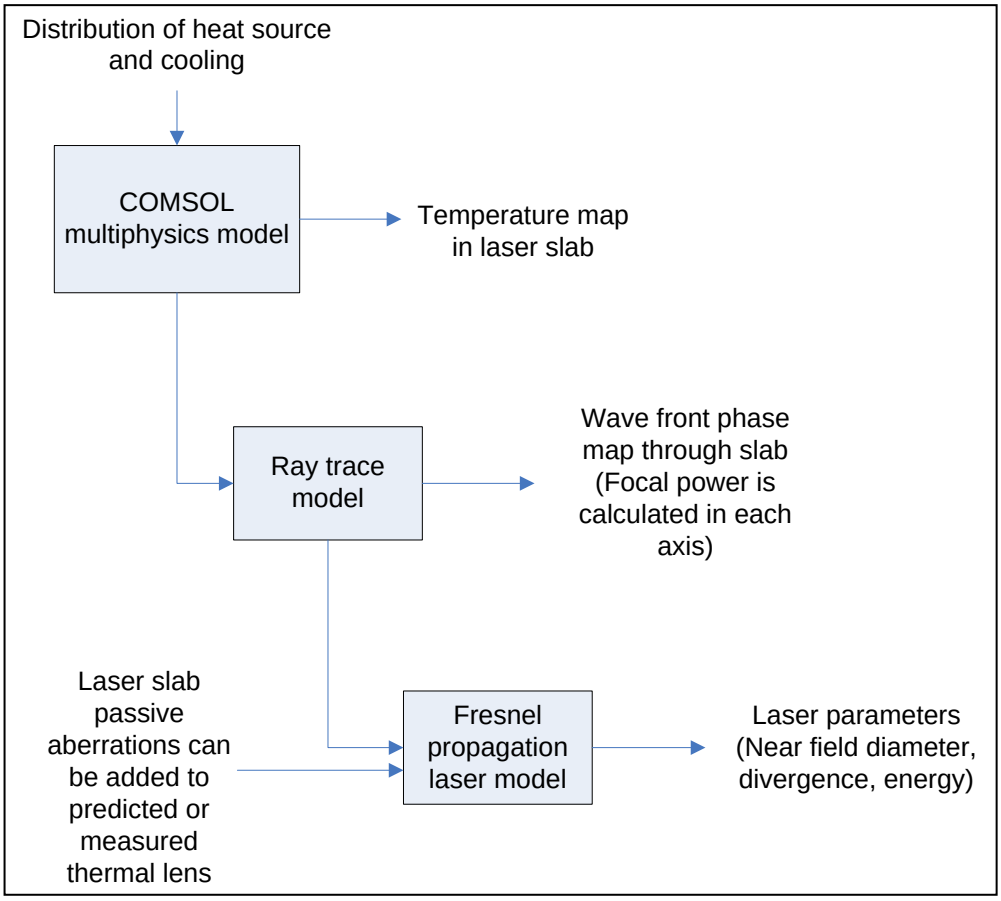

Figure 5-6: Flow diagram to summarise the use of models to predict the effects of laser slab aberrations on laser resonator performance due to thermally induced refractive index gradients

5.2.6 Effect of slab aberrations on slab laser performance

To investigate the root cause of the poor near-field beam intensity pattern of slab lasers, the aberrations in a sample of pumped slab assemblies were measured using a 633 nm Fisba interferometer supplied by Armstrong Optical [7]. These slab assemblies were also tested inside the simplified laser resonator (Figure 5-3) in order to study the correlation between the pumped slab aberrations and the laser performance.

5.2.7 Results

The results within this section are plots of various laser performance parameters measured using the simplified resonator set-up, against the average slab lens focal power, measured using the Fisba interferometer. The correlation between slab thermal lens and laser performance has been investigated for the near-field beam diameter, the standard deviation/mean intensity value over this area, and the percentage transmission through a software aperture placed at the centroid of the captured near-field beam intensity pattern. The near-field beam diameter was measured using the 90% enclosed area of the captured beam intensity patterns. Other parameters used to measure laser performance were percentage through a 4.35 mm diameter aperture and the standard deviation/mean intensity value of the near-field beam intensity pattern. All of these parameters were expected to have a dependence on the average thermal lens in the laser slab. These three laser parameters have been plotted against the average slab lens in Figure 5-7, Figure 5-8 and Figure 5-9. This data was generated using 21 Type A laser slab assemblies.

It can be seen from the graphs that a clear trend is not observed for any of the parameters. However, slab assemblies with larger average focal powers tend to have a larger near-field beam diameter, a larger standard deviation / mean value and a smaller percentage transmission through a 4.35 mm aperture. This trend is expected to be clearer if the range of slab average thermal lens focal powers was greater through analysing a larger sample. Although cylindrical lens power was generally observed to be the dominant effect, other aberrations in the laser slab will also contribute to the degradation of laser performance. If the other aberrations are significant, they will prevent the clear trend between average lens focal power and laser performance, and could explain the unclear trends observed in this data.

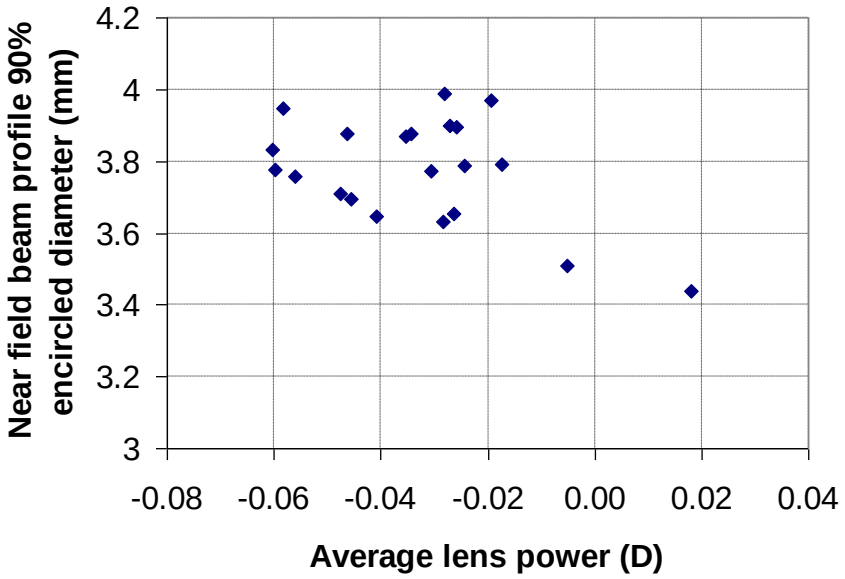

Figure 5-7: Graph of the near-field 90% enclosed energy beam diameter against the average focal power measured for each slab assembly

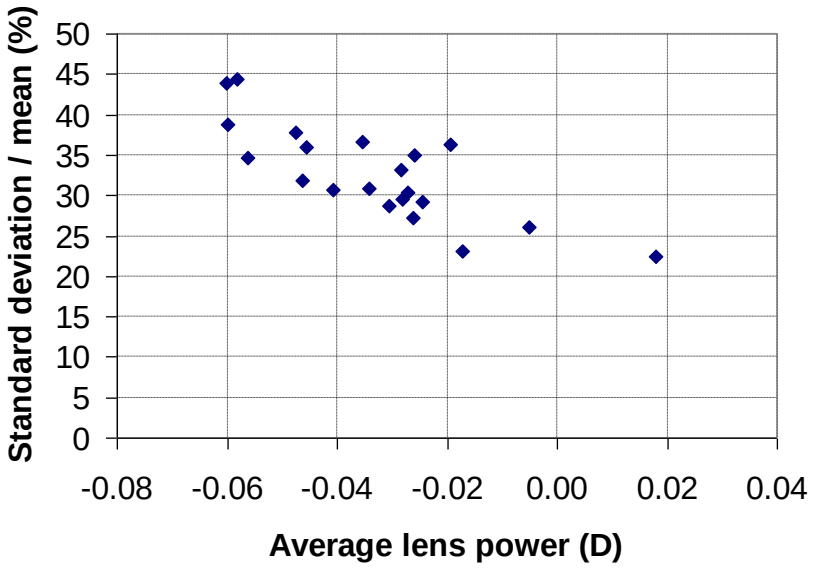

Figure 5-8: Graph of the near-field beam intensity pattern standard deviation/mean value against the average focal power measured for each slab assembly

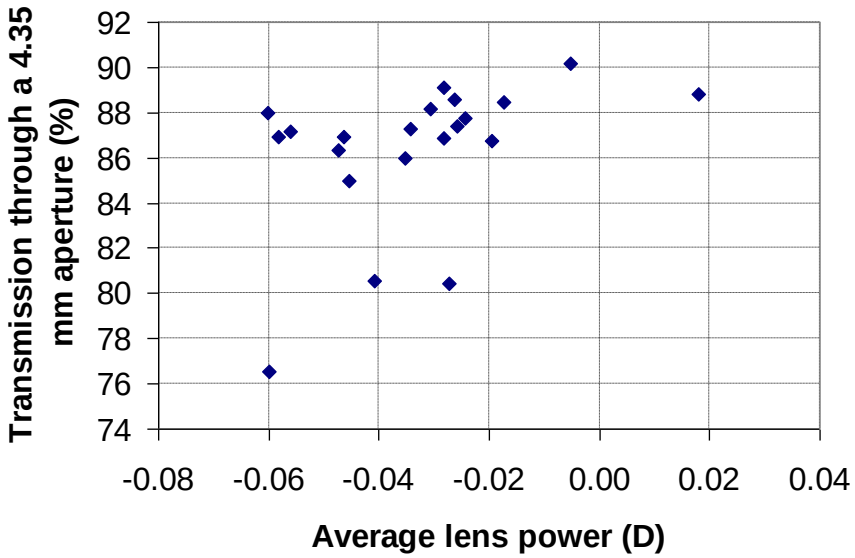

Figure 5-9: Graph of the percentage of the near-field beam intensity pattern transmission through a 4.35 mm diameter aperture against the average focal power measured for each slab assembly

The graphs include slab assemblies which were later failed after being aligned in a Type A laser resonator. Note that all of the optics, apart from the slab assembly, were different in the simplified test resonator and the Type A laser resonator. These differences in the optics, and the passive aberrations produced by them, are sufficient to prevent a clear correlation between the performances in each of the two resonators.

5.2.8 Summary

It is clear that the average focal power in the laser slab assembly is not the only factor that affects the laser performance. A loose trend is however seen, so reducing the thermal lens in the slab assembly will improve the laser beam performance. The results suggest that a weaker thermal lens in the laser slab would produce a laser near-field intensity profile with a lower standard deviation to mean value (more uniform beam) and a higher transmission through the aperture (less energy loss).

5.3 INVESTIGATE EFFECTS OF DEPOLARISATION WITHIN SLABS

5.3.1 Introduction

Stress-induced birefringence is another potential reason for a change in near-field beam intensity pattern during a firing period. The output coupling of the laser is controlled by varying the polarisation state of the oscillating field by rotating a half waveplate. A portion of the resonating laser mode is then output coupled by reflection from a polarising beam-splitting cube inside the laser cavity. If spatially varying birefringence is present in the laser slab, then the polarisation state will change across the beam intensity pattern, in turn altering the percentage coupled from the cavity across the beam intensity pattern. The problem being investigated is introduced by the thermal load in the laser slab, thus the difference in birefringence between unpumped and pumped slabs is of interest. It was shown that changing the output coupling of the laser, while maintaining the output energy of the laser, had a very significant effect on the performance. This was investigated by changing the output coupling to achieve a reduction of 10% in output energy on either side of the optimum level of output coupling. This result can be seen in Figure 5-10.

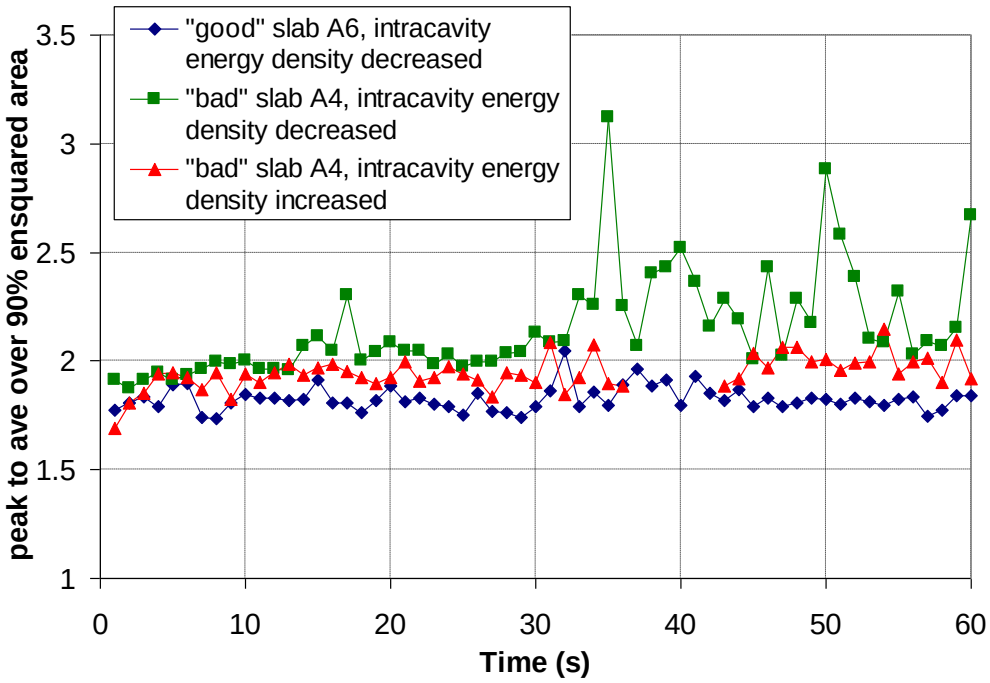

Figure 5-10: Plot of peak to average of near-field beam intensity pattern against time for a "good" slab and also a "poor" slab (tested with two levels of output coupling that gave the same output energy)

As discussed in Chapter 2, the plane-plane resonator is on the edge of stability. An increased output coupling reflectivity produces greater feedback with more round trips of the laser resonator. This may improve the stability of the laser and reduce the variation in the beam intensity pattern peak to average, shown in Figure 5-10. Alternatively, this could be explained by a variation in the output coupling for different areas of the beam intensity pattern due to thermally-induced stress. When the laser slab is pumped the resulting heat load, and the thermal mismatch between the laser slab and the adhesive which bonds it to the mount, produce stress in the Nd:YAG slab. This thermally-induced stress will cause a change in the birefringence across the laser slab. This effect would also produce a change in the beam intensity pattern as the output coupling is varied. The magnitude of effects on the beam intensity pattern due to birefringence in comparison with the effect of refractive index change (due to thermally-induced stress or the temperature gradient) and the effect due to slab shape deformation (end bulging for example) was investigated.

5.3.2 Set-up

The set-up used to investigate stress-induced birefringence in a sample of laser slab assemblies is shown in Figure 5-11. The variation of depolarisation across the slab aperture, and the effect that laser-diode side-pumping has on this was studied. The Cohu camera is a Silicon based CCD camera, produced by Coherent, used to image the 1064 nm laser emission.

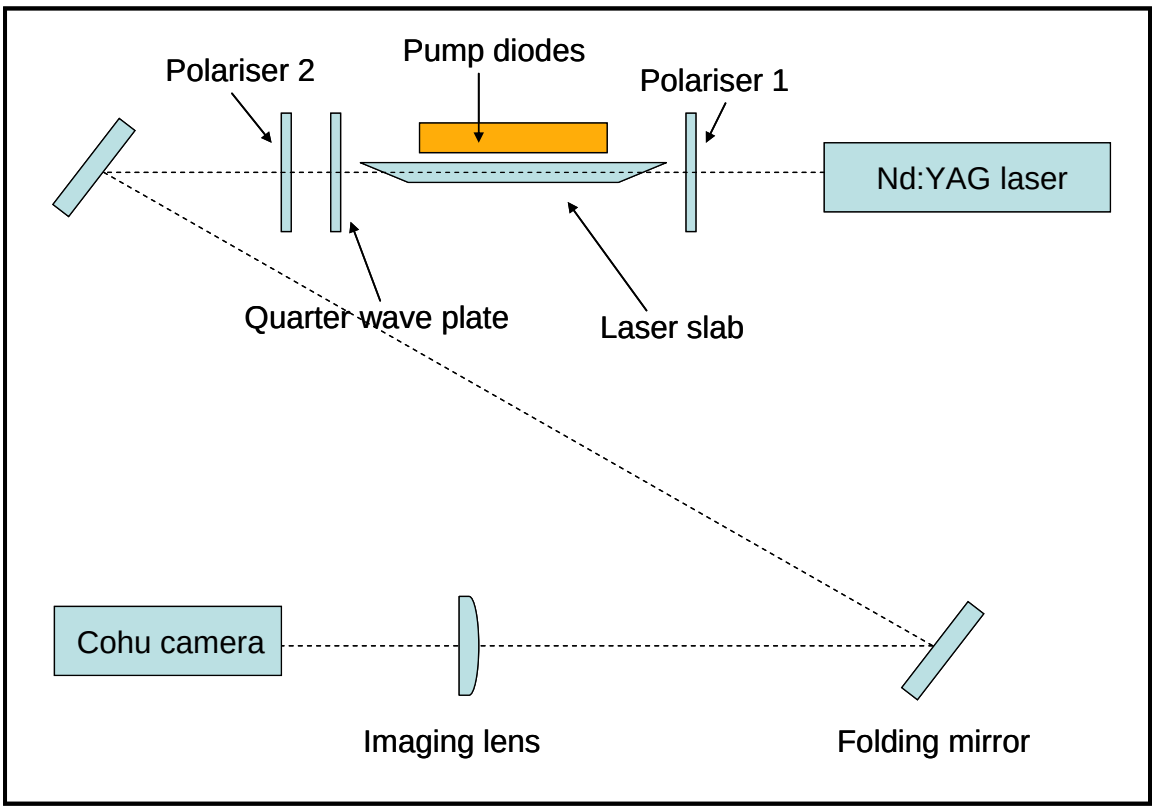

Figure 5-11: Set-up used to measure depolarisation across a laser slab while unpumped and pumped.

The concept is to place the laser slab assembly between crossed polarisers to minimise transmission so that any variation across the slab profile can be measured. The incident beam entered the slab with a polarisation of 45º to the square aperture of the laser slab, so that the linearly polarised light will be sensitive to birefringence in the laser slab in either of the two axes. Due to the odd number of bounces inside the slab, the linear polarisation state of the incident probe beam is flipped in the zig-zag axis. In addition to this, the total internal reflections inside the laser slab introduce a relative phase shift between the two orthogonal components. To cancel out both of these effects, the

second polariser was rotated to the angle that minimised the transmission of the probe laser beam and a quarter waveplate was introduced after the laser slab and rotated to the angle that minimised the transmission again. The transmission was fully minimised to the level of the camera background noise for the centre of the laser slab profile.

5.3.3 Test results

The images in Figure 5-12 show the light from the probe Nd:YAG laser on the Cohu camera. The square cross-section of the laser slab can be observed in the images. The intense parts of the images are the areas where light passed around the laser slab to the camera. The transmission inside the square cross-section of the laser slab that was observed is due to inherent birefringence within the laser slab and the change in the transmission profile when the slab is pumped is caused by a change in the thermally induced birefringence in the slab.

The transmission profile of laser slab assembly number A4 can be seen in Figure 5-12 for the unpumped and the pumped cases. Slab A4 performed badly in a laser resonator, as the near-field peak to average intensity variation changed significantly during a firing period as can be seen in Figure 5-10.

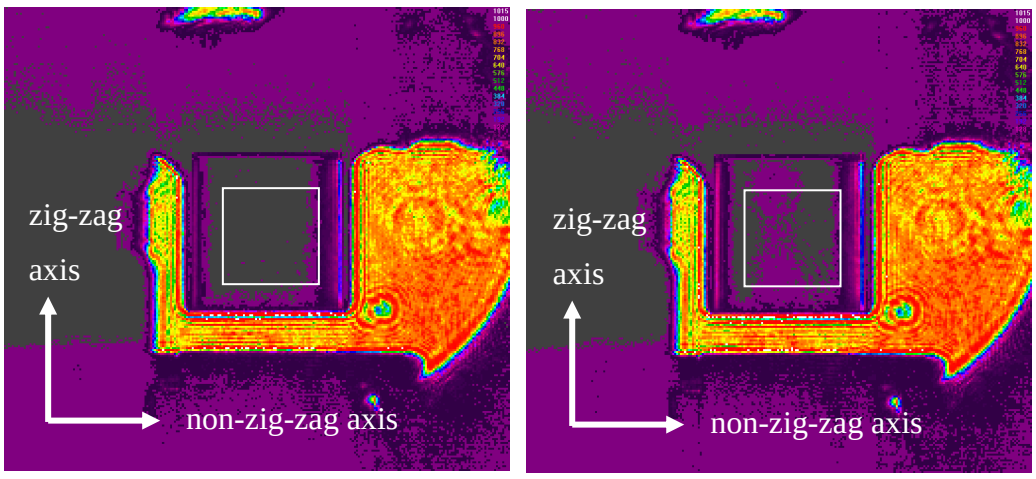

Figure 5-12: Slab number A4, unpumped and pumped cases

The areas of high transmission close to the left and right edges of the square profile of the laser slab are in the locations of the two ground surfaces of the slab. The light near these edges is caused by diffraction and scattering from these rough surfaces. Using a mask before the slab will help to reduce these two sources of confusion and is recommended if the test is repeated.

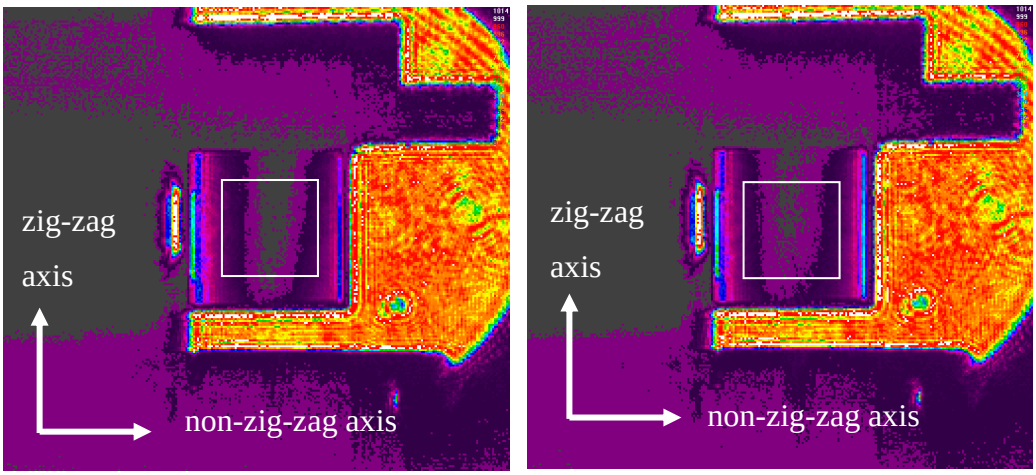

Figure 5-13: Slab number A6, unpumped and pumped cases

The transmission profile of laser slab number A6 can be seen in Figure 5-13 for the unpumped and the pumped cases. Slab number A6 produced a near-field beam intensity pattern which did not significantly change over the firing duration, as can be seen in Figure 5-10, so was considered a ‘good’ slab.

The peak transmission in each case has been measured within the central 3 mm square aperture in order to ignore the edge effects, which would have a large impact on this analysis, but a small impact on the beam intensity pattern. For slab A4 the peak transmission was 1% of the maximum transmission unpumped and 1.4% pumped. For slab A6 the peak transmission was 4.5% of the maximum unpumped and 4.6% when pumped.

5.3.4 Discussion

The effect on beam intensity pattern due to birefringence across the profile as seen in Figure 5-12 and Figure 5-13 is hard to predict. However, the fact that the transmission profile is very similar for the unpumped and pumped cases suggests that the thermal load is not having a significant impact on the birefringence in the laser slab. Therefore, a change in laser parameters over the firing duration is unlikely to be the result of a stress-induced birefringence effect.

The peak transmission in each case has been measured within the central 3 mm square aperture in order to ignore the edge effects. For slab A4 the peak transmission was 1% of the maximum transmission unpumped and 1.4% pumped. For slab A6 the peak transmission was 4.5% of the maximum unpumped and 4.6% when pumped. Therefore slab A6 has a higher inherent birefringence than slab A4, which performed worse in the laser resonator. To assess the impact of these depolarisation values, the Fresnel propagation laser model was used. For a change to the output coupling of the resonator of 5% either upwards or downwards, the output energy of the laser changed from 213 mJ to 212 mJ, which translates as a reduction of less than 0.5% of the output. Therefore, it is clear that the levels of birefringence measured within the central 3 mm of the slab cross-section, both in the unpumped and pumped cases would have an insignificant effect on the beam intensity pattern.

The results seen for both laser slabs show a small variation across the non-zig-zag direction (<5%), and insignificant variation in transmission over the zig-zag direction. This is because the zig-zag geometry of the laser slab will have an averaging effect on birefringence across this axis. The apparent birefringence across the non-zag-zag axis, which appears close to the edges of the slab, may be due to scatter from the ground surfaces of the laser slab.

5.3.5 Summary

Birefringence is not significant across a 3 mm cross section of the laser slab. Birefringence across both slabs tested was measured to be less than 5%, which is predicted to produce a reduction in laser energy of less than 0.5%. Therefore, this level

of birefringence is unlikely to cause a significant effect on the near-field beam intensity pattern of the laser. In addition, the birefringence is also largely unchanged when the laser slab is pumped. Therefore stress induced birefringence effects are discounted as the root cause of laser failures that are dependent on the heat load in the laser slab. It is also noted that the birefringence observed in a "bad" slab was not greater than that observed in a "good" slab, as would be expected if birefringence was the root cause of near-field beam intensity patterns observed. Due to the measured low values for stress-induced birefringence in a laser slab, the effect was not modelled.

5.4 TRIAL NOVEL TECHNIQUES FOR SLAB THERMAL MANAGEMENT

In this section, novel techniques for slab thermal management are described, which attempt to reduce the thermal lens that exists in the zig-zag axis. This thermal lens of negative polarity exists in the current laser slab assembly and pump head geometry. The introduction of an additional optic into the cavity to compensate for thermal lensing in the slab is investigated. The thermal lens can be reduced by changing the geometry so that the zig-zag length over which the thermal effects are averaged, are better matched to the length over which there is a temperature gradient. Alternatively, the effect of moving the relative positions of the pumped region and zig-zag bounces is explored. Another approach which is investigated is to alter the cooling path to change the distribution of the heat. Finally, the effect of reducing the magnitude of the heat load in the slab by changing the pump wavelength is investigated.

5.4.1 Fixed compensation lens

5.4.1.1 Introduction

This is a simple solution using a spherical lens to compensate for the spherical component of the net aberrations in the laser slab that are predominately caused by thermal lensing. The net lensing in the slab (passive plus thermally-induced) is cylindrical and of opposite polarity in each axis. As the beam intensity pattern is rotated by 90º after each pass of the slab by the Porro prism closest to the slab, each lens acts on

both axes of the beam intensity pattern in a single round-trip of the resonator. An example of this effect can be seen in Figure 5-14, where a wavefront profile is flipped about the diagonal line of symmetry and then summed with the original profile. The average effect is predominantly a negative spherical lens and it is therefore possible to use a positive spherical lens for compensation.

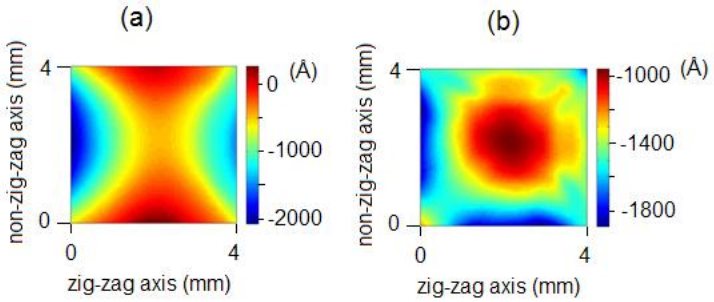

Figure 5-14: (a) Wavefront profile measured for slab assembly A5 when pumped using an interferometer and (b) the same wavefront profile added to the wavefront that was flipped about the diagonal (effect of Porro prism) .

5.4.1.2 Set-up

Two lenses were available for testing; a +30 m focal length and a +15 m focal length lens. These have focal powers of 0.033 D and 0.067 D respectively. The compensation lens was placed inside the resonator as shown in Figure 5-15, between the slab and the half waveplate. With the lens placed in this part of the resonator, the positive compensation lens is positioned close to the negative slab thermal lens, therefore the lenses will affect the laser mode size less than if they were further apart. This is desirable as a reduced laser mode size would result in an increased intracavity energy density and would increase the risk of laser induced damage to optical components. In addition to this, it is recommended that resonator optical elements such as Q-switches and polarising beam splitters are operated in a region with a plane wavefront to optimise their performance.

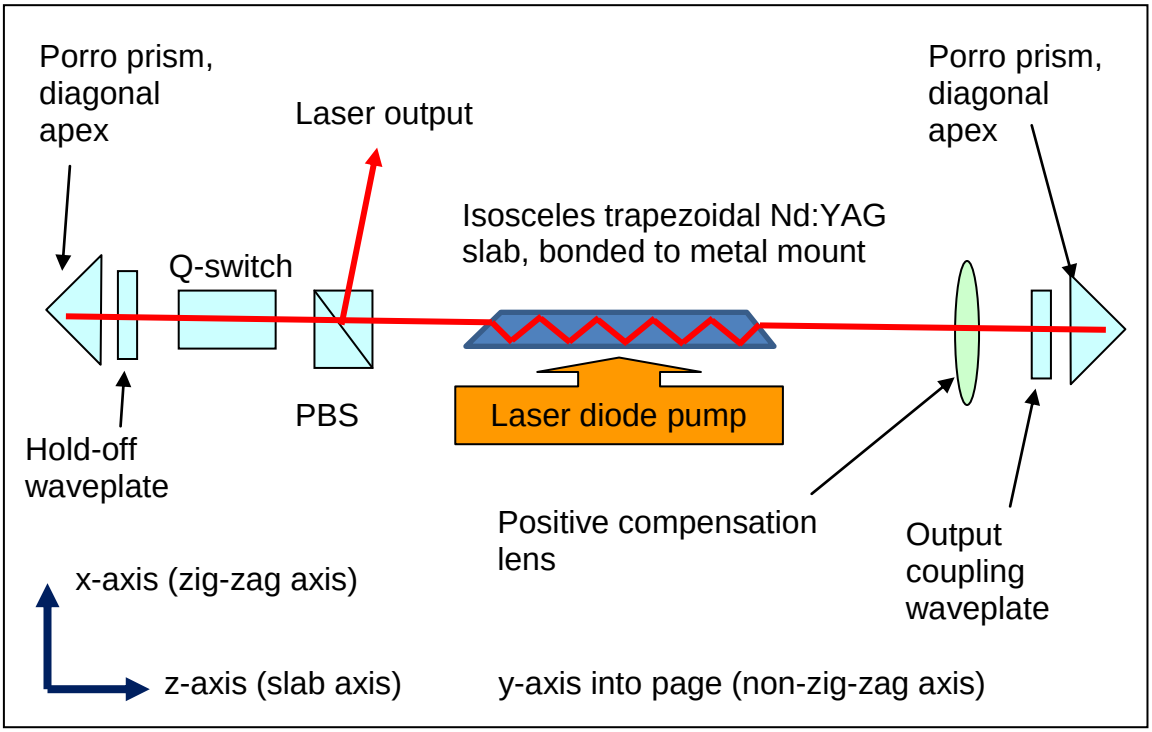

Figure 5-15: Set-up used to test an intracavity positive spherical compensation lens

5.4.1.3 Results

The plot in Figure 5-16 shows the effect of introducing an intracavity compensation lens on laser near-field peak to average intensity value, while firing the laser at 20 Hz. For the uncompensated case, the peak to average intensity rises to over 2.5:1 in approximately two seconds. This is unsurprising as the time constant of the slab is calculated to be 0.5 s (see 5.7.1 Appendix 1: Thermal time constant of a slab). Therefore, equilibrium is reached within four slab time constants. The peak to average intensity is then unstable and fluctuates from pulse to pulse with some poor beam intensity patterns with values of approximately 3.5:1. In the two compensated cases, the peak to average intensity value does not increase significantly and remains stable over the entire 60 s firing duration. The weaker 30 m focal length lens out-performs the stronger 15 m focal length lens, with an average near-field beam intensity pattern peak to average intensity value of approximately 1.7:1 compared with 2.2:1.

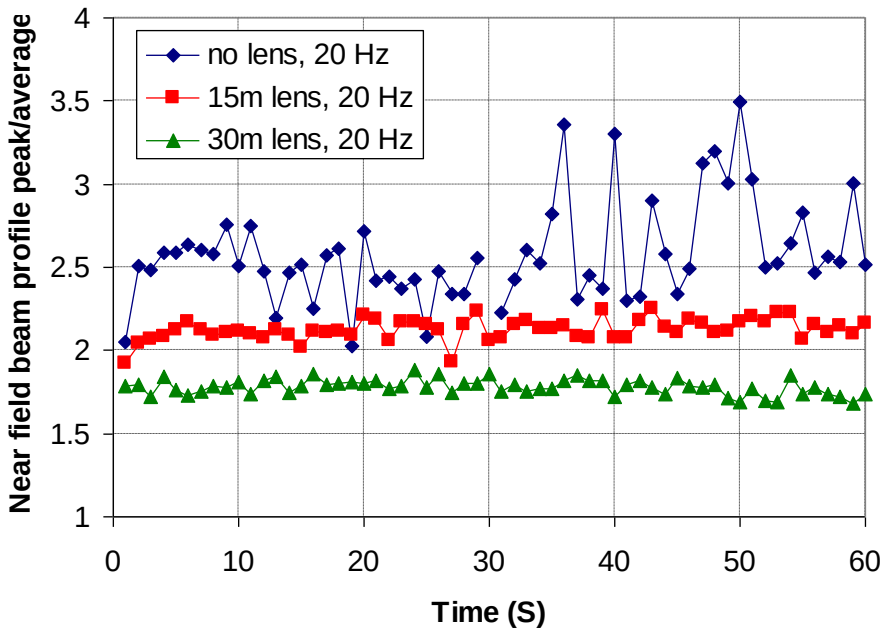

Figure 5-16: Effect of introducing an intracavity compensation lens on laser near-field peak to average value, while firing the laser at 20 Hz

The plot in Figure 5-17 shows the effect of introducing an intracavity compensation lens on laser near-field peak to average intensity value, just as in the previous figure, but while firing the laser at 30 Hz rather than 20 Hz. This is to demonstrate that a fixed compensating optic may not be as successful if the heat load is then increased. In the compensated cases the near-field beam intensity pattern peak to average is stable as before for the first 20 s. After this period, the peak to average becomes more unstable and begins to rise. At the end of the 60 s firing duration, the value is comparable to the uncompensated case.

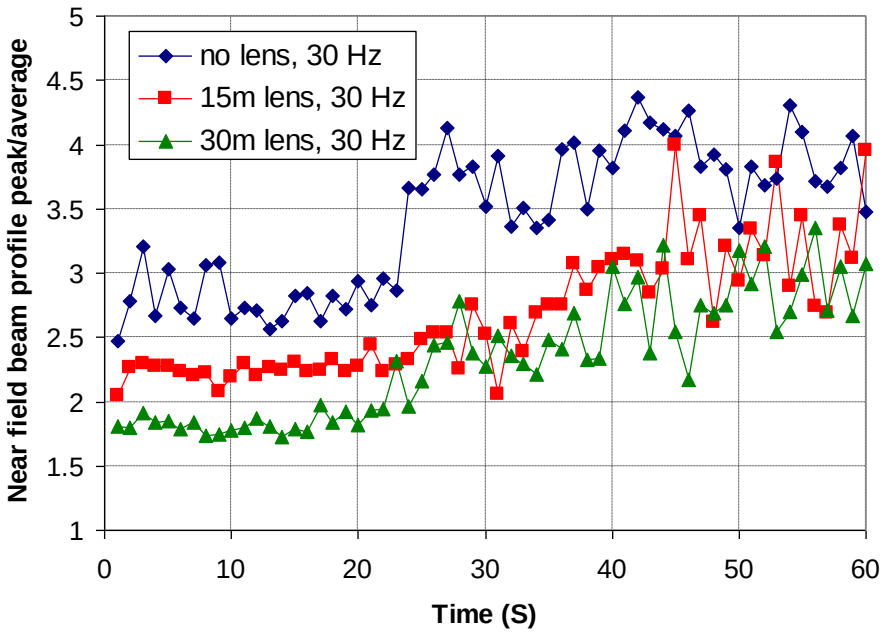

Figure 5-17: Effect of introducing an intracavity compensation lens on laser near-field peak to average value, while firing the laser at 30 Hz

5.4.1.4 Discussion

The results suggest that a fixed compensation lens can be effective at improving the near-field beam intensity pattern in terms of the peak to average intensity value, for a known range of operation. However, if the heat load is altered out with this range, the compensation can become ineffective. In the uncompensated case at 20 Hz, the temperature gradient, which causes an increase in the near-field beam intensity pattern peak to average intensity ratio, is established within the first two seconds of the firing duration. This is unsurprising as the time constant of the slab is calculated to be 0.5 s. However, when firing the laser at 30 Hz, in the compensated case, the peak to average begins to increase only after 20 seconds of firing. This suggests that the mechanism for wavefront error formation may be different for the two cases. It may be that for the 30 Hz case, the wavefront error only occurs once the slab mount reaches a particular temperature. In which case, stress induced refractive index variation, could be of greater importance than in the 20 Hz case. It is possible that the adhesive is able to prevent some mechanical stress due to its pliability. However, this masking of the slab

deformation may not be possible at greater heat loads when the thin layer of adhesive becomes compressed.

5.4.2 Investigation of the pumped region length

5.4.2.1 Introduction

In the literature [3, 4, 8], the benefits of a zig-zag path slab geometry over a rod geometry are described in terms of reduced thermal-lensing and stress-induced birefringence. For an infinitely long slab the wavefront aberrations in one axis due to a path length delta across the beam intensity pattern caused by a temperature gradient are completely cancelled out by the zig-zag path. It is however acknowledged that the end effects are very important and can have a large impact on thermal-lensing. It is suggested in the literature that the large variation between predicted and experimental values for thermal-lensing may be due to the end effects. Although the zig-zag path reduces the thermal effects across the zig-zag axis, a temperature gradient will exist in the non-zig-zag axis due to the non-flat-top gain profile and convection cooling at the ground top and bottom surfaces of the slab. A photograph of the slab assembly which illustrates the slab and cooling geometry is shown in Figure 5-1.

If an assumption is made that the temperature gradient which exists across the zig-zag axis, due to pumping and cooling on opposite sides of the slab, is limited to the length of the pumped region, then the ideal pump length can be calculated. In this simplified case, the length of the pumped region would be equal to an even integer number of bounce lengths to perfectly average out gain and birefringence and refractive index variations across the zig-zag axis. In reality, a temperature gradient along the axis of the slab will exist, due to thermal conduction in the Nd:YAG, and therefore the length of the heated region will be longer than the length of the pump source and will have a gradient at the edges. The heat load distribution will also be affected by the length of the adhesive through which the majority of the cooling of the slab is provided by conduction into the mount, which is in turn cooled by conduction into the laser chassis. This needs to be considered when choosing the length of the pumped region. The average thermal lens powers measured in a sample of 47 slab assemblies and the modelled thermal lens powers are shown in Table 5-1 for the non-lasing case.

	Zig-zag axis	Non-zig-zag axis
Modelled thermal lens power	-0.058 Dioptres	0.049 Dioptres
Measured thermal lens power	-0.135 Dioptres	0.032 Dioptres

Table 5-1: Summary of modelled and measured thermal lens power.

The measured thermal lens powers in Table 5-1 were determined by subtracting the measured passive lens powers from the measured total lens. As the strength of the measured thermal lens in the zig-zag axis is 4.2 times as strong as in the non-zig-zag axis, it is of value to reduce the zig-zag axis lens, by changing the length of the pumped region. The non-zig-zag axis thermal lens will not be significantly affected by this alteration to the pump length. The aim is to reduce the average thermal lens to zero, so that the variation in laser performance over a firing period will also be reduced to zero. Therefore, by reducing the strength of the negative zig-zag axis cylindrical lens, to match the strength of the positive non-zig-zag axis cylindrical lens, the two will cancel out to first order by virtue of the 90º beam rotation that is provided by the resonator design.

As shown in Table 5-1, the modelled thermal lens power is just 43% of the average measured value in the zig-zag axis, but is 153% of the average measured value in the non-zig-zag axis. This could be explained in the non-zig-zag axis by the partial reflection of pump light from the ground top and bottom slab surfaces, where zero reflection was assumed in the model. In the zig-zag axis, the lens is sensitive to the length of the heat load, and the "edge effects" [3, 4], which are sensitive to the cooling of the slab. In addition, the assumption of a flat-top profile along the slab axis was used in the model, whereas in reality, the laser diode slow axis divergence is in this axis, with a half-angle divergence of 5°.

5.4.2.2 Pump length matching to slab fold length

An investigation has been carried out, in which the laser diode stack spacing and the number of laser diodes has been varied and the effect on slab thermal lens and laser performance analysed. As the total length of a laser diode pump was varied, the resulting lens power in both the non-zig-zig and zig-zag axis of the slab was measured using an interferometer. This method of adjusting the pump length is not ideal, as the gap sizes in between the stacks are different for each pump length tested, and there is a large jump between the length of the pump, from 53.3 mm to 45.3 mm when a laser diode stack is removed. The electrical connections between the laser diode stacks allowed for a limited translation. When a laser diode stack was removed, the heat load value was maintained by increasing the power of the remaining four laser diodes to compensate. The output energy of the laser was unaffected by the change of pump length.

The objective was to find the optimum pump length that produced the minimum beam growth over the firing period, which was set to 30 s, as the thermal lens is established within this period. It was hypothesised that the length which would result in a zig-zag axis thermal lens of zero would be an even integer number of bounce lengths, or slightly shorter due to the heat spreading in the Nd:YAG. It was also hypothesised that the length that would result in a zero average thermal lens, would be the length that was associated with the minimum beam growth.

For this slab geometry, with a 5 mm square cross-section, the bounce length is 8.4 mm. The nominal laser diode pump length is 54 mm. This is based on five ten-bar laser diode stacks which are 10 mm wide and spaced 1 mm apart. The slow axis of the laser diode stacks are in the zig-zag plane of the slab. Therefore, the pumped region is only marginally longer than the length of the row of laser diodes.

The diagram in Figure 5-18 shows where centre and the edges of the laser mode are incident and enter the laser slab and then their total internal reflection positions on the surfaces of the slab. The nine bounce positions are shown. The tip-tip length of slab is approximately 84 mm but varies from slab to slab by ±0.75 mm due to the variation in the angle of the end surfaces and the size of the chamfers.

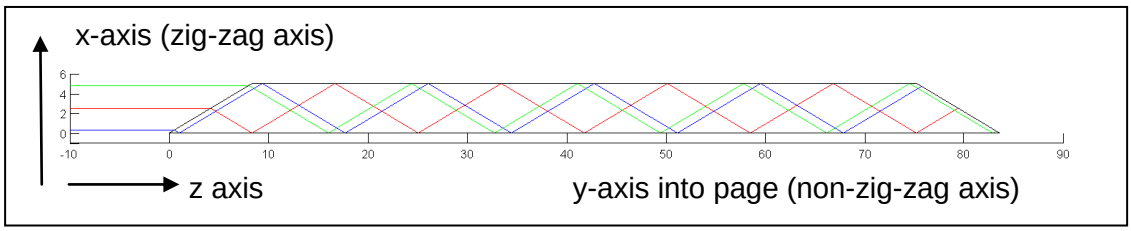

Figure 5-18: Diagram of the laser slab trapezoid cross section geometry.

The end of the slab is angled such that an incident laser mode is refracted to give a 100% fill factor in the slab for optimum gain extraction. As the angle, which is close to Brewster's angle, gives a higher transmission in the p than the s polarisation state, a coating is applied to the end surfaces of the slab, which results in an equal loss of approximately 2% for both polarisation states. The thermal components of the optical powers are plotted in each case and the passive component is removed from the wavefront measurement for a fair comparison.

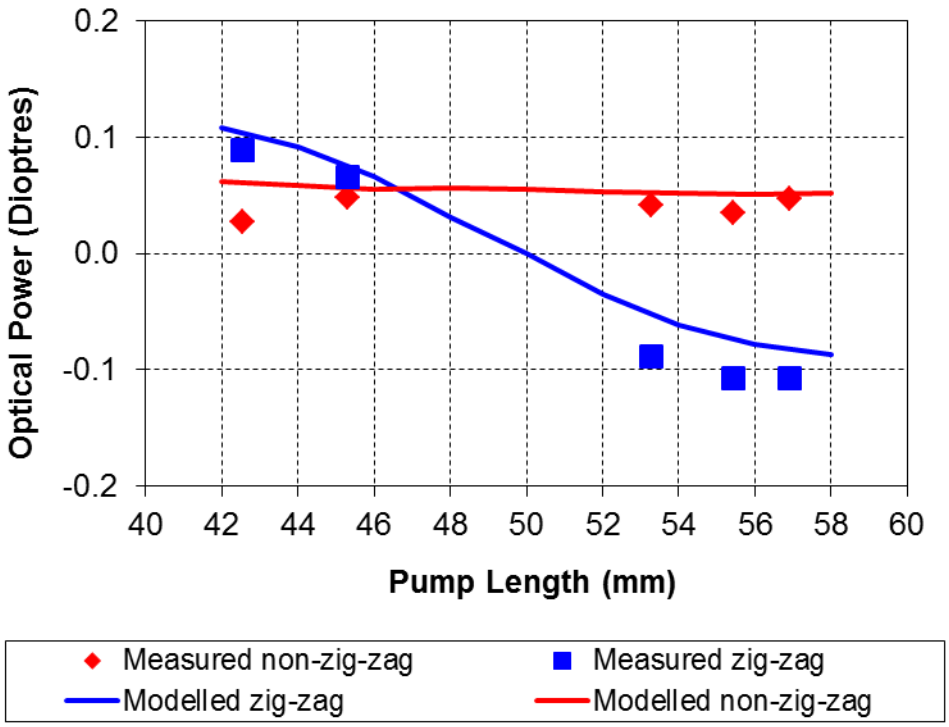

Figure 5-19: Graph to show both the theoretical and the experimental optical powers in each slab axis as a function of the pump length.

A simplified COMSOL Multiphysics thermal lens model was used here, with a calculated thermal load of 3.4 W and a super-Gaussian heat load distribution in the non-zig-zag axis. The pump was modelled as a continuous block uniformly distributed over the pumped region of the slab rather than as five discrete laser diode stacks. The plots show that there is good agreement between the measured and modelled thermal lenses for the range of pump lengths that were tested. As expected the length of the pump has a significant effect on the zig-zag axis thermal lens. The non-zig-zag thermal lens shows a comparatively insignificant variation, which was also expected. Figure 5-20 shows the plot of the average of the zig-zag and non-zig-zag axis thermal lenses in the slab as a function of pump length. This is the average thermal lens that the laser mode would experience per pass of the laser slab if the discrepancy between the lasing and non-lasing cases is ignored. In reality, the thermal lens will be slightly reduced as the heat load is 97% when in the lasing rather than non-lasing condition as explained in Section 5.2.4, and the passive lens will add to the total lens. The passive lens for the slab assembly tested was measured to be 0.047 D in the non-zig-zag axis and -0.032 D in the zig-zag axis. This average value would be the same for a cross Porro prism resonator as for a ring resonator, although the ring resonator averages over two round-trips and the cross Porro prism resonator averages over one.

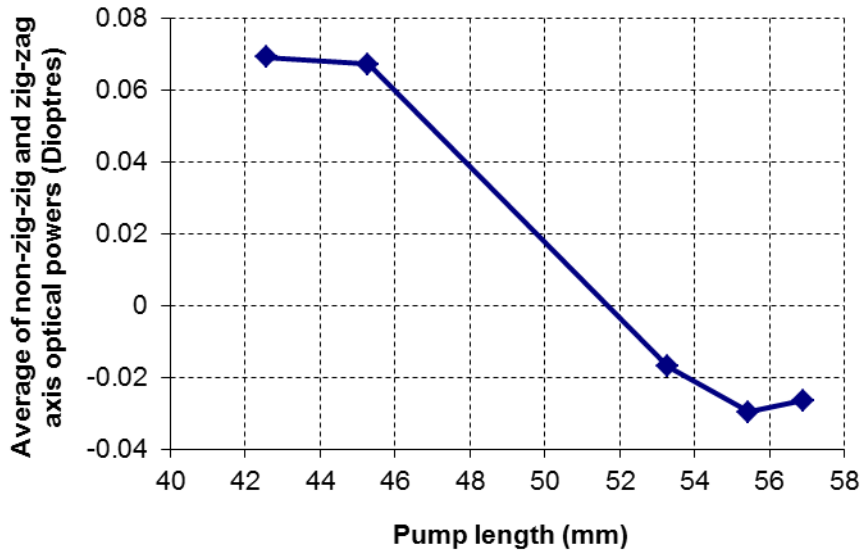

Figure 5-20: Experimental values of net average lens.

The optimum pump length which gives the average sum lens of zero is somewhere between the two lengths of 53.3 mm and 45.3 mm between which a large data gap exists. If the two points are connected with a straight line, the length of pump which corresponds to a zero average sum lens is approximately 51.5 mm. The modelled trend shows that a straight line between these points is a good first approximation. The modelled thermal lens values in Figure 5-19 predict a zero average thermal lens at a pump length of approximately 53 mm.

The same range of diode pump lengths that was tested in the interferometer was investigated inside a laser resonator to assess the effect of pump length on resonator performance. The same slab assembly was also used. In this investigation a non-planar ring-resonator (as described in Chapter 2, Section 2.6.8) was used to carry out the testing. 90° rotation of the beam intensity pattern after each pass of the Nd:YAG slab is common to both cross Porro prism and non-planar ring resonator designs. The reason for this choice was simply that the laser system, which used the ring resonator configuration more readily allowed for adjustment of the laser diode stack positions than other lasers that were available. The geometry of the resonator did not have a significant bearing on this investigation. The magnitude of beam growth during a 30 s firing duration can be a useful indication that thermal lensing is having a significant effect on the beam intensity pattern. The growth in both the near-field and far-field beam intensity patterns for a range of pump lengths can be seen in Figure 5-21.

This indicates that the best performance for near-field beam intensity pattern, where the near-field beam growth is zero, is at around 47 mm pump length. The value of average lens including the passive slab lens is approximately +0.04 dioptres for this pump length which gives the optimised performance level. The prediction of the optimum pump length of approximately 52 mm, which produces a zero average lens is shown to produce a near-field beam growth of approximately 8%, if the data points are connected with a straight line, which was not expected. Therefore, testing of a pump length of approximately 52 mm, which is predicted to produce a zero average lens, would be desirable, to directly measure the real beam growth value for this pump length.

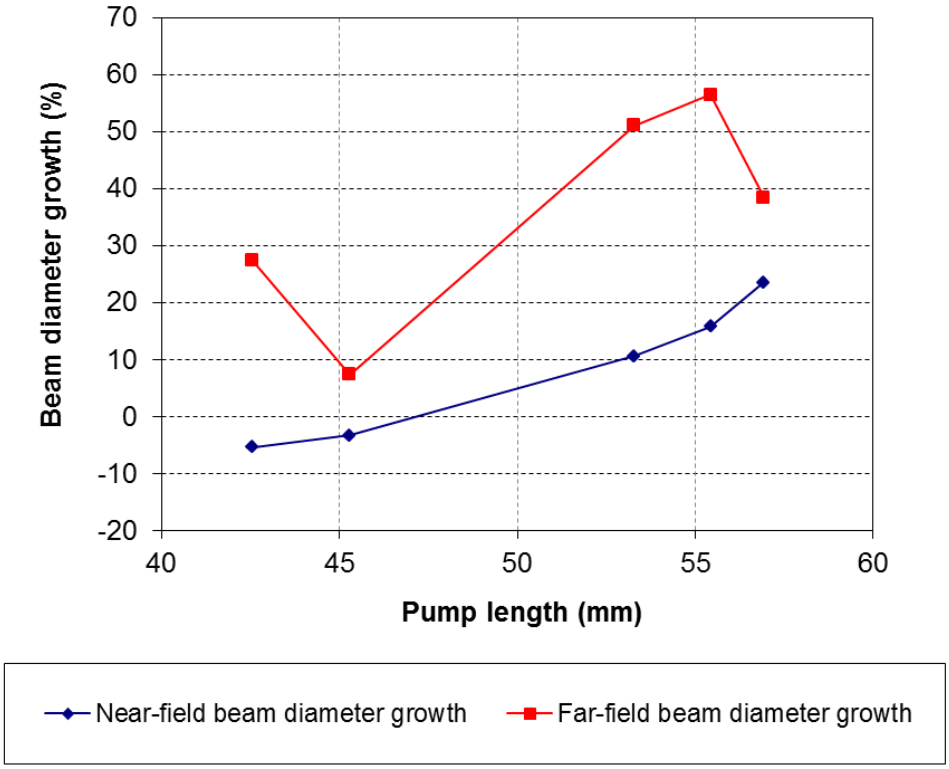

Figure 5-21: Graph of beam growth of both the near-field and far-field beam intensity patterns over the firing period for a range of pump lengths.

Both the magnitude and the variation in the divergence growth with pump length are greater than for the near-field beam growth. In Figure 5-22 it can be seen that the near and far-field beam intensity patterns are likely to be relatively small at a pump length of 47 mm, which equates to a better beam quality. This is preferable as the laser output divergence and near-field behaviour will demonstrate greater margin with respect to the specification values.

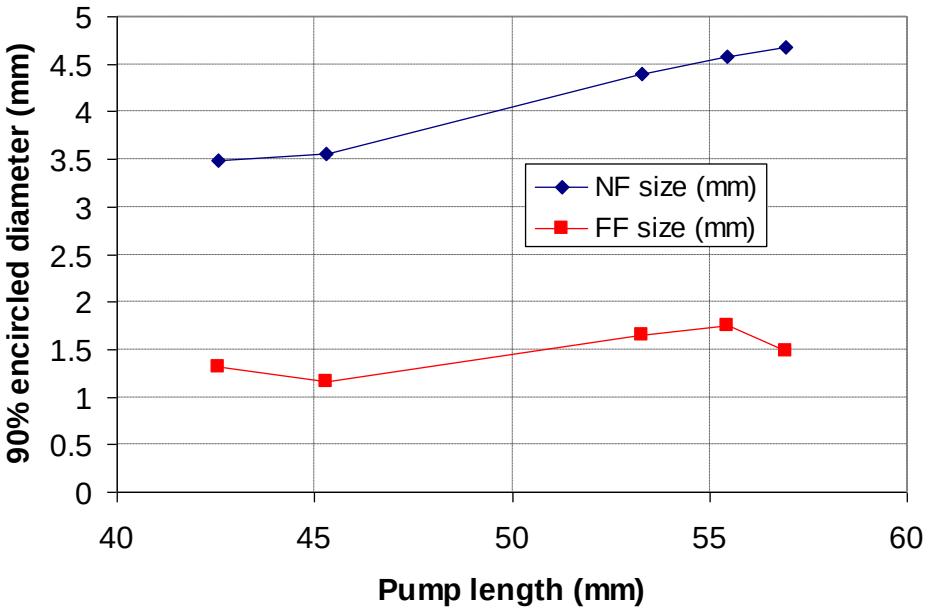

Figure 5-22: Near-field and far-field beam size for a range of pump lengths (average of 1 s firing duration in steady-state).

5.4.2.3 Discussion

In Figure 5-23 a diagram of the slab is shown with six bounce lengths marked as an ideal pump length over which x-axis temperature gradient is averaged. The actual pump length used in the current design is also shown as a comparison.

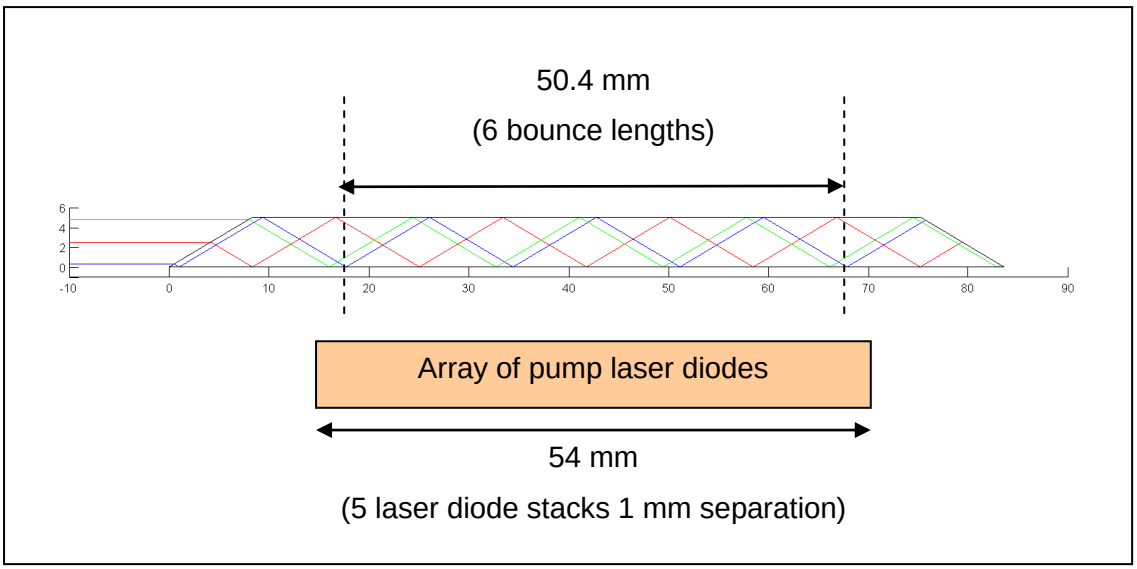

Figure 5-23: Diagram of ray trace through slab with laser diode pump length shown as a comparison.

A single bounce length for the 5 mm thick nine bounce slab is 8.4 mm. The optimised pump length (in terms of near-field beam growth) of 47 mm is actually between five and six bounce lengths. This pump length could not be achieved with the current configuration which uses five laser diode stacks, each 10 mm wide. It would be recommended in future designs to reduce the laser diode stack width, or reduce the number of laser diode stacks to four in order to achieve this optimum pump length. An alternative option would be to increase the length of the slab (and all other dimensions proportionally) so that the current pump configuration would be the optimum length. The undesirable side effect of this approach is that the larger slab would increase the limiting aperture in the resonator, hence the divergence would increase (higher resonator Fresnel number). The temperature gradient in the non-zig-zag axis would change as a consequence of the increased slab width, as a smaller percentage of the slab surface would be pumped. In addition, the slab mount would need to change along with the slab bonding jigs. This is therefore much less desirable than changing the pump length.

Experimental uncertainties in the diode positioning between the laser experiments and the interferometer measurements could partly explain the discrepancy in the optimum pump length. Differing cooling of the slab assembly may also contribute to this. It may be that the effect of lasing on the heat load magnitude and distribution was underestimated.

Further testing is recommended using a better method of pump length adjustment, for example by using an adjustable length mask. Once the optimum laser diode pump length was determined, a new size of laser diode could be procured from the supplier and tested in a laser.

5.4.3 Off-set pumped region

If it is not possible to adjust the size of the laser diode pump, then the pump should be positioned to best match the number of "hot-side-bounces" for the centre and the edge rays within the length of the pumped region. These rays are shown in Figure 5-23. Equally, the number of "cool-side-bounces" for each of the rays should also be matched. This can be done by moving the pump along the length of the slab in either direction. Alternatively, the slab could be moved in relation to laser diodes. However, if the slab is rotated by any amount, the alignment of the laser will be compromised.

An investigation into the position of the pumped region in relation to the centre of the laser slab was carried out. The distance between the slab and the laser diodes was kept constant, as was the relative position in the non-zig-zag plane.

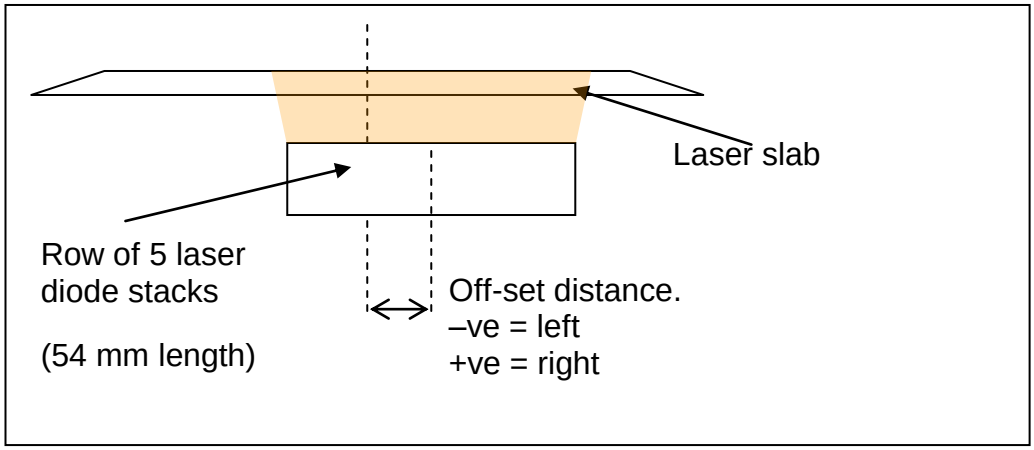

Figure 5-24: Diagram to show the off-set position of the laser diode pump in relation to the laser slab.

Slab assembly A4, which was considered to produce a “bad” near-field beam intensity pattern, showed an increasing near-field beam intensity pattern peak/average value over a three second firing duration. A number of laser diode offset positions were tested and a reduction in peak/average over this firing duration was measured, as shown in Figure 5-25.

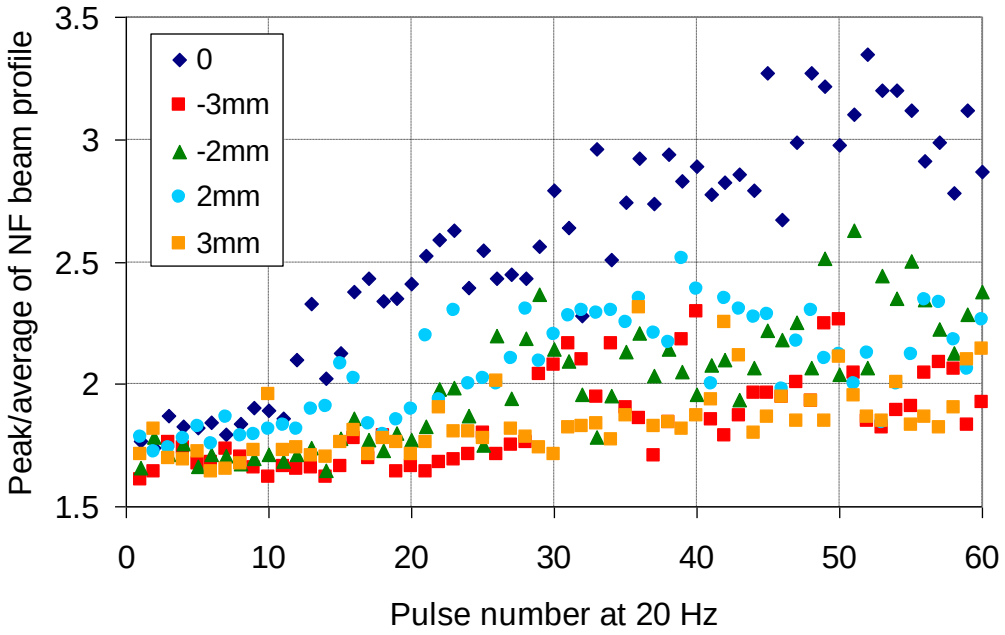

Figure 5-25: Graph of peak/average of near-field beam intensity pattern against pulse number (first 3 seconds firing duration using a "bad" slab assembly) for 5 different pump positions.

The conclusion from this work is that the near-field beam intensity pattern can be influenced by moving the pump source to manipulate the thermal lens in the laser slab. This is possible due to the fact that the length of the pumped region does not match an even number of bounce lengths, as would be ideal, as discussed in the previous section 5.4.2. The off-set pumped region solution to the increasing near-field beam intensity pattern peak/average value is a simple design change when compared with changing the slab size or pump size. Given costs and time for implementation, this could be a preferred solution. However, a potential issue has been discovered while testing this solution in a laser, whereby the boresight of a laser shifted during the warm-up period of

0-30 seconds. This is a risk to performance that requires further investigation if this solution is considered to be a good option.

5.4.4 Patterned adhesive

Rather than changing the distribution of the heat source in order to alter the temperature profile of the slab, another tactic that can be employed is to change the distribution of the cooling contact on the back of the Nd:YAG slab. Two methods that have been tested are the stepped shaping of the slab mount and patterning of the epoxy adhesive, which is used to bond the slab to the mount. The pattern of the adhesive employed in the latter method is shown in Figure 5-26.

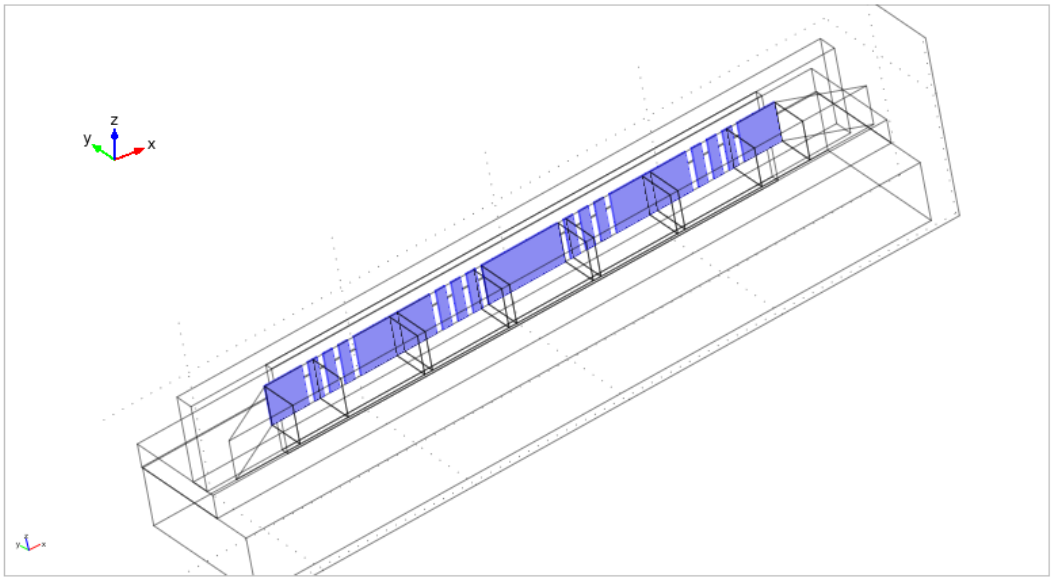

Figure 5-26: Diagram of a slab assembly with the adhesive shown in blue. The gaps in the adhesive affect the temperature profile of the slab when pumped.

The wavefront and refractive index profiles shown in Figure 5-27 were produced by the ray-trace computer model, which was used to optimise the pattern of the adhesive in the Comsol thermal model by trial and error in order to reduce the predicted zig-zag axis thermal lens. The non-zig-zag axis lens is predicted to be unaffected. A heat load of 4.3 W was calculated for use in the Comsol model.

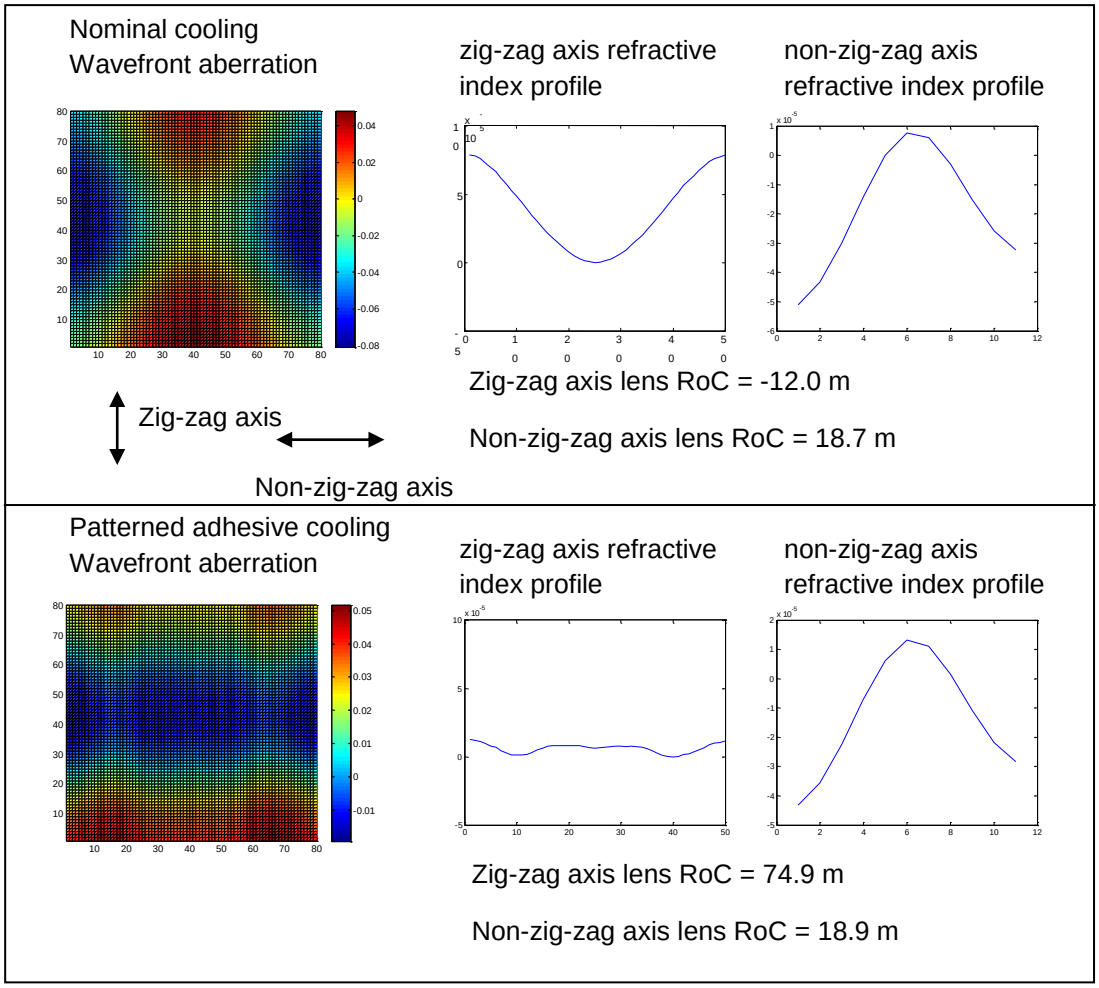

Figure 5-27: Predicted wavefront aberrations for the nominally bonded slab case and the patterned adhesive case.

The parts of the slab that are adjacent to air gaps will be at a higher temperature than they otherwise would have been. By choosing the parts of the slab which are cooled less, the thermal profile inside the laser slab can be controlled. In the nominal configuration, a negative thermal lens exists in the zig-zag axis and it is desirable to reduce the strength of the lens. To compensate for this lens in the zig-zag axis, the path length for the centre of the beam intensity pattern should be increased in relation to the rays at the edges of the beam intensity pattern. This can be achieved by increasing the temperature at the locations where the central ray is incident on the cooled slab surface relative to the locations where the edge rays are incident on the cooled slab surface. The centre and edge rays are shown in Figure 5-23.

The pattern of adhesive with air gaps shown in Figure 5-26 was created by using a plastic mask of approximately 160 µm thick. When the adhesive was applied it was left to cure for approximately an hour. While in a semi-cured state, the mask was removed, so that it did not become permanently attached to the adhesive. The mask was produced by hand and a more precise process such as laser cutting would be recommended in the future. The air gap width is difficult to control as the adhesive expands during curing, which closes up the gaps to some extent. In addition, the change to the adhesive pattern due to the removal of the mask is unclear.

The thermal lens produced when pumping the slab assembly with the patterned adhesive (Slab P4) was measured using the Fisba interferometer. This measurement is compared with six standard slab assemblies in Figure 5-28.

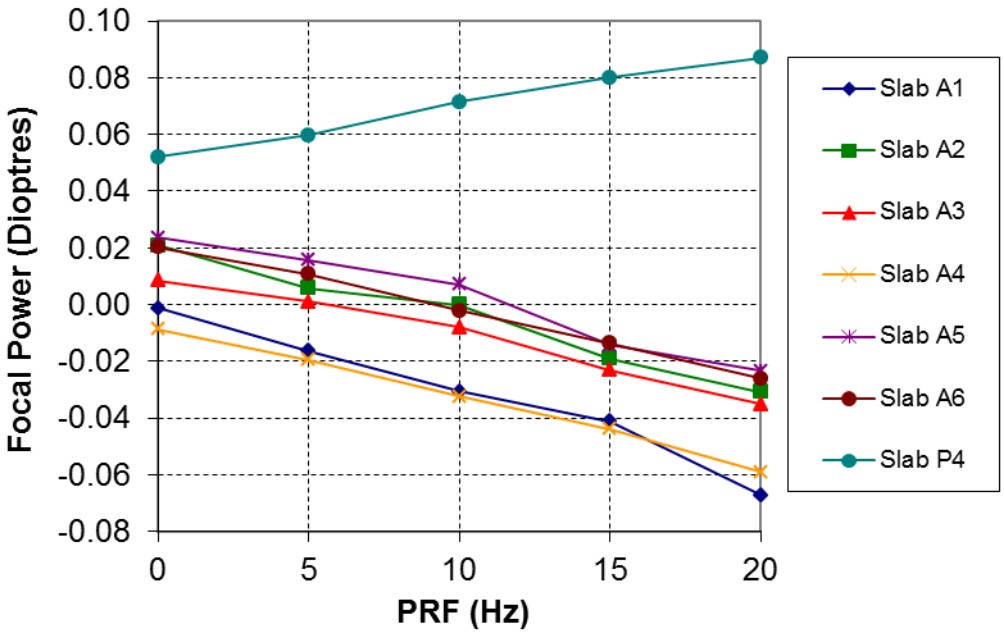

Figure 5-28: Average laser slab lens when pumped but not lasing. The average measured lens focal power is plotted against pump repetition rate.

The results in Figure 5-28 show that the thermal lens produced by the patterned adhesive slab is substantially different to the standard slab assemblies. In the one example shown, the average thermal lens produced is positive and comparatively strong when pumped at 20 Hz pulse repetition frequency, whereas all the standard slabs have a negative average thermal lens. The patterned adhesive slab assembly was tested in a

laser and was found to produce an increasing divergence and a reducing near-field beam diameter during the first 30 s pumping duration, as the positive thermal lens was increasing. The reduced near-field beam size was not an issue. However, the average divergence when using the patterned adhesive slab was 1.25 mRad compared with an average of 0.75 mRad for the six standard slab assemblies, which is a significant degradation in performance.

A positive average lens of approximately 0.05 D was expected due to the uncompensated non-zig-zag axis component. However, the zig-zag axis negative cylindrical lens was over compensated for, which increased the magnitude of the positive lens to approximately 0.09 D. In addition, the positive lens is not only due to the thermal effect, but also due to a permanent passive lens imparted on the Nd:YAG slab by the bonding process. This positive passive lens is approximately 2.5 times stronger than the strongest passive thermal lens present in any of the standard slab assemblies. Ideally, the pattern should be optimised to produce a gradient of zero to eliminate all effects due to thermal lensing in the slab.

In conclusion, this investigation shows that a large effect can be created by manipulation of the cooling geometry in order to affect the laser performance. However, in practise, the pattern of the adhesive is difficult to control due to adhesive expansion and mask removal. A process that provides a consistent cooling interface, for a number of slab assemblies, needs to be developed. Further work is required to produce the optimum cooling pattern to achieve a performance improvement. The patterned adhesive slab assembly concept has yet to be tested over the full temperature range. This is required in order to determine if significant variation in the passive lens occurs due to thermally-induced stress.

5.4.5 Patterned mount

An alternative method to achieve a variation in the cooling profile in the slab to the method described in the previous section was also considered. In this investigation, the mount was patterned with stepped areas where the adhesive was thicker, as shown in Figure 5-29.

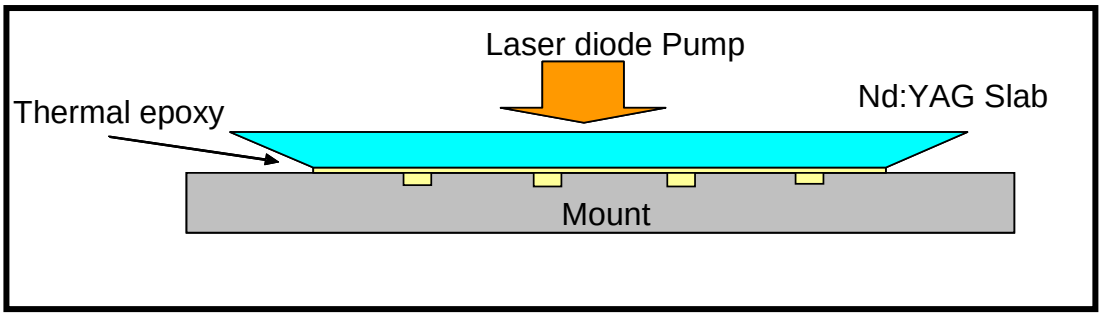

Figure 5-29: Diagram of zig-zag slab bonded to a patterned mount with thicker regions of adhesive (plan view)

In these areas, the slab would be at a higher temperature due to the relatively poor thermal conductivity of the adhesive. The Comsol thermal model was used to investigate the effect of patterning the slab mount such that the wavefront errors in the zig-zag axis of the slab were reduced in the same way as the patterned adhesive investigation.

A slab assembly mount was patterned as per the modelled mount. It was tested in the Fisba interferometer set-up and found to have improved performance. This slab assembly was then tested over temperature. This was carried out by placing the slab assembly inside a thermal chamber. A probe HeNe laser beam was passed in through the chamber window, through the laser slab and back out of the chamber. The slab was unpumped during this test. The amount of lensing in the laser slab could be measured by observing the minimum beam diameter of the probe beam in the far-field using a camera. When the probe beam divergence increased, the amount of lensing could be inferred by recollimating the beam using a telescope and recording the movement of one of the lenses required to minimise the divergence.

The conclusion from this work was that the strength of the passive aberrations in the slab changed significantly as the temperature of the slab assembly was varied within its range of temperature operation. This was attributed to stress induced in the slab by the variation in thickness of the adhesive between the slab and the mount, when the slab is at non-ambient temperatures. Therefore, this method of thermal lens reduction in the laser slab was unsuccessful. Although it has not been tested, it is predicted that the patterned adhesive method would not exhibit the same issue, as the spaces allow the adhesive to expand and contract without restriction.

5.4.6 Alternative wavelength laser diode pump

5.4.6.1 Introduction

In previous sections, a number of methods to compensate for, or reduce the impact of a thermal load in the slab on the laser parameters have been discussed. In this section, an alternative solution of reducing the heat load for a given laser output energy is investigated.

The current standard wavelength used to pump Nd:YAG slabs is 808 nm. An alternative wavelength absorption band is centred at 885 nm. This wavelength band provides pumping directly into the $^4F_{3/2}$ upper laser level, while producing a reduced heat load when compared with pumping at 808 nm wavelength. The energy level diagram showing both pumping schemes and the laser transition is shown in Figure 5-30.

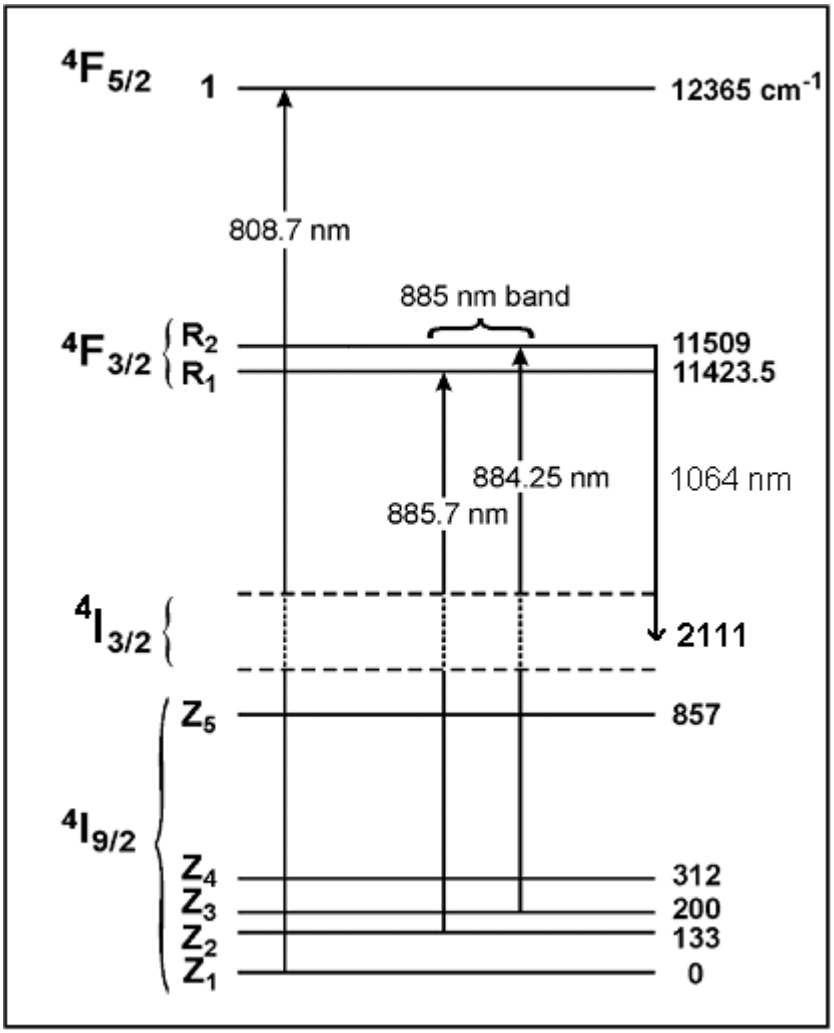

Figure 5-30: Energy level diagram which shows traditional 808 nm pumping and the alternative 885 nm pumping. The laser transition is also shown. [1]

In Figure 5-31 and Figure 5-32, the absorption spectrum for Nd:YAG in the 808 nm and 885 nm pumping bands respectively, are shown. These spectra relate to the absorption lines in Figure 5-30.

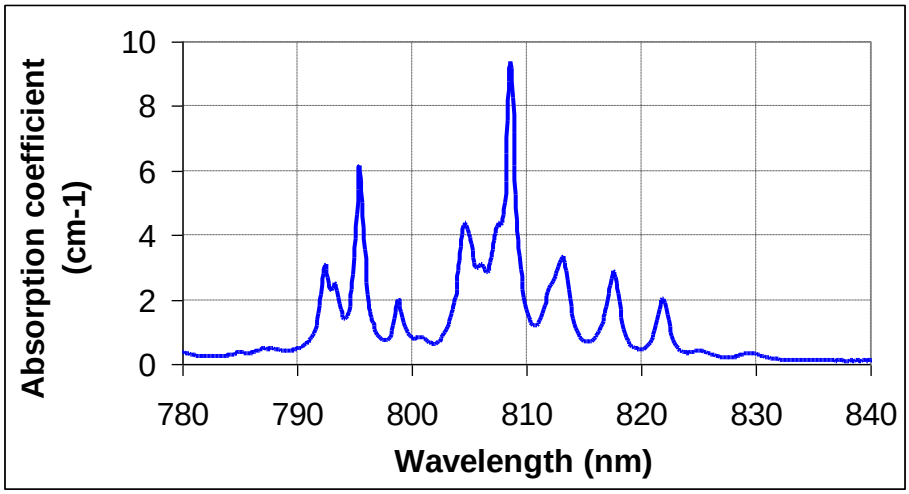

Figure 5-31: Absorption spectrum for 1.1% Nd doped YAG centred around 808 nm.

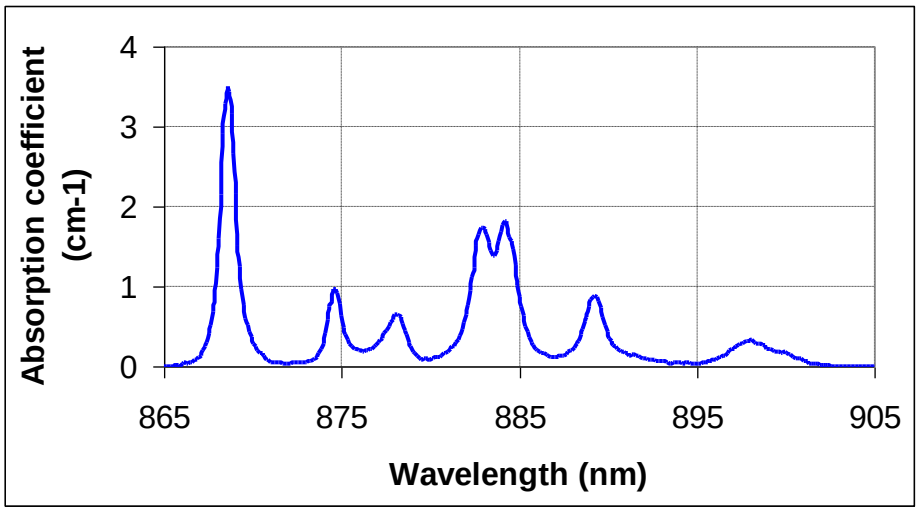

Figure 5-32: Absorption spectrum for 1.1% Nd doped YAG centred around 885 nm.

It can be seen that the peak absorption at 808 nm is approximately five times greater than that at 885 nm. As less 885 nm pump light is absorbed over a given length, a higher pumping energy is required in order to achieve the same level of population inversion in the Nd:YAG. This investigation is concerned with the improvement in laser performance associated with the thermal load reduction, due to the change in pumping wavelength. The decreased wall plug efficiency may be a price worth paying, if there is a substantial improvement to beam quality. The absorbed energy at 808 nm wavelength causes heating in the Nd:YAG due to five contributions.

1. Pumping into the $^4F_{5/2}$ level means that the electrons non-radiatively decay to the upper laser level producing heat. This is part of the quantum defect between the pump photon energy and the laser photon energy.
2. The transition from the $^4F_{5/2}$ level to the upper laser level ($^4F_{3/2}$) is not 100% efficient. The quantum efficiency or pumping efficiency is quoted as 0.9 [5] or 0.95 [2], with the shortfall leading to heating via nonradiative decay.
3. The radiative quantum efficiency for energy in the upper laser level, which follows the laser transition to the $^4I_{9/2}$ level is quoted as 0.95 [9]. This is non-unity due to parasitic effects such as concentration quenching, upconversion, and dark sites. These processes lead to heating via nonradiative decay.
4. For Q-switched operation, the significant period of laser hold-off (when compared with the upper laser level storage time), adds to the amount of spontaneous emission, which through Stokes shift, adds to the heat load. The Stokes shift is the reduction in photon energy between the upper laser level and the emitted photon.
5. The energy in the lower laser level then non-radiatively decays to the ground level, contributing to the heat load. This is part of the quantum defect between the pump photon energy and the laser photon energy.

For 885 nm pumping, the first two sources of heating in the Nd:YAG slab mentioned above are eliminated.

In addition to the reduced heating while pumping at 885 nm when compared with 808 nm pumping, there is a small cooling effect. This is due to pumping from a thermally excited Stark component of the ground level. Thermal energy is then absorbed to excite into the higher sublevels of the ground level [9]. This cooling effect is however insignificant when compared with the size of the quantum defects between the pump and laser energies.

5.4.6.2 Resonator set-up

The resonator used to test both sets of diodes was similar to the set-up in section 5.2.1, Figure 5-3. However, a different Q-switch was available to that previously used, which made a slight alteration to the resonator necessary. The two differences were the type of Q-switch used and the orientation of the left-hand side Porro prism. The Porro was

rotated by 45° so that the knife edge was vertical to the optical bench rather than at 45° as before. This was necessary as the new RTP Q-switch assembly rotated the polarisation of incident light by 45° with a half waveplate, but the old $LiNbO_3$ Q-switch assembly did not. The new set-up provides a 90° rotation per round-trip of the laser resonator rather than 180° which improves the beam mixing. This 90° image rotating design can be used to provide a more symmetrical far-field beam intensity pattern, which helps to minimise beam ellipticity. A subtle difference in the near-field beam intensity pattern due to the difference in beam rotation can also be seen. The differences in the RTP Q-switch and the $LiNbO_3$ Q-switch were discussed in section 2.4.1.

5.4.6.3 Comparison of 808 nm laser diode and 885 nm laser diode performance

A set of five (nominally) 808 nm wavelength laser diode stacks and a set of five (nominally) 885 nm wavelength laser diode stacks were available to pump a Nd:YAG slab as a direct comparison. Both sets of laser diode stacks had the dimensions of 10 mm by 5 mm, with the stacks separated by approximately 1 mm. In both cases the laser diode fast axis was in the non-zig-zag slab axis, and the slow axis was in the zig-zag plane. The divergence of the laser diode emitters was 34° full angle in the fast axis and 10° full angle in the slow axis. While modelling the laser diode pump light distribution, a flat top profile was assumed along the length of the slab, whereas the fast axis divergence was more significant, so a Gaussian distribution was modelled for each laser diode bar in the non-zig-zag slab axis.

The temperature of the 808 nm laser diodes was controlled by a water chiller which was set to 38°C. When the 808 nm laser diodes are operating, the temperature of the active region will be higher than the coolant temperature. The temperature of the 885 nm laser diodes, meanwhile, was controlled by a thermoelectric cooler (TEC), which was in turn cooled by a water chiller, which was set to 8°C. The 885 nm laser diodes were set up like this to make temperature adjustments quicker, and to allow a closer control of the temperature. A thermocouple was attached to the body of one of the 885 nm laser diodes to measure the temperature in order to provide feedback control.

The pumping levels required at each wavelength in order to produce an output energy of approximately 130 mJ at 5 Hz were determined. A pulse repetition rate of 5 Hz was

chosen in order to minimise thermal lensing in the slab so that a temporally stable energy was achieved. The output power of the laser diodes for these pumping levels was then measured using a calorimeter (Figure 5-33). The pumping current was 115 A for the 885 nm wavelength laser diodes, and 96 A for the 808 nm wavelength laser diodes.

For each test, the laser diodes were fired for long enough to enable the calorimeter to stabilise. The required duration was over two minutes.

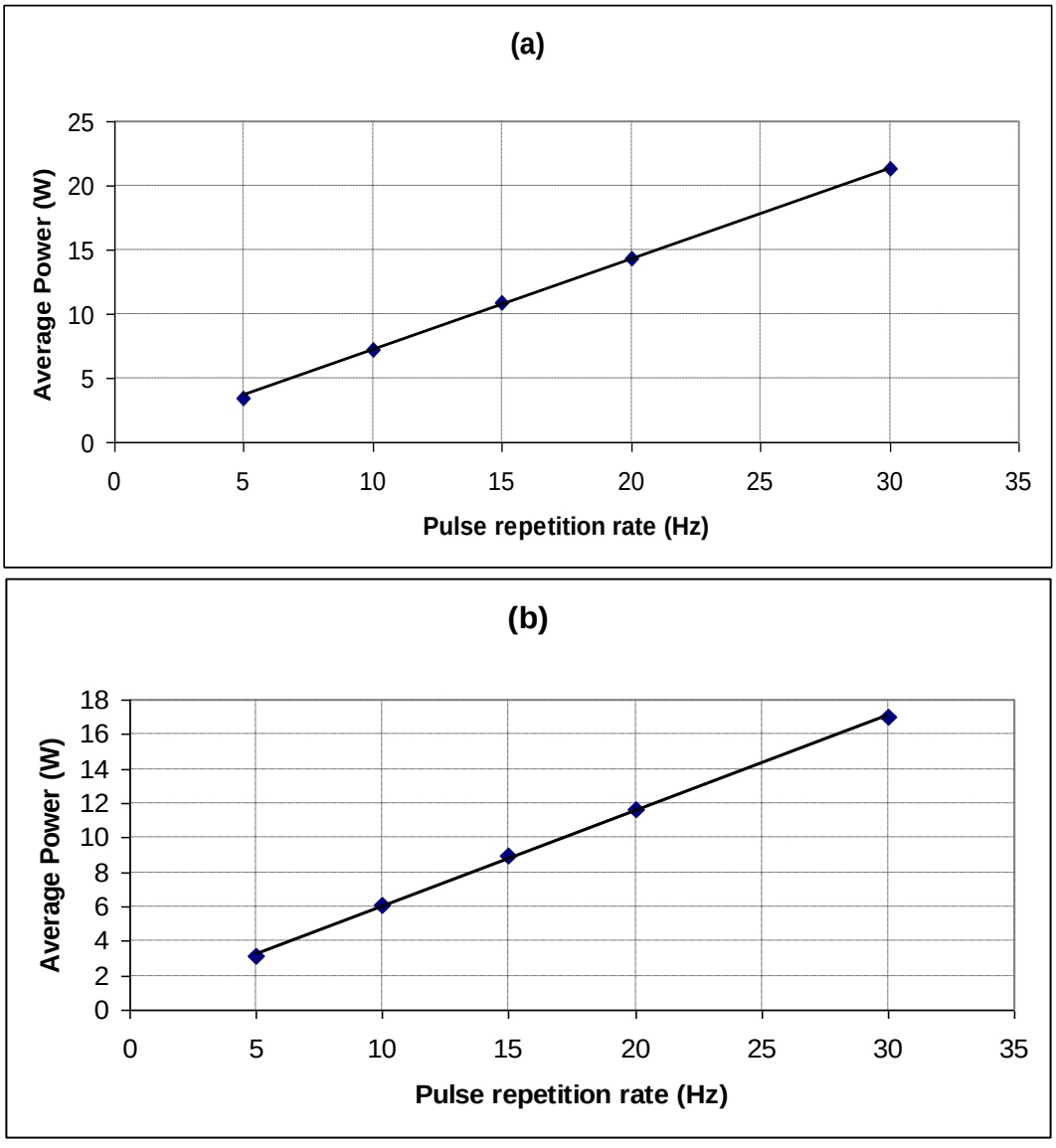

Figure 5-33: Graphs of average output power of 5 laser diodes stacks against pumping rate, for (a) 808 nm and (b) 885 nm wavelength laser diodes.

The linear fits show no thermal roll-over in laser diode average powers over the range of pulse rates used. For the same laser output energy, the 885 nm wavelength laser diodes produced a higher average output power than the 808 nm output power. When comparing the resonator performance with each set of diode stacks, the pulse repetition rate will be set to 30 Hz in order to increase the thermal loading in the slab, and hence maximise any differences between the two set-ups. The output powers at 30 Hz pulse repetition rate were 21.3 W compared with 17 W, respectively. The 885 nm wavelength laser diodes therefore produced 25% more power.

The electrical efficiency of the 885 nm wavelength laser diodes was 38% and the electrical efficiency of the 808 nm wavelength laser diodes was 39%, as shown in Table 5-2. In both cases the laser diode pulsewidth was 150 µs and the pulse repetition rate was 30 Hz.

Wavelength (nm)	**Current (A)**	**Voltage (V)**	**Electrical Power (W)**	**Output Power (W)**	**Efficiency (%)**	**Peak power (kW)**	**Pump pulse energy (mJ)**
808	96	100	43.2	17.0	39	3.78	567
885	115	107	55.4	21.3	38	4.73	710

Table 5-2: Summary of laser diode properties for 808 nm and 885 nm laser diodes.

The output of the two laser diode arrays were then imaged using a silicon based CCD camera, to compare the intensity distributions. A lens of f = 200 mm was used to provide an image magnification of approximately nine to fit the image on the camera array. The intensity distributions are show in Figure 5-34 and Figure 5-35 for the 808 nm and the 885 nm wavelength laser diode arrays respectively.

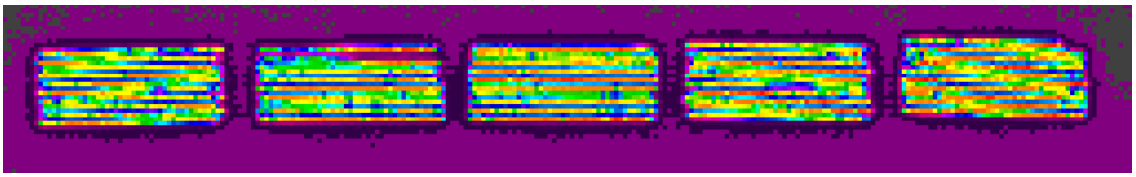

Figure 5-34: Intensity image of 808 nm laser diode stacks pumped at 30 Hz and a current of 96 A.

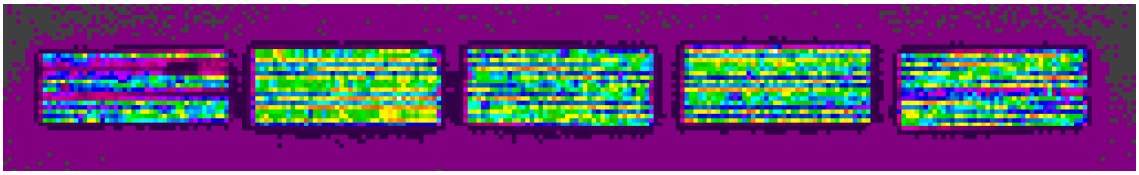

Figure 5-35: Intensity image of 885 nm laser diode stacks pumped at 30 Hz and a current of 115 A.

Fringes of a lower period than the laser diodes bars can be observed diagonally across the laser diode stacks due to frequency aliasing between the bars and the pixels of the camera. A manual aperture was drawn in the software, around each laser diode stack in turn, and the percentage of energy of the total array that was displayed by the Spiricon-LBA software, was recorded. This was then plotted on a graph to show the distribution of energy for each set of laser diode stacks. This graph is shown in Figure 5-36.

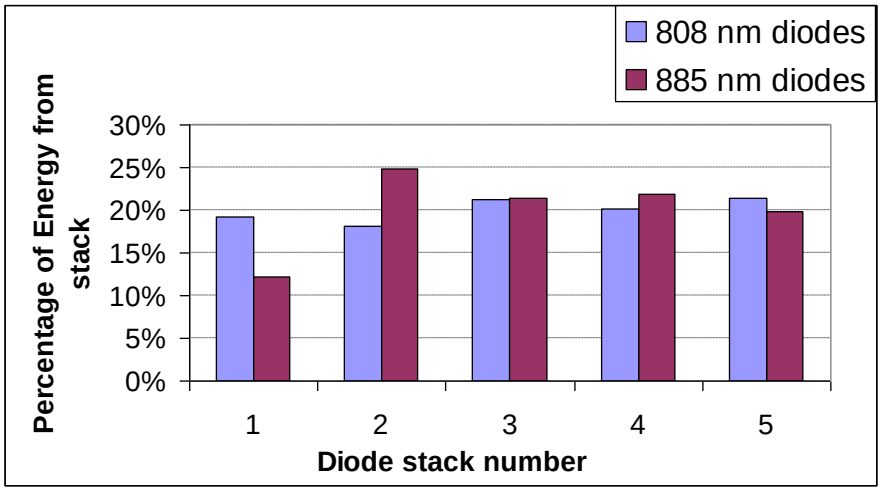

Figure 5-36: A graph to show the energy distribution over the 5 laser diode stacks for the two sets of laser diodes under test.

This graph shows that the energy distribution is more uniform for the 808 nm wavelength laser diodes than for the 885 nm stacks. The standard deviation for 808 nm laser diodes is 1% and the standard deviation for 885 nm laser diodes is 5%. The largest deviations from the average value are laser diode stacks number 1 and 2 of the 885 nm wavelength laser diodes. Number 1 is approximately 60% of the average value and number 2 is approximately 125% of the average value. This variation in pump power

along the length of the slab will have an effect on the detailed temperature distribution in the slab and therefore will also have an effect on the transmitted wavefront aberrations. The effect of the change in energy distribution has been modelled to determine if this effect is significant when compared with any effect due to the change in pump wavelength. The result of this model is summarised in Table 5-3.

Pump distribution	**Zig-zag axis**	**Non-zig-zag axis**
Modelled thermal lens power, normal pump distribution.	-0.058 Dioptres	0.049 Dioptres
Modelled thermal lens power, 25% increased pump in one diode and 40% decreased in another.	-0.057 Dioptres	0.048 Dioptres

Table 5-3: Summary of modelled thermal lens power, while the heat load generated by two of the five laser diodes were adjusted.

As can be seen, the result of adjusting the heat load for two laser diodes had a very minor effect on the slab thermal lens strength.

The wavelength spectrum of the two laser diode arrays were measured using an Ocean Optics spectrometer, while firing at 30 Hz at a power level of 17 W and 21.3 W for 808 nm and 885 nm wavelength laser diodes respectively. These are shown in Figure 5-37 and Figure 5-38, for the first and last pulses of a 60 s firing period. The width of these wavelength spectra were recorded using the full-width half-maximum (FWHM) measurements. For both sets of laser diodes, the centroid wavelength moves towards longer wavelengths, but the spectral shape is approximately maintained. In both cases the FWHM increases by 15% or less. The FWHM for the first pulse of the 808 nm wavelength laser diode array was 2.39 nm and the FWHM for the first pulse of the 885 nm wavelength laser diode array was 4.59 nm. It is not clear why the 885 nm wavelength laser diodes spectrum has a broader linewidth than the 808 nm spectrum. There is no fundamental reason why the linewidth should not be the same as the 808 nm diode stacks.

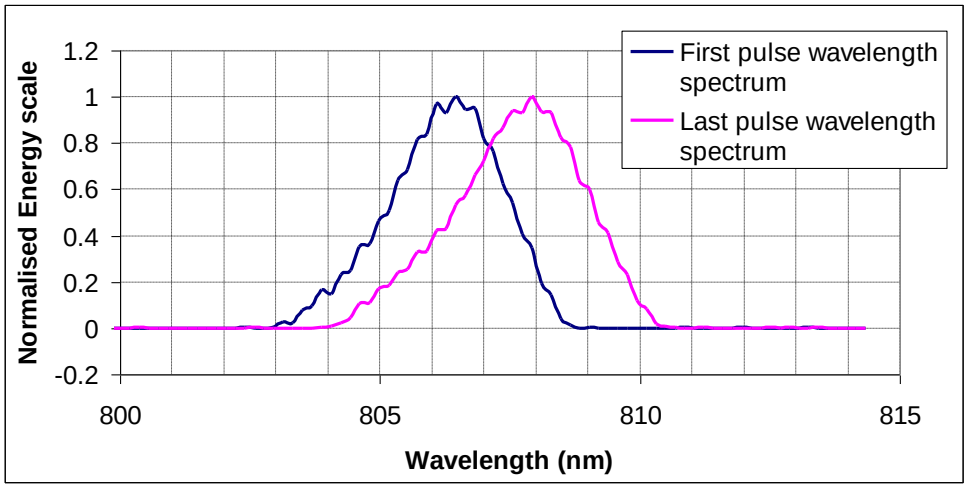

Figure 5-37: Wavelength spectrum of the 808 nm wavelength laser diode array at 38°C. The first and last pulse spectrums are shown for a 60 s firing duration.

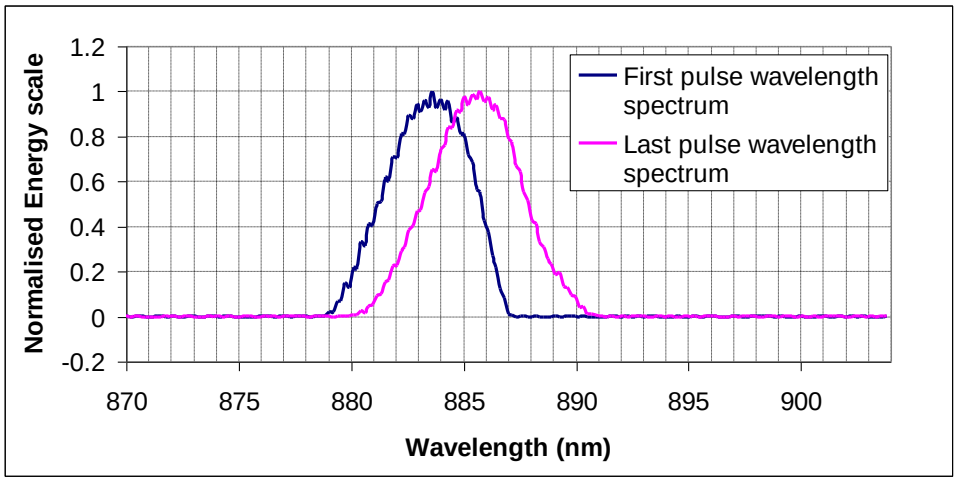

Figure 5-38: Wavelength spectrum of the 885 nm wavelength laser diode array at 36°C. The first and last pulse spectrums are shown for a 60 s firing duration.

A pump spectrum, approximated with a Gaussian lineshape, and the absorption spectra for Nd:YAG with 1.1% doping were used to calculate the absorption coefficients for the two wavelengths of pump, by convolution of the spectra. The calculated percentages of pump light absorbed were 99.8% for 808 nm and 62.8% for 885 nm as is shown in Table 5-4. Here an absorption length of 13 mm was used to calculate the effective absorption as will be discussed in section 5.4.6.6. The broader linewidth of the 885 nm diodes when compared with the 808 nm diodes has a negative impact on the effective absorption coefficient.

Pulse	Wavelength centroid (nm)	FWHM (nm)	Absorption coefficient (cm^{-1})	Effective absorption
First	806.2	2.39	3.7	0.992
Last	807.6	2.76	4.8	0.998
Average of 60 s	807.4	2.58	4.7	0.998
First	883.4	4.59	0.95	0.709
Last	885.5	4.77	0.72	0.608
Average of 60 s	885.3	4.68	0.76	0.628

Table 5-4: Summary of the laser diode spectrum measurements and calculated pump absorption.

Figure 5-39 shows a graph of the centroid wavelength of the 808 nm wavelength laser diode array when fired for 60 seconds duration.

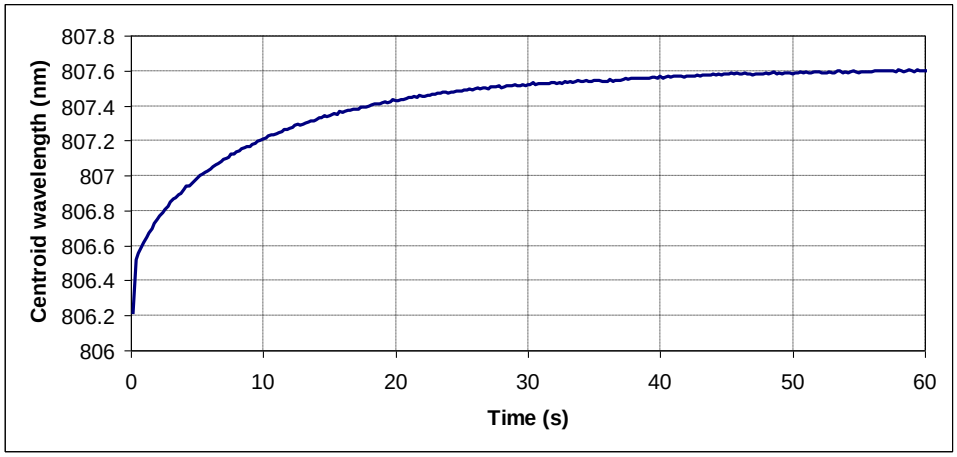

Figure 5-39: Centroid wavelength of the 808 nm wavelength laser diode array when fired for a 60 s duration.

The temperature of the water that cools the laser diodes was maintained at 38°C. The centroid wavelength initially increases rapidly and then reaches a steady state as the

temperature gradient stabilises. The centroid wavelength increases from 806.2 nm to 807.6 nm over a 60 s duration, an increase of 1.4 nm. The average value over the 60 s duration of 807.4 nm was used to calculate the absorption coefficient.

Figure 5-40 shows a graph of the centroid wavelength of the 885 nm wavelength laser diode array when fired for a 60 s duration. As previously mentioned, in this case, the temperature of the laser diodes was controlled using a TEC that was connected to a Marlow Industries PID controller.

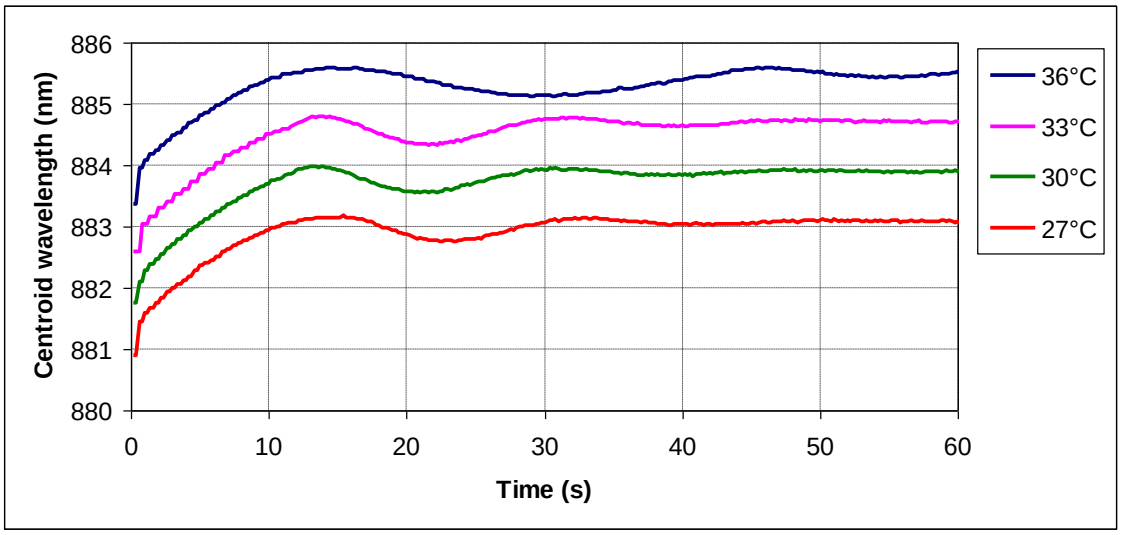

Figure 5-40: Centroid wavelength of the 885 nm wavelength laser diode array when fired for 60 s duration. Traces are shown for four different set point temperatures.

The centroid wavelength was measured for four different set-point temperatures, but the 36°C temperature was selected as optimum for best laser output energy. The centroid wavelength initially increases rapidly and the then reaches a steady state as the temperature gradient stabilises. There is also an oscillation of the wavelength which was caused by the over and under shoot of the temperature control loop. It proved difficult to fully optimise the PID control loop, given the wide range of laser firing parameters used. The centroid wavelength at 36°C increases from 883.4 nm to 885.5 nm over 60 second duration, an increase of 2.1 nm. The average value over the duration was 885.3 nm. This is a larger increase in wavelength than for the 808 nm wavelength laser diodes, which is surprising given that the TEC controls the

temperature of the 885 nm laser diodes directly with the temperature being monitored, unlike for the 808 nm wavelength laser diodes.

5.4.6.4 Comparison of performance in the resonator

The energy of the laser was recorded over a 60 s duration using a Litron energy monitor, while the laser was pumped at both 808 nm and 885 nm wavelengths. A pulse repetition rate of 30 Hz was chosen in order to increase the thermal loading in the slab, and hence maximise any differences between the two set-ups. A graph of the energy over the 60 s duration is shown in Figure 5-41. In the case of 808 nm wavelength pumping, the energy drops from an initial energy of approximately 135 mJ down to an energy of approximately 110 mJ over the 60 s duration. The drop in energy with time with 808 nm pumping correlates well with the measured drift in peak wavelength. The oscillating behaviour in energy with 885 nm pumping correlates less well with the change in peak wavelength.

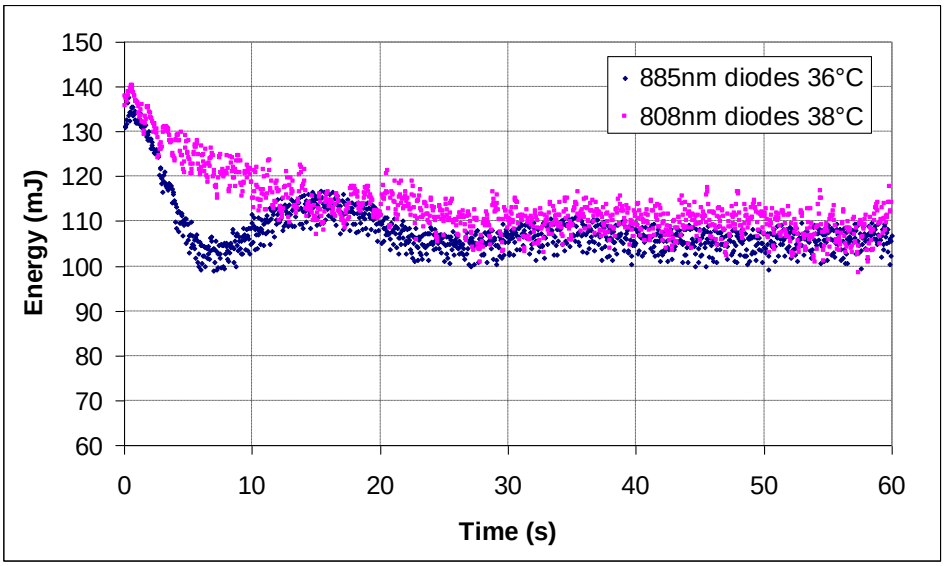

Figure 5-41: Laser output energy over a duration of 60 s, for 885 nm and 808 nm wavelength laser diodes pumping the laser at 30 Hz.

Table 5-5 summarises the energy performance for 808 nm and 885 nm pumping. The performance is comparable for the time duration between 30 and 60 seconds.

	808 nm laser diodes, 38°C	885 nm laser diodes, 36°C
Average energy (30-60 s)	109.4 mJ	106.0 mJ
Energy standard deviation (30-60 s)	3.2 mJ	2.4 mJ

Table 5-5: Summary of laser output energy for the firing period 30 to 60 s.

Beam intensity patterns were captured while firing the laser at 30 Hz pulse repetition frequency using 808 nm and 885 nm wavelength pump laser diodes. The graph in Figure 5-42 shows the size of the near-field beam intensity pattern, over a duration of 60 s while pumped at 808 nm and 885 nm wavelength. The beam size is measured in the standard way by the diameter of the circle which contains 90% of the total energy on the camera array. The circle is centred on the beam centroid position. This was the D_{EPSA} (Encircled Power Smallest Aperture Diameter) measurement using BeamGage software.

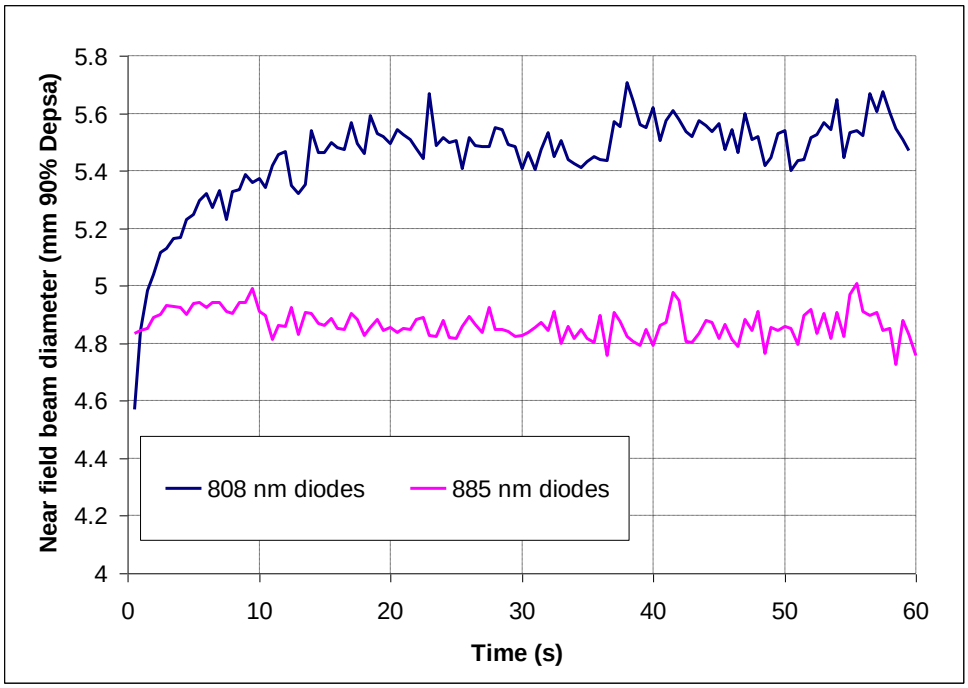

Figure 5-42: Variation of the near-field beam size over a duration of 60 s, while pumped at 808 nm and 885 nm wavelengths.

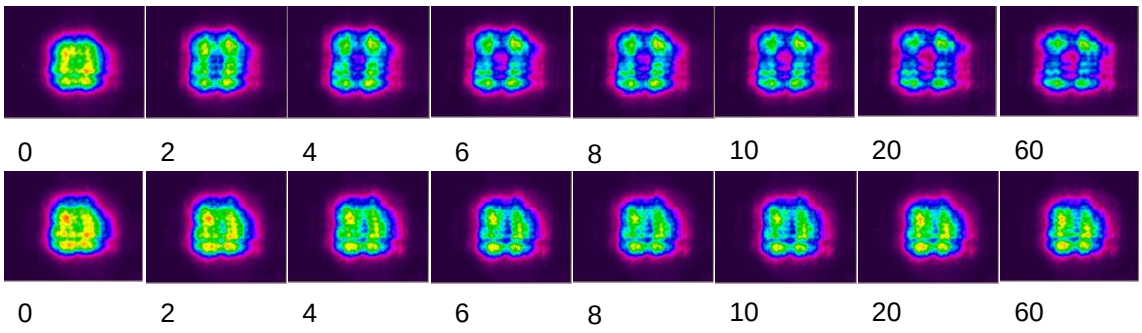

Figure 5-43: Near-field beam intensity patterns of laser pumped using 808 nm laser diodes (top) and 885 nm laser diodes (bottom).

It is desirable for the beam to remain a constant size during the firing duration. It can be seen that there is an increase in near-field beam size from approximately 4.6 mm to approximately 5.5 mm diameter when pumped at 808 nm at 30 Hz pulse repetition rate. In contrast, when pumped at 885 nm, the near-field beam intensity pattern remains a constant size of 4.9 mm.

The reason for the change in near-field beam size, while pumping at 808 nm rather than 885 nm, is the increased aberrations in the slab due to the larger thermal load. It can be seen that the first pulse, when pumped at 808 nm, has a near-field intensity image with comparable diameter to the first pulse when pumped at 885 nm. This is an expected result, as the thermal gradient is not present during the first laser pulse.

The graph in Figure 5-44 shows the variation of the laser divergence over a period of 60 seconds. The diameter was measured for the encircled 90% of the total energy, where the total energy was defined within an area of the camera array. This area was selected using a manual aperture which encompassed the largest beam image being measured. The BeamGage software “auto aperture” was also used. This technique is standard as a way of reducing the background noise to an acceptable level for an accurate beam size measurement.

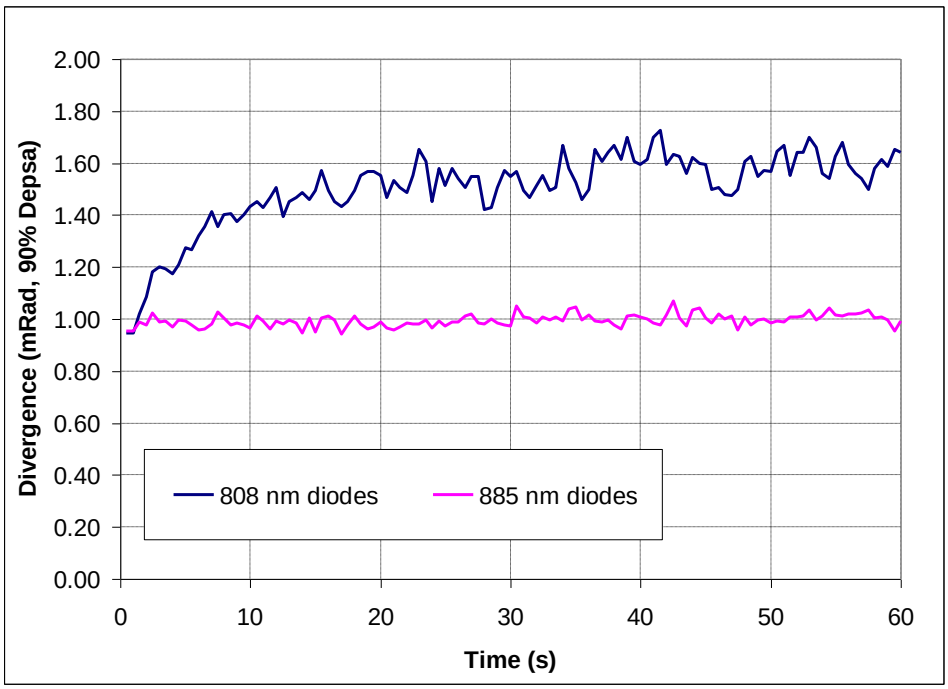

Figure 5-44: Variation of the divergence over a duration of 60 seconds, while pumped at 808 nm and 885 nm wavelengths.

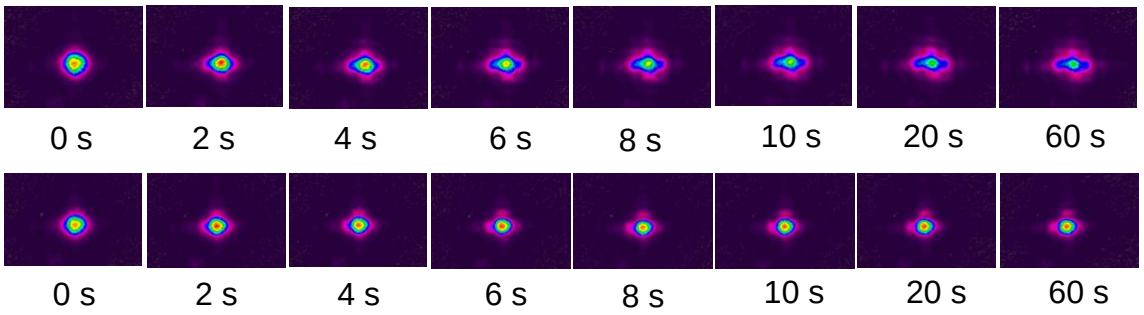

Figure 5-45: Far-field beam intensity patterns of laser pumped using 808 nm laser diodes (top) and 885 nm laser diodes (bottom).

As shown in Figure 5-44, with 885 nm pumping, the divergence is relatively unchanged during the 60 s firing duration, while a change in the far-field beam intensity pattern can be seen for 808 nm pumping. The average beam divergence is approximately 50% larger when pumped at 808 nm when compared with 885 nm, due to an increase in far-field beam size during the firing duration, when pumped at 808 nm. The 885 nm pumped laser divergence does not increase over the 60 s firing duration.

It can be seen that the near-field beam intensity pattern deteriorates from the first pulse over the 60 s duration. The 90% encircled area increases in size over this duration and a hole appears in the centre of the beam intensity pattern. However, the deterioration in the beam is much more severe when pumped at 808 nm, when compared with the 885 nm wavelength.

The far-field beam intensity pattern is shown to change over the 60 s duration. The degradation is more severe for 808 nm pumping, when compared with 885 nm pumping. The beam quality is calculated by taking the product of the near-field beam diameter and the full-angle divergence at the end of 60 s firing duration is shown in Table 5-6.

Beam parameter (measured after 60 s firing duration)	**808 nm pumping**	**885 nm pumping**
Near-field beam D_{EPSA} (mm)	5.5	4.9
Divergence, full-angle (mRad)	1.6	1.0
Beam Parameter Product (mm*mRad)	8.8	4.8
M^2	6.5	3.5

Table 5-6: Summary of beam sizes for 808 nm and 885 nm pumping.

The beam parameter product for 885 nm pumping is 56% of the 808 nm pumping value. This is a significant improvement, which could extend the functionality of a laser product, if 808 nm pumping was changed to 885 nm pumping.

5.4.6.5 Comparison of performance in the interferometer

A Fisba interferometer was used to measure the wavefront aberrations of a 632.8 nm wavelength beam after double passing through the Nd:YAG slab. The µShape software was used, which reports a wavefront radius of curvature based on an inbuilt curve fitting function. This was used to measure the focal power of the Nd:YAG slab while it was

pumped at a range of repetition rates for both 808 nm and 885 nm pumping. The results obtained were plotted in Figure 5-46 and Figure 5-47 respectively.

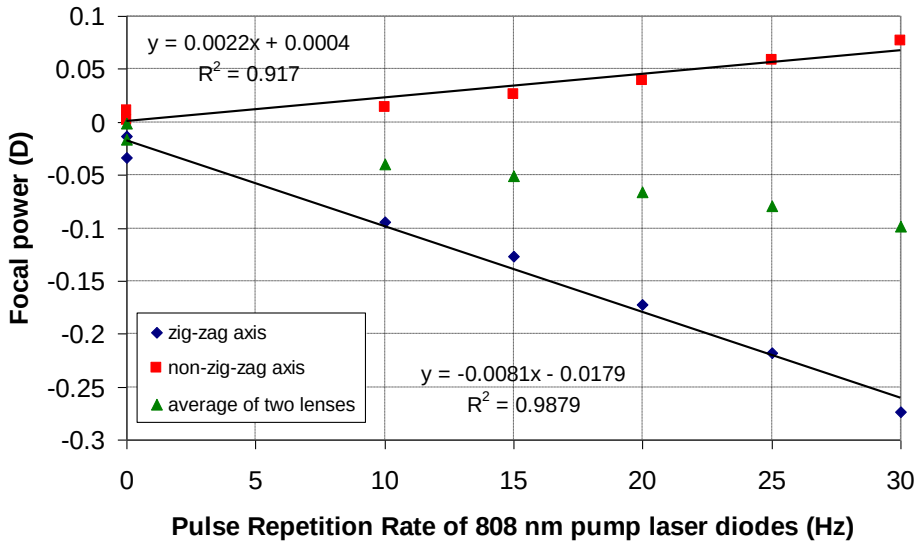

Figure 5-46: Thermal lens focal power in each axis for a slab pumped at 808 nm wavelength.

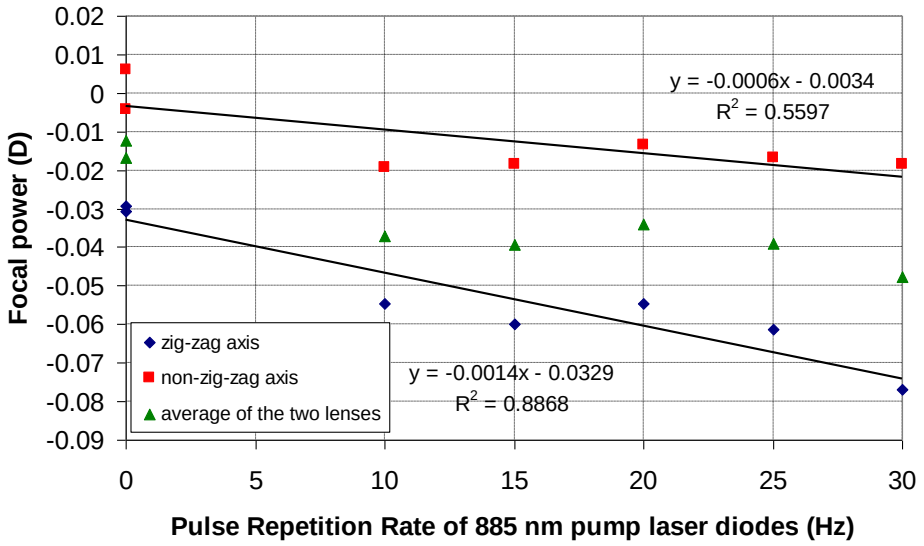

Figure 5-47: Thermal lens focal power in each axis for a slab pumped at 885 nm wavelength.

It would be expected that an increase in repetition rate would produce a proportional increase in the slab thermal lens. Therefore, a linear fit has been drawn for each axis, but the fit is poor for these data points. In the 808 nm pumping case, a quadratic function fits much better (R^2 = 99.97% opposed to 98.79%). Figure 5-46 and Figure 5-47 show that 808 nm pumping produces significantly more thermal lensing power than 885 nm pumping in both axes. The thermal lens in the non-zig-zag axis for 885 nm is of the opposite polarity to the 808 nm pumping case. It is however a small value, so will only have a small effect on a propagating beam. In both figures, the average power of the two lenses is shown as the net lens, which acts on a circulating mode in the resonator.

5.4.6.6 Comparison of Experimental results with modelled predictions

As stated in Section 5.4.6.3, the pump spectrum, approximated with a Gaussian lineshape, and the absorption spectra for Nd:YAG with 1.1% doping were used to calculate the total absorption in the laser slab for the two pumping wavelengths. A ray tracing program written by a colleague at Selex ES was used to model the ray paths from all the laser diode emitters which pass through the laser slab. The antireflection and highly reflecting dielectric coatings on the slab allow for efficient double-pass of the pump light. Some of the unabsorbed light after the second pass is then reflected by the metalwork of the diode stacks. The average physical ray path length of 13 mm was calculated, assuming that pump light incident on the ground top and bottom surfaces of the laser slab did not contribute to gain. This value of average path length was then used with the calculated value for the absorption coefficient to calculate the effective absorption of the pump light in the laser slab. The calculated percentages of pump light absorbed were 99.8% for 808 nm and 62.8% for 885 nm.

The COMSOL Multiphysics model and the Matlab beam tracing model, both referred to in section 5.2.5, were used to calculate the thermal lens produced by both 808 nm pumping and 885 nm pumping. The magnitude of the heat load was calculated for each pumping wavelength using Equation 2.1 in section 2.3 in Chapter 2. The calculated heat loads and the magnitude of the thermal lens based on the dn/dT effect are shown for lasing and non-lasing conditions for 808 nm and 885 nm pumping in Table 5-7.

Pumping wavelength	Lasing	Absorption coefficient (cm^-1)	Heat load (W)	Modelled Power x (Dioptres)	Modelled Power y (Dioptres)	Modelled Power ave (Dioptres)	Measured Power x (Dioptres)	Measured Power y (Dioptres)	Measured Power ave (Dioptres)
808	y	4.7	4.867	-0.090	0.077	-0.007			
808	n	4.7	5.046	-0.093	0.080	-0.007	-0.273	0.077	-0.098
885	y	0.76	2.378	-0.023	0.036	0.006			
885	n	0.76	2.541	-0.025	0.038	0.006	-0.077	-0.019	-0.048

Table 5-7: Summary of modelled and measured slab lenses.

The heat load calculated for 808 nm pumping is approximately twice the heat load calculated for 885 nm pumping, with the difference in the lasing and non-lasing cases only changing the values by 3% (808 nm) and 6% (885 nm). The thermal lens focal powers predicted for 808 nm pumping are of the same polarity as the measured values, where x is the zig-zag slab axis and y is the non-zig-zag axis. The lens power predicted in the x-axis was approximately a third of the measured value. The y-axis prediction was within 4% of the measured value. For 885 nm pumping, the modelled thermal lens in the x-axis was approximately a third of the measured value, as with 808 nm pumping. In the y-axis the modelled thermal lens was the opposite polarity of the measured value. The measured value was however a relatively weak lens compared with the other values (approximately a quarter of the power of other measurements).

5.4.6.7 Discussion

As discussed in Section 5.4.2.2, there is a miss-match between the standard pump length, which is used here, and the bounce length of the laser mode. This leads to the negative lens in the zig-zag slab axis. The measured thermal lens for both 808 nm and 885 nm pumping are stronger than the modelled values. This could in part be attributed to the laser diode slow axis intensity distribution, which is assumed to be a flat top distribution in the model. This means that there could be a discrepancy between the modelled and measured "edge effects", which are known to alter the performance from that of an ideal (infinite) zig-zag geometry slab [3, 4]. The cooling of the slab is also important in determining the edge effects. The model for the cooling does not take into account the thermal resistance of the adhesive layer. Only its thermal conductivity is modelled, which is the best case assuming that the adhesive has perfect contact with the slab and the mount. The improvement in the negative thermal lensing was less than

predicted by the model. The influence of stress induced index variation on thermal lens, which is not included in the model may be one reason for the discrepancy.

Due to the reduced quantum defect for 885 nm pumping when compared with 808 nm pumping and also the increase in pumping efficiency from 95% to 100%, the calculated heat load is approximately halved. This in turn, coupled with the change in the pattern of absorbed heat, reduces the calculated thermal lens produced in the slab.

The downside of using 885 nm pumping is the lower absorption coefficient (0.76 cm^{-1} compared with 4.7 cm^{-1}, for 885 nm and 808 nm pumping respectively). This means that a higher proportion of the pump energy is unabsorbed in the laser slab, and ends up elsewhere inside the laser chassis. It is unknown whether this pump light is likely to cause any issues due to heating in any other part of the laser system. In addition, the reduced absorption coefficient will reduce the wall plug efficiency of the laser system. To increase the absorption coefficient, the linewidth of the laser diode array could be reduced by better matching the individual bars and stacks, or by using external cavity laser diodes with Bragg gratings to lock the wavelengths to a more precise value. Other methods to compensate for the lower pump absorption efficiency might include increased interaction length, or increased Nd doping of the YAG [10]. It is however noted that for pulsed laser systems, increased Nd doping increases the effect of concentration quenching rapidly reducing the effective upper state lifetime of the laser medium.

5.5 CONCLUSIONS

The laser parameters were assessed against the thermal lens measurements taken for a range of slab assemblies used in the laser. There was not a clear correlation between any of the laser parameters and the average slab lens measured. However, slab assemblies with larger average focal powers tend to have a larger near-field beam diameter, a larger standard deviation / mean value and a smaller percentage transmission through a 4.35 mm aperture. It is expected that the trend would be clearer if a larger sample of slab assemblies with a greater range of average thermal lens focal powers was investigated. Other aberrations, besides average lens focal power in the laser slab, will contribute to the degradation of laser performance and should also be considered. The presence of other aberrations may have prevented a clear trend between the average lens focal power and laser performance. The repeatability in the alignment of the laser diode pump with the slab assembly may have also contributed to this. The uncertainty in diode position along the slab length was ±0.5 mm both in the resonator and in the Fisba interferometer set-up.

The differences in the aberrations of the optics in the simplified resonator and the Type A laser resonators are sufficient to prevent a clear correlation between the performance in each case. This is partly because the simplified resonator has fewer optics, but also due to variation in quality of the optics. Therefore, the simplified resonator was deemed ineffective for screening of slab assemblies.

The effect of thermally-induced birefringence was eliminated as the mechanism of near-field beam intensity pattern degradation. Therefore, the cause of poor near-field beam intensity pattern is the additional wavefront error that is produced by the thermal load in the laser slab.

The thermal model of the slab predicts that the current laser diode pump and slab geometry are not ideal as a negative lens is produced in the zig-zag axis, which is stronger than the positive lens in the non-zig-zag axis. The length of the pumped region was investigated experimentally and the thermal lens produced was in good agreement with the model. For future designs it is recommended that the length of the pumped region is designed in order to reduce this mismatch by using the thermal model. In this way, the near-field beam intensity pattern growth of over 10%, which is observed when using the standard length of pumped region, should be reduced to zero.

Other methods to reduce the net average lens and therefore improve the near-field beam intensity pattern were tested. The off-set pumped region method did show some promise as a simple short-term solution for poor near-field beam intensity pattern. However, it has been discovered that the boresight stability of the laser can be adversely affected as a consequence of the change in design. Therefore, it is recommended that this effect is further investigated before this potential solution is considered for implementation.

It has been shown that a fixed lens can be used to compensate for the negative net average lens, which is present to some degree in all slab assemblies, and can successfully improve the near-field beam intensity pattern. This solution is however limited to a range of operation, beyond which the compensation optic will be ineffective.

It was demonstrated that 885 nm pumping instead of 808 nm pumping, reduced the average thermal lens from -0.1 D to -0.05 D, due to the reduction in heat load from 4.9 to 2.4 W. This in turn produced an improvement in the laser beam quality M^2 value from 6.5 to 3.5. In addition, the divergence growth seen with 808 nm pumping over 60 s duration was eliminated. If the reduced wall-plug efficiency associated with a 20% increase in laser diode current can be accepted, then the improvements in beam quality advocate the change in laser diode wavelength.

5.6 RECOMMENDATIONS

5.6.1 Strategic objectives

The recommended long-term approach to reduce the net thermal lens is to match the length of the pumped region to an integer number of bounce lengths in the slab. To achieve this, the best solution is to reduce the length of the pumped region of the slab by reducing the size of each laser diode stack. If the average net thermal lens over a range of slab assemblies was zero, then the variation in thermal lenses would have less impact on laser performance. This solution would make the design more tolerant to a range of heat loads and not just the current heat load. Therefore, the pulse repetition frequency or output energy could be scaled to increase capability, without a significant detrimental effect to critical parameters such as beam diameter and divergence. The other potential solutions identified and tested in this report are recommended as short-term solutions if time to implementation is important or if they are deemed more cost-effective.

5.6.2 Root cause of laser failures to be identified

The root cause of laser failures due to near-field beam intensity pattern changes during the firing period is not identified. Work is continuing to find the root cause. Further investigation into the slab bonding process is being carried out. It is recommended that better identification of the slabs is implemented so that slab information from the supplier, such as position of the slab in the boule, or axis cut direction, can be linked with laser performance. This would also make reuse of slabs after failure in a laser more feasible, increasing yield hence reducing scrappage losses.

5.6.3 Improvements to the slab thermal model

The slab thermal model only deals with the effect of dn/dT, on the transmitted wavefront. In addition to this effect, stress will also change the value of refractive index. Thermal distortion of the slab shape will also have an effect on the transmitted

wavefront, but this effect has been shown to be negligible. Stress-induced birefringence effects are not modelled, but have been shown experimentally to be negligible. It is recommended that the computer model is developed to include the stress-induced refractive index gradient along with the thermally-induced refractive index gradient, both of which can be exported by the COMSOL software.

5.6.4 Near-field beam intensity pattern measurements

The long-term solution to the problems identified for measuring the near-field beam diameter of a variable shaped beam, which may have a hole in the centre, is to use a new version of the BeamGage beam profiling software. This software has an option to measure the beam size by percentage of energy contained within an aperture, using the analysis tool in the software, which would increase the efficiency over taking these measurements manually using the current LBA software.

5.6.5 Further testing of pumped region length optimisation

It is predicted that the optimum length of laser diode pump requires a pumped region of between 45.3 mm and 53.3 mm, based on the investigation in which the pump length was varied by moving the laser diode stacks and altering the number of stacks. To further prove this idea, a mask could be placed between the laser diodes and the slab which blocks a small amount of pump light to reduce the length of the pumped region. This presents risk, as laser diode light can be reflected back into the emitters. In addition, heating of the mask at the edges that block the laser diode light, will heat the slab and may skew the results. A thermally insulating backing to the mask would reduce this potential problem.

5.6.6 885 nm wavelength pump laser diodes

The use of 885 nm wavelength pump laser diodes has been shown to improve beam quality to 56% of its original M^2 value (when the identical laser was pumped at 808 nm)

in a targeting laser type resonator. This significant improvement in beam quality comes at a price, as the 885 nm diodes have to run 20% harder in order to compensate for the relatively low absorption at this wavelength. However the system efficiency could be improved by further development of the laser diodes by the supplier, to reduce the linewidth of their output. This would improve the absorption of the 885 nm pump by the Nd:YAG laser crystal.

Other pumping schemes have been investigated at Selex ES outwith this thesis, to produce a design which is less sensitive to the temperature of the pump diodes. This is achieved by increasing the pump length so that changes to the pump wavelength, and therefore the absorption coefficient, can be tolerated with minimal drop in output energy. This pumping arrangement is recommended for use with 885 nm pumping, in which the absorption coefficient is lower than with traditional 808 nm pumping.

5.6.7 Adaptive optics for compensation of slab aberrations

An approach to reducing the effect of thermal aberrations in the slab is to compensate for them. This has been investigated by using an intracavity spherical lens. The results were positive at current pump levels. However, for increased repetition rate operation, the limitations of this approach were evident. The increased thermal load was no longer compensated for and the near-field beam intensity pattern began to degrade.

An adaptive optic could be used to compensate for aberrations in the resonator. The advantage of an adaptive optic is that its shape can be changed at the same time as the aberrations change in the resonator, as the thermal load develops in the slab. Another advantage is that the same adaptive optic can be used to compensate for many slabs (and other optical elements), which have a variation of aberrations due to differing passive aberrations and inconsistencies in the slab bonding process. Also, higher order aberrations other than simple lensing can also be compensated for.

In Chapter 6, the use of an intracavity adaptive optic will be discussed, and the optimisation of the brightness of a laser resonator using a feedback loop, will be investigated. If the brightness is improved, then some of the wavefront aberrations detrimental to beam quality will be compensated for. It is expected that the near-field beam intensity pattern issues observed in this Chapter should also be improved. An

alternative approach to improving the near-field beam intensity pattern using an adaptive optic is to measure the wavefront using a wavefront sensor and adjust the mirror shape accordingly. It is clear that the take-up of adaptive optic technology within current targeting laser design will require a significant change to design and that the technology will need thorough robustness testing. However, the potential performance improvements should be investigated to allow an assessment of the cost to be made.

5.7 APPENDICES

5.7.1 Appendix 1: Thermal time constant of a slab

Equation 5.1 from paper [3] is used to calculate the thermal time constant (τ)

$$\tau = \frac{c\,\rho}{k}\left(\frac{t}{\pi}\right)^2 \qquad (5.1)$$

where:

t = the thickness in the y direction (cm)

k = the thermal conductivity ($W.cm^{-1}.k^{-1}$)

C = the specific heat ($J.g^{-1}.k^{-1}$)

ρ = the mass density ($g.cm^{-3}$)

Using the values [2] in Table 5-8, τ is calculated to be 0.5 s.

Parameter	value
C	0.59 $J.g^{-1}.k^{-1}$
ρ	4.56 $g.cm^{-3}$
k	0.14 $W.cm^{-1}.k^{-1}$
t	0.5 cm

Table 5-8: Table of values used to calculate the thermal time constant of an Nd:YAG slab.

5.8 REFERENCES

[1] V. Lupei, G. Aka, and D. Vivien, *"Quasi-three-level 946 nm CW laser emission of Nd:YAG under direct pumping at 885 nm into the emitting level"* Optics Communications, vol. 204, pp. 399-405 (2002)

[2] W. Koechner, "*Solid-State Laser Engineering",* Springer New York (2006)

[3] J. Eggleston, T. Kane, K. Kuhn, J. Unternahrer, and R. Byer, *"The slab geometry laser-Part I: Theory",* IEEE J. of Quantum Electronics, vol. 20, pp. 289-301 (1984)

[4] T. Kane, J. Eggleston, and R. Byer, *"The slab geometry laser-II: Thermal effects in a finite slab"* IEEE J. of Quantum Electronics, vol. 21, pp. 1195-1210 (1985)

[5] T. Y. Fan, *"Heat generation in Nd:YAG and Yb:YAG"* IEEE J. of Quantum Electronics, vol. 29, pp. 1457-1459 (1993)

[6] *COMSOL Multiphysics webpage*, "www.comsol.com/"

[7] *Armstrong Optical website*, "http://www.armstrongoptical.co.uk/"

[8] T. Kane, R. Eckardt, and R. Byer, *"Reduced thermal focusing and birefringence in zig-zag slab geometry crystalline lasers"* IEEE J. of Quantum Electronics, vol. 19, pp. 1351-1354 (1983)

[9] R. Lavi and S. Jackel, *"Thermally Boosted Pumping of Neodymium Lasers",* Applied Optics, vol. 39, pp. 3093-3098 (2000)

[10] N. Pavel, V. Lupei, J. Saikawa, T. Taira, and H. Kan, *"Neodymium concentration dependence of 0.94-, 1.06- and 1.34-μm laser emission and of heating effects under 809- and 885-nm diode laser pumping of Nd:YAG"* Applied Physics B: Lasers and Optics, vol. 82, pp. 599-605 (2006)

CHAPTER 6. INTRACAVITY ADAPTIVE OPTICS FOR IMPROVED LASER BRIGHTNESS

In this Chapter the use of an adaptive optic to compensate for aberrations inside a laser resonator is explored. An optimisation routine is utilised to achieve an optimised mirror shape which maximises the transmission of the laser beam through an aperture positioned at the focal plane of a parabolic mirror. This results in the divergence being minimised (without sacrificing output energy), in turn maximising the brightness. Results are presented while using the deformable mirror in both a plane-plane and a cross Porro prism laser resonator.

6.1 INTRODUCTION

The addition of an adaptive optic inside a diode-pumped Nd:YAG slab laser resonator to compensate for aberrations and optimise its performance, has been investigated [1]. As the aberrations for an individual laser resonator depend upon the optical finish of the optical elements used, the pump profile in the laser medium, and the thermal performance of the interface of the slab with its mount, the compensation of aberrations using a fixed optic is only possible where these factors are predictable. The compensation of intracavity aberrations by the use of an adaptive optic does not rely on such assumptions. In addition, it is possible that the transient laser resonator performance can be improved, so that the first laser pulses at turn on are not compromised due to the fact that the steady state thermal lens is not formed (with the resonator being optimised for steady state operation) [2]. It is not clear that the benefit would be significant in current Selex ES production laser designs, where a maximum pulse repetition frequency of 20 Hz is required. However, for future designs, with greater average power demands, hence increased thermal lensing, the benefit would be greater. An adaptive optic would allow operation over a greater average power range.

Selex ES was the end-user partner during an adaptive optic collaborative project, tasked with providing target specifications for an adaptive mirror device and carrying out the testing of the resulting deformable mirror device. During the TSB funded project

"Intracavity adaptive optics (INCAO)", one of the partners, BAE Systems, produced two Bimorph Mirror (BM) samples.

The two Bimorph Mirrors were incorporated into two laser resonator designs to determine the potential performance gains that could be realised.

6.1.1 Bimorph mirror samples

Two deformable bimorph mirrors were available for testing, which were both designed for the purpose of compensation with a Q-switched Nd:YAG laser. They were both packaged in a case designed to fit into a standard 25 mm diameter optomechanical mount and the actuators were addressed using a flexible ribbon cable, as shown in Figure 6-1.

Figure 6-1: Photographs of Bimorph Mirror samples.

In both cases, electrodes were deposited on a sandwich structure containing a piezoelectric substrate. The application of a voltage to the individually addressable electrodes forces the piezoelectric material to change shape, distorting the shape of the whole sandwich structure. The two mirrors used different top layer materials, which had differing flexibility and affected the maximum curvatures of the mirrors. Dielectric coatings were deposited on the top surface, providing high reflectivity (>99.5%) at the laser wavelength of 1064 nm. The electrode patterns of the two mirrors are shown in Figure 6-2.

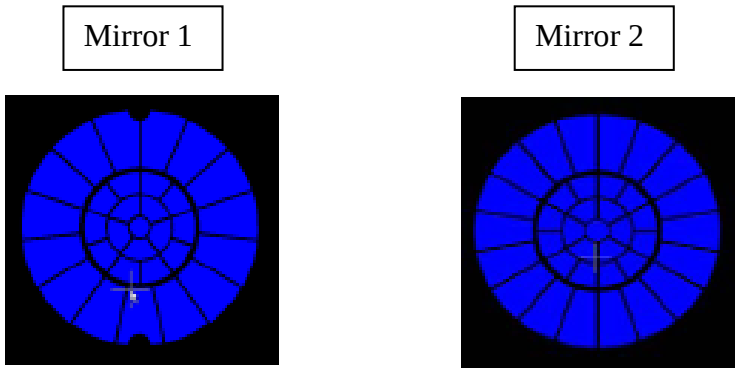

Figure 6-2: Electrode patterns of the deformable bimorph mirrors (mirror 1 with 31 actuators, mirror 2 with 37 actuators)

Bimorph Mirrors 1 and 2 had 31 and 37 actuators, respectively. This provided 5 fold symmetry for mirror 1 compared with 6 fold symmetry for mirror 2. For both mirrors the active region comprises the central electrode plus the inner two rings, which are within a diameter of 7 mm. This is matched to the nominally 5 mm square beam size expected for the Nd:YAG slab laser. The outer ring of electrodes is within a diameter of 18 mm. These provide tip-tilt control of the mirror surface at the edge of the active area. In addition this outer ring separates the physical edge of the mirror from the central active area, ensuring that edge effects do not degrade the performance of the deformable mirror.

The curvature range for each BM was measured in a phase-stepping interferometer, supplied by Zygo, by applying the maximum reverse and forward voltages in turn to all the actuators simultaneously, in effect producing a concave or convex spherical (to first order) surface respectively. The two mirrors have different curvature ranges primarily due to the top layer materials that were used in each case. The curvature measurements were made over the central 7 mm diameter of each mirror (the active area). The Bimorph Mirrors suffered from hysteresis of the piezoelectric material, meaning that the mirror shape was dependent on the previous voltages applied to the piezoelectric actuators. To compensate for this affect, the Bimorph Mirror control program has a routine, which is called every time new actuator voltages are applied, that quickly oscillates all the actuator voltages to produce a consistent starting point from which to move from. This adds a fraction of a second to the time taken to request a mirror shape,

but was not considered an issue for the intended use, where the laser repetition rate is 20 Hz.

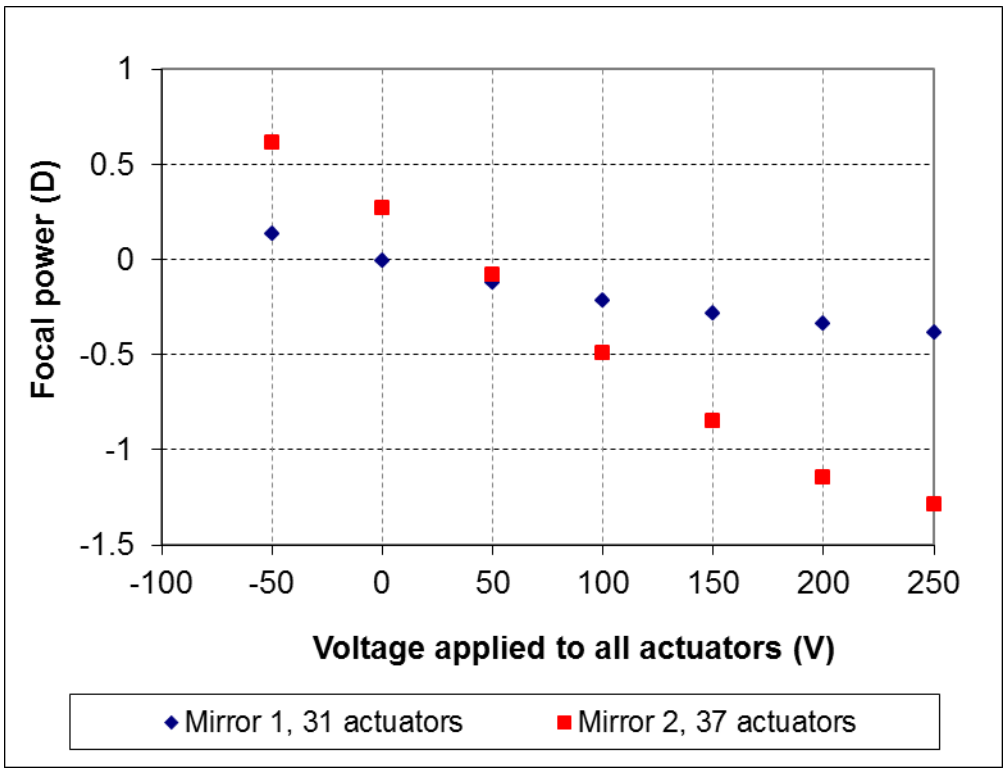

Figure 6-3: Spherical focal power of the Bimorph Mirrors as a function of the actuator voltages.

For both mirrors the focal power was approximately linearly proportional to the applied voltage, with differing actuator voltages required to flatten the two bimorph mirrors (approximately 0V and 45V for mirrors 1 and 2 respectively). When the spherical focal power was zero, there were components of opposite cylindrical lensing in the x and y axes. Therefore, further adjustments of the actuator voltages were required to produce flat surfaces, which were carried out by trial and error.

Both mirrors provided more convex than concave curvature over the permitted voltage range. The maximum curvature for mirror 2 was much greater than for mirror 1, for both the maximum convex and concave cases (mirror 1 focal power range +0.13 D to -0.39 D, mirror 2 range +0.61 D to -1.29 D).

Higher curvature allows for the compensation of stronger lensing effects in a laser (predominantly thermally induced) or aberrations of higher spatial frequency. The requirement of the Bimorph mirror flexibility was unknown at this stage.

Separate measurements, which were performed by one of the collaboration partners, confirmed the high damage threshold of both of the Bimorph Mirrors. They have operated reliably in an Nd:YAG laser generating 1.2 kW of average power at incident energy densities of 6 $J.cm^{-2}$, with the actual damage threshold being at least a factor of 5 greater. This was greater than the specification supplied by Selex ES (5 $J.cm^{-2}$).

6.1.2 Testing of the bimorph mirrors in an intracavity arrangement

In Chapter 5, the effect of thermal lensing in the Nd:YAG slab on the near-field intensity pattern was shown to be an issue. In this Chapter, the ability to address the thermal lensing issue in order to improve the beam quality produced by the laser resonator is investigated. Simple resonator design can alleviate the effects of the unaberrated spherical component of the thermal lensing [3]. This was demonstrated in Chapter 5, Section 5.4.1, when a spherical lens was introduced inside a laser resonator to compensate for some of the thermal aberrations when in steady state operation. However, the non-spherical aberrations remain uncorrected, and these scale significantly with increasing power. Detailed knowledge of the thermally induced distortions can allow an appropriate phaseplate to be manufactured and incorporated as an intracavity component. However, this is not an ideal solution for laser manufacture due to the delays introduced, and in addition, the correction provided is at a fixed operating condition only, and will become less effective if changes occur e.g. lifeing of the pump diode power with time.

The two Bimorph Mirror samples were integrated inside laser resonators and the performance improvement that they provided was compared. Two types of laser resonator were used in this investigation. In the first place, for simplicity, the BMs were used as the back mirror of a plane-plane resonator, to allow the improvement in the resonator performance to be analysed. Then the adaptive optics were used inside a cross Porro prism resonator, which is the type used in laser systems manufactured at Selex ES. The main difference in the resonator designs was the resultant thermal lens produced when the laser slab was pumped. In the case of the cross Porro prism

resonator, the laser beam was folded through the diagonal line of symmetry through the square beam intensity pattern, which had the effect of averaging the thermal lenses produced in the x and y axes, as described in Chapter 5, Section 5.2.1. In the plane-plane resonator, where no folding was present the thermal lenses in the x and y-axis were not equal, and therefore a different divergence in the x and y axes was expected.

A Shack-Hartmann wavefront sensor was considered to provide active feedback, but was discounted on the grounds of complexity and cost. Another problem that was envisaged with using a wavefront sensor was that the surface shape of the Bimorph Mirrors could not be accurately predicted given the voltages applied to the actuators. Therefore, an iterative algorithm would be required in order to optimise the mirror shape to produce a plane intracavity wavefront. This means that this method loses any advantage of speed over other methods that use an iterative algorithm but do not require a wavefront sensor for optimisation.

6.2 PERFORMANCE IMPROVEMENT OF A PLANE-PLANE RESONATOR WHEN USING AN INTRACAVITY ADAPTIVE OPTIC

A plane-plane resonator has a near plane wavefront travelling through it, which becomes distorted primarily when passing through the thermal lens produced in the laser gain medium, and also by the other optical elements which can introduce wavefront aberrations. The change from a plane wavefront produces an increased beam divergence and a reduced beam quality. This is thought to be related to the number of transverse resonator modes that are supported. The introduction of a Bimorph Mirror into the resonator provides a mechanism for control of the resonator stability for these modes, and therefore has the potential to improve beam quality.

6.2.1 Experimental set-up of a plane-plane laser resonator with brightness measurement feedback

The experimental set-up is detailed in Figure 6-4.

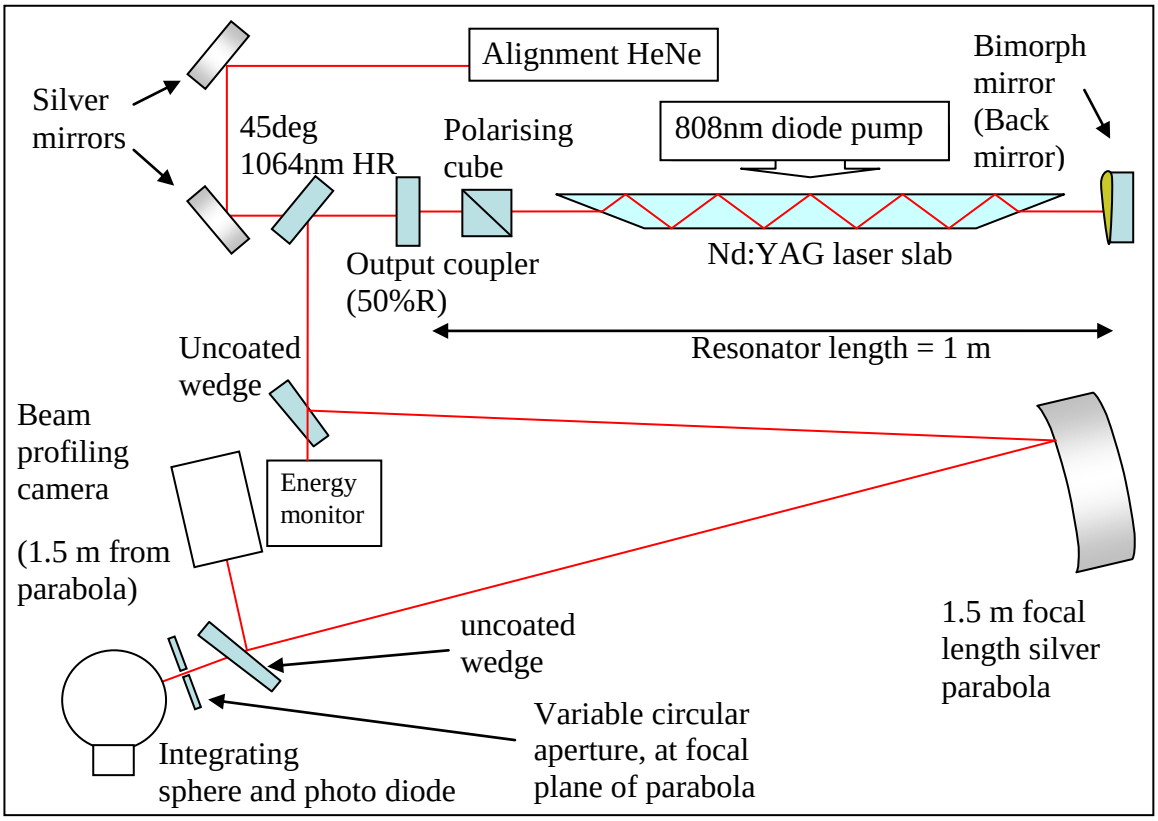

Figure 6-4: Plane-plane resonator: experimental arrangement including feedback loop.

The pump head consisted of an array of five quasi-CW diode stacks with a pulse repetition frequency of 20 Hz side-pumping a 5 mm square cross-section Nd:YAG isosceles trapezoidal shaped slab (standard doping concentration of 1.1%). This is a standard Nd:YAG slab and pumping regime, as used in the previous Chapters. A similar slab mount was used, which the slab was bonded to along its entire back surface (opposite the pumped surface). The fine detail of the temperature gradient in the slab when pumped, which was not measured here, could account for a difference in performance to the previously measured slabs (see Chapter 5). The transmitted wavefront error for the unpumped Nd:YAG was measured using a phase-stepping interferometer, as was used to measure the performance of the Bimorph Mirrors previously. The single-pass transmitted wavefront profile using a 4 mm square mask is

shown in Figure 6-5, and the measurements of the wavefront radius of curvature were 23.1 m and 5.7 m in the x and y axes respectively (0.043 D and 0.18 D focusing power).

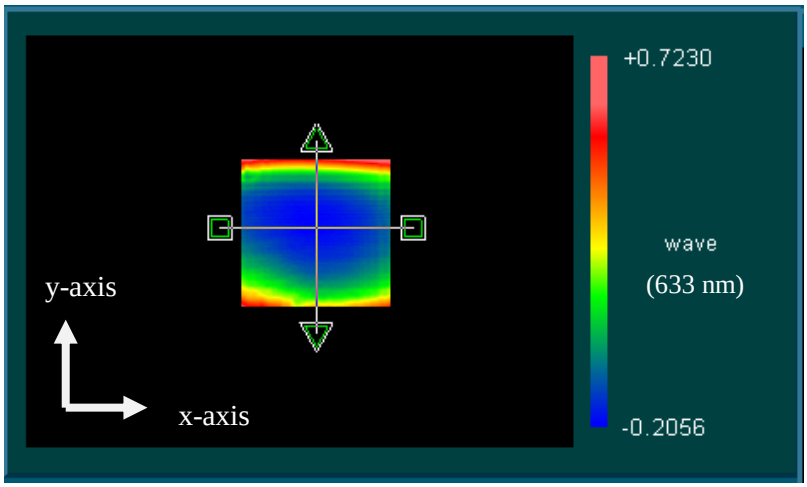

Figure 6-5: Interferometer measurement of the unpumped Nd:YAG slab.

In Chapter 5, section 5.4.2, the transmitted wavefront profiles for a sample of 47 pumped slab assemblies were measured. The average thermal lens was measured to be -0.135 D in the zig-zag axis and 0.032 D in the non-zig-zag axis, and these axes are equivalent to the x and y axes shown in Figure 6-5 respectively. These thermal lens measurements are assumed to be representative and are added to the measured passive focal powers to produce the resultant total Nd:YAG slab lens powers of 0.040 D in the x-axis and 0.075 D in the y-axis. By assuming that there were no significant aberrations in the other resonator optical elements, it was predicted that an improvement to performance would be seen if the mirror shape was convex in both axes, and approximately twice as strong in the y-axis (-0.02 D in the x-axis and -0.04 D in the y-axis).

A pair of plane mirrors were symmetrically arranged about the Nd:YAG slab to give a resonator length of 1 m (output mirror reflectivity 50%). The resonator has a polarising beam splitter cube to ensure linearly polarised output (since the slab end faces are coated to support operation in both s- and p-polarisations). An uncoated wedge was used to pick off a small percentage of the laser output, which was then directed onto a 1.5 m focal length parabola (the transmitted energy being simultaneously recorded by an energy meter). A variable size aperture was placed at the focal plane of the parabola (i.e. in the far-field). An integrating sphere placed behind this aperture captured all the

transmitted energy, which was subsequently measured on a silicon photodiode at the exit port of the integrating sphere. The transmitted energy through an aperture in the far-field is a direct measure of the brightness of the laser output beam, and it is the optimisation of this parameter that was of interest. The voltage from the photodiode was hence used as a fitness value for feedback to the bimorph mirror control program so that various mirror shapes could be assessed. A second wedge allowed the far-field beam intensity pattern to be simultaneously monitored on a silicon CCD camera connected to a beam profiling system. Using this set-up, any changes in output energy and far-field beam intensity pattern could be monitored, as the Bimorph Mirror surface shape was altered. All beam diameters (and hence divergence measurements) were calculated using a 90% of enclosed energy measurement in the LBA-PC beam profile software supplied by Spiricon.

Initially the plane-plane resonator was constructed using a standard high reflectivity dielectric back mirror. With the diode pump power available the maximum output energy measured was 171±4 mJ, in a beam with a divergence of 1.1 mrad (horizontal) by 1.87 mrad (vertical). Bimorph Mirror 1 was then substituted for the plane dielectric back mirror, and it was aligned while in a relatively flat shape. The shape of the mirror was then optimised to produce the maximum fitness, i.e. the highest brightness, using a simplex (or gradient descent) type algorithm called the Nelder-Mead algorithm [4, 5]. Given the relatively low repetition rate of the laser (20 Hz), the random shot-to-shot variations in the laser output, and the relatively high number of variables (31 or 37 actuators for the mirrors being tested), this class of algorithm was considered appropriate. A fixed starting mirror shape is not required when using this algorithm. Instead the algorithm starts using random values for all the actuator voltages. Therefore it is less likely that the initial guess for a starting mirror shape will cause the algorithm to optimise to a local, rather than the desired global, maximum. Each iteration of the algorithm changes the voltage values on all the actuators to a new random value simultaneously. Given that the actuators do not behave completely independently of each other, together with the requirement for any changes to be greater than the random shot-to-shot variations, it was considered that the fastest optimisation is likely to be achieved by altering all of the actuator voltages at each iteration, rather than by altering them independently. Typical optimisation run times are approximately ten minutes, however it should be noted that the feedback loop was not optimised for high speed operation. The control software ran on a standard laptop which also controlled other parts of the system hence impacting the data rates, and the algorithm and mirror control

code was not optimised for speed. An alternative algorithm (simple random search) was also tested; in this case only a single randomly selected actuator voltage was altered per iteration. The amount altered was also random and the cases were either accepted or denied, depending on the fitness value measured. As with the Nelder-Mead algorithm, an average of four pulses was used to account for noise when measuring the fitness value. The simple random search algorithm was allowed to run for a laser firing during of ten minutes, but no steady-state optimised solution was found in this case. Therefore, further work was carried out using the Nelder-Mead algorithm only.

6.2.2 Aperture size optimisation

The far field beam intensity patterns in Figure 6-6, show the result of optimisations of Bimorph mirror 1 using a range of aperture diameters.

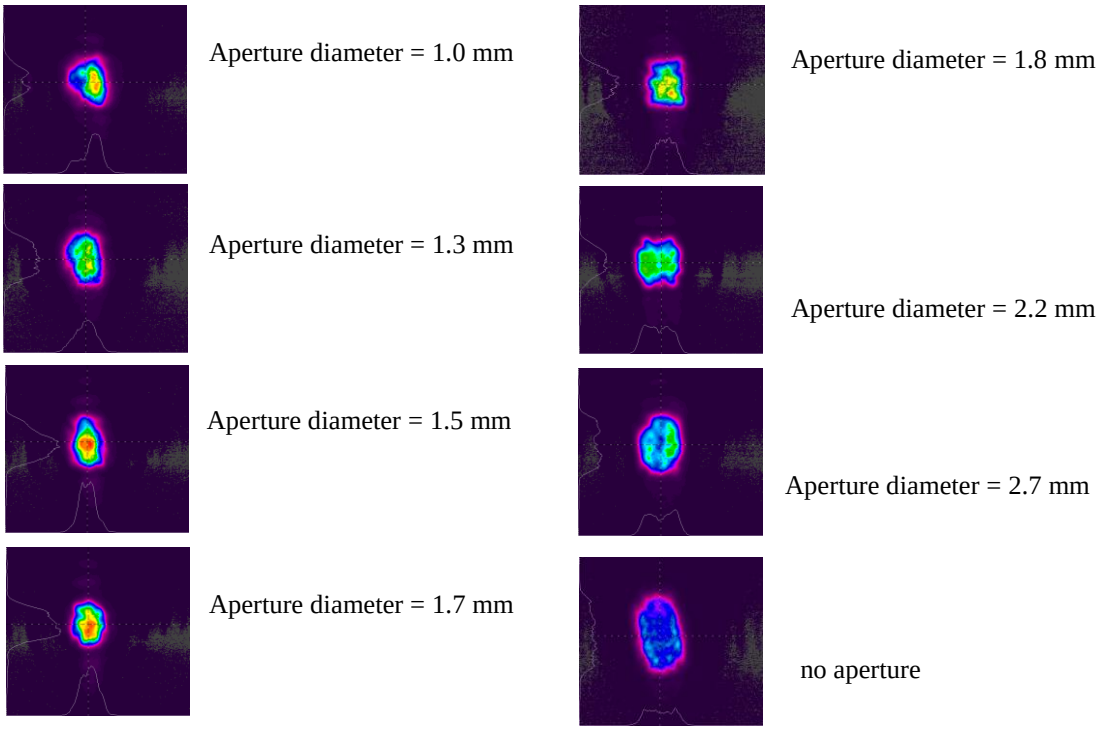

Figure 6-6: Far field beam intensity patterns resulting from a range of aperture sizes.

A figure for the laser brightness was calculated by dividing the pulse energy in Joules by the solid angle of the laser beam in Steradians. A factor of two was also applied

under the assumption that the far-field laser intensity pattern could be approximated to a Gaussian profile, which has twice the peak amplitude of a flat-top profile. The graph in Figure 6-7 shows the brightness enhancement for a range of aperture sizes used for the optimisation of Bimorph Mirror 1.

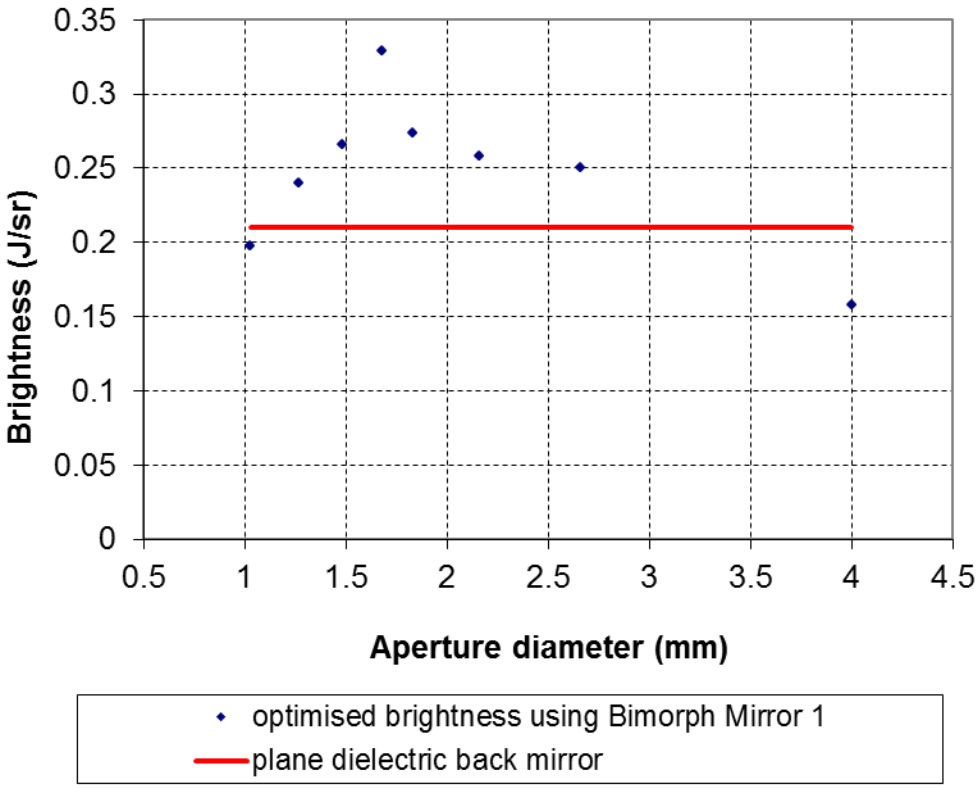

Figure 6-7: Relationship of brightness of the plane-plane resonator and aperture size.

In each case, the Nd:YAG slab and the optomechanical supports and mount for the slab were allowed to cool before the beam intensity patterns were captured. The case of no aperture is shown on the graph as an aperture diameter of 4 mm, although in reality it was >10 mm. An optimum aperture size of 1.7 mm produced the largest brightness enhancement factor of approximately 1.6, as shown in Figure 6-7. In the case where no aperture was used, the brightness was actually slightly degraded when compared with the plane dielectric back mirror. This is not surprising as the pulse energy was optimised in this case, rather than a measurement of the brightness.

6.2.3 Repeatability of optimisation of mirror 1

The aperture size of 1.7 mm was used and the optimisation routine was repeated three times to assess the variation and the results achieved while using mirror 1 are summarised in Table 6-1. The results shown are calculated for the average of 20 laser pulses in steady-state operation (after 30 s) and the standard deviation used to show the uncertainty in the measurements due to pulse to pulse variations.

	Energy (±4% mJ)	**Horizontal divergence (±10% mrad)**	**Vertical divergence (±4% mrad)**	**Brightness (±17% J.sr^{-1})**
Planar dielectric mirror	171	1.10	1.87	0.21
Run 1	159	1.01	1.42	0.28
Run 2	132	1.04	1.49	0.22
Run 3	145	0.99	1.47	0.25
Run 1 values re-tested after laser had cooled down	155	1.21	1.33	0.24

Table 6-1: Plane-plane resonator output: bimorph mirror 1 in comparison with a planar mirror.

A brightness enhancement of a factor approximately 1.2 is obtained in comparison with the plane mirror (taking the average of the measured optimised brightness numbers). The decrease in beam divergence is offset by a drop in energy, limiting the overall brightness increase. It should be noted that during the 10 minutes required for optimisation the temperature of the Nd:YAG zigzag slab increases by more than 15°C despite being bonded to a stainless steel heatsink. If allowed to cool down and then operated with the deformable mirror in its previously optimised shape, the beam intensity pattern typically appears more symmetrical, but not necessarily as bright.

6.2.4 Repeatability of optimisation of mirror 2

The equivalent results obtained using mirror 2 instead are summarised in Table 6-2.

	Energy (±4% mJ)	**Horizontal divergence (±9% mrad)**	**Vertical divergence (±11% mrad)**	**Brightness (±24% J.sr^{-1})**
Planar dielectric mirror	171	1.10	1.87	0.21
Run 1	112	0.91	1.12	0.28
Run 2	125	1.41	1.08	0.21
Run 3	129	0.99	1.03	0.32
Run 1 values re-tested after laser had cooled down	109	1.17	1.25	0.19

Table 6-2: Plane-plane resonator output: bimorph mirror 2 in comparison with a planar mirror.

In this case a greater reduction in beam divergence was achieved (particularly for the vertical divergence component where >40% reduction in the average divergence was achieved). However there was little brightness enhancement due to an associated marked drop in output energy (typically in excess of 30%); the maximum enhancement was a factor of 1.5 for one of the optimisations (run 3), whereas in one case no enhancement was observed (run 2), and indeed a 10% drop was found when the laser was first left to cool. Compared to mirror 1 the spread in results is much larger, implying poorer repeatability. In fact repeatability is an issue in general with this laser due to the inherent instability of the plane-plane resonator. The typical far-field beam intensity patterns for the Nd:YAG laser, when optimised using mirrors 1 and 2, are shown in Figure 6-8.

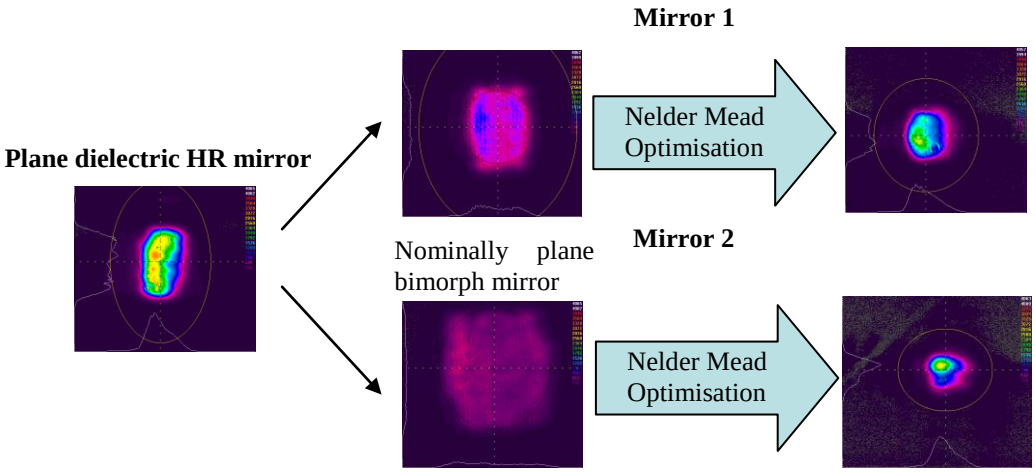

Figure 6-8: Deformable bimorph mirrors in the plane-plane resonator: changes to the far-field beam intensity pattern with optimisation.

It is clear that the optimised far-field intensity patterns are more symmetrical with a smaller diameter than the unoptimised case using a plane dielectric mirror. The corresponding change to the near-field beam intensity pattern when using mirror 1 is shown in Figure 6-9.

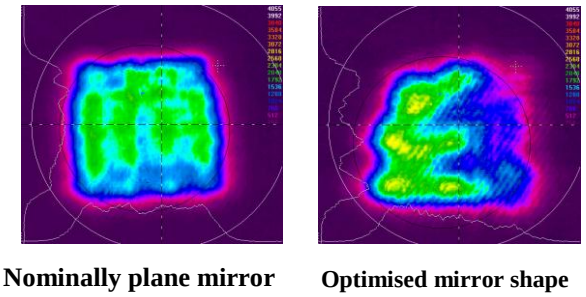

Figure 6-9: Typical near-field beam intensity pattern produced by the plane-plane resonator with an incorporated bimorph mirror.

In the case of the nominally plane bimorph mirror, the near-field beam intensity pattern is close to a square with a dimension of approximately 4.5 mm, as expected given the 5 mm square cross-section of the slab, which is the limiting aperture in the resonator. In the optimised case some redistribution of the optical intensity is evident, but the overall beam size is largely unchanged. The reason that the intensity distribution is less symmetrical is unclear, but it is not expected to be biased towards the pumped face of the slab where the gain is higher as the laser mode is folded inside slab to average this effect. Therefore the far-field optimisation does not significantly impact the overlap of the lasing mode with the pumped volume in the slab.

The optimised shapes of the two bimorph mirrors were analysed using the Zygo phase-stepping interferometer and are shown in Figure 6-10. The measurements were masked to a diameter of 7 mm, which corresponds to active area of the bimorph mirrors and the region which the laser beam was incident upon. MetroPro analysis software was used and the tilt component was removed before analysing the results.

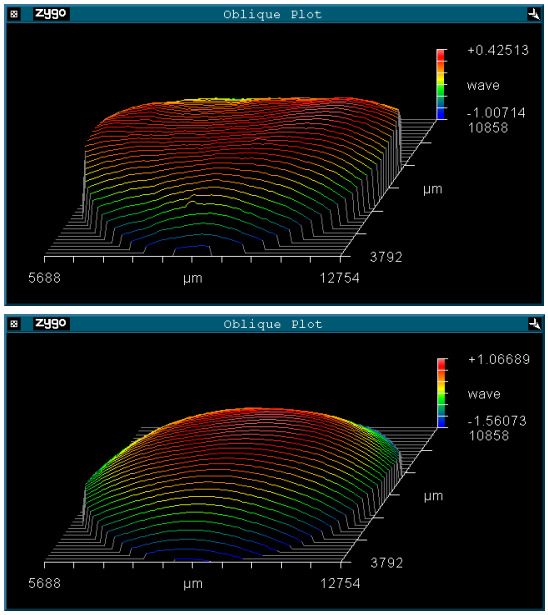

Optimised shape of mirror 1.

Radius of curvature (x-axis) = -26.6 m

Radius of curvature (y-axis) = -8.0 m

Optimised shape of mirror 2.

Radius of curvature (x-axis) = -7.9 m

Radius of curvature (y-axis) = -3.9 m

Figure 6-10: Comparison of the two optimised bimorph mirror shapes.

The resulting optimised mirror shapes of both mirrors are convex in both the x and y axes. The strongest radius of curvature listed equates to a focal power of approximately -0.5 D (for mirror 2). Neither mirror reached its maximum curvature range, implying that the maximum focusing power of both mirrors was sufficient for the optimisation of

the laser performance. They both show a higher focusing power in the y-axis than the x-axis, which corresponds to the non-zig-zag axis of the Nd:YAG slab. This is in line with the prediction made based on the total lens in the Nd:YAG slab. The focusing power of the optimised bimorph mirror shapes is however stronger than predicted (approximately 13 times in the worst case when using BM 2).

6.3 PERFORMANCE IMPROVEMENT OF A CROSS PORRO PRISM RESONATOR WHEN USING AN INTRACAVITY ADAPTIVE OPTIC

The cross Porro prism laser resonator, as discussed in previous Chapters, can be used in the place of a traditional plane-plane laser resonator to overcome some of the problems associated with thermally induced birefringence in the laser slab. This improvement is brought about because the beam intensity pattern is folded across its diagonal line of symmetry by the apex edges of the orthogonal Porro prisms. An additional benefit of this effect is that thermal lensing which occurs in the two axes (the non-zig-zag and zig-zag slab axes) is averaged out, so the lens focal power per round trip in each axis is equal. This in turn produces a more symmetrical far-field beam intensity pattern since the divergence is the same in both axes. The cross Porro prism resonator is more tolerant to angular misalignment than the plane-plane resonator. Misalignment is due to thermal and mechanical stresses in both the laser chassis and the resonator components. An optical path is always possible, due to the insensitivity of the Porro prisms to misalignment, in one axis each, which are set orthogonal to one another, and the resonator is therefore said to be “self-aligning”. The beam path axis will remain when the components are slightly misaligned and therefore no significant energy loss is experienced. This is in contrast to the classical plane-plane resonator, which is the most sensitive resonator type and is on the limit of the resonator stability diagram (Figure 2-7, Chapter 2). In this case, a small misalignment can have a significant effect on output energy.

As with the plane-plane resonator set-up, both Bimorph Mirrors were tested as an intracavity element. The experimental set-up is detailed in Figure 6-11. Note that the feedback loop used is identical to that used with the plane-plane resonator.

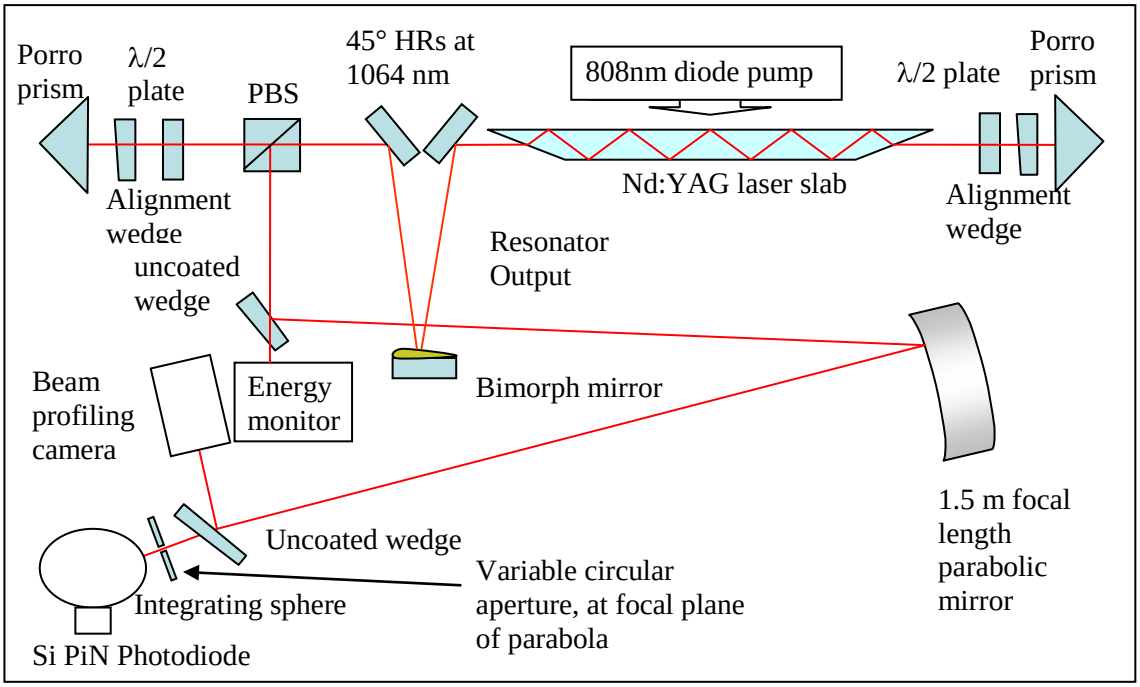

Figure 6-11: Cross Porro prism resonator: experimental arrangement with feedback loop.

The cross Porro prism resonator had a physical length of 1 m, identical to the plane-plane resonator in Figure 6-4. However in this case it was not possible to build the resonator symmetrically around the laser slab. The bimorph mirror was included in the cross Porro prism resonator by introducing an additional fold using two high reflecting dielectric mirrors. The angle of incidence of the laser mode on the bimorph mirror was approximately 14°. The dielectric coating on the bimorph was designed for plane incidence. However there was no evidence that the coating performance was significantly degraded operating away from normal incidence.

The output coupling reflectivity is adjusted for optimum output pulse energy exiting from the polarising beam splitter, and is typically approximately 50% in fixed-Q operation and approximately 70% in Q-switched operation. This is achieved by rotating the half waveplate (the one on the right hand side in Figure 6-11) through the appropriate angle in order to produce output coupling at the polarising beam splitter (PBS). The end surfaces of the Nd:YAG slab are coated to allow lasing with both s- and p-polarised light, with equal loss of approximately 2% per surface.

6.3.1 Aperture size optimisation

As with the plane-plane resonator, an investigation was carried out into the optimum aperture size for brightness enhancement. The following beam intensity patterns show the far-field beam intensity patterns for various aperture diameters.

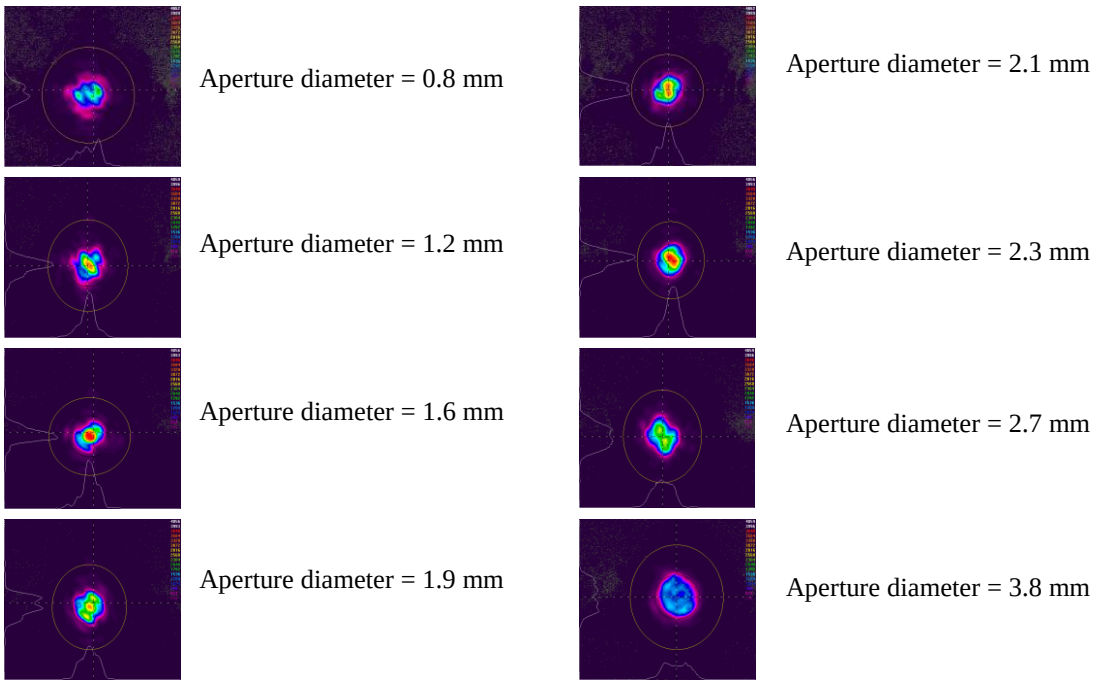

Figure 6-12: Far field beam intensity patterns for a range of aperture sizes.

These tests were carried out using Bimorph Mirror 2 because it provided a slightly better brightness enhancement in the best case, when used in the plane-plane resonator. The graph in Figure 6-13 shows the variation in brightness enhancement with aperture size.

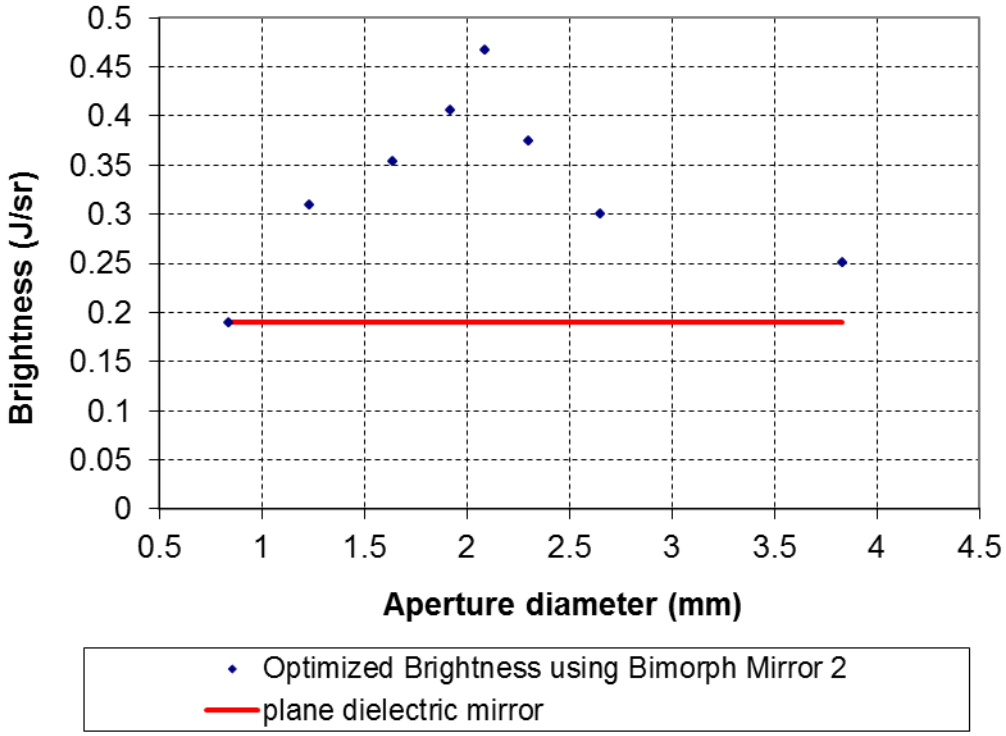

Figure 6-13: Relationship of brightness of the cross Porro prism resonator and aperture size.

The optimum aperture diameter was found to be 2.1 mm and was used for further testing of Bimorph Mirror 2.

The repeatability of the brightness optimisation using mirror 1 was tested and the results are summarised in Table 6-3. In this case the best results were achieved when the aperture was set to a diameter of 1.5 mm rather than 2.1 mm.

	Energy (±1% mJ)	Horizontal divergence (±3% mrad)	Vertical divergence (±4% mrad)	Brightness (±9% J.sr^{-1})
Plane dielectric mirror	156	1.38	1.53	0.19
Run 1	144	0.95	1.01	0.38
Run 2	142	0.99	1.03	0.35
Run 3	144	1.05	1.09	0.32
Run 1 values re-tested after laser had cooled down	145	0.90	0.99	0.41

Table 6-3: Cross Porro prism resonator output: bimorph mirror 1 in comparison with a plane mirror.

It is worth noting that the energy obtained with the planar dielectric mirror in the cross Porro prism resonator is reduced (typically by less than 10%) compared with the equivalent plane-plane resonator. This can be attributed principally to the greater number of surfaces inside the cross Porro prism resonator increasing the intracavity losses and hence decreasing the efficiency.

The pulse-to-pulse energy variation is significantly less than with the plane-plane resonator (standard deviation typically 1 mJ compared to 4 mJ). In general the laser performance variation between the separate optimisations is also less than with the plane-plane resonator (brightness value repeated to within 17% over three runs). The reduced performance variation is a result of the improved resonator stability of the cross Porro prism resonator design compared to the simple plane-plane resonator.

In this case an enhancement in brightness of approximately 1.9 was obtained (based on the average of the three optimisation results in Table 6-3), with a maximum enhancement factor of 2.2, and in the best case the far-field beam divergence is reduced from 1.46 mrad to 0.95 mrad. This corresponds to a reduction in the M^2 value from 4.8 to 3.2, when calculated using the Beam Parameter Product (BPP). It was noted that the divergence of the laser showed a variation, which was dependent on the temperature of the Nd:YAG slab. If the slab was left to cool and the laser operated with the mirror in its optimised shape a less divergent beam was produced (typical reduction 5% as in

Table 6-3), with no reduction in output energy; hence the brightness is further enhanced by approximately 10%.

As shown in Figure 6-13, for mirror 2, the optimum far-field aperture diameter was found to be 2.1 mm. The repeatability of the optimisation is shown in the results which are summarised in Table 6-4.

	Energy (±1% mJ)	**Horizontal divergence (±3% mrad)**	**Vertical divergence (±4% mrad)**	**Brightness (±9% J.sr^{-1})**
Plane dielectric mirror	156	1.38	1.53	0.19
Run 1	146	1.04	1.21	0.30
Run 2	146	1.04	1.19	0.30
Run 3	145	1.21	1.39	0.22
Run 1 (laser left to cool)	148	0.88	1.05	0.41

Table 6-4: Cross Porro prism resonator output: bimorph mirror 2 in comparison with a plane mirror.

The reduction in energy when the brightness is optimised is slightly less than with mirror 1 (approximately 6% compared with 10%). However, the decrease in beam divergence is also not as great, and the net effect is a decreased brightness enhancement; a factor of approximately 1.6 based on the average of the three optimisation runs in Table 6-4. The maximum enhancement was a factor of 2.2. As with mirror 1 the divergence was observed to be less when the slab was allowed to cool, but here this decrease was greater, typically being at least 10%. In the best case the far-field beam divergence is reduced from 1.46 mrad to 0.96 mrad. The M^2 value is reduced from 4.8 to a minimum of 3.2, as for Bimorph Mirror 1.

Based on these results the two Bimorph Mirrors gave approximately the same performance in the cross Porro prism resonator in terms of enhancing the brightness. The tabulated performance for the plane-plane and cross Porro prism resonators highlights clearly the smaller uncertainty in the brightness results for the cross Porro

prism resonator (standard deviation 9% versus approximately 20%). Both the energy and the beam divergence contribute to this reduction in standard deviation. This behaviour can be attributed to the improved stability of the cross Porro prism resonator design.

The far-field beam intensity patterns in Figure 6-14 show the effect of replacing the plane dielectric mirror with each of the two bimorph mirror designs, in the cross Porro prism resonator.

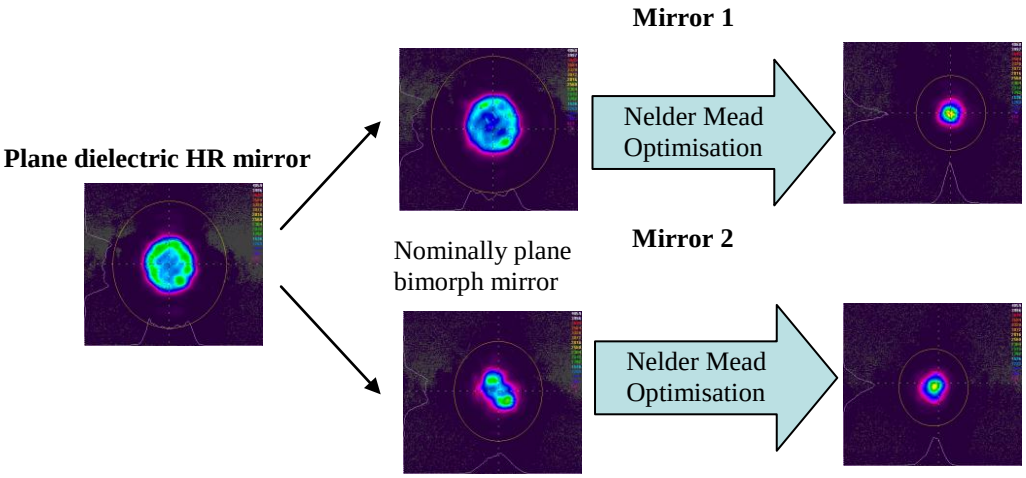

Figure 6-14: Comparison of far field beam intensity patterns produced by two bimorph mirror designs in the cross Porro prism resonator.

The far-field beam intensity patterns are shown for the plane dielectric mirror, the nominally plane BMs and for the optimised BM shapes. For both mirror designs the symmetry of the optimised beam intensity pattern and the divergence are an improvement to the beam intensity pattern recorded with a plane dielectric high reflector in the place of the bimorph mirrors. The reduction of the divergence when the deformable mirrors are optimised is clear. The corresponding change in near-field beam intensity pattern is shown in Figure 6-15.

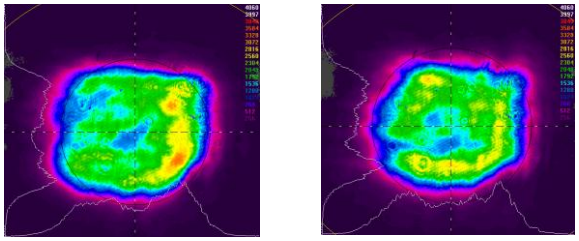

Nominally plane mirror **Optimised mirror shape**

Figure 6-15: Typical near-field beam intensity pattern produced by the cross Porro prism resonator with an incorporated bimorph mirror.

As with the plane-plane resonator set-up, the near-field beam diameter (approximately 4.5 mm) does not change significantly when the bimorph mirror shape is optimised for an improved brightness. In the optimised case some redistribution of the optical intensity is evident, although to a lesser extent than in the plane-plane resonator case, indicating that the far-field optimisation does not significantly impact the overlap of the lasing mode with the pumped volume in the slab. This helps to explain the lesser reduction of pulse energy, due to brightness optimisation, in the cross Porro prism resonator case. The optimised mirror shapes for both deformable mirrors were again measured in the Zygo phase-stepping interferometer and are shown in Figure 6-16.

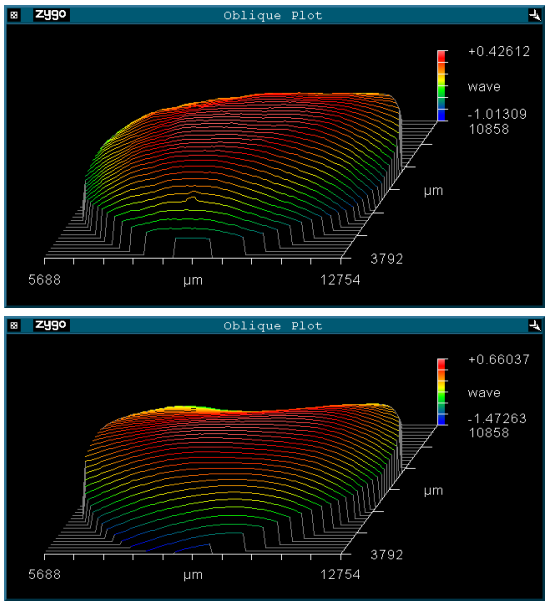

Optimised shape of mirror 1.

Radius of curvature (x-axis) = -10.7 m

Radius of curvature (y-axis) = -8.9 m

Optimised shape of mirror 2.

Radius of curvature (x-axis) = -11.6 m

Radius of curvature (y-axis) = -5.5 m

Figure 6-16: Comparison of the two optimised mirror shapes.

The resulting optimised mirror shapes of both the BMs are again convex, as for the plane-plane resonator and as predicted. As for the plane-plane resonator, the lens power is stronger in the y-axis than the x-axis. The strongest radius of curvature equates to a focal power of approximately -0.3 D (for mirror 2), which is approximately eight times the predicted value. The resulting focal power is a small fraction of the total focal power available from this mirror.

6.3.2 Long-term recall of optimised bimorph mirror shapes

The optimised Bimorph Mirror shapes were recalled after a period of time (of order five minutes) to allow the Nd:YAG slab to cool to ambient temperature. After this period of time, the mirror shape is assumed to be accurately recalled, which is confirmed by the brightness performance of the laser output. However, it was discovered that if the actuator voltage values were recalled the following day, in some cases, the far-field intensity pattern was no longer uniform and was markedly increased in size. To investigate the cause of this, Bimorph Mirror 2 was optimised and the shape measured using the Zygo phase-stepping interferometer a short time afterwards (within 60 minutes). The Bimorph Mirror shape was then remeasured the following day using the same actuator voltages. By subtracting the initial wavefront profile from the second day

wavefront profile, it was discovered that the predominant change overnight was a tilt. This was attributed to a drift in the ambient temperature overnight, and to the design of the Bimorph Mirrors, in which the edges of the deformable surface were not rigidly held in place to allow for expansion and contraction of the surface.

6.4 CONCLUSIONS

Two deformable bimorph mirrors have been tested in a high energy diode-pumped Nd:YAG slab laser resonator. The measured curvature range available with mirror 1 was from +0.13 D to -0.39 D, and with mirror 2 was from +0.61 D to -1.29 D, this difference in curvature range being attributed primarily to the different mirror surface materials used. These mirrors operated successfully in both a plane-plane resonator and a cross Porro prism resonator, in both cases using a resonator length of 1 m. The brightness was optimised in each case using a feedback loop to control and optimise the mirror shape.

In the plane-plane resonator the largest measured enhancement in brightness was a factor of 1.5 when mirror 2 was used. However repeatability of performance was a serious issue with this resonator (both with the bimorph mirrors and the plane dielectric mirror), and can be attributed primarily to the inherent instability of this resonator design.

In the inherently more stable cross Porro prism resonator repeatable performance was much more readily achieved. Both BMs produced brightness enhancements when compared with the plane dielectric mirror. The largest measured enhancement in brightness was a factor of 2.2 using BM 1. This equated to a reduction in the divergence from 1.46 mrad to 0.95 mrad, and a corresponding decrease in the M^2 parameter from 4.8 to 3.2. In this optimised configuration the maximum focal power of the bimorph mirror was measured to be approximately -0.2 D, which is not at the limit of curvature for either BM.

It was predicted that an improvement in the performance would be seen if the mirror shape was convex in both axes, and approximately twice as strong in the y-axis (-0.02 D in the x-axis and -0.04 D in the y-axis). It was the case that both BMs were convex when optimised in the plane-plane and the cross Porro prism resonator. The focal

power was stronger in the y-axis in every case as predicted. The focusing power of the BMs in the optimised shape was however stronger in every case than the predicted values and was approximately 13 times as strong in the worst case in the plane-plane resonator. This could be due to an underestimation of the thermal lens strength in the y-axis, an underestimation of the thermal lens strength in the x-axis, or a contribution to the intracavity aberrations from other optical elements, such as the plane dielectric mirrors or the alignment wedges in the cross Porro prism resonator. Another explanation is that the resultant wavefront, which provides the optimum laser brightness, is not plane.

One of the impediments for the use of adaptive optics inside laser resonators is the high cost of the devices. In this project the aim was to develop the Bimorph Mirror devices, which could be produced at low cost. It is not yet clear whether the cost is low enough to attract investment. The problem with using commercially available adaptive optic devices inside high energy lasers is the low damage threshold of the reflecting surface and also the mechanical robustness of the device which needs to be tolerant to an environment of vibration and large variation in operating temperature. The BMs tested are certainly resistant to laser damage up to required levels, but the tolerance to environmental conditions is largely untested thus far.

Incorporation of a Bimorph Mirror into an existing cross Porro prism resonator design is not straightforward and the additional folding of the resonator is not ideal. The use of the Bimorph mirror with a beam at an incidence of 45° for replacement of an existing fold optical element may simplify the design. This would require an alteration of the dielectric coating on the Bimorph Mirror and may require a change to the actuator pattern to increase its length in the horizontal axis. It will be easier to incorporate the bimorph mirrors in new laser designs, where this component can be included from the beginning of the design cycle.

6.5 RECOMMENDATIONS

Recommendations for further work include the use of a BM to predict the required shape of a fixed compensating optic for a particular laser resonator. This would require the measurement of the BM shape using an interferometer after the brightness was optimised. An alternative would be to use a wavefront sensor to measure the total aberrations in the laser resonator and then use this information to produce a fixed compensating optic under the assumption that a plane wavefront is optimum. It is unclear which method would produce better results.

Further testing over the full environmental range is required, and feedback to the device fabricator could allow more robust designs to be produced. The incorporation of a feedback loop into a fully productionised laser system using the internal energy meter with the introduction of an aperture placed at the focal plane of the focusing lens is recommended. This would provide the mechanism for laser brightness optimisation and would demonstrate the benefits in a real system, which could then be tested over the full environmental range. It would be interesting to see if parameters such as laser boresight and pulse energy could be maintained more consistently over the temperature range, with the use of the BM for optimisation.

A second type of deformable mirror, produced in collaboration with UWS and UKATC in a TSB funded project, was tested using the Zygo phase-stepping interferometer [6]. The research programme did not allow time for this mirror design to be integrated into a laser resonator for experimental testing of performance enhancement. However, a similar beam quality enhancement would be anticipated to that achieved using the Bimorph Mirrors. It is recommended that this device, which could potentially incorporate extension sensing technology, be incorporated into a cross Porro prism resonator and used to optimise brightness as was carried out using the BMs. The main advantage of the extension sensing is to minimise any hysteresis by actively monitoring the mirror surface shape. If the adaptive optic control program was not required to compensate for the hysteresis in the device, then the speed of brightness enhancement may be increased due to faster calling of the mirror shape. In addition, the algorithm used may find an optimum value more efficiently in the absence of hysteresis.

6.6 ACKNOWLEDGEMENTS

The work reported in this Chapter was supported by the Technical Strategy Board (TSB) contract CHBT/006/00049 entitled Intracavity Adaptive Optics (INCAO). The author is particularly grateful to Leslie Laycock and Mike Griffith of BAE Systems ATC (Great Baddow) for the loan of the deformable mirrors used in this work.

6.7 REFERENCES

[1] J. Beedell, I. Elder, and D. Hand, *"Performance of a deformable mirror in a high-energy Nd:YAG laser"* Proceedings of SPIE, vol. 7338, p. 733805 (2009)

[2] W. Lubeigt, M. Griffith, L. Laycock, and D. Burns, *"Reduction of the time-to-full-brightness in solid-state lasers using intra-cavity adaptive optics"* Optics Express, vol. 17, pp. 12057-12069 (2009)

[3] D. Burns, G. J. Valentine, W. Lubeigt, E. A. Bente, and A. I. Ferguson, *"Development of high-average power picosecond laser systems*" (Invited Paper) [4629-29], pp. 129-143 (2002)

[4] V. V. Nikulin and D. Zhang, *"Simplex-based wavefront control for the mitigation of dynamic distortions caused by atmospheric turbulence"* pp. 131-139 (2005)

[5] J. A. Nelder and R. Mead, *"A Simplex Method for Function Minimization"* Computer Journal, vol. 7, pp. 308-313 (1965)

[6] J. D. Beedell and I. Elder, *"EO AR121-01 Laser Technologies. WP1.1 Adaptive Optic Mirror Assessment: Final Report"*, Selex ES report no. AP50061035 (2012)

CHAPTER 7. COMMON RESONATOR INTRACAVITY OPO

Selex ES produces laser systems for targeting applications which incorporate an extracavity OPO to produce an eye-safe wavelength of 1573 nm, as discussed in Chapter 2. In this Chapter, an alternative design is investigated, which uses an intracavity OPO using a common resonator for the 1064 nm and 1573 nm wavelengths. This brings advantages of a common beam path for the two wavelengths over the full range of environmental conditions encountered, the possibility of a more compact design, and improved efficiency. The OPO M^2 value is found to be greater than that of the current extracavity OPO design by a factor of approximately two. A computer model was written to predict the pulseshapes and output energy of the intracavity OPO. There was good agreement in the output energy, but less so with the pulseshapes.

7.1 INTRODUCTION

As described in Chapter 2, current laser system designs use an extracavity OPO design based on potassium titanyl phosphate (KTP) in a noncritically-phasematched (NCPM) geometry to shift the 1064 nm wavelength to 1573 nm. The non-planar ring geometry is used as it is a perturbation insensitive design. A non-planar ring geometry is also used for some of the Nd:YAG lasers manufactured at Selex ES. If all of the optical components in the laser resonator were antireflection coated for 1573 nm as well as 1064 nm as is standard, then the KTP crystals could be introduced into the laser resonator, such that both wavelengths oscillate in the common resonator. With this design the output can be rapidly switched between 1064 nm and 1573 nm via electrical control of the intracavity polarisation states. In this Chapter this idea is investigated and the relative performance is compared with currently manufactured laser systems using separate resonator OPOs.

7.2 MOTIVATION

Current Selex ES target designation lasers in full production use an extracavity OPO geometry, which typically produce an optical-to-optical conversion efficiency of 35%. An extracavity OPO arrangement requires setting up of the common boresight of the two output wavelengths, which is susceptible to variation over the full operating environment. The common boresight of the two wavelengths over the full operating environment is a key parameter for an airborne targeting laser source switching between the two wavelengths. In the common resonator design, these outputs will have a common boresight due to the intracavity oscillating energy at each wavelength sharing a common resonator beam path, even if the movement of an optical element causes the shared beam path to change.

The efficiency of the OPO is dependent on the intensity of the pump (fundamental) beam. By using an intracavity geometry for the OPO the maximum pump intensity is available, thereby lowering the OPO threshold and enhancing conversion efficiency. Here the OPO acts as the output coupler for the pump laser.

This design reduces part count and complexity when compared to an extracavity OPO design. When comparing with a currently manufactured laser, which has an extracavity OPO, a reduction in optics of approximately 50% was calculated, which will bring an associated cost saving. Further cost saving may be realised due to a reduction in alignment stages that would be necessary to separately optimise laser and OPO outputs and to set up common boresight of the two wavelengths. A reduction in footprint of approximately 15% was calculated, when compared with a current compact laser resonator and extracavity OPO.

As well as the common resonator design, separate resonator designs have also been tested both intracavity and extracavity to increase understanding of the effects of resonator length, intracavity loss, pump intensity, and intracavity fundamental mode depletion on the performance. The intracavity and extracavity OPO resonators are essentially the same, using plane mirrors, except that with the intracavity design, part of the laser and OPO resonators overlap so that the KTP crystals are exposed to a higher pump intensity than they would be in an extracavity OPO design.

7.3 TYPICAL PERFORMANCE OF AN EXTRACAVITY NON-PLANAR RING KTP OPO.

The schematic diagram in Figure 7-1 shows the typical system level set-up for a laser system produced at Selex ES.

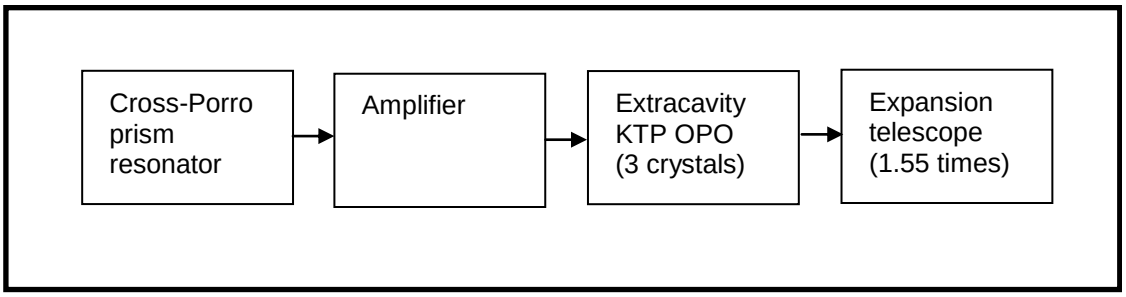

Figure 7-1: Schematic diagram of a typical production laser system.

The performance of a typical laser system (type B laser system), which incorporates an extracavity OPO, is summarised in Table 7-1, in order to allow assessment of the intracavity OPO being investigated. All beam size measurements are 90% encircled energy.

Parameter	Magnitude	Units	Measurement type
Pump pulse energy	300	mJ	
OPO pulse energy	113	mJ	
Conversion efficiency	38	%	
Pump near field beam diameter	~5	mm	
Pump divergence	980	µRad	camera measurement
OPO near field beam diameter	6.1	mm	camera measurement
OPO divergence	< 3.9	mRad	pinhole measurement
OPO Pulse width	16.3	ns	
OPO Beam Parameter Product	< 24	mm.mRad	
OPO M^2	< 12		
OPO physical resonator length	Approx. 200	mm	
OPO optical round trip length	Approx. 254	mm	
OPO diffractive length	Approx. 168	mm	

Table 7-1: Output parameters of a typical extracavity OPO and pump laser.

The OPO signal divergence of this laser system (1573 nm) is < 3.9 mRad, as measured using the transmission through a pinhole technique. The parameters in Table 7-1 provide a target specification for the common resonator, intracavity OPO.

7.4 COMMON RESONATOR INTRACAVITY OPO

7.4.1 Experimental set-up

Lasers and OPOs for use in fieldable systems where severe environmental conditions will be experienced require resonator designs that are insensitive to alignment perturbations. Resonator designs that are less sensitive to misalignments include a resonator using cross-Porro prisms and polarisation output coupling [1]. In a cross-Porro prism resonator the self-aligning feature of the Porro prisms is exploited in both

axes of the propagating beam by orienting the apex of each Porro prism orthogonally. This design is usually folded to reduce the footprint of the resonator using a corner cube, which also rotates the beam image by 180°. A cross-Porro prism resonator is essentially a ring resonator where the propagating beam is folded back on top of itself so that the laser slab is passed twice per round trip. Therefore a ring resonator that rotates the propagating beam by 90° will provide the same misalignment tolerance as a cross-Porro prism resonator with the same beam rotation. When any element is misaligned by a small amount, the resonator mode can always respond by making small changes in beam position and direction to find a new closed and aligned path [2].

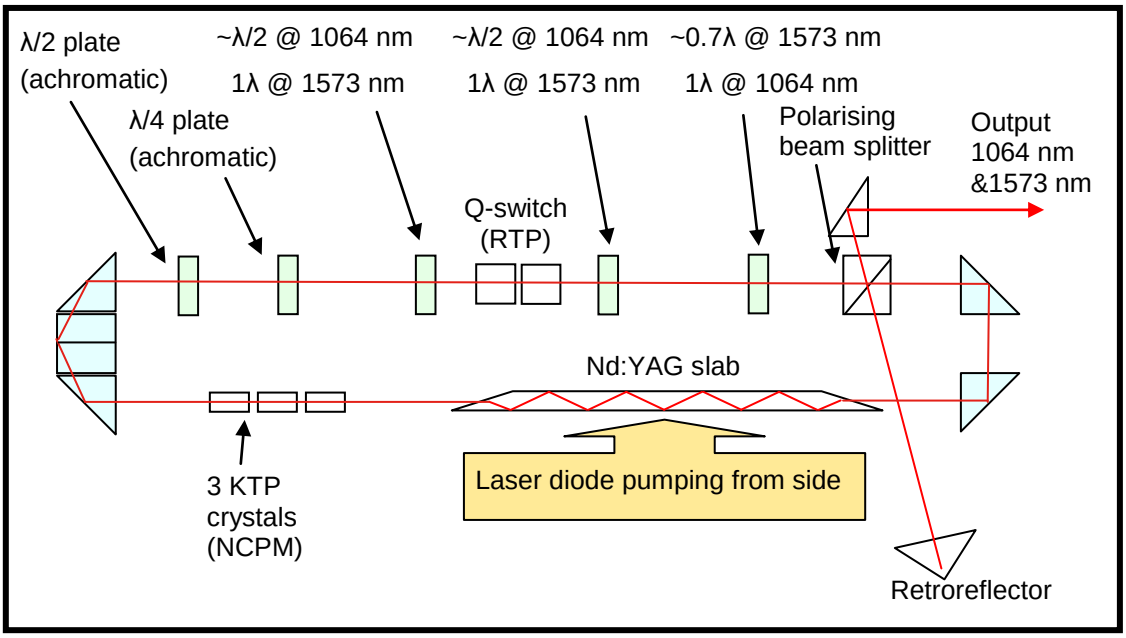

Figure 7-2: Common resonator, Nd:YAG laser and intracavity OPO, non-planar ring resonator.

In this investigation a breadboard ring resonator design, shown schematically in Figure 7-2, was used for the common resonator Nd:YAG laser and KTP OPO, using right-angle prisms to fold the beam path. Right-angle prisms were used in this proof of concept design due to their low cost and availability as commercial off-the-shelf broadband-antireflection-coated components. The transmission of light at 1064 nm and 1520 nm wavelengths was 98% per prism, which had broadband transmission coatings on the transmitting surfaces that covered the wavelengths of interest. The right hand side of the resonator used two right-angle prisms to fold the beam (acting as a folding

prism) whilst the left hand side of the resonator utilised three right-angle prisms to give 90° image rotation. The isosceles trapezoidal shaped laser slab acts like a dove prism to fold the mode in the horizontal plane, which ensures an even number of reflections as required for a perturbation insensitive resonator. The out of plane reflections, which result in the 90° rotation of the laser intensity profile, make the resonator resilient to small perturbations of the resonator optics. This also produces a more symmetrical output beam as the astigmatic thermal lens in the laser slab is averaged by this beam rotation.

The physical round trip length of this resonator was 832 mm, which was as short as possible while allowing flexibility for alignment and insertion of optics required for testing. All the optical components within the ring resonator were AR coated at both 1064 nm and 1573 nm wavelengths to allow both wavelengths to resonate. The only exception to this was the Nd:YAG laser slab which was uncoated on its end faces. The end faces of the slab were cut at 59° from the normal, to allow zig-zagging of the laser mode with a maximized fill factor and therefore pump extraction. The Nd:YAG slab, with a refractive index of 1.81 at 1573 nm has a Brewster's angle of 61.6°. Therefore almost all of the p-pol radiation is transmitted through the surface of the laser slab. In this resonator arrangement, only p-pol radiation is present, so loss at the ends of the slab is very low. A measurement of the uncoated slab 1573 nm transmission was found to be 86%. This loss can be attributed to absorption within the bulk material of the Nd:YAG crystal and is therefore unavoidable in this design. This is confirmed by one source [3] that presents Nd:YAG absorption data in the region of interest providing an absorption coefficient value of approximately 0.02 cm^{-1} for 1573 nm. This corresponds to 83% transmission along the zig-zag path in the Nd:YAG slab, which is comparable with the measured value of 86%.

The Nd:YAG slab had a square cross-section of 5 mm, and allowed nine bounces of the laser mode. The fill factor is optimized for the 1064 nm wavelength, but the change in fill factor for the 1573 nm wavelength is negligible. This was confirmed using the "Fresnel propagation model" written by David Legge in MathCAD, which was explained in Chapter 2. The program uses a chief ray finding routine and a ray trace which works out the resonator apertures. The Nd:YAG slab was pumped from one side using five laser diode stacks, which had a wavelength of approximately 808 nm, and each had dimensions 5 mm by 10 mm. The laser diodes were operated in a pulsed regime of 150 µs pulses at a pulse repetition rate (PRF) of 10 Hz. The repetition rate

was chosen so that the thermal lens in the slab was not significant and therefore any transient behaviour of the laser was reduced to simplify this initial investigation. A pump pulse energy of 675 mJ was produced for a diode drive current of 96 A. In all cases, the laser resonator was aligned to produce the optimum pulse energy at 1064 nm, without regard to the beam quality. Although this does not precisely mirror common practice during laser production at Selex ES, this method removes the subjectivity of laser alignment.

Three KTP crystals were inserted into the resonator after the Nd:YAG slab so that the 1064 nm laser output (OPO pump) and the 1573 nm OPO signal could follow the same path around the ring resonator. The KTP crystals had the dimensions, 9 mm square cross-section and 20 mm long. They were non-critically-phase-matched and therefore no walk-off of the 1064 nm and 1573 nm was introduced. This is a Type II interaction; therefore the 1573 nm radiation produced by the KTP crystals was of the same horizontal linear polarisation state as the 1064 nm pump incident at the crystals. The achromatic wave plates in the resonator were adjusted to ensure that the 1064 nm laser was in hold-off mode, while the Q-switch was off. The 1573 nm whole wave plates, which are approximately half wave at 1064 nm, were then used to rotate the 1064 nm polarisation by 45°, so that the RTP Q-switch would alter the polarisation when the voltage was applied. The 1573 nm polarisation state remained vertical, aligned to one of the axes of the RTP crystals and was therefore unaffected by the Q-switch. The 1064 nm whole wave plate was a 0.7λ wave plate at 1573 nm. A simple model was used to calculate that the range of 1573 nm output coupling achievable using this wave plate was 0 – 66% reflectivity. The output coupling of the 1064 nm mode remained maximised (for maximum OPO pump power density) and was unaffected by this wave plate. The 1573 nm output coupling was optimised for maximum 1573 nm output, but the final value was unknown. From an alignment point of view, the output coupling was used to reach a peak energy value and was insensitive to the wave plate angle in either direction.

The output coupled portion for both wavelengths was the s-pol light incident on the polarizing beam splitter and the percentage of this s-pol light was controlled using the Q-switch voltage for the 1064 nm mode. The retroreflector couples back the counter-propagating beam, which enhances the gain in the forward direction, selecting it preferentially for unidirectional operation.

In Figure 7-3, the common resonator intracavity OPO is shown schematically with the polarisation state for 1064 nm and 1573 nm wavelengths shown at various positions in the resonator. The output coupling polarising beam splitter defines the polarisation state for both wavelengths as being linear and horizontal in relation to the optical bench. The key to the polarisation states in Figure 7-3 is shown in Figure 7-4.

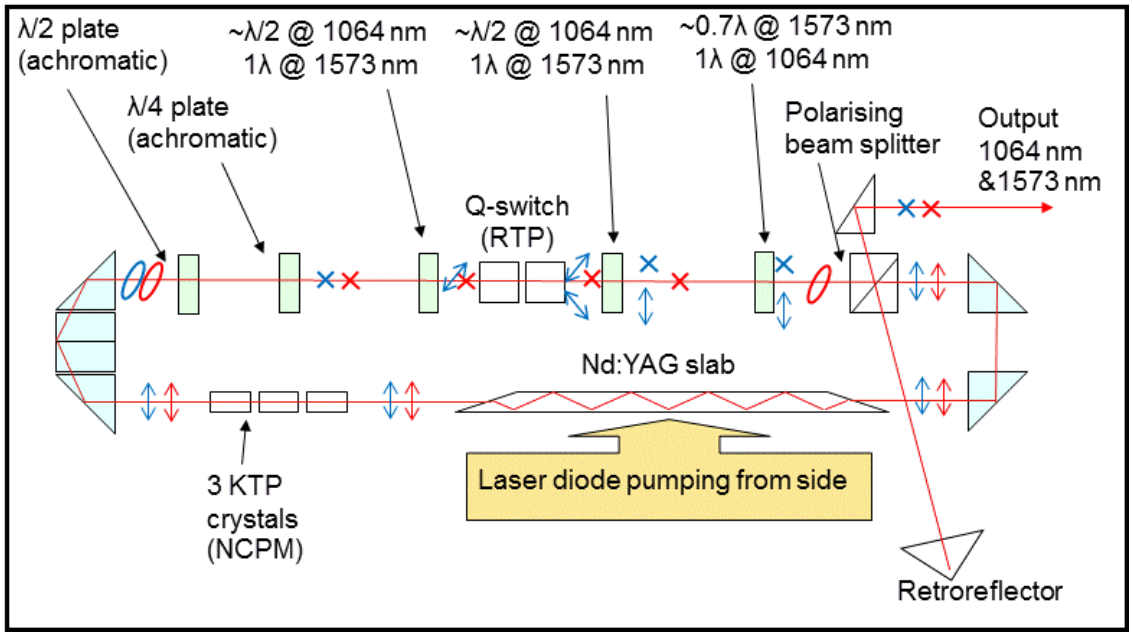

Figure 7-3: Layout of intracavity, common resonator, KTP OPO and Nd:YAG pump laser, with polarisation state for 1064 nm and 1573 nm wavelength shown at various positions in the resonator.

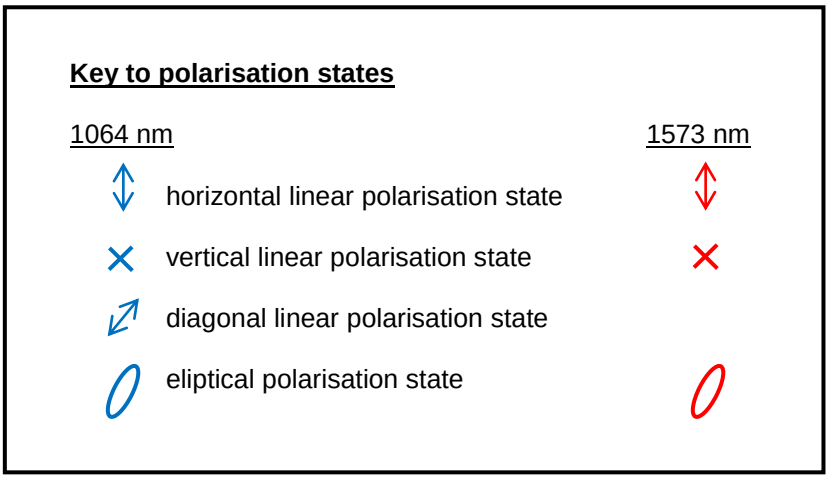

Figure 7-4: Key to polarisation states in Figure 2.

The polarisation state of the 1064 nm light is shown in red and the 1573 nm light in blue. Two alternative polarisation states are shown for 1064 nm light after the Q-switch depending on the voltage applied to the Q-switch (top 0 V and bottom half-wave voltage). The 1573 nm light only has one state after the Q-switch as the incident polarisation state is vertical and aligned to one of the RTP crystal axes, and is therefore unaffected by the Q-switch regardless of the voltage applied.

The length of the common resonator was measured and the optical round trip time and the diffractive length were both calculated using the values of refractive index at 1573 nm of all the optical elements shown in Table 7-2.

Optical element	**Material**	**refractive index**
Slab	Nd:YAG	1.818656
OPO crystal	KTP	1.73809
Q-switch	RTP	1.78
Turning prisms	BK7	1.50663
polarising beam splitter	Fused Silica	1.459

Table 7-2: Values for refractive indices of optical elements used to calculate non-physical resonator lengths.

The length of the common resonator was 832 mm physical length (chief ray path length, which zig-zags through the Nd:YAG slab), the calculated optical round trip length was 1017 mm and the diffractive length (or vacuum equivalent length) was 722 mm.

7.4.2 Sources of intracavity loss

In Table 7-3 the losses in the common resonator for both the 1064 nm and 1573 nm wavelengths are shown.

Intracavity Optic	Number of surfaces per round trip	Transmission at 1064nm	Transmission at 1573nm
uncoated Nd:YAG slab	2	1.00	0.86
RTP Q-switch	4	0.98	0.96
Output polarising cube (for resonated light)	2	1.00	0.99
waveplates	10	0.98	0.98
turning prisms	10	0.89	0.89
KTP crystals	6	0.99	0.99
Total per round-trip	**34**	**0.84**	**0.71**

Table 7-3: Measured losses in the common resonator for 1064 nm and 1573 nm

In this configuration, the greatest intracavity loss at 1573 nm was due to the loss in transmission through the Nd:YAG crystal. The loss at the surfaces of the slab were negligible. The loss was due to absorption in the Nd:YAG as was explained previously. Therefore, at a wavelength of 1573 nm, this loss is unavoidable in this resonator design. This absorption in the Nd:YAG leads to thermal lensing because the absorbed energy is dissipated as heat. However, this is put into perspective when you consider that the thermal lensing due to absorption of laser diode pump light is much greater

(approximately 6 times, see Appendix 1). In addition, at the 10 Hz repetition rate investigated, no significant effects due to thermal lensing have been observed for either the 1064 nm laser wavelength or 1573 nm OPO signal wavelength.

The second greatest intracavity loss at 1573 nm was due to the loss in transmission through the turning prisms (COTS 1050-1620 nm band AR coated N-BK7 20 mm right-angle prisms). The specification on the supplier website (Thorlabs) suggests that a loss of approximately 0.5% per prism should be expected, but in reality the loss was measured to be greater than 2% per prism at 1064 nm and 1520 nm. The opportunity to reduce this loss is discussed in the recommendations section.

Prelase problems were experienced with this design, but have been overcome by careful alignment and a stable output energy is thus achieved. The prelase was suspected to be the result of spurious reflections incident on the RTP Q-switch electrical terminals, which would cause heating and prevent the thermal expansion compensation between the crystal pair being effective. No optical damage has occurred in this design (even when prelase was present) and high efficiency is demonstrated.

7.4.3 Experimental Results

The pulse energy at 1064 nm and 1573 nm was recorded while the Q-switch voltage was increased. As is shown in Figure 7-5, the conversion to 1573 nm starts before the 1064 nm reaches a maximum. This prevents the 1064 nm pulse energy reaching its maximum value of 90 mJ, which is achieved with the KTP crystals removed from the resonator.

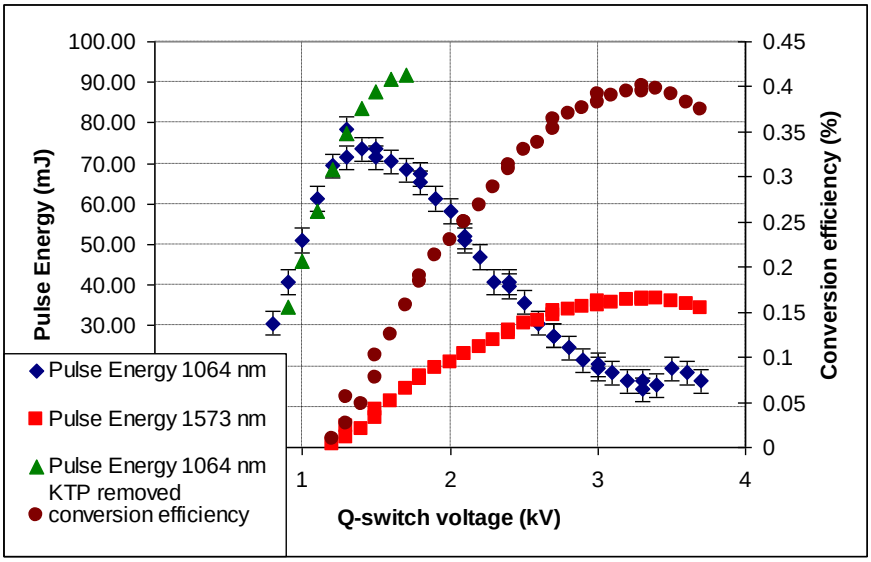

Figure 7-5: Pulse energy at 1064 nm and 1573 nm, and conversion efficiency both as a function of the Q-switch voltage.

The conversion efficiency from 1064 nm to 1573 nm was calculated by using the maximum 1064 nm output of 90 mJ. A maximum output of 36 mJ at 1573 nm is shown, which represents a conversion efficiency of 40%. This is superior to the typical extracavity OPO conversion efficiency value of 35%.

In this set-up, the electronic control to select a single output wavelength was not ideal, as neither wavelength could be switched off altogether. At the maximum 1573 nm output of 36 mJ (RTP voltage 3.5 kV) 15-20 mJ of 1064 nm leaked out through the polarising beam splitter. The maximum 1064 nm output was 73 mJ at 1.4 kV where 4 mJ of 1573 nm was also coupled out.

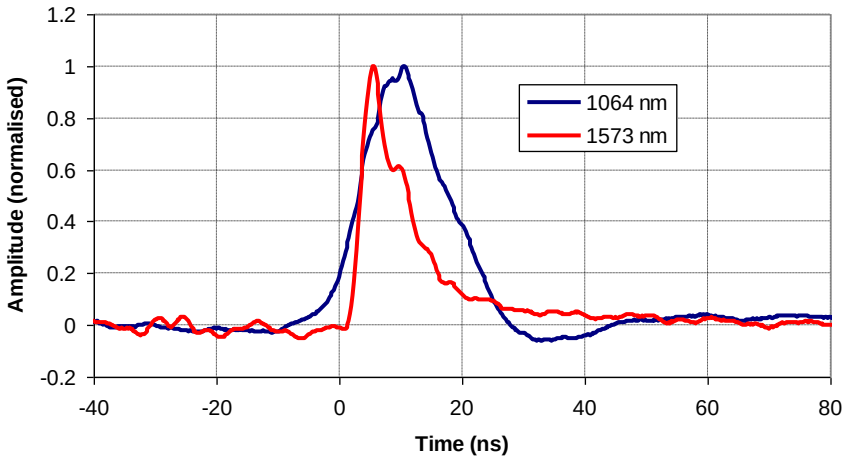

Figure 7-6: Normalised pulseshapes of undepleted 1064 nm pulse and 1573 nm pulse.

The pulseshapes in Figure 7-6 show that the 1573 nm pulse is narrower than the 1064 nm OPO pump wavelength as expected. (8.4 ns and 14.9 ns respectively) The 1573 nm pulse has a sharper leading edge than the 1064 nm pulse, and the pulses have a comparable falling edge. Note that the pulses recorded do not occur simultaneously, as the 1064 nm pulse was recorded while the KTP crystals were not present in the resonator.

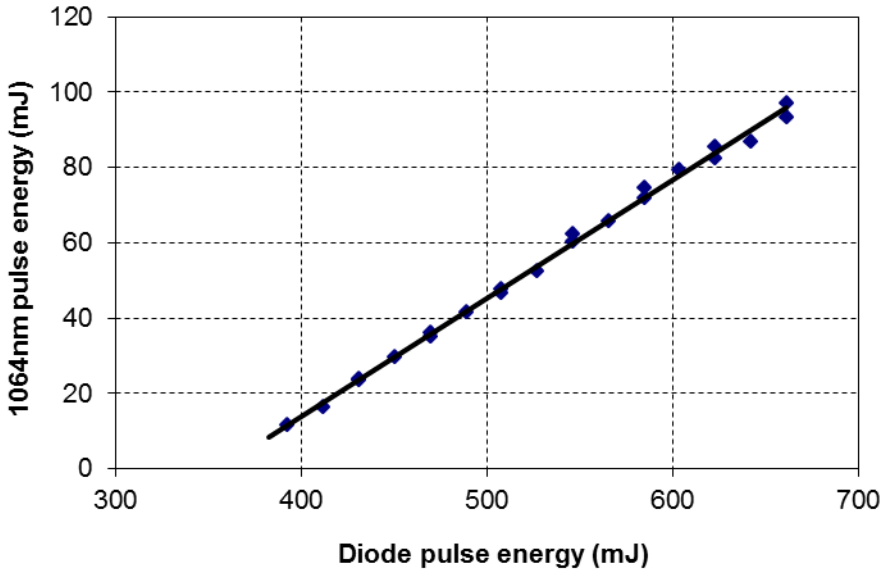

Figure 7-7: Energy curve for the 1064 nm laser output.

Figure 7-7 shows a plot of the 1064 nm laser output energy against the diode energy while no KTP crystals were present in the laser resonator. The laser energy is shown to have a linear relationship with the pump energy and the threshold pump energy is approximately 350 mJ. The slope efficiency is 31% and the maximum conversion efficiency is 15%.

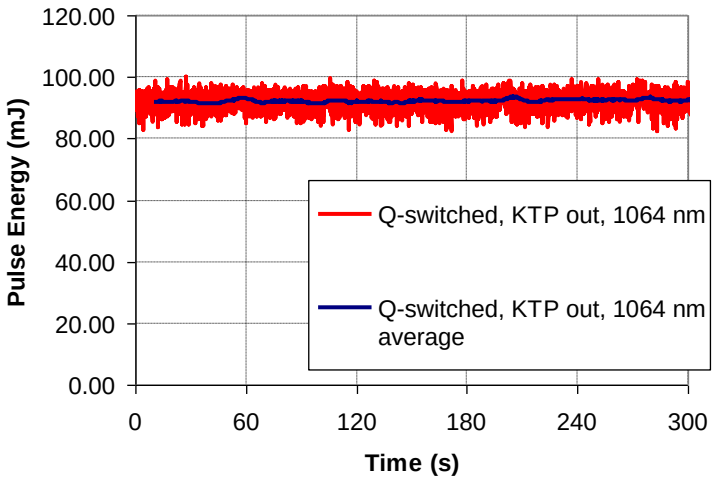

Figure 7-8: Laser pulse energy.

In Figure 7-8, the laser pulse energy is shown for 300 s duration (PRF = 10 Hz), and also the average pulse energy of the last 100 pulses. The average pulse energy and standard deviation over the 300 s duration were 92±3 mJ. The KTP crystals were then inserted into the resonator and the OPO pulse energy at 1573 nm was recorded, while the residual 1064 nm was removed using dichroic beam splitters.

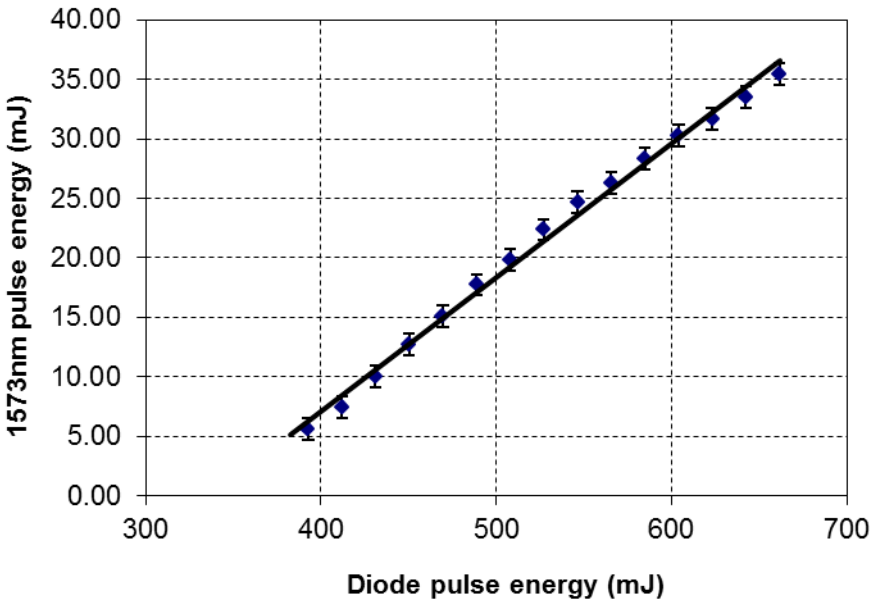

Figure 7-9: Energy curve for the 1573 nm OPO output.

Figure 7-9 shows a plot of the 1573 nm laser output energy against the diode energy. The OPO energy is shown to have an approximately linear relationship with the 808 nm laser diode pump energy ($R^2 > 99\%$). The threshold laser diode pump energy is estimated to be 350 mJ as was the case for the laser output. The low threshold of the OPO conversion is due to the very high output coupling reflectivity of the fundamental wavelength in the OPO resonator and the associated high pump power density. The slope efficiency is 11% and the maximum conversion efficiency is 5%.

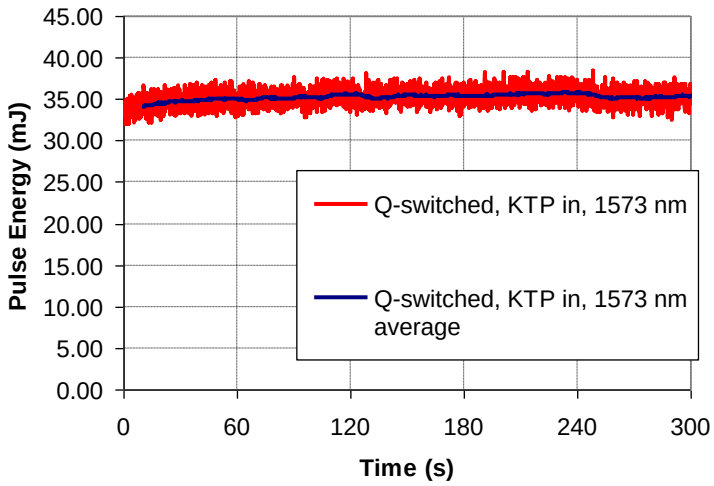

Figure 7-10: OPO signal output pulse energy.

In Figure 7-10, the OPO signal pulse energy (1573 nm) is shown for 300 s duration (PRF = 10 Hz), and also the average pulse energy of the last 100 pulses. The average pulse energy and standard deviation over the 300 s duration were 35±1 mJ. The OPO output shows more energy drift at the start of the firing period than the laser output. The increase in energy at the start of the period is however <5%, which is not significant.

The intensity profile was captured using an InGaAs Xenics CCD camera and BeamGage beam profiling software. The near field intensity profile was imaged using a single positive lens. The image plane was just after the output coupling polarising beam splitter/periscope assembly, and the image (partially obscured by a metal ruler at the image plane) was bought into focus by adjusting the position of the camera. The magnification was calculated to scale the size of the image and calculate the near field beam size.

(a) (b)

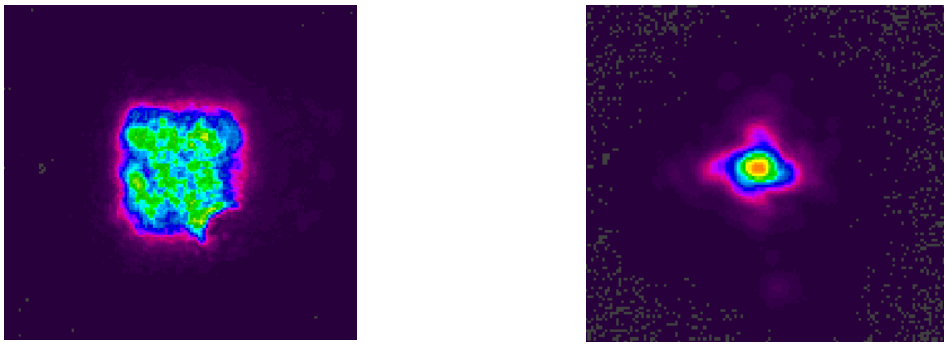

Figure 7-11: The 1064 nm laser near field intensity profile (a) and the far field intensity profile (b).

The far field intensity profile was captured by positioning the camera at the focal plane of a focusing optic in this case a 1 m focal length parabolic mirror. Images representing the intensity profiles are shown in the near and far field in Figure 7-11(a) and Figure 7-11(b) respectively. Both the intensity patterns are considered typical of this type of resonator. Calculations based on the intensity patterns using the BeamGage software produced the parameters shown in Table 7-4. These parameters are also typical for this type of resonator. In all cases where intensity profiles are used, intensity profiles were

captured every 0.5 s for a duration of 60 s. Statistics based on the average of these 120 intensity profiles were then calculated and recorded.

Diameter (encircled 90% energy)	5.1 mm
Divergence (encircled 90% energy)	1.2 mRad
Beam Parameter Product	6.1 mm.mRad
M^2	~4.5

Table 7-4: 1064 nm laser beam parameter measurements.

The procedures described above were repeated to capture the intensity patterns of the 1573 nm OPO signal beam in the near and far field image planes and these are shown in Figure 7-12.

(a) (b)

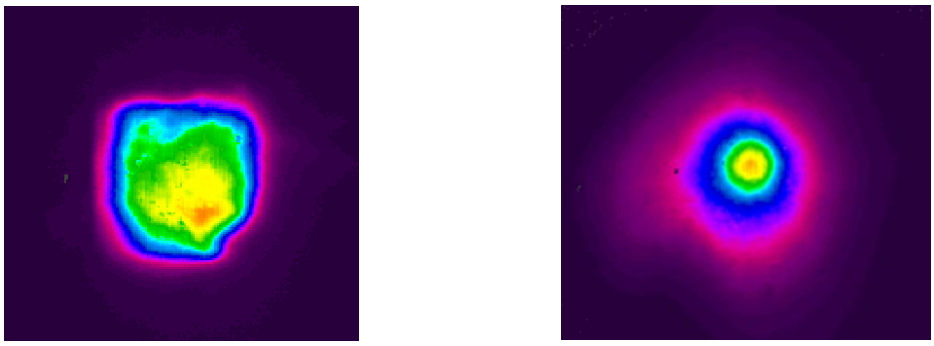

Figure 7-12: The 1573 nm OPO signal near field intensity profile (a) and the far field intensity profile (b).

These image profiles have a greater amount of light surrounding the beam (the beam has larger "wings" than a Gaussian intensity profile). A lot of the finer details of intensity fluctuations seen in the 1064 nm intensity profiles have been "blurred" when the OPO signal intensity patterns are compared, so they appear more uniform. This is a common observation for extracavity OPOs. The OPO signal output beam parameters deduced

from the near and far field intensity profiles using the BeamGage software are shown in Table 7-5.

Diameter (encircled 90% energy)	7.5 mm
Divergence (encircled 90% energy)	10 mRad
Beam Parameter Product	75 mm.mRad
M^2	~37

Table 7-5: 1573 nm laser beam parameter measurements.

It is immediately clear that the beam diameter is larger than for the 1064 nm mode (47% increase) and that the divergence is far greater (8 times larger). This means that the beam quality has degraded significantly (M^2 has increased by 8 times). A change in divergence for a change in wavelength from 1064 nm to 1573 nm is expected, as diffraction will have a stronger effect on the 1573 nm beam (1.5 times). The divergence of the OPO signal may be unacceptable for the application, as a larger telescope would be required than used in existing laser system designs, to reduce the divergence, which would also increase the near field beam size more than desired.

As was shown in Figure 7-5, for lower than optimum values of voltage, the efficiency was reduced. The graph in Figure 7-13 shows the variation in OPO signal divergence for a range of Q-switch voltages. This shows that for lower values of fundamental (1064 nm) power density, where the conversion is lower, the divergence is also lower.

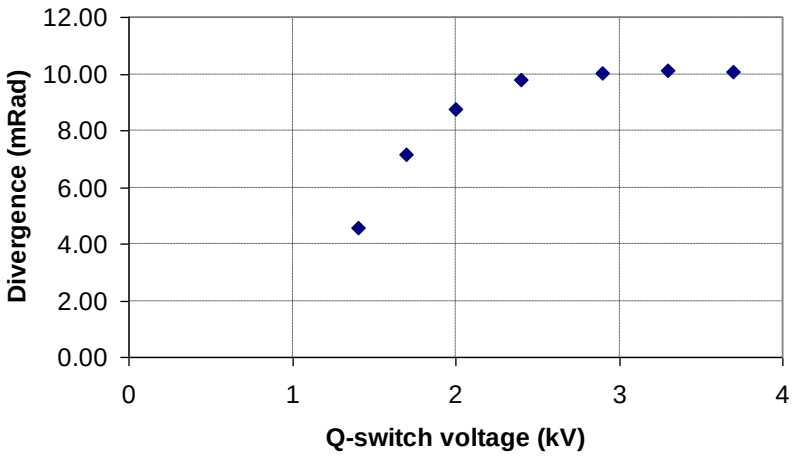

Figure 7-13: Divergence of 1573 nm OPO signal for a range of Q-switch voltages.

The Nd:YAG laser output divergence was also investigated over a range of Q-switch voltages. The output coupling of the laser is altered as the Q-switch voltage is changed. It is shown in Figure 7-14 that an increase in Q-switch voltage also increases the laser divergence, when the KTP crystals are removed from the resonator. The graph also shows two points for fixed-Q operation, one with the KTP crystals present, and one with the KTP crystals removed. It is shown that the presence of the KTP crystals in the resonator increases the laser divergence by 67%. This result is repeated for Q-switched operation by rotating the KTP crystals by 90° about the laser mode axis to prevent OPO conversion. Again, the laser divergence is increased when the KTP crystals are present in the resonator but by a smaller percentage than for the fixed-Q case (26% compared with 67%). The depolarisation produced by KTP in this orientation may have a small effect on the output coupling for the Nd:YAG laser.

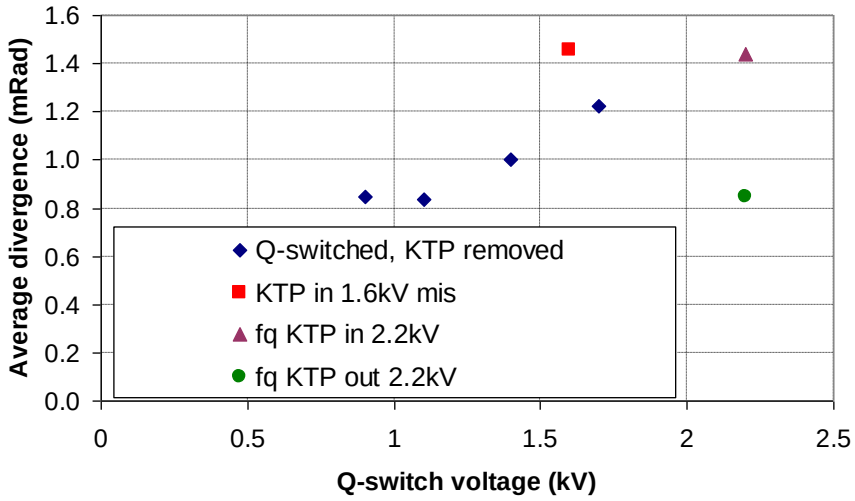

Figure 7-14: Divergence of the undepleted laser mode for a range of Q-switch voltages.

The divergence of the depleted Nd:YAG laser beam was also observed over the full range of Q-switch voltages. At approximately 3.5 kV the maximum OPO output is reached and the laser output is depleted by the maximum amount. However, some undepleted 1064 nm fundamental mode is measured (approximately 15-20 mJ as shown in Figure 7-5).

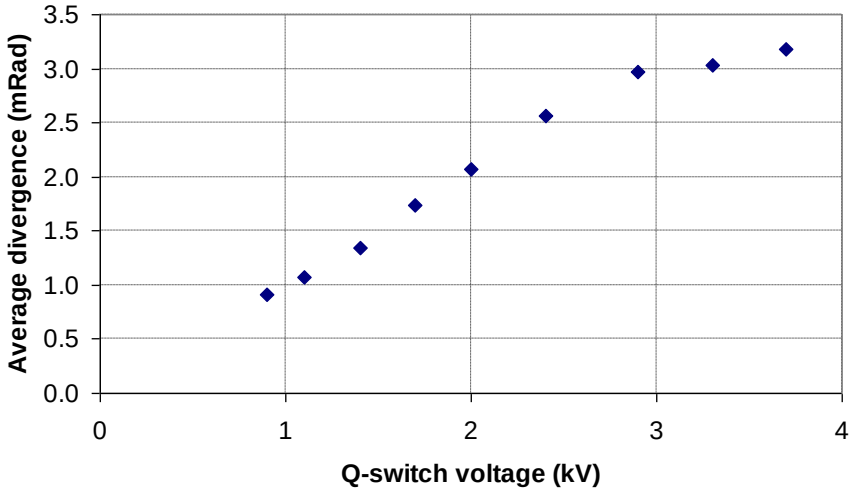

Figure 7-15: Divergence of the depleted laser mode for a range of Q-switch voltages.

An increase in divergence is observed for an increase in Q-switch voltage. The relationship appears linear until approximately 3 kV is reached and above this voltage the increase in divergence is less sensitive to Q-switch voltage. The divergence of the depleted pump beam is less than 1 mRad when the OPO is just above threshold at 0.9 kV. This is close to the value for the 1064 nm divergence, when the KTP crystals are removed from the resonator, shown in Figure 7-14.

The divergence of the 1573 nm OPO signal was monitored for a 60 s period to access any variation in divergence due to thermal lens in the slab, which the OPO signal mode passes through. As is shown in Figure 7-16, the divergence reduces by <5% in the first 30 s and is then stable for the remaining duration. It follows to conclude that transient effects due to thermal lensing are negligible in this pumping regime (PRF = 10 Hz).

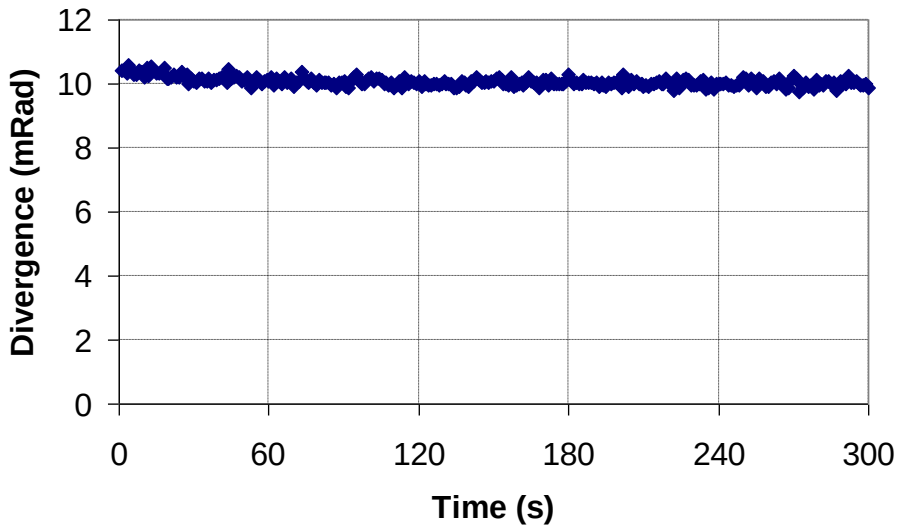

Figure 7-16: Divergence of 1573 nm OPO signal over a 300 s duration.

The degree to which the 1064 nm laser output and 1573 nm OPO signal are common boresighted is fixed in this design and expected to be unchanged over the environmental range, since a shared resonator path cannot change for each mode independently. The degree of the common boresight was measured to be within 250 µRad angular separation. This represents 21% of the 1064 nm laser beam divergence, and 3% of the 1573 nm OPO signal beam divergence.

7.4.4 Effect of 1573 nm absorption in Nd:YAG crystal

It was thought that the measured 14% 1573 nm absorption in the Nd:YAG crystal could affect the resonating mode. The effect of the absorption in the slab was investigated by passing a 1573 nm beam through a Nd:YAG crystal and measuring the change in divergence. A Nd:YAG laser with an extracavity OPO, which had a OPO signal (1573 nm) divergence of 3.48 mRad, was monitored using an IR camera at the focal plane of a parabolic mirror. In the transmission path, before the parabolic mirror, a Nd:YAG isosceles trapezoidal shaped crystal with uncoated end surfaces was positioned such that the probe beam boresight direction was unaffected.

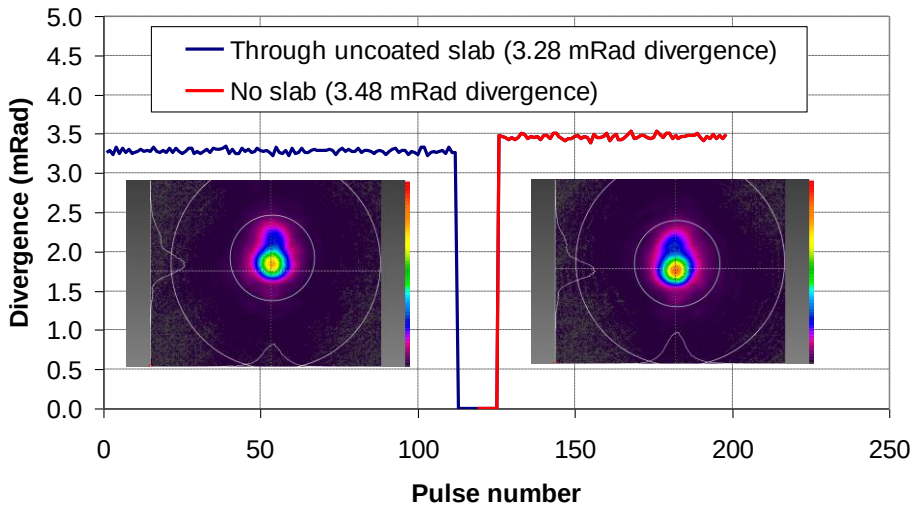

Figure 7-17: Divergence of 1573 nm beam with and without a Nd:YAG crystal in the transmission path.

The graph in Figure 7-17 shows the divergence of the probe beam with and without the Nd:YAG crystal in the beam path and a reduction of 6% of the divergence is shown when the Nd:YAG crystal is present. It can be seen by the far field intensity profiles in the figure that there is little difference in the intensity distribution caused by the transmission of the 1573 nm energy through the laser slab. Inside the common resonator, it is suspected that the 1573 nm power density will be higher (depending on the OPO output coupling value). A higher power density will produce higher absorption and thermal loading, and thus a greater potential to affect the oscillating mode. However, the fact that the Nd:YAG slab improves the 1573 nm divergence, and

the fact that the effect is small, is an indication that this is not the cause of the poor 1573 nm divergence seen from the common resonator.

7.4.5 Discussion

The greatest challenge for this design is achieving a divergence of the 1573 nm beam which is comparable with the performance of a typical Nd:YAG targeting laser with an extracavity OPO (< 2.5 mRad). To understand the effects of resonator length and resonator losses on the divergence performance of an intracavity OPO, an intracavity OPO was set-up with a separate resonator to the ring laser resonator. In addition, an extracavity OPO was set up in order to determine the effect of intracavity pumping compared to extracavity pumping of an OPO. Both the separate resonator types used a plane-plane resonator type rather than the ring resonator used by the common resonator design. This simplified the alignment of the OPO resonator. The efficiency of a ring resonator is greater than for an equivalent plane-plane resonator of the same diffractive length, as the round-trip length of the plane-plane resonator is longer. The round-trip length of the resonator should therefore be considered when comparing OPO resonator efficiencies.

The reason for the poor divergence of the 1573 nm OPO signal is not immediately obvious, but potential reasons include:

a) Single-pass operation of the resonator where optical parametric amplification (OPA) rather than optical parametric oscillation (OPO) is observed. In OPOs, some amount of both OPA and OPO will occur, but the ratio of OPA to OPO will be increased if the intracavity OPO losses are high. As the OPA light will be less directional than the OPO light, if a higher proportion of OPA exists, the divergence of the output will be larger. The investigation of the separate resonator OPO with lower intracavity loss was used to test this theory (Section 7.5).
b) Depletion of the high intensity parts of the 1064 nm beam intensity pattern, by conversion to 1573 nm, causing its divergence to increase. This larger divergence pump beam then producing a larger divergence signal beam.
c) OPO signal light passing around the sides of the laser slab could increase the divergence of the OPO signal by allowing higher order resonator modes to

resonate. This theory was discounted when this light at the sides of the slab was blocked and the intensity profile was unchanged.

7.5 SEPARATE RESONATOR INTRACAVITY OPO

7.5.1 Experimental set-up

For the separate resonator OPO, it was assumed that the pump and OPO signal beam sizes were approximately constant throughout the resonator, and therefore the position of the KTP crystals within the resonator was unimportant. This should be a fair assumption, as the use of a plane-plane resonator dictates that the oscillating mode has a plane wavefront at the position of both of the plane resonator mirrors. In addition, the separate resonator intracavity OPO does not have any significant lens optics in the resonator, unlike the common resonator which has the Nd:YAG slab inside the OPO resonator, which is subject to thermal lensing. The set-up of the Nd:YAG ring resonator pump source and the separate intracavity KTP OPO resonator is shown schematically in Figure 7-18.

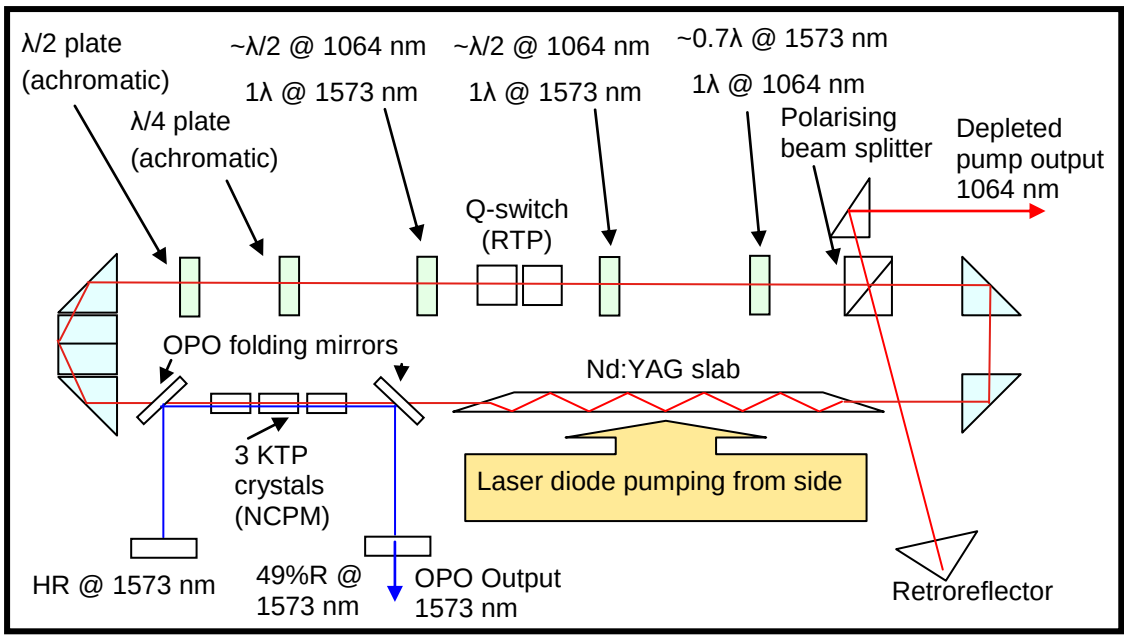

Figure 7-18: Layout of diode-pumped Nd:YAG ring laser with intracavity KTP OPO using a separate OPO resonator.

An output coupler of 49% was used as this was found to give the best efficiency out of three tested (41%, 49% and 65%). Both the output coupler and the HR at 1573 nm back mirror optics were plane. The plane OPO folding mirrors were HT at 1064 nm and HR at 1573 nm for 45° incidence, and were used to separate the OPO signal from the laser mode to allow the separate resonator mirrors to be used.

7.5.2 Experimental Results

The OPO resonator physical length was varied over the range 207-684 mm. The energy as a function of the laser diode current is plotted for all the resonator optical round trip lengths that were investigated in Figure 7-19.

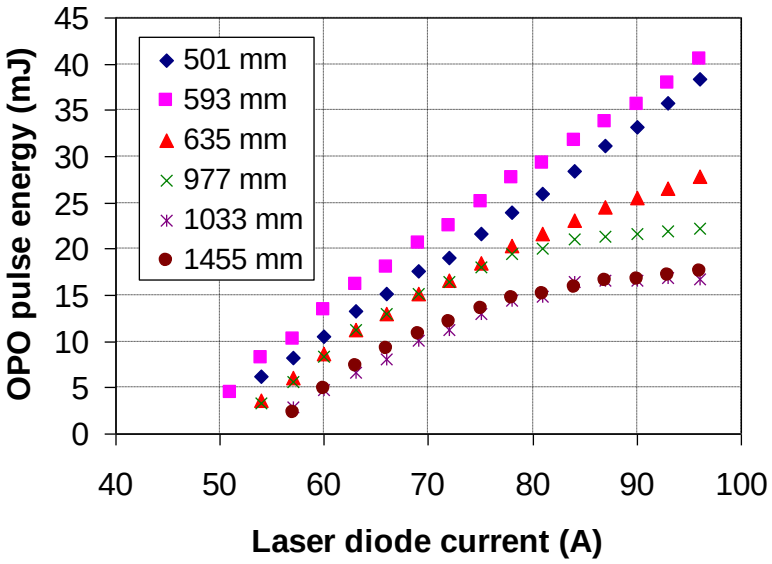

Figure 7-19: Energy for a range of laser diode current is plotted for all resonator optical round trip lengths investigated.

It can be seen that the threshold increases with an increase in the resonator length. For short resonators, the relationship between pulse energy and laser diode current is linear. However, for longer resonators, the energy rolls off for higher laser diode current.

The pulse energy is dependent on the resonator optical round trip length and therefore the pulse energy is plotted against the resonator optical round trip length for easy comparison with the common resonator result. It is shown that an increase in resonator optical round trip length generally decreases the output energy of the OPO. A clear trend is however not observed.

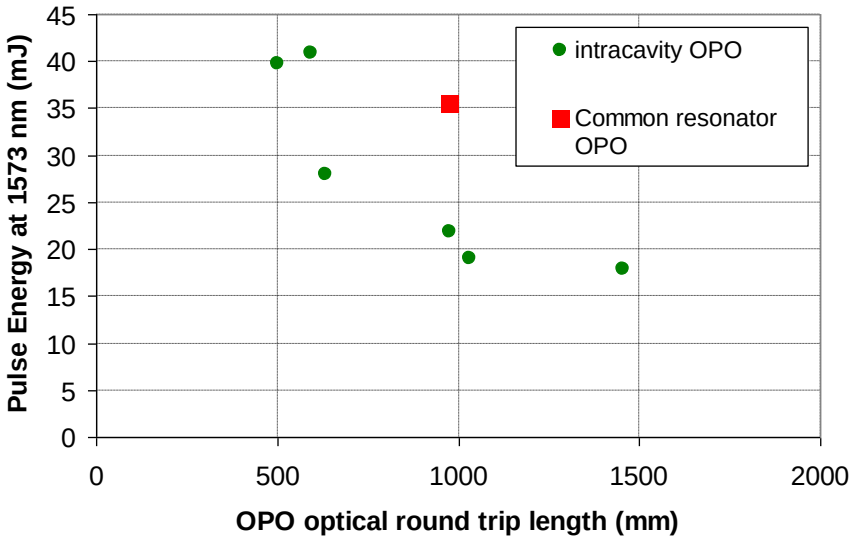

Figure 7-20: OPO signal pulse energy for a range of OPO resonator lengths.

The common resonator produces a larger output pulse energy than a separate resonator OPO with the same optical round trip length, despite both OPO resonators utilising intracavity pumping. This is surprising since the common resonator has greater intracavity loss than the separate resonator OPO (29% and 4% respectively).

The divergence of the OPO signal is dependent on the diffractive length of the OPO resonator, so these parameters are plotted in Figure 7-21.

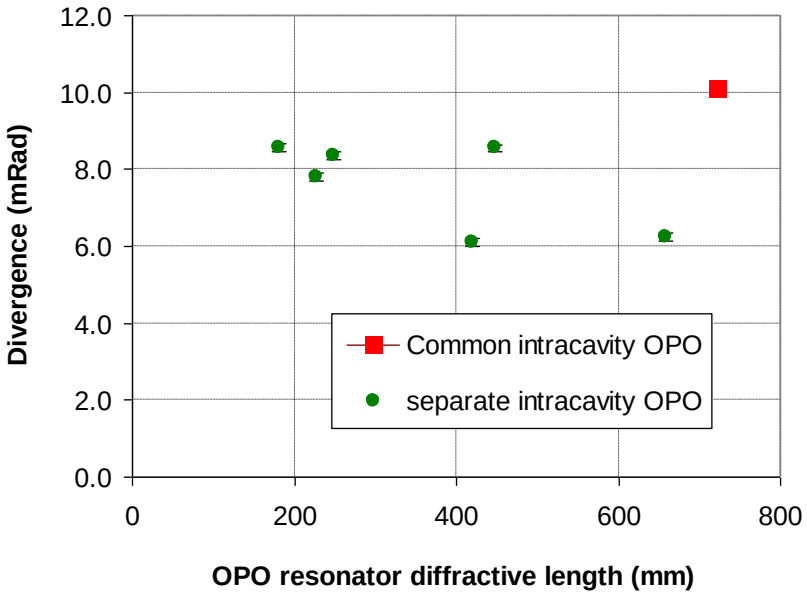

Figure 7-21: OPO signal beam divergence for a range of OPO resonator lengths.

The divergence tends to be smaller for longer resonator lengths as would be expected for these lower Fresnel number resonators. A clear trend is however not observed. The divergence for the separate resonator intracavity OPO is smaller than for the common resonator intracavity OPO, even when the separate resonator length is much shorter than the common resonator OPO. Error bars show the standard deviation of the divergence (0.1 mRad), which is far smaller than the variation between the divergence measurements at different resonator lengths.

7.5.3 Discussion

The pulse energy was not proportional to the pump energy for longer resonators. The reason for this could be because the longer resonators are more susceptible to diffraction losses, which would be increasing with pump energy due to thermal lensing. This thermal lensing is due to absorption of the OPO idler (3288 nm) by the KTP crystals. The diffractive losses may be due to poor overlap with the pump rather than aperturing of the OPO signal mode. An explanation why this effect is not seen in the common resonator OPO, even though its diffractive length is longer than the separate resonator intracavity OPO, maybe because the thermal lens acts equally on both the 1064 nm and 1573 nm wavelengths, the mode overlap is less affected.

An explanation that was considered for the greater common resonator efficiency, compared with separate resonator efficiency, was the phenomenon of cavity length resonances as described in [4]. This was however discounted when the separate resonator OPO length was continuously adjusted by placing one of the plane OPO resonator mirrors on a translation stage and adjusting its position. As the OPO resonator round-trip length was increased and passed through the calculated half round-trip length of the laser resonator, a peak in efficiency was not observed; rather a gradual decrease in efficiency was seen, due to longer build-up time and resonator misalignment. An explanation for the superior efficiency of the common resonator could be the guaranteed alignment of the OPO resonator and the overlap of the fundamental and signal wavelengths. The separate resonator design requires optimisation of the OPO mirror alignment and manual overlapping of the fundamental and signal wavelengths, which may have been slightly different sizes.

The divergence of the separate resonator is improved when compared with the common resonator for all resonator lengths. This suggests that the high intracavity losses in the common resonator, which shifts the proportion of OPA light to OPO light in favour of OPA, is causing the divergence to increase.

7.6 SEPARATE RESONATOR EXTRACAVITY OPO

7.6.1 Experimental set-up

The initial set-up of an extracavity plane-plane resonator KTP OPO is shown schematically in Figure 7-22.

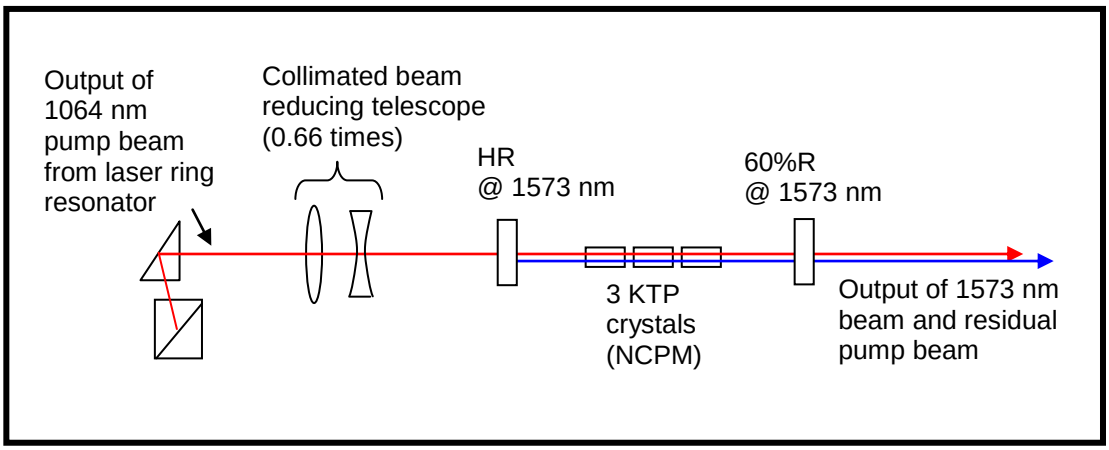

Figure 7-22: Layout of an extracavity KTP OPO using a plane-plane resonator, which is single-pass-pumped by a diode-pumped Nd:YAG ring laser.

The same laser ring resonator is used to pump an extracavity OPO as was used to pump the separate resonator intracavity OPO. A plane-plane resonator is used again. The differences in this extracavity OPO and the separate resonator intracavity OPO are:

1. The extracavity OPO does not have the 1573 nm 45° mirrors to turn the OPO signal used in the intracavity separate resonator OPO, which decreases the intracavity loss at 1064 nm and 1573 nm by a small amount. In addition, the

absence of these optics allows for shorter OPO resonator lengths in the extracavity case.

2. The extracavity OPO uses a 60%R output coupler, rather than a 50%R output coupler as for the separate resonator intracavity OPO. This change of output coupler optimised the efficiency of the extracavity OPO.
3. Due to poor efficiency achieved using the extracavity OPO, it was necessary to use a reducing telescope of 0.66 times, in order to increase the pump power density by 2.3 times. Laser systems produced at Selex ES that do not use an amplifier stage also use a beam reducing telescope to achieve an adequate efficiency from the OPO stage, so the need to use a telescope was not surprising. An insertion loss of 5% was observed when the telescope was introduced.

7.6.2 Experimental Results

The OPO resonator physical length was varied over the range 125-274 mm. The longest resonator investigated was shorter than in the separate resonator intracavity OPO case due to the poorer conversion efficiency. The pulse energy as a function of the laser diode current is plotted for all the resonator optical round trip lengths that were investigated in Figure 7-23.

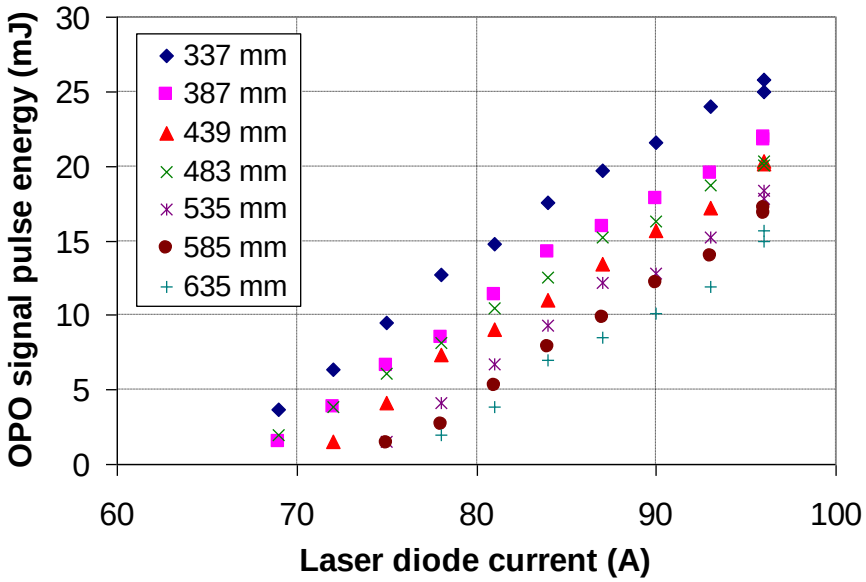

Figure 7-23: Energy for a range of laser diode current is plotted for all resonator optical round trip lengths investigated.

It can be seen that generally the threshold increases with an increase in the resonator length as was the case for the intracavity OPO. For all resonator lengths, the relationship between pulse energy and laser diode current is approximately linear. This is in contrast to the intracavity OPO case where for longer resonators, the energy rolls off for higher laser diode current.

The pulse energy is plotted against the resonator optical round trip length in Figure 7-24 and is compared with the common resonator and the separate resonator intracavity OPO results. It is shown that an increase in resonator optical round trip length decreases the output energy of the OPO. An approximately linear trend is observed, with an R^2 value of 0.97 for the line of best fit. The energy produced by the extracavity OPO is less than for both the intracavity OPO designs and a shorter resonator length is required to improve the efficiency of the extracavity OPO.

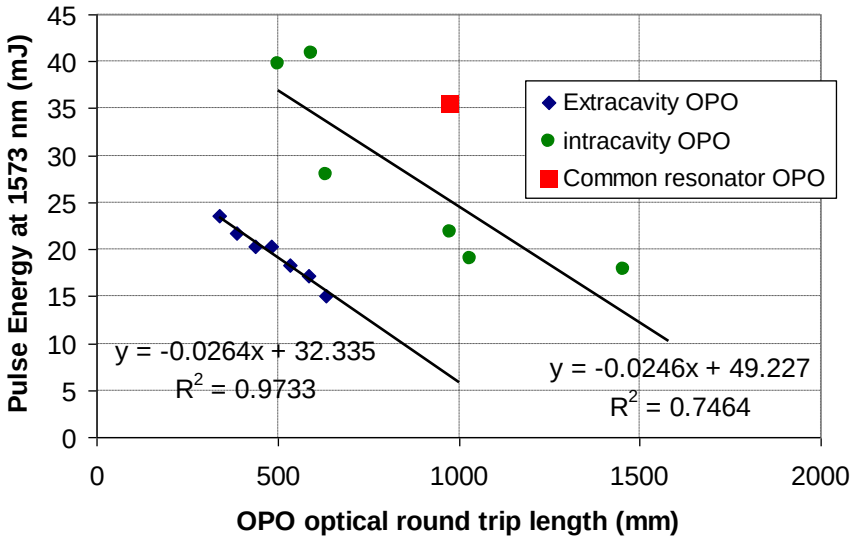

Figure 7-24: OPO signal pulse energy for a range of OPO resonator lengths.

The divergence of the OPO signal is plotted against the diffractive length of the OPO resonator in Figure 7-25.

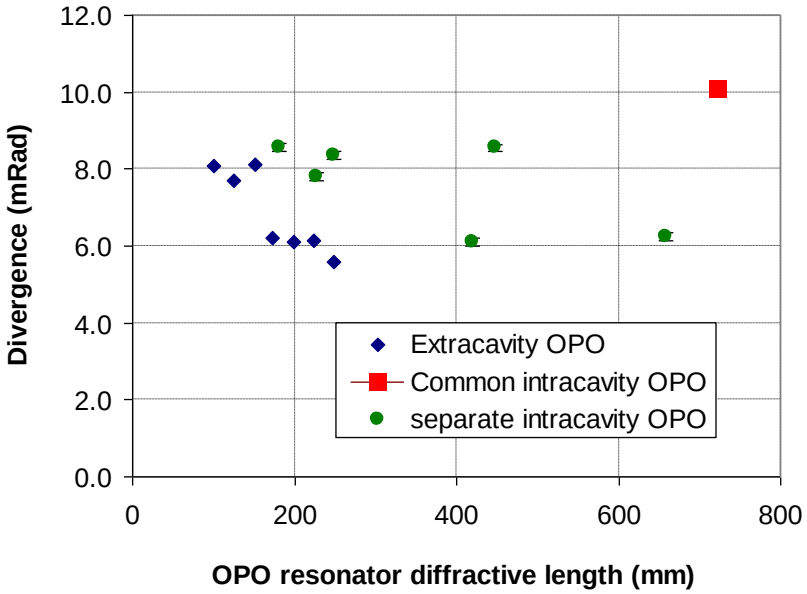

Figure 7-25: OPO signal beam divergence for a range of OPO resonator lengths.

The divergence tends to be smaller for longer resonator lengths as would be expected for these lower Fresnel number resonators. A clear trend is not observed, but the resonator length seems to have a stronger effect on divergence for the extracavity OPO than for the intracavity OPO. The divergence for the extracavity OPO is smaller than for the separate resonator intracavity OPO, even when the extracavity resonator length is much shorter than the separate resonator intracavity OPO.

The near field intensity profile was captured using a camera and the beam diameter was calculated using the 90% of encircled energy measurement in the BeamGage software. Table 7-6 summarises the near field beam sizes for the three OPO resonator types. The near field beam size for the common resonator was measured at two positions:

1. At the exit of the Nd:YAG slab.
2. Just after the output coupling beam splitter/periscope assembly.

It was found that the beam size grew by 49% between positions 1 and 2. When this amount of beam growth is observed over a (diffractive) distance of 532 mm within the resonator, it is not surprising that the divergence is large.

Resonator type	Analysis plane	Resonator diffractive length (mm)	Beam diameter (mm)
Common resonator intracavity OPO	Back of Nd:YAG slab	722	5.05±0.05
Common resonator intracavity OPO	After polarising beam splitter	722	7.48±0.05
Separate resonator intracavity OPO	After output coupling mirror	182	7.30±0.05
Separate resonator intracavity OPO	After output coupling mirror	659	9.02±0.03
Extracavity OPO	After output coupling mirror	100	5.43±0.07
Extracavity OPO	After output coupling mirror	249	6.71±0.04

Table 7-6: Summary of near field intensity profile diameter measurements of OPO signal beam, (90% encircled area, average of 120 profiles recorded over 60 s duration).

The OPO signal near field beam sizes for the intracavity and the extracavity separate resonator OPOs, were measured at the plane output coupler. This measurement was repeated for the shortest and the longest resonators in each case. In both cases, the near field beam size is larger for the longer resonator. This is considered to be due to less defined laser transverse modes being present in longer resonators, in which fewer round trips of the resonator are possible. The extracavity OPO has a smaller beam size even with a longer resonator length than the intracavity OPO. This is unsurprising as the extracavity OPO pump beam size was approximately 0.8 times the size of the intracavity OPO pump beam. The Nd:YAG laser near-field beam size was also measured in the two positions for the common resonator (with the KTP crystals removed) as shown in Table 7-7. The increase in Nd:YAG laser beam size was only 21% compared with the 49% increase in OPO signal mode size over the same distance.

Resonator type	Analysis plane	Resonator diffractive length (mm)	Beam diameter (mm)
Common resonator intracavity OPO	Back of Nd:YAG slab	722	4.23±0.07
Common resonator intracavity OPO	After polarising beam splitter	722	5.1
Extracavity OPO	After beam reducing telescope (calculated)	N/A	5.1*0.66 = 3.4

Table 7-7: Summary of near field intensity profile diameter measurements of Nd:YAG laser beam, (90% encircled area, average of 120 profiles recorded over 60 s duration).

The conversion efficiency for all three OPO resonator types is plotted against OPO optical round trip length, plus that of the type B laser system (image rotating ring resonator OPO) in Figure 7-26.

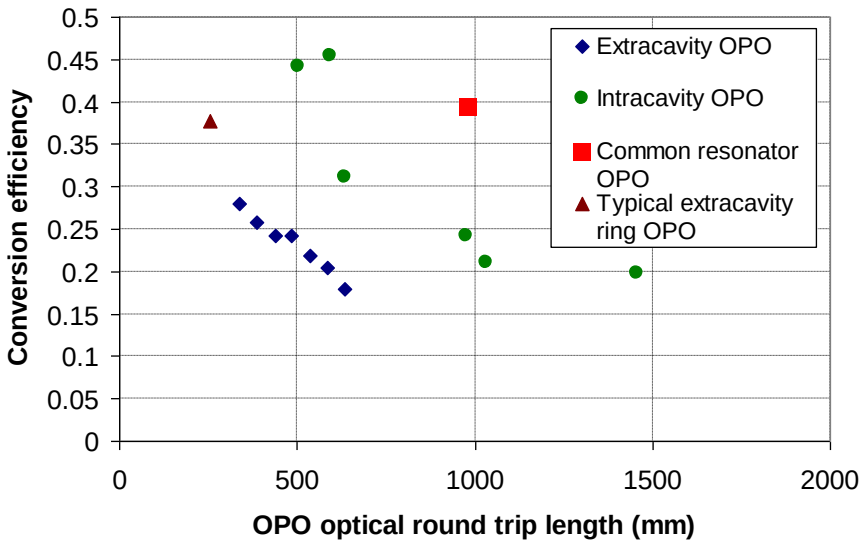

Figure 7-26: Conversion efficiency as a function of the OPO optical round trip length for all three OPO resonator types.

The best conversion efficiency achieved was using the separate resonator intracavity OPO, which produced a conversion of 45% for an OPO optical round trip length of 593 mm. The common resonator OPO, which had a fixed optical round trip length of 978 mm, demonstrated a conversion efficiency of 39%. The conversion efficiency of the extracavity OPO was reduced, even with the beam reducing telescope, with a best conversion of 28% with an optical round trip length of 337 mm (which was shorter than the shortest intracavity OPO). The conversion efficiency of the extracavity ring OPO found within a typical targeting laser system is better than for the plane-plane extracavity OPO investigated. This can be explained by the shorter resonator length, which reduces the build-up time of the OPO and increases efficiency.

In Figure 7-27, the M^2 value is plotted against the OPO resonator diffractive length for all three resonator types, plus that of the type B laser system (image rotating ring resonator OPO) so that beam quality can be compared.

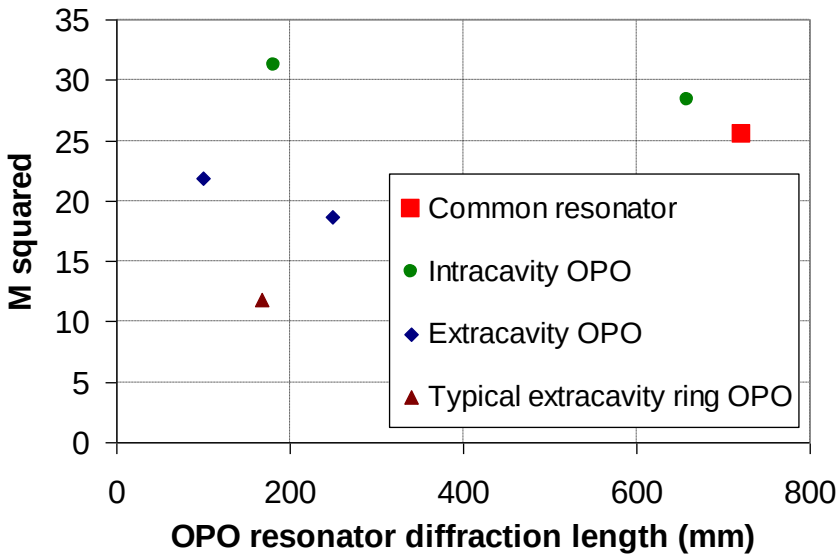

Figure 7-27: M^2 value against OPO resonator diffractive length for all three resonator types.

The beam quality is actually better for the common resonator than for the separate resonator intracavity OPO (at both the shortest and longest resonator lengths). This result for common resonator M^2 uses the smallest near field beam size which was measured at the position of the Nd:YAG slab exit, and was assumed to be the beam waist. The earlier measurement of 37 for the M^2 (in Table 7-5) was calculated using the near field beam size at the output coupler, which was 49% larger than at the exit of the Nd:YAG slab.

The beam quality for the extracavity OPO is better than for the intracavity OPO in all cases. The resonator length of the extracavity OPO is shorter than for the intracavity OPO, but the pump size is also smaller.

The beam quality of the extracavity ring OPO found within a typical targeting laser system (type B) is better than for the plane-plane extracavity OPO investigated (M^2 of 12 compared with approximately 20). The reasons for this include:

1. The image rotating OPO provides better averaging of aberrations than the plane-plane resonator.
2. The ring resonator has a shorter build-up time and will make more round-trips than the plane-plane resonator for an equal diffractive length, so will form resonator modes more readily.
3. The image rotating OPO divergence was measured using the pinhole technique rather than the camera technique used with the plane-plane extracavity OPO investigation. The difference in measurement techniques would account for a 10% difference in M^2 measurements, due to camera measurements for the 1573 nm wavelength typically measuring 5% larger diameters than pinhole measurements.

7.6.3 Discussion

The beam quality is better for the extracavity OPO than for the intracavity OPO, but the efficiency is poorer. The pump intensity is not accurately known for the intracavity OPO. If pump intensity inside the intracavity OPO is greater than for the extracavity OPO, then the OPA will be greater. The OPO output will also be greater, but the intracavity losses in the common resonator case will reduce the feedback of the resonator. In the two separate resonator cases, which have essentially the same

intracavity loss, it is not clear why the extracavity OPO should have a superior beam quality to the intracavity OPO, since the resonator Fresnel number is the same.

In both the extracavity and intracavity OPO cases, when the OPO resonator length is increased from the shortest to the longest length, the beam quality is slightly improved (M^2 reduced by 15% and 9%, respectively). Note that the OPO resonator diffractive length was increased by 149% from the shortest to the longest resonator length in the extracavity case and by 262% in the intracavity case.

7.7 COMPARISON OF EXPERIMENTAL RESULTS WITH THEORETICAL MODELLING

A computer model was co-written by David Legge and the author using the MathCAD programming language. This model was based on the work carried out in the paper by Dabu *et al.* [5, 6], and predicts the temporal evolution of the inversion population in the Nd:YAG slab and the development of the fundamental (1064 nm) and signal (1573 nm) photon densities inside the resonator. This model uses the Q-switched rate equations and the coupled equations for parametric interaction in the KTP crystals, and is resolved using an iterative calculus method. The predicted temporal profiles of the fundamental and signal pulses are integrated to calculate the pulse energies.

The rate equations for a Q-switched solid-state laser given in reference [1] are modified to include the loss of the fundamental photons ϕ_p during a round-trip of the resonator due to conversion. These modified rate equations are shown in Equations 7.1 and 7.2.

$$\frac{\partial \phi_p}{\partial t} = \phi_p \left[c\sigma\eta \frac{l_r}{l_l} + \frac{\ln(1-\delta_p)}{t_{RL}} \right] - \frac{\Delta\phi_p}{t_{RL}} \quad (7.1)$$

$$\frac{\partial \eta}{\partial t} = -\phi_p c\sigma\eta \quad (7.2)$$

where

η = inversion population density

c = speed of light

σ = stimulated emission cross section of the laser medium

δ_p = round-trip pump wave intensity losses

l_r = optical path length inside the Nd:YAG slab

l_l = optical length of the laser cavity

t_{RL} = laser resonator round-trip time

The relations between the photon flux intensity I_m, the photon flux density ϕ_m, and the complex electric field $\tilde{E}_m$ in the nonlinear crystal, are shown in Equations 7.3 to 7.5 [7].

$$I_m = \frac{\phi_m \, h \, \upsilon_m c}{n_m} \quad (7.3)$$

$$I_m = \frac{1}{2} n_m \, c \, \varepsilon_0 \left| \tilde{E}_m \right|^2 \quad (7.4)$$

$$\phi_m = \frac{1}{2} \frac{\varepsilon_0 \, {n_m}^2}{h \, \upsilon_m} \left| \tilde{E}_m \right|^2 \quad (7.5)$$

where

h = Planck's constant

ε_0 = permittivity of free space

n_m = refractive index where m = p,s,i corresponding to the three wavelengths.

The coupled equations for the parametric interaction along the crystallographic x-axis were taken from [8] and substitutions were made to produce Equations 7.6 to 7.9, where all the electric fields are real.

$$\frac{dE_p}{dx} := -\alpha_p \cdot E_p + \frac{(\omega_p \cdot d_{eff})}{n_p \cdot c} \cdot E_s \cdot E_i \cdot \sin(\theta) \tag{7.6}$$

$$\frac{dE_s}{dx} := -\alpha_s \cdot E_s - \frac{(\omega_s \cdot d_{eff})}{n_s \cdot c} \cdot E_p \cdot E_i \cdot \sin(\theta) \tag{7.7}$$

$$\frac{dE_i}{dx} := -\alpha_i \cdot E_i - \frac{(\omega_i \cdot d_{eff})}{n_i \cdot c} \cdot E_p \cdot E_s \cdot \sin(\theta)$$

$$\frac{d\theta}{dx} := \left(\frac{\omega_p}{n_p} \cdot \frac{E_s \cdot E_i}{E_p} - \frac{\omega_s}{n_s} \cdot \frac{E_p \cdot E_i}{E_s} - \frac{\omega_i}{n_i} \cdot \frac{E_p \cdot E_s}{E_i} \right) \cdot \frac{d_{eff}}{c} \cdot \cos(\theta) \tag{7.8}$$

where

d_{eff} = effective nonlinear coefficient

α_p, α_s, α_i = attenuation coefficients in the KTP crystal for the three wavelengths

The initial phases of the signal and idler fields are not imposed by the interaction, so it is assumed that they adjust themselves to maximise the energy transfer from the pump field to the signal and idler fields. The initial value for the relative phase ($\theta = \phi_p - \phi_s$ -

ϕ_i) is chosen for maximum signal energy. The change in θ can induce back and forth conversion from the pump to the signal and idler.

The iterative method of calculus essentially iterates between the modified Q-switched rate equations and the coupled equations for parametric gain (and pump depletion). Equations 7.3 to 7.5 allow the conversion between the two by relating the intracavity intensities and the electric fields of the three wavelengths.

The KTP was considered uniformly distributed throughout the resonator in the model, and the iteration time for calculation of the Q-switched 1064 nm intensity was a 20^{th} of the laser cavity round-trip time. Within each of these steps 50 iterations of the coupled equations for parametric gain were made. The parameters used in the computer model are summarised in Table 7-8.

Parameter	**Value**	**Parameter**	**Value**
Loss at pump wavelength (L_p)	0.16 + 0.1 (diffraction)	Loss at signal wavelength (L_s)	0.29 + 0.15 (diffraction)
Attenuation coefficient (α_p)	0.7 m^{-1}	Attenuation coefficient (α_s)	0.7 m^{-1}
Attenuation coefficient (α_i)	40 m^{-1}	Refractive index (n_p)	1.748
Refractive index (n_s)	1.737	Refractive index (n_i)	1.771
Optical length of laser (l_{laser})	1.02 m	Optical length of OPO (l_{OPO})	1.02 m
Physical length of KTP crystals (l_{KTP})	3 × 0.02 m	Stimulated emission cross-section (σ)	2.8×10^{-19} cm^2
effective nonlinear coefficient (d_{eff})	3.4×10^{-12} mV^{-1}	Population inversion density (η)	1.124×10^{18} cm^{-3}
Output coupling reflectivity at 1573 nm	50%		

Table 7-8: Parameters used in intracavity OPO computer model.

The optimum 1064 nm output was calculated using a 1064 nm output coupling reflectivity of 65% and a d_{eff} reduced to suppress conversion to signal and idler. The output energy at 1064 nm was 108 mJ and the pulsewidth 14 ns. This is slightly higher than the measured value of output energy of 92 mJ, which could be explained by a non-optimal alignment of the resonator or the pump laser diodes in the experimental set-up.

The output energy at 1573 nm was calculated to be 37 mJ with a pulsewidth 3.4 ns. This compares with a measured value of 36 mJ output energy and 8.4 ns pulsewidth (full width, half maximum value). In the experimental set-up the 1573 nm output coupling reflectivity was optimised for maximum output energy, but the actual value of output coupling was unknown. The value of 50% was taken from the separate resonator result, where the value of the output coupler that produced optimum efficiency was known.

The pulseshapes measured for maximum output energy at 1064 nm and 1573 nm wavelengths are shown in Figure 7-28, along with the depleted 1064 nm pulseshape. The integrated intensity profiles were scaled to their pulse energy to ensure the relative intensities were to scale and the intensities were then normalised to the peak intensity of the pump pulse.

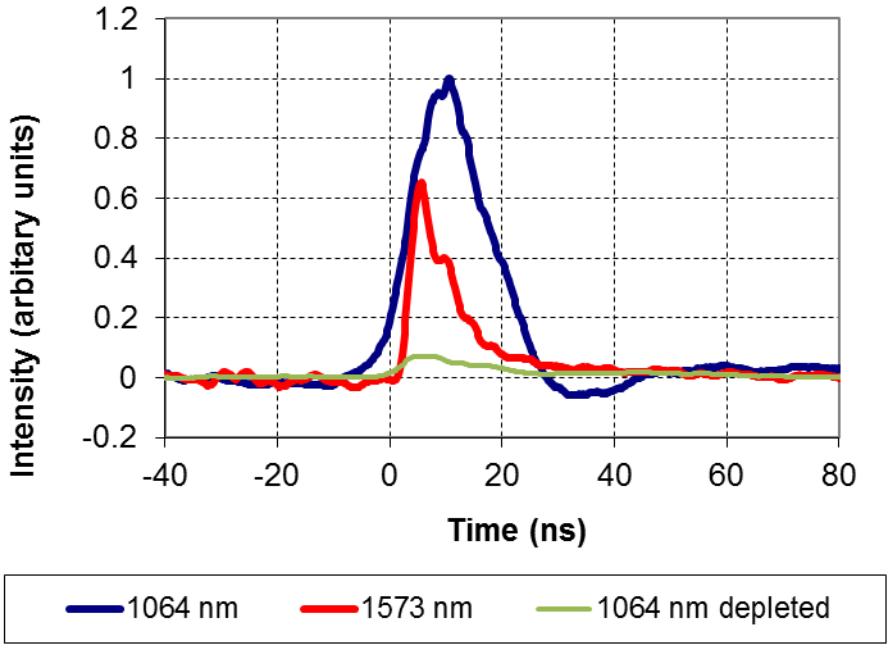

Figure 7-28: Measured pulseshapes of 1064 nm output and 1573 nm output.

The equivalent pulseshapes that were produced by the computer model are shown in Figure 7-29.

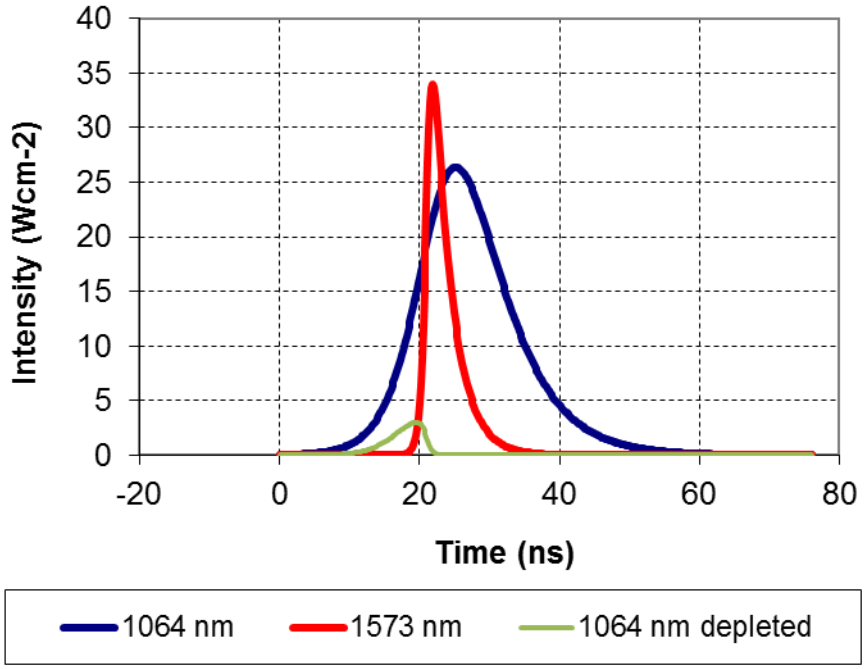

Figure 7-29: Modelled pulseshapes of 1064 nm output and 1573 nm output.

There is good agreement with the output energy measured and predicted. However, the measured pulsewidth value was approximately 2.5 times wider than the predicted value. The reason for this is unclear. The sensitivity of the output energy to output coupling was shown to be low in both experimental and modelled cases, with the reflectivity varying from 40% to 60% producing a maximum reduction in output energy of approximately 10% in both cases (with the 60% reflectivity output coupler). The effect of output coupling on 1573 nm pulsewidth was assessed using the computer model. For variation in output coupling reflectivity from 40% to 60% the pulsewidth changed from 3.2 ns to 4.4 ns, respectively. This range of pulsewidths is shorter than the 8.4 ns experimental value.

7.8 CONCLUSIONS

A common resonator intracavity OPO design was successfully aligned in a breadboard demonstration using a combination of dual wavelength versions of preferred production-standard and COTS optics. A conversion efficiency of 40% was achieved for 36 mJ output of 1573 nm eye-safe light from a 90 mJ laser at 1064 nm. This is superior to the typical extracavity OPO conversion efficiency value of 35%. No laser induced damage occurred in this design, even when prelase was observed during the alignment stages. A value for the common boresight of the 1573 nm and 1064 nm beams was measured to be within 250 µRad angular separation. This common boresight value will be unaffected by ambient temperature variations, and vibrations.

The 1573 nm output divergence was measured to be 10 mRad, which is likely to be unacceptable for the application. The reason why the 1573 nm output divergence is 8 times larger than the undepleted 1064 nm output divergence is suspected to be partly due to a proportion of OPA output rather than the transverse mode selective OPO output, due to high intracavity loss at the signal wavelength. The greatest contributor to the signal loss in this design is the absorption in the Nd:YAG slab, which was measured to be 14%, and is therefore unavoidable. This theory for the large divergence is supported by the result from the separate resonator, which had 4% rather than 29% intracavity loss at 1573 nm. This OPO resonator had a divergence of 8.55 mRad for a diffractive resonator length of 448 mm, which is compared with a divergence of 10 mRad for a diffractive resonator length of 721 mm in the case of the common resonator intracavity OPO.

Another reason for the reduced beam quality of the signal output is the reduced beam quality of the depleted pump when compared with the undepleted pump (divergence increasing from approximately 1 to 3 mRad). The higher intensity parts of the pump beam are converted more efficiently, which degrades its beam quality. In an intracavity OPO arrangement, this changing pump intensity pattern is resonated and therefore affects the signal intensity pattern, unlike in an extracavity OPO arrangement which dumps the non-converted pump. If the spatial beam intensity pattern could be time-resolved, the back end of the pulse would be expected to have a worse beam quality.

In addition to the effects described, backconversion from the signal and idler to the pump wavelength is known to have a detrimental effect on the signal beam quality [10].

The magnitude of backconversion is expected to be relatively small due to the strong absorption of the idler wavelength in the KTP crystals and other optical elements. The model used to predict the ICOPO energy did not show any effects of backconversion to the pump wavelength in the temporal pulseshape and neither did the experimental results.

The extracavity OPO had reduced conversion efficiency of 18-28% compared with 20-45% for the intracavity OPO (variation due to change in resonator lengths). The extracavity OPO had a divergence of 5.6 mRad for a diffraction resonator length of 249 mm. The improved divergence in this case may be explained partly by a reduction in the relative OPA to OPO ratio. The extracavity OPO would have lower intracavity pump intensity than the intracavity OPO, and therefore less conversion. In addition, the worsened beam quality of the depleted pump does not affect the signal beam quality as for the intracavity OPO case. A change to the output coupling from 50% to 60% reflectivity was required in the extracavity arrangement to maintain good conversion efficiency.

Note that the camera measurement overestimates the beam size, when compared with pinhole measurement, (by 6% for the 1573 nm beam and 15% for the 1064 nm beam).

The computer model confirmed the 1573 nm output energy measured, but the pulseshapes showed some discrepancy, with the measured 1573 nm pulsewidth approximately 2.5 times the modelled pulsewidth.

7.9 RECOMMENDATIONS

The larger divergence of the common resonator OPO is an issue and hence it is recommended that the root cause of this is determined. Investigation of the effect of thermal lensing due to idler absorption in the KTP crystals is recommended by using KTA crystals as an alternative, which do not absorb the idler wavelength.

A fail-safe mechanically positioned filter is required to block 1064 nm light when operating at the 1573 nm wavelength. Approximately 20 mJ needs to be reduced to an eye-safe level and a solution, such as a dichroic mirror, needs to be tested.

An alternative design, which has an output at 1573 nm only, could be investigated. An optimised design for this purpose may be a separate resonator, intracavity, nonplanar, unstable ring OPO, which would reduce the OPO signal divergence, when compared with a stable OPO resonator design. An unstable resonator can be made very compact with less effect on the beam quality or divergence. If the compactness of the design is crucial and a lower output energy is considered acceptable, a reduced slab size could be explored as a means of reducing the resonator Fresnel number and improving both the pump and the signal beam qualities.

The procurement of a dual-wavelength folding prism to replace the two prisms on the right hand side of the resonator (see Figure 7-2), would reduce the number of optical surfaces, hence the loss. In addition, the alignment would be simplified. Similarly, the procurement of a custom dual-wavelength image rotating prism to replace the three right-angle prisms on the left hand side of the resonator (see Figure 7-2) would again reduce loss and simplify alignment.

The common resonator could be shortened to decrease the build-up time of the OPO and increase the conversion efficiency. Unfortunately, this would be likely to have the effect of increasing the OPO M^2 value, due to the increased Fresnel number of the OPO resonator. However, an increased OPO output, relative to OPA output (due to the reduced build-up time loss), will offset this effect to some degree.

Measurement of the 1573 nm output coupling in the common resonator, the signal threshold and the slope efficiency for a number of output coupling reflectivities would enable calculation of the total intracavity loss in the common resonator at 1573 nm, using both Findlay-Clay and Caird analysis [9]. As the intracavity loss at 1573 nm due

to coating reflections and material absorption is known, the diffractive loss could be calculated. This would increase confidence in the value for diffractive loss used in the computer model, which was an approximate value based on previous work carried out at Selex ES. Measurement of the 1573 nm output coupling could be achieved using a suitable 1573 nm probe source reflected into the resonator and co-aligned with the output from the resonator. The proportions of reflected and transmitted light from the output polarising beam splitter is then measured to determine the resonator reflectivity.

It is recommended that a computer model to predict the divergence of the OPO output is created. This would work in the same way as the current laser model (described in Section 2.9.1), with the addition of parametric gain, which depletes the laser intensity profile inside the resonator, and produces a second transverse mode distribution at the signal wavelength, which also resonates. A third transverse mode distribution at the idler wavelength is also required to predict the effect of backconversion.

7.10 REFERENCES

[1] W. Koechner, "*Solid-State Laser Engineering",* Springer New York (2006)

[2] A. E. Siegman, "*Lasers",* University Science Books (1986)

[3] J. S. Lounsbury, *"Distributed Temperature Sensing with Neodymium-Doped Optical Fiber"* PhD thesis, Oregon State University (2012)

[4] M. Henriksson, L. Sjöqvist, V. Pasiskevicius, and F. Laurell, *"Cavity length resonances in a nanosecond singly resonant optical parametric oscillator",* Optics Express, vol. 18, pp. 10742-10749 (2010)

[5] R. Dabu, A. Stratan, C. Fenic, C. Luculescu, and L. Muscalu, *"Eye-safe singly resonant KTP parametric oscillator pumped inside a Nd:YAG laser cavity"* Optical Engineering, vol. 40, pp. 455-459 (2001)

[6] R. Dabu, C. Fenic, and A. Stratan, *"Intracavity Pumped Nanosecond Optical Parametric Oscillator Emitting in the Eye-Safe Range*", Applied Optics, vol. 40, pp. 4334-4340 (2001)

[7] M. J. McCarthy and D. C. Hanna, *"All-solid-state synchronously pumped optical parametric oscillator"* Journal of Optical Society, Am. B, vol. 10, pp. 2180-2190 (1993)

[8] Byer. R. L, *"Optical parametric oscillators"*, IEEE J. of Quantum Electronics, 588-702 (1975)

[9] R. Scheps, J. F. Myers, and S. A. Payne, *"End-pumped Yb-doped fluorapatite laser",* IEEE Photonics Technology Letters, p. 1285 (1993)

[10] A. V. Smith, W. J. Alford, and T. D. Raymond, *"Comparison of a numerical model with measured performance of a seeded, nanosecond KTP optical parametric oscillator",* Journal of Optical Society, Am. B, vol 12, no. 11 p. 2253 (1995)

7.11 APPENDIX 1: HEAT DUE TO 1573 NM ABSORPTION VS HEAT DUE TO LASER QUANTUM DEFECT IN THE SLAB.

The heat in the laser slab due to quantum defect between pump energy and laser energy

=1-808/1064 = 24% of absorbed pump energy

The heat in the laser slab due to 1573 nm absorption

=0.76×0.4×0.14 = 4% of absorbed pump energy

(quantum defect in laser × efficiency of OPO × percentage absorbed)

The ratio of these heat values is 6.

CHAPTER 8. CONCLUSIONS

8.1 SUMMARY OF KEY ACHIEVEMENTS

A variety of research areas have been explored, all with the common goal of improving the current laser system designs which are manufactured at Selex ES, and used on airborne platforms for targeting applications. A number of products rely on the same resonator design, which is the subject for most of this thesis.

The design investigated during Chapters 3 to 6 is a diode-side-pumped Nd:YAG slab laser which uses a zig-zag beam path within a cross Porro prism resonator. This resonator design, which supports a plane-wavefront, is used because it is insensitive to perturbations of the resonator optics, which is important when operating over the full military environment of vibration and temperature.

In Chapter 3, an investigation was carried out to ensure that all resonators had adequate output coupling adjustment, set by the polarisation state of the laser mode, following some issues encountered during laser system production. A computer model was used to analyse both the polarisation state inside the resonator and the output coupling that was possible, while optical element angles were adjusted. Experimental results verified the modelled output coupling. A short-term and a long-term solution, which improved output coupling adjustability, were successfully put in place for a number of laser system designs. These solutions were firstly simple adjustments to optical element angles and secondly a change to the retardance value of a waveplate that was used for polarisation adjustment.

Motivated by another laser system production issue, the long-term intermittent pre-lase problem, a change to the laser resonator design was explored in Chapter 4. An expensive phase-matched coating on the TIR surfaces of a Porro prism was tested over temperature, and found to perform poorly. The important parameter is the extinction ratio of the polarisation state, which ensures hold-off of the Q-switched laser resonator. An alternative design was investigated in which the phase-matched coating was removed, and the retardance value of an existing waveplate in the resonator was altered to compensate for the depolarisation produced by the Porro prism. A computer model

was used to calculate the required waveplate retardance, for which two possible solutions existed. These two waveplates were procured and tested experimentally, showing good agreement with theory. The 398° retardance value was chosen due to superior tolerance to angular adjustment and temperature variations. The Q-switch leg of the new resonator design was tested over the required temperature range above ambient and found to out-perform the original design. In addition, angular tolerance analysis of the resonator optics was carried out to ensure that the design was robust and suitable for manufacture. There were significant cost savings associated with this design change, due to both the removal of the reliance on the low-yield optical coating and on the increased production efficiency enjoyed with the eradication of pre-lase issues due to the Porro prism assembly. This work package attracted Finmeccanica's most prestigious "Gold Innovation Award" in recognition of the value to the business.

Chapter 5 encompassed a number of studies into the cause, effects, and potential solutions to thermal lensing in the Nd:YAG slab. The beam quality of laser systems was found to be adversely affected by thermal lensing and an issue related to the growth of the near-field intensity pattern was the focus of this Chapter. Depolarisation due to stress-induced birefringence was ruled out as the cause of beam quality degradation early in the investigation. Modelling of the slab assembly was carried out using finite element analysis and this improved understanding of the problem and helped to develop a number of potential solutions which were tested experimentally. Two solutions stood out as showing promise for long-term laser resonator design. The Nd:YAG slab is isosceles trapezoidal in shape to produce a zig-zagging of the laser transverse mode, which effectively averages the temperature gradient and gain distribution in one axis. The first solution involved the matching of the slab pump length to the laser transverse mode folding length in the Nd:YAG slab, and was shown to affect the thermal lens experienced by the laser beam. The second solution which showed promise was the change to 885 nm pumping instead of the traditional 808 nm pumping, which had the effect of reducing the heat load in the Nd:YAG slab to approximately half the original value. A reduction of the average thermal lens from -0.1 D to -0.05 D was demonstrated, which led to an improvement in the laser beam quality M^2 value from 6.5 to 3.5. In addition, the divergence growth exhibited with 808 nm pumping over a 60 s firing duration was eliminated. There is a reduced pump absorption associated with the change in wavelength, which requires a 20% increase in laser diode current to compensate. The wall-plug efficiency is reduced in this case, but is potentially avoidable with the redesign of the pumping arrangement to increase the absorption

length in the Nd:YAG slab. Alternatively redesign can be avoided if the reduction in efficiency is deemed acceptable.

Two deformable bimorph mirrors (BMs) were tested in a high energy diode-pumped Nd:YAG slab laser resonator, reported in Chapter 6. They were used to improve the beam quality in both the plane-plane resonator and the inherently more stable cross Porro prism resonator, in which repeatable performance was much more readily achieved. Both BMs produced brightness enhancements in the laser resonators when compared with the unmodified resonators. The largest measured enhancement in brightness was a factor of 2.2 using BM 1 in the cross Porro prism resonator. This equated to a reduction in the divergence from 1.46 mrad to 0.95 mrad, and a corresponding decrease in the M^2 parameter from 4.8 to 3.2. In this optimised configuration the maximum focal power of the bimorph mirror was measured to be approximately -0.2 D, which is not at the limit of curvature for either BM.

The final investigation in Chapter 7 saw a common resonator intracavity OPO design successfully aligned in a breadboard demonstration. A conversion efficiency of 40% was achieved for 36 mJ output of 1573 nm eye-safe light from a 90 mJ laser at 1064 nm. This is superior to the typical extracavity OPO conversion efficiency value of 35%. A value for the common boresight of the 1573 nm and 1064 nm beams was measured to be within 250 μRad angular separation, which is within typical requirements. This important common boresight value will be unaffected by ambient temperature variation, and vibration, which is not so readily achieved in the current laser system design using an extracavity OPO.

The 1573 nm output divergence was measured to be 10 mRad, which is not ideal for the application. The reason why the 1573 nm output divergence is 8 times larger than the 1064 nm output divergence, rather than the 3-4 times seen in the current extracavity set-up, was found to be in part due to a large proportion of OPA compared with OPO output, due to high intracavity fundamental intensity and high intracavity loss at the signal wavelength. Additionally, a change to the fundamental transverse mode, due to spatially selective depletion of the high intensity regions, was subsequently found to have an adverse effect on the signal beam quality. Backconversion in an OPO is also known to reduce beam quality. Although the magnitude of backconversion in the ICOPO and the effect on the signal beam quality is unknown, it is expected to be relatively small due to the strong absorption of the idler wavelength in the KTP crystals

and other optical elements. No evidence of backconversion was observed in the temporal pulseshape measurements.

An intracavity OPO computer model was used to predict the 1573 nm output energy, which was in good agreement. The modelled pulseshapes however showed some discrepancy with the measured results, and the measured 1573 nm pulsewidth was approximately 2.5 times wider than the modelled pulsewidth. The reason for the discrepancy is unclear, but the model did not consider the overlap of the pump and the signal beam intensity patterns.

8.2 PROSPECTS FOR FUTURE WORK

When developing laser systems in future, it is recommended that a model driven engineering method is used. The established laser modelling software can be updated to include new optical elements and predict the performance of new resonator designs. The issues that were addressed in Chapters 3 and 4 can both be avoided by predicting the polarisation state at the polarising beam splitter. This will predict the output coupling that is achievable and the extinction ratio that is produced in the Q-switch leg of the resonator. A robust laser model will allow the resonator design to be optimised before optical elements are procured.

It is clear that the use of optical coatings to produce a relative phase shift between s- and p-pol components of light is generally a bad idea due to the variations in supply and the cost. The use of uncoated TIR surfaces and retardance plates is much more reliable and predictable. Compound optical elements which produce an equal phase shift on both polarisation components are highly recommended if they are cost effective, as their performance will be consistent over temperature. These could be used to produce simpler designs without using custom retardance waveplate, as was done in Chapter 4.

The recommendation for thermal lens reduction in new resonator designs is that the pump width is designed to match an integer number of bounce lengths. Other pumping schemes have been investigated out with this thesis, to produce a design which is less sensitive to the temperature of the pump diodes. This is achieved by increasing the pump length so that changes to the pump wavelength, and therefore the absorption

coefficient, can be tolerated with minimal drop in output energy. This pumping arrangement is recommended for use with 885 nm pumping, in which the absorption coefficient is lower than with traditional 808 nm pumping.

Incorporation of a Bimorph Mirror into an existing cross Porro prism resonator design is not straightforward. It will be easier to incorporate the bimorph mirrors in new laser designs, where this component can be included from the beginning of the design cycle. Recommendations for the use of intracavity adaptive optics are dependent on the specification requirements of future laser products and on the development of other methods to reduce thermal lensing. If higher average power laser resonators are required, and some residual thermal aberrations are unavoidable, then transient effects will exist in the first few seconds of firing before the thermal lens is established. In this case, intracavity adaptive optics would be recommended for the compensation of this effect by keeping the resonator stable while the thermal aberrations change. However, significant development of the technology including the drive electronics is required. A compact set-up for optimisation of the resonator brightness inside the product chassis would need to be investigated. In addition, a change to the bimorph mirror design to allow 45° incidence is recommended to make the resonator design simpler. Environmental testing and possibly subsequent development of the bimorph mirror technology is required before it is used inside a laser product.

There are other opportunities for investigation of a bimorph mirror inside a resonator demonstrator, without incorporating them into laser system products. It would be informative to use a wavefront sensor to measure the wavefront profile before and after the optimisation of the resonator brightness. In addition, the measurement of an optimised bimorph mirror shape could be used to produce a fixed refractive phaseplate for aberration correction inside a resonator. This could also be achieved using a measurement produced by the wavefront sensor, once the relationship between initial wavefront and the required mirror shape for optimised brightness is established.

Based on the research in Chapter 7, the investigation into the common resonator intracavity OPO has continued in 2013. The beam quality has been improved by a factor of approximately two by the rotation of the KTP crystals about the z-axis away from normal incidence. There is not currently a clear explanation for this phenomenon. Further work is recommended to extend the computer modelling to increase understanding of the parameters which affect the signal beam quality, by resonating both the fundamental and signal complex electric field patterns. An increased

confidence would result from additional verification of the models. By carrying out Findlay-Clay and Caird analysis of the resonator losses, a more accurate value for the diffractive loss as a function of resonator length would be gained.